Characterising ^{111}In-anti-γH2AX-TAT in targeting the DNA damage signal associated with Wnt activated Colorectal Cancer

PhD

Maria Konstantinou

2014 - 2017

Sêr Cymru Richard Whipp Studentships

Contents

Declarations

This work has not been submitted in substance for any other degree or award at this or any other university or place of learning, nor is being submitted concurrently in candidature for any degree or other award.

Signed…… (candidate) Date …….

STATEMENT 1

This thesis is being submitted in partial fulfillment of the requirements for the degree of Ph.D.

Signed…… (candidate) Date …….

STATEMENT 2

This thesis is the result of my own independent work/investigation, except where otherwise stated, and the thesis has not been edited by a third party beyond what is permitted by Cardiff University's Policy on the Use of Third Party Editors by Research Degree Students. Other sources are acknowledged by explicit references. The views expressed are my own.

Signed…… (candidate) Date …….

STATEMENT 3

I hereby give consent for my thesis, if accepted, to be available online in the University's Open Access repository and for inter-library loan, and for the title and summary to be made available to outside organisations.

Signed…… (candidate) Date …….

Acknowledgements

I am very grateful for being given the opportunity by the late Prof Alan Clarke to work on this project and be part of his group. I would like to thank my supervisors Prof Matt Smalley, Dr Trevor Hay and Dr Paul Shaw for their constant support, and for the hours they have spent to read through this thesis. This project was in collaboration with Dr Bart Cornelissen and his group member Dr James Knight to whom I am very grateful for performing the radioactive-treatments and SPECT imaging and for sharing with me their knowledge in nuclear medicine.

This project would not have been possible without my funders, the Life Sciences Research Network and the Richard Whipp studentship which was generously provided by Anne Whipp.

I would like to thank all the members of both ARC and MJS groups for their invaluable help. Special thanks to Matt Zverev who for a long time was performing the mouse genotype and to Valerie Meniel, Karen Reed, Boris Shorning, Maddy Young, Howard Kendrick, Geraint Parfitt, Juan Menendez Gonzalez and Giusy Tornillo for teaching me various techniques. I would also like to thank Prof Owen Sansom who kindly offered to help on any issues we faced on our projects, after the sad loss of Prof Alan. I would like to acknowledge the valuable guidance of my assessor, Prof Trevor Dale, and his group members, Luned Badder and Andrew Hollins, for providing the human CRC spheroids for my project.

Special thanks to Dr Lee Parry and Dr Steph May for providing mice for my experiments, to Dr Catherine Hogan and Dr Fernando Afonso for reassuring me that everything was going to be okay and to Dr Joaquín De Navascues for his smart mathematical mind that taught me how to automate a tedious staining quantification procedure.

I am thankful to Noha Mohamed and my flatmates Andreia Silva, Ana Padilha and Carlotta Olivero, for being there for me, anytime I needed to talk to someone. Lastly, I owe a big thank you to my mum who has always been supportive and encouraged me to follow my dreams.

List of Figures

List of Tables

Abbreviations and definitions

Symbols		CRC	Colorectal Cancer
°C	Degrees Celsius	CIN	Chromosomal Instability
µg	Micrograms	CBC cells	Crypt-Base-Columnar cells
µl	Microlitres	cm	Centimetre
µm	Micrometre	Cre	cyclization recombination
µM	Micromolar	Cre^{ER}	Cre recombinase-Estrogen
>	Higher than		receptor fusion transgene
<	Lower than	CT	Computer Tomography
≥	Equal to or higher than	**D**	
≤	Equal to or lower than	DAB	3,3-diaminobenzidine
±	Plus and minus	dH2O	distilled water
=	Equal to	DMEM/F12	Dulbecco's Modified Eagle
A	Adenine	DNA	Deoxyribonucleic Acid
ABC	Avidin Biotin Complex	DSB	Double strand breaks
Apc	Adenomatous Polyposis Coli	DSH	Dishevelled
ATM	Ataxia Telangiectasia Mutated	DTT	Dithiothreitol
ASEF	APC-stimulated GEF	DLG	Discs large homolog
APH1	anterior pharynx-defective 1	DLL	Delta-like
B		dRP	5' deoxyribose-phosphate
BMP	Bone Morphogenic Protein	dpc	days post coitum
BMPRIA	bone morphogenetic protein	DTPA	diethylenetriaminepentaacetic
	receptor, type IA		acid
BSA	Bovine Serum Albumin	DOTA	Tetraazacyclododecane-1,4,7,10-
BER	Base Excision Repair		tetraacetic acid
bp	Base Pair	**E**	
BLAST	Basic Local Alignment Search	E-cadherin	Epithelial Cadherin
	Tool	EDTA	Ethylenediamine Tetra-acetic
BSA	Bovine Serum Albumin		Acid
bp	Base Pair	EGFP	Enhanced Green Fluorescent
Bmi1	B cell-specific Moloney murine		Protein
	leukemia virus integration site 1	EPR	enhanced permeability and
BrdU	Bromodeoxyuridine		retention
C	Cytosine	EGFR	Epithelial Growth Factor
CK-1 α	casein-kinase 1α		Receptor

ERCC1	excision repair cross-complementing-1		Virus-1
		I	
EMA	European Medicines Agency	ITLC	Instant Thin Layer
EpCAM	epithelial cell adhesion molecule		Chromatography
ER	Estrogen Receptor	IgG	Immunoglobulin-G
EC	electron capture		Medium: Nutrient Mixture F-12
F		IP	Intraperitoneal
FAP	Familial Adenomatous Polyposis	IHC	Immunohistochemistry/cal
		IBD	inflammatory bowel disease
FBS	Fetal Bovine Serum	IR	Ionizing Radiation
FSC	Forward Scatter	IDL	insertion-deletion loops
Frz	Frizzled GPCR receptor	K	
FISH	fluorescent *in situ* hybridization	KDa	Kilodaltons
FDA	Food and Drug Administration	kg	Kilograms
G		K-RAS	Kirsten Rat Sarcoma viral oncogene homolog
GPCR	G-Protein Coupled Receptor		
GRG	Groucho-related gene	L	
GEF	guanine nucleotide-exchange factor	l	Litre
		Lgr5	Leucine-rich repeat-containing G-protein coupled receptor 5
G	Gauge		
GSK-3	Glycogen Synthase Kinase-3	LEF	Lymphoid enhancer factor
Gy	Gray	loxP	Locus of crossover of Bacteriophage P1
GLI	Glioma-associated protein		
GREM	Gremlin	LRP	low-density lipoprotein-receptor related protein
GAB	Grb2–associated binding		
H		LKB1	liver kinase B1
H&E	Heamatoxylin and Eosin	LNTD	linear no-threshold dose
H2AX	H2A histone family member X	Lrig1	Leucine-rich repeats and immunoglobulin-like domains protein 1
h	Hour		
Hh	Hedgehog		
HBSS	Hank's Balanced Salt Solution	LRC	label-retaining cell
HRP	Horse Radish Peroxidase	M	
HECTD1	HECT domain 1	MUGA	multigated acquisition
Hopx	Homeodomain-only protein homeobox	Msi1	Musashi homologue 1
		MLH1	mutL homolog-1
Hhip-1	hedgehog interacting protein	MSH	MutS homologue
HIV-1	Human Immunodeficiency	mTORC	mechanistic target of rapamycin

	complex
M-cells	Microfold cells
MEF	Mouse Embryonic Fibroblasts
mg	Milligrams
MIN	Multiple Intestinal Neoplasia
min	minutes
mm	Millimeters
MMR	Mismatch Repair
MBq	Megabequerel
mRNA	Messenger Ribonucleic Acid
MYH	MutY homolog
MAP	MYH-Associated Polyposis
MRI	Magnetic Resonance Imaging
miRNA	microRNA
Math1	Mouse Atonal homologue 1
mGy	milligrays
N	
NGS	Normal Goat Serum
NRS	Normal Rabbit Serum
NLS	Nuclear Localisation Signal
NEU	N-nitroso-N-ethylurea
O	
o/n	Overnight
OCT	Optimal cutting temperature compound
P	
PBS	Phosphate Buffered Saline
Pen-Strep	Penicillin - Streptomycin
PFA	Paraformaldehyde
PLL	Poly-L-Lysine
p.i.	Post induction
PI3K	Phosphatidylinositol-3-Kinase
PTEN	Phosphatase and tensin homolog deleted on chromosome ten
Prom1	Prominin 1
pSer	Phospho-Serine
PEN2	presenilin enhancer 2
PTCH1	patched homologue-1
PIK3CA	PI3K catalytic subunit-α
PTB	phoshotyrosine binding
PIP3	phosphatidylinositol-3,4,5-trisphosphate
PDK	phosphoinositide-dependent kinases
PP-2A	protein phosphatase-2A
PHLPP	PH-domain leucine-rich-repeat-containing protein phosphatases
POL	Polymerase
PCNA	proliferating cell nuclear antigen
PMS2	Postmeiotic Segregation Increased, S. Cerevisiae, 2
PDGFRA	platelet-derived growth factor receptor alpha
PET	Positron Emission Tomography
R	roentgen
RBP-J	recombination signal binding protein for immunoglobulin κ J region
RNA	Ribonucleic Acid
RTK	receptor tyrosine kinase
RISC	RNA-induced silencing complex
rpm	Revolutions Per Minute
rt	Room Temperature
rcf	Relative Centrifugal force
RIC	Radioimmunoconjugate
ROS	Reactive Oxygen Species
RPA	replication protein A
RIA	radioimmunoassay
S	
SDS	Sodium Dodecyl Sulphate
SDS-PAGE	Sodium Dodecyl Sulphate Polyacrylamide Gel Electrophoresis
sec	Seconds

SSC	Side Scatter	**U**	
SMAD	small body size/mothers against decapentaplegic	U	Units
		USP15	Ub-specific protease 15
SH2	SRC homology 2	UV	Ultraviolent
SE-HPLC	Size Exclusion-High Performance Liquid Chromatography	UNG	uracil-DNA glycosylase
		V	
		V	Volts
SOS	Son of Sevenless	*VilCre^{ER}*	Villin Cre-recombinase ER transgene
SSBs	Single strand breaks		
T	Thymine	v/v	Volume per Volume
TERT	telomerase reverse transcriptase	**W**	
TA	Transit-Amplifying	w/v	Weight per Volume
Taq	DNA polymerase from Thermusaquaticus	wt	Wild Type
		Wnt	Wingless-related Integration site
TAT	Transactivator of transcription		
TOP1	topoisomerase 1	**X**	
TBE	Tris Borate EDTA	XP	xeroderma pigmentosum
TBS/T	Tris Buffered Saline with Tween 20	X, x	times
		XRCC1	X-ray repair cross-complementing protein 1
TEMED	N,N,N,Nteramethylethylenediamine		
		Other	
Tcf/Lef	T-cell factor and Lymphoid enhancer factor	^{111}In	Indium-111
		$^{111}InCl_3$	Indium-111 Chloride
TGF-β	Transforming Growth Factor-β	3D	Three-dimensional
TACE	Tumour necrosis factor-α-converting enzyme	18F-FDG	fluorodeoxyglucose-18
TFIIH	transcription factor II Human	β-TrCP	Beta-transducin repeat-containing protein
T/B	tumour-to-blood	βNF	β-napthoflavone

Abstract

Background: Colorectal cancer (CRC) is the third most commonly diagnosed cancer in the UK and has a poor 60% 5-year survival rate. The Wnt signalling pathway is fundamental for homeostasis of the intestinal epithelium and its deregulation drives development of CRC and induces DNA damage. Histone-2AX (H2AX) is a component of the nucleosome whose phosphorylated form, γH2AX, is a marker of DNA damage.

Objectives: Using a well-characterised inducible CRC mouse model of early Wnt deregulation, and established *Apc*-deficient driven tumour and *ex vivo* organoid models, we have assessed whether the spontaneous DNA damage generated in these models can be targeted using ^{111}In-anti-γH2AX-TAT (RH2AX), a radio-labelled antibody targeting γH2AX.

Methods: Deletion of the Apc gene was effected in the intestine of *Vil*Cre^{ER}*Apc*$^{fl/fl}$ and *Lgr5*Cre^{ER}*Apc*$^{fl/fl}$ models by intraperitoneal or oral induction with tamoxifen. γH2AX immunohistochemical (IHC) characterisation of intestines were performed as well as γH2AX whole mount immunofluorescent analysis on organoids derived from them. RH2AX, an anti-γH2AX antibody conjugated to the cell-penetrating peptide TAT to allow cellular internalisation and nuclear localisation, was used in these models as an imaging agent SPECT/CT imaging and biodistribution studies were conducted after oral induction of *Vil*Cre^{ER}*Apc*$^{fl/fl}$ and intravenous injection of RH2AX. γH2AX and Lgr5 FACS analysis were carried out on intestinal crypt cells of *Vil*Cre^{ER}*Apc*$^{fl/fl}$ mice expressing *Lgr5*-EGFP reporter.

Results: Intestinal *Apc* deficiency increased DNA damage levels in the small intestine of both dysplastic (*VilCre^{ER}Apc$^{fl/fl}$*) and tumour CRC mouse (*Lgr5Cre^{ER}Apc$^{fl/fl}$*) models. *Apc*-deficiency-associated DNA damage is most likely generated through WNT signalling pathway activation and, more specifically, by *c-Myc* transcription. For the first time, we demonstrated that intestinal dysplasia can be identified through *in vivo* SPECT imaging, using low SA RH2AX treatment. Low SA RIC treatment in intestinal dysplasia increased the DNA damage levels in healthy and *Apc*-deficient small and large intestines, increased proliferation in the *Apc*-deficient tissue and resulted in variable levels of apoptosis depending on the tissue.

Conclusion: These findings together indicate that DNA damage is induced by *Apc*-deficiency, and that there is the possibility to exploit the endogenously-increased DNA damage signal, γH2AX, to attract the RH2AX for *in vivo* imaging of intestinal dysplasia. This could help diagnose early stages of CRC to provide patients with the appropriate treatment sooner and increase their survival.

1. Introduction

1.1 The Mammalian Intestine

1.1.1 Gross structure and function of the small intestine

The small intestine is an organ of the gastrointestinal system that has evolved to efficiently absorb nutrients from the breakdown of food. The small-intestinal wall is comprised of the mucosal surface, the submucosal stroma, the muscularis propria and the serosa. The mucosal surface is the innermost layer that surrounds the lumen of the intestinal tube and comprises the continuous simple columnar epithelium, the lamina propria (which contains blood and lymphatic vessels originating from the submucosa) and the muscularis mucosae (a thin smooth muscle layer; Young *et al.* 2013). The mucosal epithelium is responsible for the secretion of various digestive enzymes (disaccharidases, peptidases, phosphatases) to facilitate the breakdown of macronutrients (Miller and Crane 1961; Peters 1970). The epithelial cells are able to absorb monosaccharides, amino-acids, free fatty-acids and monoglycerides (Goodman 2010). The submucosa is connective tissue in which blood and lymphatic vessels, as well as enteric neuronal cells, reside. The muscularis propria facilitates the movement of partially digested food (or chyme) through the lumen of the intestine by peristalsis, which is the coordinated contraction between the circular muscle layer and the longitudinal muscle layer. Finally, the serosa is a connective tissue with a simple squamous epithelial layer that helps to prevent friction which occurs during movement of the bowel. Lymph nodes present in the mucosa or the submucosa of the small intestine (Peyer's patches) initiate the immune response in the lamina propria or the epithelium (Macdonald 2003).

1.1.2 Organization of the mucosal epithelium

The intestinal mucosa consists of a continuous monolayer of epithelial cells. The epithelial layer extends from the intestinal invaginations (the crypts of Lieberkühn), towards the tip of finger-like structures called villi (Figure 1.1). These structures, forming the intestinal 'brush border', increase the absorptive surface area of the intestine and topographically distinguish progenitor cells (in the crypt) from terminally differentiated cells (in the villus; Helander and Fandriks 2014; Barker *et al.* 2007).

The brush border is constantly exposed to various dietary antigens as well as commensal microbiota or parasitic microbial pathogens from food consumption. Therefore, multiple innate defence mechanisms are employed to sustain epithelial integrity, such as quick cell turn-over (every 4-5 days), cell extrusion and innate immunity (Kim *et al.* 2010). All the cells that reside in the epithelium originate from stem cells situated at the bottom of the crypts of Lieberkühn (Barker *et al.* 2007). There are approximately 5-6 active stem cells [crypt base columnar (CBC) cells] per human crypt, which divide every 48-72 hours (h) symmetrically or asymmetrically to give rise to other stem cells (self-renewal) or progenitor cells (Yang *et al.* 2015; Morrison and Kimble 2006; Potten *et al.* 1992). Murine crypts are significantly shorter than in humans and the intestinal stem cells divide 3 times more rapidly (every 24h) (Kellett *et al.* 1992). At the forth position from the base of the crypt, the +4 quiescent stem cells reside. The +4 cell identity is still under investigation; however some studies suggest that, upon CBC stem cell loss they divide to replace them (Carulli *et al.* 2014). The immature progenitor cells, generated after CBC stem cell division, are known as transit-amplifying (TA) cells and they occupy the rest of the crypt length. TA cells divide 2-3 times, once every 12h, while migrating gradually towards the crypt-villus junction. Their highly proliferative nature is essential for the repopulation of the epithelium and therefore, its integrity. When they finally reach the base of the villus, they stop proliferating and commit to an absorptive or secretory cell lineage (Carulli *et al.* 2014). Cells committed to an absorptive lineage become enterocytes whereas those committed to a secretory lineage become either goblet, Paneth, enteroendocrine, Tuft or Microfold cells (M-cells). The terminally-differentiated cells continue their gradual migration towards the top of the villus, where they eventually die and are shed into the lumen. Figure 1.1 shows a schematic representation of the different cell types in the intestinal epithelium.

The cells at the base of the TA region can differentiate to give rise to Paneth cells which stay within the crypt base (Barker 2014). Paneth cells are specialized secretory cells that migrate towards the bottom of the crypt and are intermixed with stem cells. Their position facilitates the maintenance and modulation of stem and progenitor cells through secretion of signals. Moreover, the secretion of antimicrobial molecules by Paneth cells is one of the innate immune

mechanisms against pathogens and concomitantly helps the establishment of microbiota (Clevers and Bevins 2013). Enterocytes are the predominant differentiated epithelial cells of the mucosa, which absorb nutrients. Goblet cells are also present in the epithelium and secrete mucus, which is essential for epithelial lubrication and anti-bacterial protection (Johansson and Hansson 2013). Another type of matured cell of the intestinal epithelium is the enteroendocrine cell. Upon stimulation by micronutrients and microbial products, they secrete hormones into the bloodstream to achieve an endocrine effect, transmit the hormonal signal to the enteric nervous system or diffuse hormones locally in an autocrine or paracrine mode. Enteroendocrine cells modulate food intake, gastrointestinal tract movement as well as mucosal immunity and repair (Engelstoft *et al.* 2008; Moran *et al.* 2008). Tuft or brush cells, whose function is still unclear, are thought to play a role in chemoreception and initiation of type-2 mucosal immunity after parasitic infection or allergic reaction (Gerbe *et al.* 2016; Chandrakesan *et al.* 2016). M-cells are responsible for the immunosurveillance of the lumen. These differentiated cells reside on the epithelium over Peyer's patches and lymphoid follicles and they sample antigens and whole microbes in order to present them to the immune system lying underneath them (Peterson and Artis 2014).

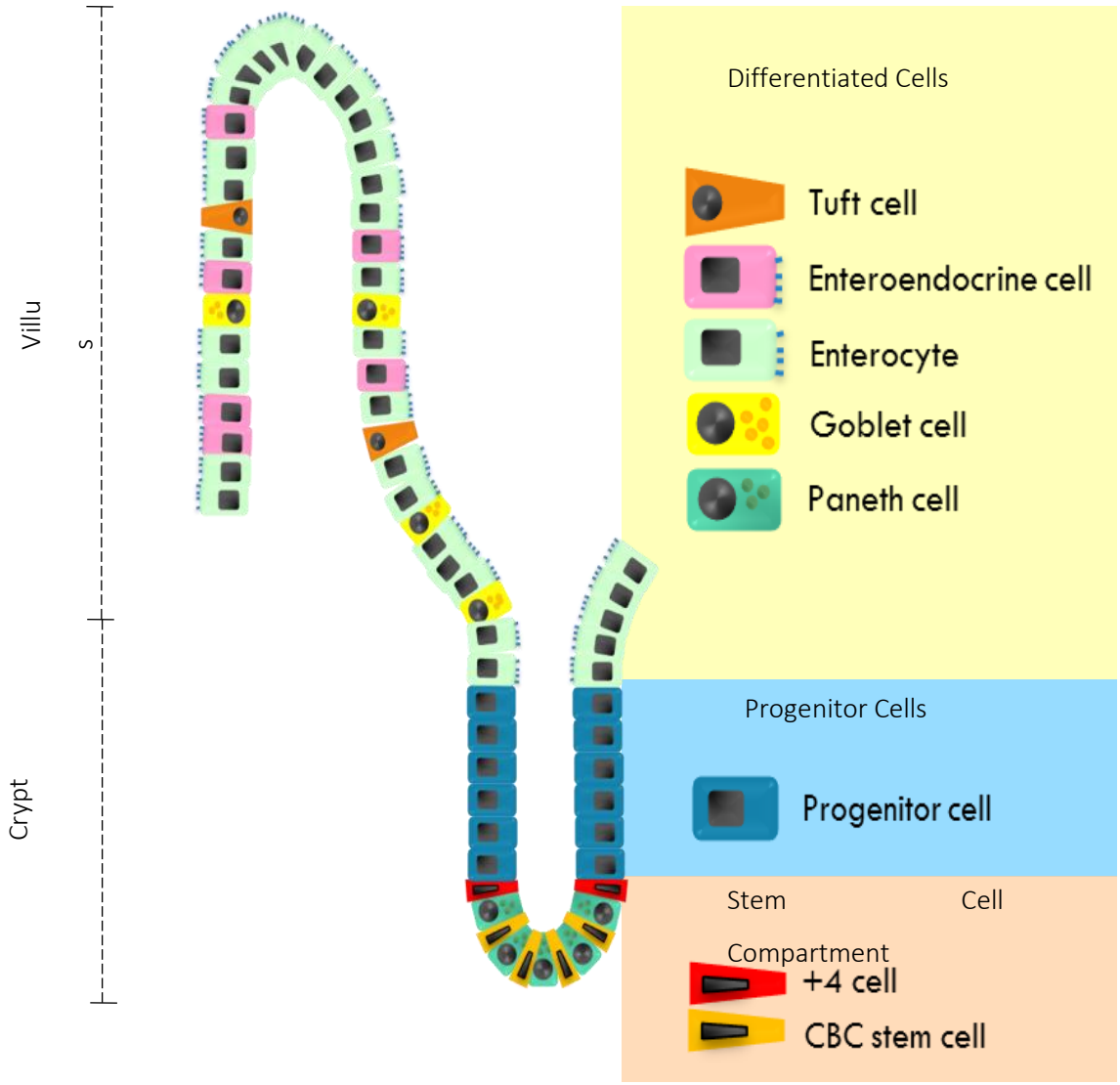

Figure 1.1 Mammalian small intestine crypt-villus structure.

The structure of the small intestinal epithelium is divided into crypts and villi. Within the bottom of the crypt, crypt base columnar (CBC) cells reside next to paneth cells. A more quiescent stem cell, namely +4 cell, is present at the fourth cell position from the bottom of the crypt. Progenitor cells are localized within the transit-amplifying region of the crypt; these cells divide and differentiate into absorptive enterocytes, secretory goblet, enteroendocrine, tuft and Paneth cells (Carulli *et al.* 2014).

1.1.3 Intestinal stem cells

Adult stem cells, residing within the base of the intestinal crypt, are responsible for the renewal of the tissue (Cheng and Leblond 1974). Stem cell behavior is sustained by the microenvironment or 'niche' (Schofield 1978). The stem cell niche in the intestine consists of the surrounding epithelial cells (mainly Paneth cells), myofibroblasts, enteric neurons, infiltrating immune cells, extracellular matrix as well as cell-associated ligands and soluble signals present within the stroma which surrounds the crypts, or provided by Paneth cells (Brittan and Wright 2004; Tan and Barker 2014).

A true stem cell is potentially able to self-renew indefinitely and generate progenitor cells that in turn will give rise to the rest of the terminally differentiated intestinal cell types, during homeostasis or injury, whilst the parental stem cells remain undifferentiated (Potten and Loeffler 1990). Stem cell replication is a highly-regulated process which needs to be coordinated with the rate of cell death, occurring at the villus tip, in order to avoid excessive cell loss or aberrant accumulation of cells.

Stem cell division can result in three outcomes. The maintenance of the stem cell population under normal circumstances is achieved by asymmetric division, the most common of all three, which results in one daughter stem cell and a daughter progenitor cell. This allows the self-renewal of the stem cell compartment as well as the expansion of the TA region that will repopulate the crypt-villus (Potten and Loeffler 1990). In contrast, upon tissue injury, stem cells divide symmetrically into two stem cells to expand their numbers and replenish the stem cell pool. Alternatively, a stem cell divides into two daughter progenitor TA cells, which will eventually differentiate; this leads to the extinction of that stem cell lineage. Hence, symmetric cell division contributes to intestinal population homeostasis rather than individual cell homeostasis (Shahriyari and Komarova 2013). When stem cells are damaged and incapable of repopulating the TA zone, a potential stem cell from the TA zone, which is the progeny of a crypt base stem cell, can de-differentiate back to true-stem cells (Potten and Loeffler 1990). This concept is discussed in detail below. The plasticity of outcomes from a stem cell division is important for the maintenance of normal intestinal homeostasis, given the numerous damaging factors which cells face persistently, including carcinogens, digestive enzymes and microorganisms (Barker 2014).

Adult stem cell identity

Intestinal stem cell identity has been debated since the 1970s. The 'stem cell zone' model was suggested by Cheng and Leblond (1974) and postulated that stem cells are the crypt base columnar (CBC) cells. In contrast, the model suggested by Potten (1977) proposed that stem

cells reside immediately above the Paneth cells. Based on recently discovered markers for both candidate stem cell populations, it seems like the truth lies somewhere in the middle, with distinct stem cell populations responsible for adult epithelial homeostasis and regeneration upon damage.

The stem cell zone model

Cheng and Leblond (1974) performed one of the first intestinal stem cell lineage experiments which suggested that CBCs were the cells of origin of the terminally differentiated epithelial lineages. Taking advantage of their observation that CBCs could phagocytise neighbouring dead cells, they induced intestinal cell death by irradiating mice and showed that the surviving fraction of CBCs contained phagosomes with tritiated thymidine, which had been administrated to mice before irradiation and was incorporated into all replicating cells. By 6h, the labelled thymidine was present in cells at the crypt-villus junction and by 12h in those at the tip of the villus. Those cells included the four major epithelial cell types. However, all four radiolabelled cell types could not be identified in the same crypt, arguing against the hypothesis of CBCs being the multipotent stem cells.

Bjerknes and Cheng (1999) introduced heritable somatic mutations, using N-nitroso-N-ethylurea (NEU) mutagenasis, in random cells of crypts. Persistent labelled clones which contained all epithelial cell lineages always included a CBC cell, successfully proving the presence of a self-renewing stem cell and reinforced the idea of CBC cells being these cells. Short-term mutant clones that existed for 14 days were also observed which signified that mutations in TA cells can be passed, through division and differentiation, to all intestinal epithelium lineages, but as those cells could not replenish their own TA cell population; these mutations were lost with the death of their progeny.

In the stem cell zone model, adult stem cells reside at the crypt base, where the niche is, and divide giving rise to daughter progenitor cells residing in the midcrypt above the 5^{th} position from the crypt base (+5 cells). Away from the niche these cells commit to differentiation. Progenitor cells localized in the transit-amplifying region divide and differentiate migrating towards the villus whereas Paneth progenitor cells differentiate and migrate towards the base of the crypt, intercalating with CBC cells. Barker *et al.* (2007) used *in vivo* lineage tracing and *ex vivo* studies to identify that CBCs express the Leucine-rich repeat-containing G-protein coupled receptor 5 (LGR5) receptor, now one of the most widely used intestinal stem cell (ISC) markers (Sato *et al.* 2009; Barker *et al.* 2007).

LGR5 is an intestinal stem cell Marker

Leucine-rich repeat-containing G-protein coupled receptor, LGR5, is an adult ISC marker (Sato et al. 2009; Barker et al. 2007). In vivo, LGR5 expressing (LGR5+) cells are highly proliferative, as demonstrated by BrdU assays, and they can give rise to long lasting (at least 60 days) multilineage clones that all originate from CBCs (Barker et al. 2007). Moreover, single cell LGR5 flow-sorted cells can give rise to *in vitro*/*ex vivo* organoid cultures containing all epithelial lineages (Sato *et al.* 2009). *In vitro,* LGR5 is activated upon R-SPONDIN ligand binding which in turn activates canonical Wnt signalling (Carmon *et al.* 2011); *in vivo*, *Lgr5* depletion in adult intestine has little or no effect on Wnt signalling, ISC renewal or Paneth cell production (Garcia *et al.* 2009) in contrast to its homologue *Lgr4* (Carmon *et al.* 2017). Despite the fact that *Lgr4* deficient mice had a 2-fold reduction in proliferation and 85% fewer Paneth cells compared to wt, sorted $LGR4^{+}$ single cells were unable to give rise to organoids, signifying that they are not stem cells (de Lau *et al.* 2011). In addition, combined IHC and *in situ* mRNA expression of *Lgr4* showed staining in both CBCs and Paneth cells of the small intestine whereas in the large intestinal there was a widespread cytoplasmic staining which excluded the cells at the base of the crypts where CBCs reside (Yi *et al.* 2013). Hence, only LGR5 is considered as a true multipotent ISC marker despite it being apparently dispensable for ISC function *in vivo*. $LGR5^{+}$ cells were present in APC^{Min} adenomas (Barker *et al.* 2007) and it was later demonstrated that *Apc (Adenomatous Polyposis Coli)* tumour suppressor loss from the LGR5 cells could initiate tumourigenesis (Barker *et al.* 2009). Recently, LGR5 receptor, in the absence of R-SPONDIN, was demonstrated to promote cell to cell adhesion in normal adult crypt stem cells and colon cancer cells (Carmon *et al.* 2017). Considering the observations that stem cells usually have high levels of integrins that attach on the extracellular matrix of the basal lamina facilitating stem cell retention within the niche (Fuchs *et al.* 2004), $LGR5^{+}$ cells may have a competitive advantage over the differentiated $LGR5^{-}$ cells in remaining within the niche and therefore retaining their stem cell potentials through the signals that they receive (Carmon *et al.* 2017).

A model for population homeostasis driven by $LGR5^{+}$ CBCs

Insights into how CBCs maintain population homeostasis, by regulating their individual cell division towards self-renewal and/or differentiation, was provided by multi-colour Cre-reporter lineage tracing (Snippert *et al.* 2010). $LGR5^{+}$ cells labelled with different fluorescent proteins, unexpectedly divided in a symmetrical pattern giving rise to either two stem cells or two TA cells, which favoured population homeostasis rather than individual stem cell feature retainment. This means, for example, that an injured epithelium can be repopulated faster by symmetric division of stem cells compared to asymmetric division. This approach also provided evidence for stem cell neutral competition which was also supported by a mathematical model

(Snippert *et al.* 2010). Neutral competition allowed the initially multi-colour labelled CBC population to gradually, over time, become mono-chromatic due to stochastic refinement (neutral drift) of the stem cell population remaining within the niche through cell-cell competition and persistence of the CBC clone with the most advantageous characteristics.

In contrary, Quyn *et al.* (2010) study showed that +1 to +7 cells, from the crypt base, (which included both CBCs and the putative +4 stem cell) preferentially divide asymmetrically (Figure 1.2), retaining the template strand in the daughter stem cells and not differentiated cells (called the 'immortal strand' hypothesis), based on the relationship between mitotic spindle orientation and DNA segregation. However, apart from the lack of detail in this study regarding exactly which stem cell compartment preferentially divides asymmetrically, multiple subsequent studies have shown random DNA strand and chromosome segregation during division (Bellis *et al.* 2012; Escobar *et al.* 2011; Schepers *et al.* 2011; Steinhauser *et al.* 2012).

The symmetric CBC stem cell division model predominates the field; however, it remains unknown whether stem cell fate decisions, at the individual level, are purely stochastic or taken based on cell positioning and access to niche or other biochemical factors.

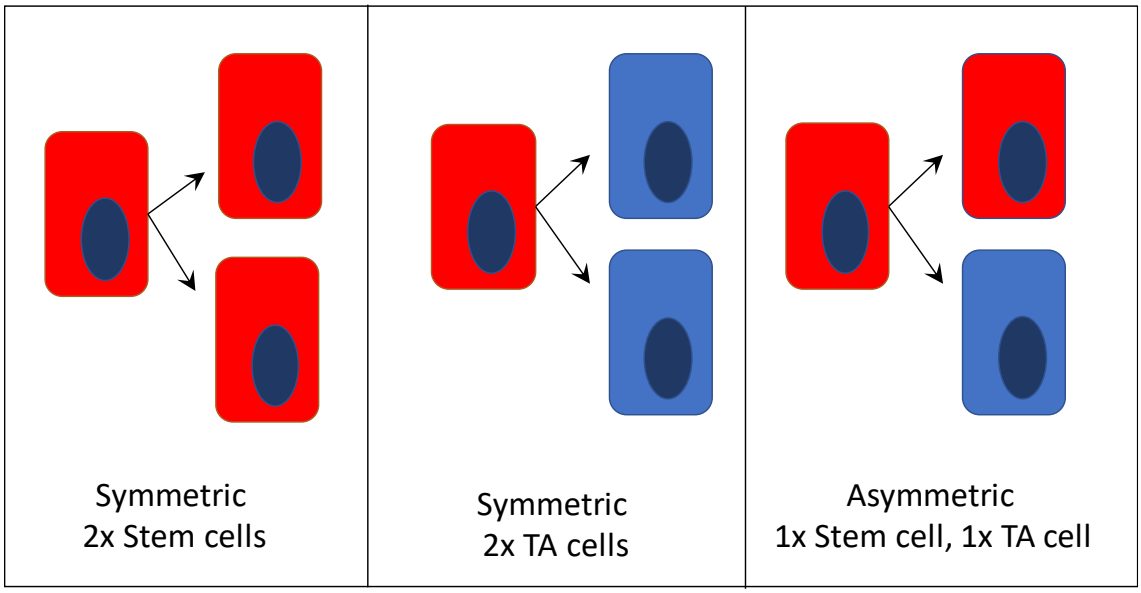

Figure 1.2 Symmetric and asymmetric stem cell division

Additional Intestinal stem cell Markers of the CBC cells

Sox9 is a Wnt target gene which encodes for the SOX9 transcription factor which modulates intestinal proliferation (Blache *et al.* 2004). *In vivo* enhanced GFP expression under the *Sox9* promoter (*Sox9-EGFP*) highlighted high and low GFP expression (*Sox9-EGFP*^{hi} and *Sox9-EGFP*^{low}, respectively) around the crypt base (Formeister *et al.* 2009). *Sox9-EGFP*^{hi} cells were post-mitotic enteroendocrine cells located around +4-6 crypt positions. *Sox9-EGFP*^{low} cells were co-localized with CBC cells and demonstrated to have stem-cell behaviours *ex vivo* (being capable of generating multilineage organoids) and *in vivo* using cell-lineage tracing (forming persistent clones stemming from SOX9^{+} cells throughout the intestine) (Van Landeghem *et al.* 2012; Furuyama *et al.* 2011; Formeister *et al.* 2009). Sometimes Paneth cells were also *Sox9-EGFP*^{low}; the authors of this study speculated that it was remnant GFP protein originating from SOX9^{+} cells, Paneth cell progenitors, before they become mature Paneth cells (Formeister *et al.* 2009).

Musashi homologue 1 (*Msi1*) encodes a RNA-binding protein which regulates NOTCH signalling and plays a role in the proliferation of stem cell in the nervous system (MacNicol *et al.* 2015). Antibody-based staining identified CBC cells as MSI1^{+} and showed that APC^{Min} tumours had high expression of MSI1 (Potten *et al.* 2003; Kayahara *et al.* 2003). In addition, fluorescent *in situ* hybridization (FISH) identified the expression of single *Msi1* mRNA molecules in the TA region (Itzkovitz *et al.* 2012).

Prominin 1 (*Prom1*) or CD133 encodes for a cell-surface glycoprotein whose role as a cancer stem cell marker of epithelial cancers has been debated (O'Brien *et al.* 2007; Shmelkov *et al.* 2008). Its usefulness as an intestinal CBC stem cell marker is also unclear. FISH on small intestine has identified CBC cells expressing Prom1 mRNA and through *in vivo* cell lineage tracing it was demonstrated that some PROM1^{+} cells have adult stem cell behaviours (Zhu *et al.* 2009). However, an independent study suggested that PROM1^{+} cells include most of the proliferative crypt zone and that it was mostly TA cells giving rise to the clones observed through the cell lineage tracing (Snippert *et al.* 2009)

The +4 model

Cell-tracking studies by Cairnie *et al.* (1965) brought about the first indications of cells residing at the 4th position from the crypt base, named +4 cells, behaving like stem cells. Later, Potten (1977) also described the presence of a stem-cell like population at +2 to +7 cell positions of the crypt (+4 position on average) that was radio-sensitive, a a surrogate feature of stem cells that could possibly protect their progeny from acquiring mutations. He reported that these +4 cells divided every 24h, as demonstrated by BrdU label incorporation, and that they were able to divide asymmetrically, such that the DNA label was retained in one of the daughter cells under

physiological conditions (Potten *et al.* 2009). These features of the putative +4 stem cell were attributed to the 'immortal strand hypothesis' (Cairns 1975), according to which the (labelled) template DNA strand is preferentially retained upon division, while the newly synthesized DNA strand is inherited by the TA progeny cells as a protective mechanism to spare stem cells from possible mutations arising from DNA replication errors (Potten *et al.* 2009). However, this hypothesis is based on the assumptions that +4 cells only divide asymmetrically and that DNA exchange between sister chromatids does not occur as normally happens in somatic cells (Lansdorp 2007).

An alternative explanation to the DNA label-retaining features of +4 cells is the "Silent Sister" hypothesis. Falconer *et al.* (2010) used the consistent orientation of pericentric major satellite DNA, with respect to murine chromosome telomeres, to label by fluorescence *in situ* hybridization sister chromatid segregation in post-mitotic cells. They identified a subset of cells having a non-random sister chromatid segregation pattern. This was attributed to the different epigenetic status of sister chromatid centromeres which permits chromatid-specific chromosomal segregation during metaphase through kinetochore microtubules preferentially binding on one of two sister chromatids (Westhorpe and Straight 2015). The epigenetic marks of genes are regulated, by preservation or alteration, during DNA replication (Lansdorp *et al.* 2012). Therefore, the regulation of epigenetic marks on stem cell genes present on sister chromatids differentially inherited from the parental stem cell might be another mechanism by which cell self-renewal and/or differentiation decisions are made during daughter cell maturation (Lansdorp 2007). The progeny cells, depending on which sister chromatid they have received, would have differential transcriptional patterns, allowing them to retain the parental stem or differentiated cell features. The "Silent Sister" hypothesis however, remains to be confirmed through combination of sister chromatid identity information and gene expression data (Lansdorp 2007).

Currently, the lack of reliable and solely +4 cell markers make it difficult to prove the radio-sensitivity or any other stem cell trait of this cell population. Multiple genes have been found to be expressed in the candidate +4 cell stem cell population based on *in vivo* lineage tracing studies. However, each candidate label-retaining cell (LRC) gene (discussed below) proposed marked phenotypically distinct epithelial cell populations which did not correlate with the originally proposed LRC characteristics described by Potten (1977).

+4 cells and putative stem cell markers

Bmi1 which encodes a ring finger protein and is a component of the polycomb group complex 1, is responsible for self-renewal of hematopoietic and neural stem cells (Sangiorgi and Capecchi

2008). *Bmi1* mRNA FISH analysis in the proximal small intestine highlighted the +4 cell position, a finding validated using the *Bmi1-EGFP* transgenic mouse model (Tian *et al.* 2011). *In vivo* cell lineage tracing using a knock-in transgenic mouse model under the *Bmi1* promoter, has proven that BMI1 cells have adult stem cell features and that their ablation hampered intestinal epithelium renewal. In addition, isolated $BMI1^+$ cells when cultured *ex-vivo* in 3D produce multilineage organoids (Yan *et al.* 2012; Tian *et al.* 2011). However, these studies did not specifically locate BMI1 cells to the +4 region. Multiple subsequent studies have found BMI1 expression present throughout the proliferative crypt region (Muñoz *et al.* 2012; Powell *et al.* 2012; Montgomery *et al.* 2011; Itzkovitz *et al.* 2012) and *Bmi1-CreER^{T2}* mouse models have also shown the presence of $BMI1^+$ cells throughout the crypt area, including the CBC region, which might explain the cell-lineage data initially observed (Tian *et al.* 2011).

Homeodomain-only protein homeobox (Hopx) gene encodes for an atypical homeodomain protein which cannot bind DNA (Mariotto *et al.* 2016). *Hopx-lacZ* reporter mice showed expression of HOPX at the +4 cell position throughout the intestine (Takeda *et al.* 2011). In this study, $HOPX^+$ cells were radio-resistant and able to exit from their quiescent state and proliferate, upon IR injury. *In vivo* cell lineage tracing, using the *Hopx–ires–CreER^{T2}* mouse model, supported the multipotent stem cell features of cells at the +4 position. In addition, evidence supporting the interconversion between the two candidate intestinal stem cell populations (i.e. $LGR5^+$ CBCs and +4 cells) was provided by gene expression profiling of $HOPX^+$ and their progeny, showing that the progeny of $HOPX^+$ cells have high expression of *Lgr5* and other CBC markers. In contrast, *ex vivo* organoid assays showed that the progeny of self-renewing $LGR5^+$ CBCs give rise to $HOPX^+$ cells (Takeda *et al.* 2011). Contrary to this study, which showed expression of HOPX solely in +4 cells, are the findings of Muñoz *et al.* (2012) which demonstrated by FISH expression analysis that *Hopx* is expressed not only in +4 cells but throughout the crypt, with the highest expression being at the CBC $LGR5^+$ cells. The correlation between protein and mRNA expression levels is subject to numerous biological (e.g. translation regulators, protein half-life) and technical factors (e.g. identification technique and experimental errors) (Maier *et al.* 2009). Thus, HOPX is not a robust marker for the identification of the +4 quiescent cell population, specifically.

Leucine-rich repeats and immunoglobulin-like domains protein 1 (*Lrig1*) is a transmembrane protein which functions as a negative feedback regulator of the ERBB receptor tyrosine kinase (RTK) family in adult tissues. It is a marker of epidermal stem cells and regulates their proliferation (Jensen *et al.* 2009). *In vivo* lineage tracing using the *Lrig1-ires-CreER^{T2}* transgenic mouse model identified the presence of long-term clones throughout the small intestine, suggesting the behaviour of a multipotent stem cell (Powell *et al.* 2012). Despite this, the LRIG1

gene reporter was present in a range of crypt base and lower TA compartment cells (+2 to +5 positions) which was also confirmed by *in situ* and IHC analyses (Wong *et al.* 2012; Powell *et al.* 2012; Muñoz *et al.* 2012). There is evidence showing co-expression of *Lrig1* and *Lgr5* in both the small and large intestine. Muñoz *et al.* (2012) performed a transcriptome analysis of $LGR5^+$ cells in the small intestine showing that they highly expressed *Lrig1*. Similarly, in the colon, *Lrig1* was sometimes co-localized with $LGR5^+$ CBC cells. Added to these, some $LRIG^+$ cells were actively proliferating whereas others were quiescent, but could proliferate upon IR-induced injury (Powell *et al.* 2012) which suggests that this marker is expressed in two different stem cell populations. The expression profiles of $LRIG^+$ and $LGR5^+$ colonic cells showed distinct transcriptomes, reiterating their distinctive features, but had similarities in the levels of candidate +4 marker expression (BMI1, PROM1 and TERT, discussed in the next paragraph). The main difference between the cell types was the expression of oxidative stress response markers and negative regulators of proliferation specifically in $LRIG^+$ cells only (Powell *et al.* 2012). *Apc* gene loss from $LRIG^+$ cells, using the *Lrig1-*$Cre^{ERT2/+}$*;*$Apc^{fl/+}$ mice, caused adenoma formation, suggesting that these cells divide and pass their mutations to their progeny, of which some remain within the crypt, suggesting multipotent stem cells (Powell *et al.* 2012). LRIG1 cannot, therefore, be used as a specific marker of +4 stem cells only.

High expression of telomerase reverse transcriptase (TERT) in stem cells is thought to guard against replication-induced senescence (Breault *et al.* 2008). While *TERT-GFP* reporter mice showed rare GFP expression at the +4 position (Breault *et al.* 2008), in quiescent, LGR5-negative radio-resistant cells (Montgomery *et al.* 2011), FISH analysis showed, in contrast, *Tert* mRNA expression in $LGR5^+$ cells and TERT activity, as measured by RT-PCR (reverse transcription-polymerase chain reaction), in all crypt proliferative cells (including strongest activity in $LGR5^+$ CBC cells) (Schepers *et al.* 2011; Itzkovitz *et al.* 2012). Although apparently contradictory, the findings of these studies are consistent with *in vivo* lineage tracing, which showed a small portion of $TERT^+$ cells being actively cycling and contributing to adult intestinal homeostasis, whereas the quiescent cell fraction could only proliferate upon IR induced damage in both small and large intestines (Montgomery *et al.* 2011). Thus, it seems that different *Tert* labelling and detection approaches detect different functional compartments.

An intestinal cancer stem cell?

The existence of a small portion of cancer cells, the 'cancer stem cells', which can initiate and sustain tumourigenesis because of their ability to self-renew, like non-malignant stem cells was firstly hypothesized by Schofield (1978). Evidence supporting this hypothesis was provided by Bonnet and Dick (1997) who showed that only a subset of human acute myeloid leukaemic cells (CD34++/CD38-) could initiate leukaemia in immunocompromised mice. Similar transplantation

studies have been carried out on subsets of cells from human colorectal cancer (Dalerba *et al.* 2007; Ricci-Vitiani *et al.* 2007; O'Brien *et al.* 2007). Successful transplants, which indicated the presence of cancer stem cells within the fraction of transplanted cells, were those that could colonize the site of transplantation and develop tumours histologically similar to the primary tumour. Dalerba *et al.* (2007) identified that transplantation potential (of cancer stem cells) was highly enriched in cells with high expression of epithelial cell adhesion molecule (EpCAM) and cell surface expression of CD44 and CD166 ($EpCAM^{hi}$/CD44+/CD166+). Ricci-Vitiani *et al.* and O'Brien *et al*. also showed that CD133 (PROM1) cells could initiate tumourigenesis, hence CD133 was proposed as a CRC stem cell marker. Contradictory data from subsequent studies, however, have shown that $CD133^-$ cells could also establish tumours when transplanted in mice, sometimes even more efficiently than $CD133^+$ cells, and that CD133 was expressed throughout the crypt-villus axis (Shmelkov *et al.* 2008).

A recent study showed that human $LGR5^+$ cancer cells act as cancer stem cells. Shimokawa *et al.* (2017) introduced a Cre-inducible multi-colour rainbow reporter into the *LGR5* locus of cells from human CRC organoids and showed that their xenotransplantation in immunodeficient mice, and subsequent induction of Cre recombination, initially labelled cells on the outside region of the engrafted organoid. Over several days, the colour-labelled clones took over the whole tumour area and persisted for months. Despite all tumour cells being labelled, signifying their cancer stem cell origin, not all of them were $LGR5^+$, evidence of the ability of $LGR5^+$ cancer stem cells to give rise to differentiated daughter cells as well as self-renew. Shortly after genetic ablation of $LGR5^+$ cancer stem cells (in LGR5-iCaspase9 organoids that in the presence of a dimerizer, $LGR5^+$ cells expressing an inucible form of Caspase9 undergo apoptosis due to Caspase9 homodimerization) $LGR5^+$ cells were completly eradicated and the tumour decreased in volume. However, after some days tumours regrew and $LGR5^+$ cells re-emerged. It was speculated that re-emergence of $LGR5^+$ cells was due to plasticity of a small fraction of $LGR5^-$ and fully differentiated *KRT20* (*keratin-20*; a differentiation marker of intestinal epithelium) expressing cells. Collectively, these studies are in agreement with the cancer stem cell hypothesis but also indicate the potential of cells that do not initially have stem cell capacities to revert to stem cells under appropriate conditions.

1.1.4 Epithelial homeostasis

Intestinal epithelial homeostasis is a highly regulated process as any perturbation of the balance between proliferation, cell death, differentiation, migration and cell localisation may lead to abnormal accumulation or loss of cells, or aberrant organ function. The major signalling pathways responsible for the regulation of these processes through their cross-talk are: wingless-related integration site (Wnt) signalling, Notch/Delta signalling, transforming growth factor-β (TGF-β) and bone morphogenic protein (BMP) signalling, Hedgehog (Hh) signalling and phosphatidylinositiol 3- kinase (PI3K)/Akt signalling.

Wnt signalling pathway

The Wnt signalling pathway is important in morphogenesis during both embryogenesis and in adult tissue self-renewal homeostasis (Giles *et al.* 2003; Clevers 2006). The canonical Wnt signalling pathway has been thoroughly studied in the context of intestinal homeostasis due to the strong link between tumourigenesis and Wnt signalling dysregulation (Kinzler *et al.* 1991; Nishisho *et al.* 1991). It is activated in over 90% of all CRC cases (Giles *et al.* 2003).

In the absence of Wnt ligand, β-CATENIN binds to the 'β-CATENIN destruction complex', a scaffold formed by axis inhibitor-1 (AXIN-1) and APC that allows glycogen synthase kinase-3β (GSK-3β) and casein kinase-1α (CK-1α) to phosphorylate β-CATENIN (Figure 1.3). Beta-transducin repeat-containing protein (β-TrCP) of the E3 ubiquitin ligase complex recognizes β-CATENIN phosphorylation and catalyses its ubiquitination (Staal and Clevers 2005; Barker and Clevers 2006). Subsequently, ubiquitinated β-CATENIN undergoes proteasomal degradation (Clevers 2006), resulting in low levels of free β-CATENIN in the cytoplasm. This allows the interaction of Groucho-related gene (GRG) family repressors with the DNA bound Lymphoid enhancer factor/T-cell factor (LEF/TCF) proteins, which inhibits Wnt target gene transcription. Wnt signalling is normally activated by the binding of Wnt ligands on the Frizzled (FRZ) and low-density lipoprotein-receptor related protein (LRP) co-receptor complex (Clevers *et al.* 2014). Dishevelled (DSH) binds to activated FRZ and oligomerizes at the plasma membrane. The assembly of DSH allows the recruitment of GSK3β, which phosphorylates LRP, and AXIN-1 which is relocated at the plasma membrane (Gao and Chen 2010; Clevers *et al.* 2014; Clevers 2006). This prevents formation of the destruction complex, allowing β-CATENIN to become stabilized. The increased cytoplasmic levels of β-CATENIN, which is a transcriptional activator, allow its translocation to the nucleus where it interacts with LEF/TCF family proteins and recruits more co-activators that ensure efficient transcription of Wnt targeted genes (Barker and Clevers 2006; Clevers *et al.* 2014).

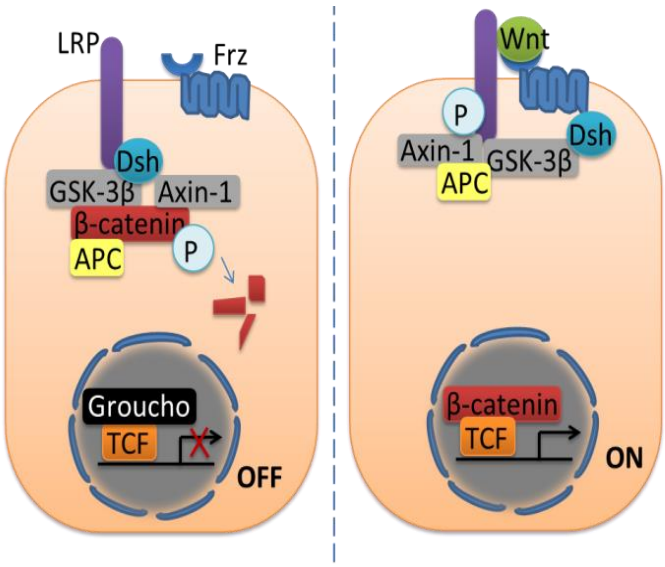

Adapted from Clevers *et al.* (2014)

Figure 1.3 Canonical Wnt signalling pathway.

In the absence of Wnt, β-CATENIN binds to the destruction complex consisting of AXIN-1, APC, GSK3β and CK-1α to be phosphorylated. Phosphorylated and ubiquitinated β-CATENIN undergoes proteasomal degradation (Clevers 2006). LEF/TCF protein activity in the nucleus is repressed by GRG family members' binding that does not allow the Wnt target gene transcription. Wnt signalling is normally activated by the binding of Wnt ligands on FRZ and LRP co-receptor complex which is aided by DSH (Clevers *et al.* 2014). DSH binds to FRZ and oligomerizes at the plasma membrane. The assembly of DSH allows the recruitment of GSK3β, which phosphorylates LRP, and AXIN-1 (Gao and Chen 2010; Clevers 2006; Clevers *et al.* 2014). The destruction of the AXIN-1, APC, GSK3β complex results in the stabilization of β-CATENIN and ultimately its translocation to the nucleus where it binds to LEF/TCF allowing the transcription of Wnt targeted genes (Clevers *et al.* 2014).

The base of the crypt, where the stem cells reside, exhibits the strongest Wnt signalling activation, gradually diminishing to being inactive at the crypt-villus boundary. Cells further up the crypt receive less Wnt signal from their surrounding cells and in addition to that, Wnt activity is suppressed by BMP pathway at the crypt-villus junction (Biswas *et al.* 2015). Therefore, cells within the crypt are able to proliferate due to activation of Wnt signaling target genes such as *c-Myc* and *Cyclin-D,* which allow progression through the cell cycle (Scoville *et al.* 2008).

The shape and migration of the cells within the crypt-villus axis is controlled by EPH receptors, which remodel the actin-cytoskeleton. The expression of EPHB2/B3 receptors and EPHRIN-B1 ligands is inversely regulated by β-CATENIN/TCF signaling on the transcriptional level (in the presence of an active β-CATENIN/TCF signaling *Eph2/B3* are transcribed, whereas *Ephrin-B1* transcription is downregulated; Batlle *et al.* 2002). The absence of EPHB3 receptor expression is restricted to the crypt base only, where the Paneth cells and CBC cells reside and is responsible for the Paneth cell positioning. EPHB2 is expressed strongly at the CBC zone and gradually declines towards the crypt-villus junction, where its expression is minimal. EPHRIN-B1 ligands on the other hand, are strongly expressed in the villi and gradually reduce within the crypt where they exhibit their lowest expression close to the CBC-Paneth cell zone.

CBCs and Paneth cells, present strictly at the bottom of the crypt, usually have nuclear β-CATENIN, indicative of an active Wnt pathway, compared to the membrane bound β-CATENIN present in cells elsewhere in the crypt. In EPHB2/B3 receptor-deficient mice, non-differentiated cells and their differentiated progeny (i.e. CBCs and TA or Paneth cells, respectively) are intermingled throughout the crypt axis. It is important to note that nuclear β-CATENIN localization is not strictly cell-autonomous, and is dependent on the positioning of the cell. This was evidenced by the absence of nuclear β-CATENIN in the stem and Paneth cells positioned away from the base of the crypt in EPHB2/B3 receptor-deficient mice, which highlights the importance of the niche signals and the supportive myofibroblasts. However, in CRC, nuclear β-CATENIN localization becomes a fully cell autonomous process, due to Wnt signalling hyperactivation coupled with loss of EPHRIN-B ligand expression (Batlle *et al.* 2002). EPHB2 receptor loss of expression has also been linked with poor CRC prognosis (Jubb *et al.* 2005; Lugli *et al.* 2007).

Cell fate determination is also regulated by Wnt signalling. *Tcf4* intestinal loss or the Dkk1 Wnt inhibitor block the generation of enteroendocrine cells, whereas overactivation of Wnt signalling halts differentiation of all cell types apart from Paneth cells (Madison *et al.* 2005; Pinto *et al.* 2003; Sansom *et al.* 2004). Early stages of enteroendocrine differentiation are dependent on Wnt signals, and hyperactivation of Wnt signalling at that stage can even result in

serotonin-expressing adenoma formation. However, the later stages of enteroendocrine lineage are Wnt signaling-independent (Moran *et al.* 2008) which is in agreement with the fact that Wnt signalling dysregulation alone in terminally differentiated cells cannot lead to progression of poorly proliferating lesions (Schwitalla *et al.* 2013).

The microenvironment can also modulate Wnt signaling which in turn, influences the fate of cells. For instance, dedifferentiation of post-mitotic intestinal epithelial cells with increased Wnt signaling activation is also possible upon concomitant activation of NF-κB signalling, a key transcription factor of inflammation, because it interacts with and enhances β-CATENIN DNA binding activity, further enhancing Wnt signalling activation effects. Dedifferentiation of non-stem cells with elevated Wnt signaling, allows their conversion into cells with tumour initiating capacity (Schwitalla *et al.* 2013), which also helps explain the reason that chronic intestinal inflammation increases the risk of CRC incidence (Axelrad *et al.* 2016).

Another way that Wnt signalling activation modulates cell fate determination is through the *Sox9* target gene. Its absence results in poor negative modulation of Wnt signalling through down-regulation of groucho-related corepressors, which leads to Wnt signalling hyperactivation and increased cell cycle activity, as well as affecting the secretory lineage development characterized by absence of Paneth cells and reduction in goblet cells (McDonald *et al.* 2012).

APC: A tumour suppressor

Structure and function of APC

The *APC* gene is located on chromosome 5q22.2 in humans, and in mice on chromosome 18 (Gene Cards/Human Gene Database; Kwong and Dove 2009). There is a high conservation of the *APC* gene coding regions between these two species with 90% of the amino acid sequence being identical (BLASTp search query ID: P25054 against the database of Mus musculus).

As Figure 1.4 depicts, the mammalian APC protein contains an oligomerization domain, an armadillo repeat-domain, a 15- or 20-amino acid residue repeat domain allowing β-CATENIN binding, an AXIN binding domain, a basic region for microtubule binding and a C-terminal domain that allows binding to the EB1 and DLG proteins (Polakis 1997).

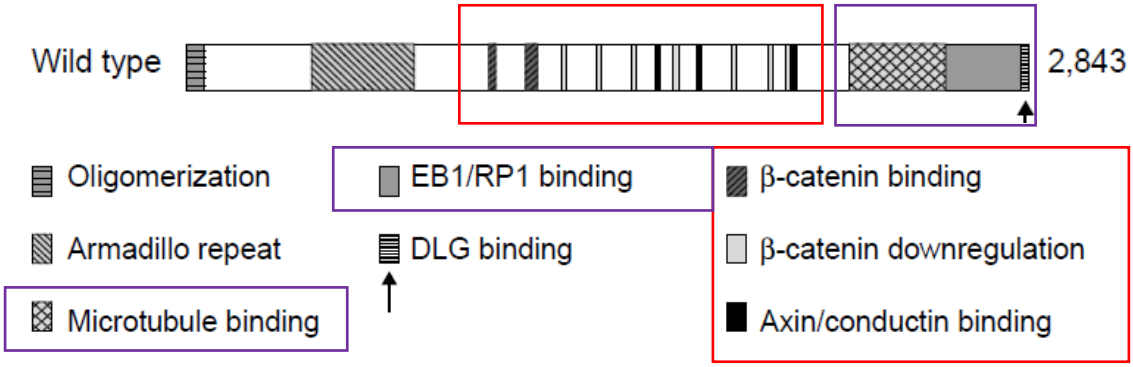

Figure 1.4 Apc protein structure.

Shapes and shaded boxes represent binding regions of the Apc protein with other proteins. Figure was adapted from (Riccardo Fodde, Kuipers, *et al.* 2001).

The N-terminus and central regions of APC facilitate binding with β-CATENIN, AXIN-1 and AXIN-2, a negative regulator of Wnt signalling which shares similar structure with AXIN-1, to facilitate formation of the β-CATENIN destruction complex. The C-terminus of the protein allows direct binding to microtubules of the cytoskeleton, as well as with EB1 family members, which bind to the extended ends of spindle and cytoplasmic microtubules and on centrosomes (Fodde et al. 2001; Fodde et al. 2001). In 2001, two groups demonstrated that APC mutation in embryonic stem cells result in chromosomal instability and spindle aberrations, evidence of APC involvement in chromosomal segregation (Kaplan *et al.* 2001; Fodde *et al.* 2001). Cytoplasmic APC can be found either in membrane protrusions, bound to the extending end of the microtubule cytoskeleton, or bound to the plasma membrane via actin cytoskeleton (Näthke *et al.* 1996; Rosin-Arbesfeld *et al.* 2001). APC is able to bind through its armadillo repeat domain to a RAC-specific guanine nucleotide-exchange factor (GEF), termed ASEF (APC-stimulated GEF; Kawasaki *et al.* 2003). This interaction can regulate the actin cytoskeletal network during lamellipodia formation and membrane ruffling. The binding of APC to ASEF stimulates its GEF activity, which decreases the E-CADHERIN and β-CATENIN mediated cell-cell adhesion, promoting cell migration (Kawasaki *et al.* 2003). This is an important aspect in CRC metastasis as it has been demonstrated using CRC cell line which contains APC truncations (SW480), that this leads to the aberrant motility of the cells (Kawasaki *et al.* 2003). Usually in CRC, APC is truncated in such a way that the β-CATENIN and microtubule binding domains of APC are missing, but the armadillo repeat domains are still functional. This seems to be sufficient for ASEF constitutive activation and aberrant cell migration of APC truncated cells which as it has been reported, cells with specific APC truncations have similar proliferation rates to APC wild-type (wt) cells early after transformation (Oshima *et al.* 1997), however due to their aberrant cell migration they are retained in the crypt and form early lesions (Kawasaki *et al.* 2003).

APC regulation

The regulation of APC activity is complex and takes place at the transcriptional, post-trancriptional and post-translational levels. In cancer, promoter hypermethylation of the *APC* gene leads to reduced APC expression in 18% of sporadic CRC and adenomas (this underscores its occurrence early during the development of CRC); methylation is more frequent (95%) at loci of wt *APC* alleles which is likely the reason that it does not occur in Familial Adenomatous Polyposis, FAP, CRC patients with germline *APC* mutations (Derks *et al.* 2006; Esteller *et al.* 2000; Arnold *et al.* 2004). At the post-transcriptional level, microRNAs (miRNA), ~22-nucleotide-long noncoding RNAs, are able to introduce the RNA-induced silencing complex (RISC) to complementary sites of their mRNA target, repressing in this way the mRNA translation or forcing them to be cleaved. Nagel and colleagues identified miR-135a and miR-135b (miR-135a&b) as regulators of APC whose function increases Wnt signalling activity. They have also observed the increased expression of miR-135a/b within colorectal adenomas and carcinomas coupled with reduction of *APC* mRNA levels suggesting their involvement in CRC development (Nagel *et al.* 2008). Moreover, a number of post-translational modifications occurring on effectors of the Wnt pathway can alter the status of the pathway (Gao *et al.* 2014). APC phosphorylation by GSK-3β increases the binding affinity of APC for β-CATENIN (Ikeda *et al.* 2000); similarly, the phosphorylation of APC on Ser-1279/Ser-1392 by CK1ε is crucial for the regulation of β-CATENIN (Rubinfeld *et al.* 2001). It was also shown that, Trabid, an uncharacterised deubiquitinase, interacts and deubiquitinates APC, and although its function remains unclear there is some evidence from epistasis analysis suggesting that it regulates TCF-mediated transcription (Tran *et al.* 2008). Ub-specific protease 15 (USP15) stabilizes APC by ubiquitination (Choi *et al.* 2004; Huang *et al.* 2009) while E3 ubiquitin-protein ligase HECTD1 (HECT domain 1)-mediated ubiquitination of APC leads to an enhanced binding to AXIN-1 which inhibits WNT signalling (Tran *et al.* 2013).

Regulation of Wnt target gene transcription

The mammalian LEF/TCF transcription factor family, which consists of LEF1, TCF1 (encoded by *Tcf7*), TCF3 (encoded by *Tcf7l1*), and TCF4 (encoded by *Tcf7l2*) plays the main role in the regulation of transcription of Wnt target genes. Differences in the transcriptional effects of different transcription factors occur; for example TCF3 and TCF4 usually lower the transcriptional levels of their target genes whereas TCF1 and LEF1 mostly enhance the transcription of their targets (Merrill *et al.* 2004). LEF/TCF proteins that recognize a consensus DNA-binding motif therefore may have redundant but also distinct functional features depending on cell type (Galceran *et al.* 1999; Merrill *et al.* 2001). Wnt signalling activation allows β-CATENIN to bind LEF/TCFs and also to attract co-factors for chromatin modification

(CBP/p300 and BRG1) that allow target genes to be efficiently transcribed (Lien and Fuchs 2014). An example of a co-activator is PYGO, the homologue of the *Drosophila* Pygopus protein (Hoffmans *et al.* 2005). In the absence of β-CATENIN, LEF/TCF is able to repress gene transcription by interaction with a tetramer of transducin-like enhancer of split (TLE) proteins, the mammalian homologues of the *Drosophila* Groucho transcriptional co-repressor (Roose *et al.* 1998). TLEs act as scaffolds for the recruitment of histone deacetylases (HDACs) to modify chromatin structure in a repressive way, and halt target gene transcription (Chen *et al.* 1999) rather than competing β-CATENIN for LEF/TCF binding (Daniels and Weis 2005; Chodaparambil *et al.* 2014). For example, in the absence of Wnt signal, TCF3 or TCF4 bound to Wnt response element on the promoter region of a gene target, recruits TLE tetramer which binds lysine 20 (K20) methylated histone H4 tails and promotes chromatin silencing. This results to more repressive complexes than when TLE is bound to TCF1 and LEF1 (Chodaparambil *et al.* 2014). Repressive complexes are also formed between C-terminal-binding protein (CtBP) and TCF4 that halt *Axin-2* transcription (Valenta *et al.* 2003). Thus, both TLE and CtBP have higher affinity for TCF3 or TCF4 rather than TCF1 or LEF1.

The binding of β-CATENIN on LEF/TCF proteins allows the transcription of different sets of genes implicated in essential cellular functions, such as proliferation (e.g., *MYC*, *CCND1*, *PPARD*), stem cell fate (*ASCL2*), survival (*ABCB1*, *BIRC5*), differentiation (*ID2*, *ITF2*, *ENC1*), migration (*MMP7*, *MMP14*), and angiogenesis (*VEGF*) (He *et al.* 1998; Tetsu and McCormick 1999; Shtutman *et al.* 1999; He *et al.* 1999; Jubb *et al.* 2006; Yamada *et al.* 2000; Kim *et al.* 2003; Rockman *et al.* 2001; Willert *et al.* 2002; Fujita *et al.* 2001; Crawford *et al.* 1999; Brabletz *et al.* 1999; Hlubek *et al.* 2004; Zhang *et al.* 2001).

TGF-β/BMP signalling pathway

The bone morphogenic protein (BMP) signalling pathway is important for intestinal development and homeostasis (Roberts 2000; Scoville *et al.* 2008). Juvenile polyposis and hereditary mixed polyposis are two hereditary CRC syndromes that occur from autosomal dominant dysfunctional members of the TGF-β/BMP signalling pathway. Moreover, 70% of sporadic CRC have inactivated BMP signalling. These data show the importance of the BMP signalling pathway in normal intestinal homeostasis and cancer (Kodach *et al.* 2008).

The transforming growth factor-β (TGF-β) ligand superfamily consists of two subfamilies, the BMP and the TGF-β ligands. These ligands bind on the TGF-β receptors which are classified into two types. Type I consists of the BMP receptor type (BMPR) -IA, -IB, or activin receptor-like kinase-2 (ALK2) and type II is comprised of activin receptor (ACVR-) IIA or IIB (Wakefield and Hill 2013; He *et al.* 2004; Shi and Massagué 2003; Scoville *et al.* 2008). BMP ligands bind the type II

TGF-β receptor homodimers, which are constitutively active, which in turn recruit, phosphorylate and activate type I receptor homodimers (Wakefield and Hill 2013; He *et al.* 2004; Shi and Massagué 2003; Scoville *et al.* 2008). This process is antagonised by the BMPRI inhibitor Noggin (Groppe *et al.* 2003). Activated Type I receptors phosphorylate SMAD (small body size/mothers against decapentaplegic) transcription factors. The receptor-activated SMADs (R-SMADs) 1, 5 and 8 form heterodimers with the co-SMAD SMAD-4 (Wakefield and Hill 2013). During active signalling, SMAD heterodimers are transported into the nucleus, where they bind to 5′-CAGAC-3′ and G/C-rich DNA sequences with low affinity. The affinity of SMAD heterodimers to DNA is increased by association with transcriptional co-activators or co-repressors (Shi and Massagué 2003). The activation of the TGF-β or BMP sub-family results in the engagement of distinct groups of R-SMAD proteins, which in turn can interact with various cell-type specific DNA-binding co-factors which allows selectivity of the target genes in response to distinct receptor-ligand interactions (Massagué 2000).

In 2004, Haramis *et al.* developed a mouse model expressing transgenic noggin under the *Villin* promoter which abolished both epithelial and stromal BMP signalling. Ectopic crypts in the villus epithelium were formed in adult mice, resembling Juvenile Polyposis syndrome associated with hamartomatous polyposis. Interpretation of this data suggested that BMP signalling suppresses *de novo* crypt formation and polyp growth in adult intestinal tissue (Haramis *et al.* 2004). However, Auclair *et al.* using a the *Villin*-Cre *Bmpr1a*$^{fl/fl}$ mouse model, which specifically ablated the activation of the BMP pathway within the intestinal epithelium only, showed that BMP is important for the terminal differentiation of cells towards the secretory lineage but is not sufficient for ectopic *de novo* crypt formation (Auclair *et al.* 2007). This supports the hypothesis that BMP signalling loss within the stromal compartment, rather than the epithelium, is driving neoplasia.

Notch/Delta Signalling

Notch signalling is important for development, stem cell regulation and cancer. The effects of the absence of this evolutionarily conserved signalling pathway was first observed in 1914 by John S. Dexter when he identified a subset of a *Drosophila melanogaster* fly population with characteristic notched wings, from which Thomas Hunt Morgan isolated the mutant *Notch* allele (Morgan 1917). The phenotype was a result of haploinsufficiency of the Notch receptor, which was sequenced in the mid-1980s (Wharton *et al.* 1985; Kidd *et al.* 1986).

Activation of Notch signalling begins with the interaction between a Notch receptor on one cell and a transmembrane ligand on an adjacent cell (Wilson and Radtke 2006). In mammals, there are multiple Notch receptors (Notch 1- 4) and multiple ligands namely, Jagged1 and 2 (the

Serrate ligand homologues of *Drosophila*) and Delta-like (DLL) 1, 3 and 4 (the Delta ligand homologues of *Drosophila)* (Radtke *et al.* 2004). The Notch receptor is expressed as one protein which is subsequently cleaved while transported to the cell membrane where the two pieces of the protein form a heterodimer. The interaction of the receptor with its ligand results in extracellular cleavage of the receptor by tumour necrosis factor-α-converting enzyme (TACE). The extracellularly cleaved Notch receptor is subsequently endocytosed by the ligand-expressing cell. Further cleavage occurs on the transmembrane part of the receptor by γ-secretase multiprotein complex comprised of presenilin, nicastrin, APH1 (anterior pharynx-defective 1) and PEN2 (presenilin enhancer 2). The released cytoplasmic tail of the receptor (the Notch Intra-Cellular Domain, NICD) translocates to the nucleus, where it binds to its transcription factor, CSL [CBF1 (C promoter-binding factor 1) in humans, Suppressor of Hairless in *Drosophila,* LAG in *Caenorhabditis elegans* and RBP-J (recombination signal binding protein for immunoglobulin κ J region) in mice] (Wilson and Radtke 2006) and displaces its co-repressors including NCOR1/2, CIR and KyoT2 (Wu *et al.* 2002) allowing the binding of co-activators including PCAF, GCN5, Mastermind-like-1 (MAML1) and p300 (Kurooka and Honjo 2000; Wu *et al.* 2000; Oswald *et al.* 2001). This activates the transcription of Notch target genes, including genes of HES (hairy and enhancer of split-1) and HEY (HES-related with YRPW motif) subfamilies such as *Hes-1* to *Hes-7* and *Hey1/2*. These encode transcription factors with basic helix-loop-helix (bHLH) domain (Katoh and Katoh 2007).

Tissue-specific Notch target gene transcriptional activation is achieved by expression of different transcriptional activators in various tissues and through expression of multiple Notch receptor paralogues, allowing the formation of different transcriptional complexes with CSL (Barolo and Posakony 2002; Tang *et al.* 2010). Added to these, the interaction of NICD with other transcriptional effectors, for example LEF-1, can also activate transcription (Ross and Kadesch 2001). Notch-independent expression of *Hes-1* and *Hey-2* through other pathways is also possible, though this mechanism of abrogation of CSL repressive function is unclear (Cave 2011).

Multiple studies have demonstrated the importance of Notch signalling in the regulation of intestinal homeostasis. In the context of the small intestine, post-natal conditional removal of *CSL, the transcriptional regulator* of Notch signalling (Artavanis-Tsakonas 1999), the use of γ-secretase inhibitors (Alzheimer's disease drug in clinical trials) (Milano *et al.* 2004; Wong *et al.* 2004), genetic depletion of both Notch-1 and Notch-2 receptors (Riccio *et al.* 2008) or DLL-1 and DLL-4 ligands in rodents (Pellegrinet *et al.* 2011) all lead to differentiation of the highly proliferating TA cells into goblet cells, at the expense of absorptive enterocytes, in normal intestinal crypts and adenomas. Reciprocal gain-of-function studies that over-expressed a

dominant active form of the Notch-1 receptor showed the opposite effect, i.e. the accumulation of progenitor cells within the crypt and the prevention of their differentiation (Fre *et al.* 2005; Stanger *et al.* 2005).

Math-1 (*Mouse Atonal homologue 1*) is a basic helix-loop-helix (bHLH) transcription factor regulated by CSL and HES-1. The activation of Notch signalling allows the binding of CSL on *Math-1* promoter which promotes *Math-1* expression, whilst at the same time Notch signalling indirectly repressing *Math-1* expression *via Hes-1* binding on its promoter (Shi *et al.* 2012). MATH-1 has an indispensable role in cell-fate regulation, as *Math-1* expression alone is sufficient for cell differentiation into the secretory lineage, whereas *Math-1* repression favours enterocyte differentiation (Yang *et al.* 2001; Shroyer *et al.* 2007; VanDussen and Samuelson 2010). Moreover, lineage tracing studies of Notch-active cells showed that they were long-lived progenitors that could generate all the intestinal epithelial cell types (Vooijs *et al.* 2007; Pellegrinet *et al.* 2011) and that Notch signalling activity in CBC stem cells is necessary for their proliferation and survival (VanDussen *et al.* 2012). Thus, Notch signalling modulates two important intestinal homeostatic functions: the sustainability of the progenitors, and the choice between the secretory or absorptive enterocyte lineage (Wilson and Radtke 2006).

Similarly to Wnt, Notch signalling is activated not only during normal intestinal homeostasis, but also in CRC. Recently, it has been described that Notch signalling plays a role in asymmetric division of $LGR5^+$ CBCs (the long lived active cycling stem cells) and $BMI\text{-}1^+$ cells (the postulated +4 quiescent ISC), as well as the inter-conversion between CBCs and +4 ISC (Srinivasan *et al.* 2016). Nevertheless, it remains to be elucidated whether it was abrogation or over-activation of Notch signalling, or simultaneous effects on other signalling pathways critical for stem cell homeostasis, through which these changes could have occurred. Further insides into the mechanism of CRC stem cell regulation by the Notch pathway, could potentially lead to clinical Notch signalling targets to induce differentiation in adenomas (Radtke and Clevers 2005; Wilson and Radtke 2006).

Hedgehog Signalling

The Hedgehog (HH) signalling pathway is critical for intestinal development. HH components act as morphogens that contribute to the formation of the crypt-villus structure (De Santa Barbara et al. 2003). They are rarely mutated in CRC, however, they are important for intestinal homeostasis and repair (Watt 2004; Liang et al. 2012; Barker et al. 2007). Since 1990 three *Hedgehog* (*Hh*) gene homologues, encoding glycoproteins, have been identified in vertebrates; *Sonic Hedgehog* (*Shh*), *Indian Hedgehog* (*Ihh*), and *desert hedgehog* (*Dhh*) of which only SHH and IHH were detected in the intestinal epithelium (Rimkus *et al.* 2016). *Shh* mRNA levels were

detected by *in situ* hybridization at high and low levels in the adult small (SI) and large intestines (LI), respectively, only within the crypt base. However, protein levels were so low that could not be identified by IHC in both SI and LI (van den Brink *et al.* 2002). *Ihh* mRNA expression levels in the SI were strongly detected at the crypt-villi junction with a gradual decrease progressing towards the tip of the villus (Batts *et al.* 2006) whilst IHH protein was present on the upper half of villi and only within the absorptive enterocytes at the top of the colonic crypts (Jones *et al.* 2006).

In the absence of HH ligand, PTCH-1 (patched homologue-1), a 12-transmembrane receptor, is associated on the cell membrane with SMO [Smoothened co-receptor of the G-Protein Coupled Receptor (GPCR) family], which inhibits its function. Furthermore, the microtubule-bound inhibitory proteins COSTAL-2/KIF7 and Suppressor of Fused (SUFU) bind to glioma-associated (GLI) transcription family proteins (GLI-1, GLI-2, and GLI-3 in mammals), sequestering them in the cytoplasm where they are phosphorylated by CK1, GSK3 and PKA, and ultimately processed by the proteasome into C-terminally truncated proteins. These then translocate into the nucleus and repress HH target gene expression (Zadorozny *et al.* 2015).

The binding of HH ligand, on the extracellular domain of PTCH-1 realises SMO, preventing the full length GLI protein truncation into the repressor forms, possibly by dissociation of GLI from its inhibitory proteins COSTAL-2/KIF7 and SUFU (Zadorozny *et al.* 2015). Full length GLI Zn-finger transcription factors translocate to the nucleus, activating transcription of the HH signalling target genes, including those associated with HH pathway feedback (*Ptch-1*, *Gli-1*, *Hhip-1* [hedgehog interacting protein; a HH antagonist]), proliferation (e.g., *Cyclin-D1*, *Myc*), apoptosis (e.g., *Bcl-2*), angiogenesis (e.g., *Ang1/2*), epithelial-to-mesenchymal transition (e.g., *Snail*), stem cell self-renewal (e.g., *Nanog*, *Sox2*) and differentiation (e.g., *Bmp-4*) (Stecca and Ruiz I Altaba 2010; Scales and de Sauvage 2009; Ingham and McMahon 2001; Hui and Angers 2011).

Although, most studies on HH signalling pathway have investigated its role during development, they have also given insights into how it contributes to adult intestinal homeostasis. Mice deficient for $Ihh^{-/-}$, which is normally expressed in the intervilli region (from the base of the villi), die perinatally and exhibit short villi due to decreased proliferation, which suggests that the HH pathway is involved in crypt-villus axis morphogenesis and stem-cell proliferation (Ramalho-Santos *et al.* 2000). Defective Hh signalling in neonatal small intestine and adult colon could therefore predispose to cancer formation, due to its pro-proliferative effect (Madison *et al.* 2005). Moreover, *Ihh* mutants had ~50% reduction in endocrine cells in the small intestine, which might also imply a role for the HH pathway in intestinal cell fate decisions (Ramalho-Santos *et al.* 2000). Similarly, in the colon, cyclopamine inhibition of SMO resulted in preferential differentiation of cells towards the goblet cell lineage (Pathi *et al.* 2001), whilst

another study showed that HH activity was necessary and sufficient for colonic epithelial differentiation (van den Brink *et al.* 2004).

As well as through epithelial autonomous mechanisms, HH signalling regulates the crypt-villus morphology by regulating the stroma and epithelium cross-talk, as even the subepithelial myofibroblasts and the smooth muscle cells of the submucosa express HH signalling components (Ramalho-Santos *et al.* 2000). Mesenchymal cells secrete pro-proliferative signals to adjacent epithelial cells; during adult intestinal homeostasis, HH intestinal activity pattern restricts mesenchymal cell population to the crypt base and as a consequence their signals too, contributing in this way to the normal intestinal homeostasis (van den Brink *et al.* 2004). Over-expression of the pan-hedgehog inhibitor, HHIP, within the epithelium affects the surrounding mesenchymal cells, causing their mislocalisation or overexpansion. This can result in ectopic epithelial expansion, ectopic crypt formation, remodelling and villus development in the neonatal intestine (Madison *et al.* 2005). In inflammatory bowel disease (IBD), it was shown that re-activation of the HH pathway decreases colitis and colitis-mediated adenocarcinoma formation by increasing IL-10 stromal secretion and thus suppressing inflammation. This further supports the model that HH pathway actively contributes to the cross-talk between stromal cells and epithelium (Lee *et al.* 2016).

PI3K/AKT signalling

The phosphatidylinositol-3 kinase (PI3K)/AKT signalling pathway plays a central role in growth, cell survival and proliferation, and overstimulation of this pathway has been linked to tumourigenesis in multiple tissues. 20-30% of sporadic human CRC have *PI3K catalytic subunit-α (PIK3CA)* gene mutation and more than 40% have mutations that affect PI3K effectors (Yueh *et al.* 2016; Scoville *et al.* 2008).

Cellular stimuli or toxic insults can initiate the PI3K/AKT signalling cascade through binding to RTKs, integrins, B- and T-cell receptors, cytokine receptors and GPCRs (Carnero *et al.* 2008). Specifically, upon extracellular binding of growth factors, RTKs dimerise and become activated by cross-phosphorylation of intracellular tyrosine residues. The phosphorylated RTK C-terminus serves as a docking platform on which various intracellular proteins with SH2 (SRC homology 2) or PTB (phoshotyrosine binding) domains bind (Carnero *et al.* 2008). PI3K is a lipid kinase consisting of the p110 catalytic subunit and the p85 regulatory subunit. Increased levels of monomeric p85 antagonize p85-p110 dimer binding on adaptor proteins; so far, this is the only known mechanism by which p85 elicits its repressive function on p110 (Luo and Cantley 2005). p85 can either bind directly to the activated RTK or *via* adaptor proteins (e.g. Grb2–associated binding, GAB, a scaffold protein) which assist p85 binding and induce conformational changes to

release the repression on p110. Alternatively, SOS (Son of Sevenless), which contains a RAS-GEF (Guanine exchange factor) domain that activates RAS, binds to activated RTK-bound GRB2. RAS-GTP then activates p110 (Carnero *et al.* 2008). P110 activation brings it closer to the cell membrane where its substrate resides. The main substrate of PI3K, phosphatidylinositol-4,5-bisphosphate (PIP2), is anchored in the cell membrane and is phosphorylated by the p110 catalytic subunit to produce phosphatidylinositol-3,4,5-trisphosphate (PIP3) (Carnero *et al.* 2008). PIP3 phospho-lipids can directly bind intracellular proteins containing a pleckstrin homology domain which include serine-threonine kinase AKT (Protein Kinase B) and phosphoinositide-dependent kinases-1/-2 (PDK-1/-2). This brings them in close proximity, allowing PDK-1 to phosphorylate AKT at Thr-308, which partially activates AKT. Full enzymatic activation of AKT requires Ser-473 phosphorylation catalysed by multiple kinases including PDK-2, ILK (integrin-linked kinase), mTORC2 (mechanistic target of rapamycin complex) and DNA-PK (DNA-dependent protein kinase) (Bozulic and Hemmings 2009).

There are three AKT isoforms (AKT-1/-2/-3), which all recognize substrates with the consensus phosphorylation motif RxRxxS/T. There are isoform-specific AKT substrates as well as shared substrates, and numerous downstream AKT targets involved in protein synthesis, survival, migration, proliferation, glucose metabolism, neural function and NF-κB function (Manning and Cantley 2007; Hers *et al.* 2011).

When the cell stimulation is over, PIP3 levels decrease and negative regulators, e.g. protein phosphatase-2A (PP-2A) and PH-domain leucine-rich-repeat-containing protein phosphatases (PHLPP-1/2), de-phosphorylate AKT. The tumour suppressor PTEN de-phosphorylates PIP3, causing the same effect (Carnero *et al.* 2008).

The PI3K/AKT pathway has been linked to intestinal homeostasis and tumourigenesis, and along with the BMP and Wnt pathways, all contribute to ISC homeostasis. PI3K/AKT signalling is involved in β-CATENIN nuclear accumulation (Scoville *et al.* 2008). Although Wnt signaling is active throughout the intestinal crypts, as demonstrated by the presence of activated Wnt receptors (i.e. phospho-LRP), BMP signaling is blocked at the crypt base in order to promote the nuclear accumulation of β-CATENIN. Inhibition of BMP signaling by niche signals leads to increased PTEN degradation, which activates AKT kinase potential (Waite and Eng 2003). Active AKT phosphorylates β-CATENIN at multiple Ser/Thr sides, including Ser-552, to enhance β-CATENIN /TCF interaction (Daugherty *et al.* 2007; Scoville *et al.* 2008). AKT activation also inhibits glycogen synthase kinase 3β (GSK-3β). This destabilizes the β-CATENIN destruction complex leading to the accumulation of β-CATENIN in the cytoplasm, its translocation to the nucleus and activation of Wnt signalling target gene transcription (Scoville *et al.* 2008).

Therefore, the interplay between BMP and PI3K/AKT signalling restricts full activation of the Wnt pathway to the base of the crypt, allowing ISC division (He *et al.* 2004).

He *et al.* (2007) have shown that PTEN deficiency in both epithelial and stromal cells, by wide-spread PTEN recombination (i.e. *Mx1-Cre*$^{+}$ *Pten*$^{fl/fl}$ mouse model), can initiate neoplasia, highlighting the tumour suppressive function of PTEN. In contrast, Marsh *et al.* (2008), have shown that *PTEN* deficiency in the intestinal epithelium alone did not perturb intestinal homeostasis, alter the number of ISCs or crypt clonogens, or abrogate p53-mediated apoptosis. This implied that epithelial-stromal interactions are fundamental for normal intestinal homeostasis. BMPRII stromal deletion results in hamartomatous polyposis, the same phenotype observed in germline PTEN mutations (Beppu *et al.* 2008). As shown by Marsh *et al.* (2008), the combination of *Apc* and *PTEN* deficiency can fully activate AKT (phospho-Akt^{Ser473}), promoting the nuclear localization of β-CATENIN (as described above) within the villi of the small intestine, and contributing to the progression of *Apc*-deficient adenomas to adenocarcinomas.

Figure 1.5 shows an overview of the pathways involved in intestinal epithelium homeostasis.

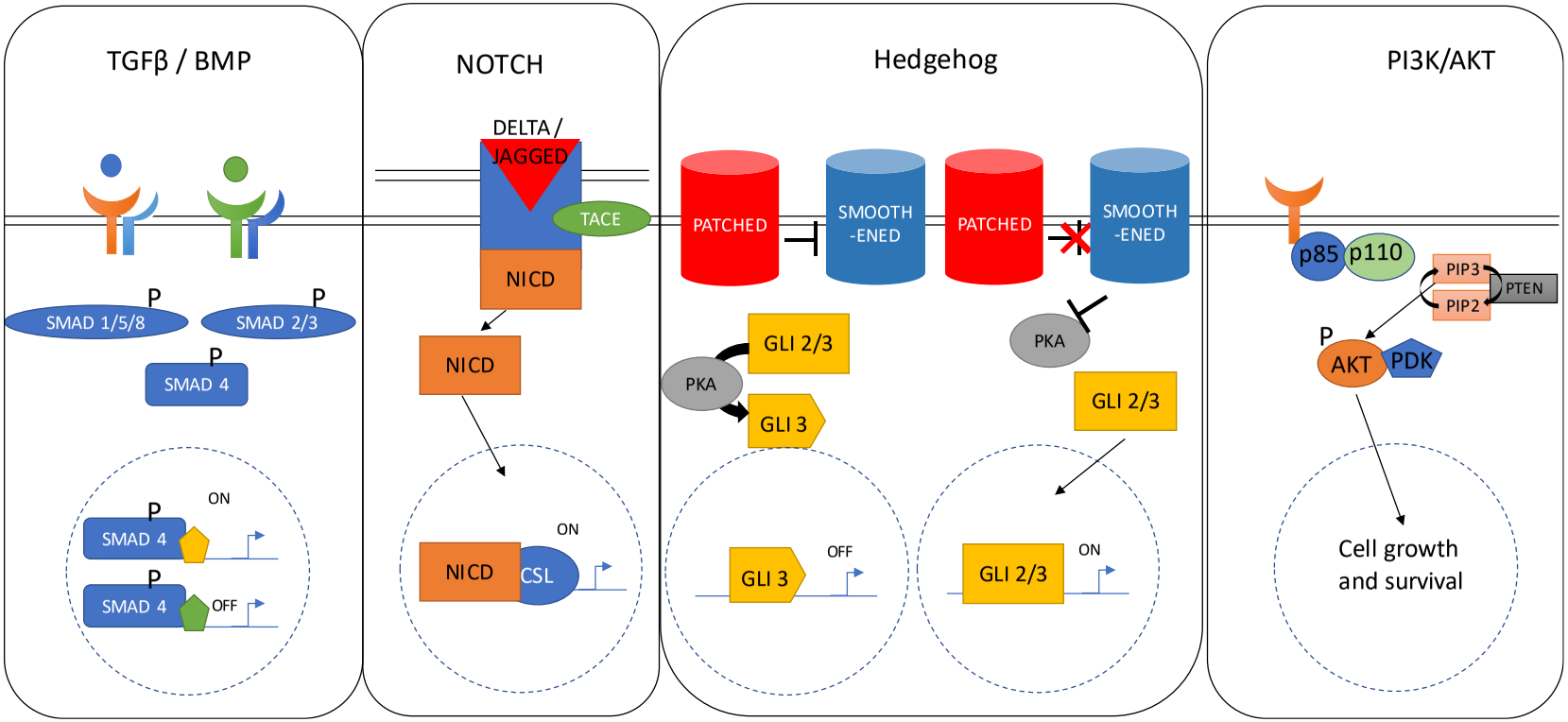

Figure 1.1 Signalling pathways involved in intestinal epithelium homeostasis

1.2 DNA damage

1.2.1 Sources of DNA damage

Endogenous sources of DNA damage

Endogenous DNA damage is naturally occurring and is caused by metabolic and hydrolytic processes within a cell. Cell metabolism, including apoptosis and inflammatory responses, generates chemical compounds that harm the DNA. These include reactive oxygen species (ROS), reactive nitrate species, reactive carbonyl species, lipid peroxidation products, alkylating agents etc., whereas hydrolytic processes within a cell cleave chemical bonds on the DNA molecule (De Bont and van Larebeke 2004). Cells must be able to respond to extensive DNA damage; for example, oxidative DNA damage may happen 10 000 - 11 500 times per day in a human cell (Ames *et al.* 1993; Helbock *et al.* 1998). Other endogenous sources of DNA damage/breaks include: replication fork stalling during cell cycle progression, programmed DNA breaks (e.g. variable, diversity and joining or V(D)J gene segments somatic recombination), meiotic crossing-overs, gene rearrangements and apoptosis (Crosetto *et al.* 2013; Tonegawa 1983). Mutations usually occur when DNA replication mistakes are not repaired, when DNA polymerases copy damaged templates (Marnett and Plastaras 2001) and when there are defects in the DNA repair pathway (O'Driscoll 2012).

Exogenous sources of DNA damage

Exposure to exogenous physical agents such as ionizing radiation (IR), ultraviolet (UV) radiation or chemical compounds including platinum-based compounds (e.g. cisplatin); intercalating agents (e.g. benzo[a]pyrenes, daunorubicin and actinomycin-D); DNA alkylating agents (e.g. nitrogen mustards, methyl methanesulphonate, *N*-nitroso-*N*-methylurea and *N*-ethyl-*N*-nitrosourea); and naturally occurring mutagens such as psoralen, cause DNA damage in numerous ways as explained below in section 1.2.2 (Helleday *et al.* 2014).

1.2.2 Types of DNA alterations and damage

Causes of Nucleotide transversions

A review by Thomas Lindahl (1993) intelligibly explains the liability of *N*-glycosylic bonds (formed between the pentose sugar and their DNA nucleobases) to hydrolysis. It has been estimated that 0.2-10^4 spontaneous depurination events (when a N-glycosidic bond connecting a purine with a deoxyribose sugar is hydrolytically cleaved releasing an adenine or guanine) happen every day in mammalian cells, and that depurination occurs more frequently than depyrimidination (when a N-glycosidic bond connecting a pyrimidine with a deoxyribose sugar is hydrolytically cleaved releasing a thymine or cytosine) (Lindahl and Nyberg 1972). This

generates apurinic and apyrimidinic sites, and depending on either adenine or guanine purine loss, A=T→T=A or G≡C→T=A transversions arise (Helleday *et al.* 2014). Cytosine and its methylated form (5-methylcytosine) are more susceptible to hydrolytic deamination, compared to the rest of the nucleobases, and are converted to uracil or thymine, resulting in DNA base mismatches. Compared to cytosine, 5-methylcytosine moieties are more slowly repaired following deamination than cytosine which makes the methylated CpG islands preferential zones for spontaneous point mutations, such as G≡C→T=A transversions (Ehrlich *et al.* 1990; Lindahl and Nyberg 1972).

Causes of DNA oxidation

Endogenous or exogenous sources (e.g. metabolism or IR, respectively) of DNA oxidation (e.g. hydroxyl radicals) usually cause 8-hydroxylguanine formation. This preferentially binds to adenine and, if not repaired post-replication, may generate transversions (Kasai and Nishimura 1984; Shibutani *et al.* 1991). Moreover, oxidation may also cause the formation of ring-saturated pyrimidines which are non-coding bases (Wallace 1988; Breimer 1990). Covalent bonds between the nucleobases and the sugar ring or between two purines of different DNA strands are also caused by ROS (Dirksen *et al.* 1988; Carmichael *et al.* 1992).

Single and Double strand breaks and their causes

Single strand breaks (SSBs) are formed in a number of ways: after the disintegration of oxidized deoxyribose; upon cleavage of the deoxyribose phosphate by specialised enzymes when a base needs to be changed; by collision of defective topoisomerase 1 (TOP1) with RNA or DNA polymerases during transcription or replication, respectively; or by defective DNA ligase activity (Caldecott 2008; Kazak *et al.* 2012). Double strand breaks (DSBs) are more dangerous than single-stranded breaks, as genomic rearrangements or even loss of genomic information may occur if left unresolved. DSBs can be formed by IR, in a similar way to SSBs, but if two SSBs occur in opposite strands close to each other this may lead to DSBs (Wang *et al.* 2003). Furthermore, DSBs usually occur when a cell is in S-phase of the cell cycle, as the unravelling of DNA, renders it susceptible to breaks (McGowan 2003). Similarly, when a replication fork collapses due to DNA damage, this can also lead to DSB formation (Helleday *et al.* 2014). Generally, during cell division, a cell is more vulnerable to DNA damage from both endogenous and exogenous sources (McGowan 2003).

Enzymatic DNA methylation is fundamental for the regulation of gene expression in mammalian cells. However, some small reactive molecules within the cell such as *S*-adenosylmethionine, can also non-enzymatically methylate DNA (Paik *et al.* 1975). Apart from the increased number of methylated nucleobases, which increases the chance of having a non-repaired transition, this

can also inhibit gene transcription and could lead to cancer (Varela-Rey *et al.* 2014; Schmidt *et al.* 2016).

Platinum-based chemotherapeutics form bulky adducts on the nucleobases or cross-links between the same or the opposite DNA strand (Nouspikel 2009). Intercalating agents such as benzo[a]pyrene diol epoxide, a carcinogenic by-product of tobacco smoking, cause transversions of G≡C→T=A preferentially on endogenously methylated CpG dinucleotides of genes including *p53* (Pfeifer *et al.* 2002). Psoralens, used in the treatment of psoriasis, constitute another form of intercalating agents. Upon therapeutic UV radiation, they form monoadducts or covalent intra-strand crosslinks between thymidines preferably spaced in 5'-TpA sites of the genome (Papadopoulo *et al.* 1993; Yang *et al.* 1994).

DNA alkylating agents were first used against cancer as chemotherapeutics; they are methylating agents that form adducts on the nucleobases and favour mutagenic transition of C≡G→T=A. Therefore, non-replaced methylated bases could lead to DSB formation and as cancer cells usually have non-fully functional DNA repair mechanisms, this makes them susceptible to cell death compared to cells which are able to repair DNA (Kondo *et al.* 2010). A thorough insight into the defective DNA repair pathways of cancer cells is needed for optimal selection of chemotherapeutic agents that will be given to the patient.

In general, any alterations or damage on the DNA molecule, if left un-repaired, can become mutagenic. Consequently, cells employ various DNA repair pathways as mechanisms to protect their genetic information.

1.2.3 DNA damage repair pathways

The importance of DNA integrity is highlighted by the fact that cells use a vast amount of their energy in order to repair their DNA (Hoeijmakers 2009). Cells employ elaborate mechanisms for the resolution of DNA damage. In the following paragraphs, only the major DNA repair pathways will be described (Figure 1.6). The choice of which DNA repair pathway will be used is dependent on many factors, one of which is the phase of the cell cycle.

Base excision repair (BER) pathway

The BER pathway mediates the excision and replacement of a single nucleobase. BER is employed following cytosine deamination and conversion into uracil or thymine, nucleic base oxidation or non-enzymatic methylation, and depurination or depyrimidination due to hydrolysis. The pathway initiates with the excision of the unwanted base. This is facilitated by a family of DNA glycosylases, which flip the nitrogenous base and then cleave the N-glycosylic bond, generating a repairable apurinic or apyrimidinic site while keeping an intact pentose-

phosphate DNA backbone (Lindahl 1986). Uracil is removed by uracil-DNA glycosylase (UNG). The DNA backbone is then incised (by cleavage of the 5'- phosphodiester bond), adjacent to the abasic site, by DNA-(apurinic or apyrimidinic site) lyase APEX1. The removal of the 5' deoxyribose-phosphate (dRP) is mediated by dRP lyases creating a single strand break, and DNA polymerase β (POL β) fills the nucleotide gap that was formed. Lastly, X-ray repair cross-complementing protein 1 (XRCC1) acts as a scaffold for the attraction of Ligase 3, which joins the newly added nucleotide to the rest of the DNA backbone (Helleday *et al.* 2014).

Nucleotide excision repair (NER) pathway

The NER pathway repairs distortions of the DNA double-helix, caused by adducts including those generated by UV radiation and platinum-based drugs. The deformed sites in DNA are recognized either during transcription or in the global repair taking place throughout the genome. The former is believed to be caused by stalling of RNA polymerase at the distorted site of the template strand and the latter by XPC [DNA repair protein complementing xeroderma pigmentosum (XP)-C cells] in complex with RAD23B. XPC recognition allows the formation of the preincision complex. This comprises of XPA, which binds the damaged DNA; transcription factor II Human (TFIIH), which aids both recognition mechanisms by opening the DNA double helix; XPG, which cuts the 3'-end of the damaged DNA; XPF, which works together with excision repair cross-complementing-1 (ERRC1) to incise the 5'-end of the damaged DNA; and replication protein A (RPA) which binds single stranded (ss) DNA to stabilize the DNA repair complex. The 26-29 nucleotide-long gap, generated after incision of the DNA, is filled by POLδ or POLε or on some occasions, by POLκ, assisted by the proliferating cell nuclear antigen (PCNA), which acts as a DNA clamp (Helleday *et al.* 2014).

Mismatch repair (MMR) pathway

MMR is another excision repair mechanism which removes mismatched nucleobases or misincorporated bases during DNA replication generating insertion-deletion loops (IDL). The heteromeric complex MUTSα consists of MSH2 and MSH6 (MutS homologue-2 and -6) which are ATPases that recognize mismatches and IDLs of 1-2 unpaired nucleotides, whereas MUTSβ (comprising of MSH2 and MSH3) recognizes longer IDLs. MUTS recruits the MUTL heterodimeric complex, consisting of MUTL homologue 1 (MLH1) and PMS2 (postmeiotic segregation increased), whose endonuclease activity incises the lagging strand on the distal site of the mismatch in order to remove the mismatched nucleotides. MUTL creates incisions for the mismatches on the leading strand, generating a free 5'-end on which exonuclease-1 (EXO1) binds to excise the erroneous nucleotides in the presence of RPA and PCNA, while POLδ copies the template strand where the nucleotides were excised (Kazak *et al.* 2012).

Homologous recombination (HR) pathway

The alternative route for repairing DSBs is through HR, but only in the presence of sister chromatid during late S and G2 phases of the cell cycle. This mechanism is preferred over NHEJ because is less error-prone. ATM and the MRN complex recognize and bind to DNA ends, while EXO1 or a complex of SGS1–TOP3–RMI1 (STR)/DNA-2 exonucleases resect one strand of the DNA to generate a 3′ ssDNA site (Alterman *et al.* 2007; Williams *et al.* 2007; Kazak *et al.* 2012). RAD51 then assembles with the ssDNA to create a nucleoprotein filament that promotes DNA strand exchange. RAD51 searches for the undamaged homologous strand to pair this region with its complementary DNA molecule creating a crossover. RAD54 binds to RAD51, stimulating its DNA pairing function, and stabilizes the nucleoprotein filament (Khanna and Jackson 2001; Mazin *et al.* 2003). BRCA2 plays an important role in moving RAD51 from its site of synthesis to the nucleus (Bhattacharyya *et al.* 2000). DNA POL can then synthesise the missing parts of the broken DNA from the 3' end of the invading strand, using the homologous strand as a template (Mcllwraith *et al.* 2005). LIG1 creates a hetero-duplexed DNA molecule, referred to as Holliday junction, which is resolved by sliding and cleavage of the DNA which unfolds the junction (Modesti and Kanaar 2001).

Non-homologous end-joining (NHEJ) pathway

NHEJ is one of the two main pathways that are used for the resolution of DSBs caused by IR or nucleases that cleave DNA. It is used when a cell acquires the DSB while it is in G1 or G0 phase. DSBs are repaired by microhomology at ends. However, ends of DSBs generated by DNA nucleases or IR cannot be easily ligated; they usually need to be processed and trimmed before new nucleotides are incorporated. Hence, during resynthesis of the new DNA, errors may occur which may give rise to mutations (Helleday *et al.* 2014). Upon a DSB formation, in the absence of a template strand for HR-directed repair, the MRN complex, consisting of MRE11, RAD50 and NBS1, binds to DSBs via NBS1, in order to recruit and activate ataxia telangiectasia mutated protein (ATM). KU70/80, which is a DNA-end binding protein complex, binds on the DNA ends to structurally support and protect them from further degradation, and to facilitate the recruitment of other DNA repair proteins. The catalytic subunit of the DNA-depended protein kinase (DNA-PKcs) is then recruited to the DNA ends, where it is activated by Ku70/80. The MRN complex and the activated DNA-PK together pull the DNA ends (Kazak *et al.* 2012). ARTEMIS, a nuclease, is then attracted to the DNA ends by DNA-PK, and removes 4 nucleotides from the 5′- and 3′-single stranded overhangs in order to join the two DNA ends (Li *et al.* 2014). POLμ fills the gap, followed by binding of XRCC4 (X-ray repair cross-complementing protein 4) on the nucleoprotein complex attracted by the DNA-PKcs, to assist ligase-4 (LIG4) in end-joining the DNA strands and resolving the break (Kazak *et al.* 2012).

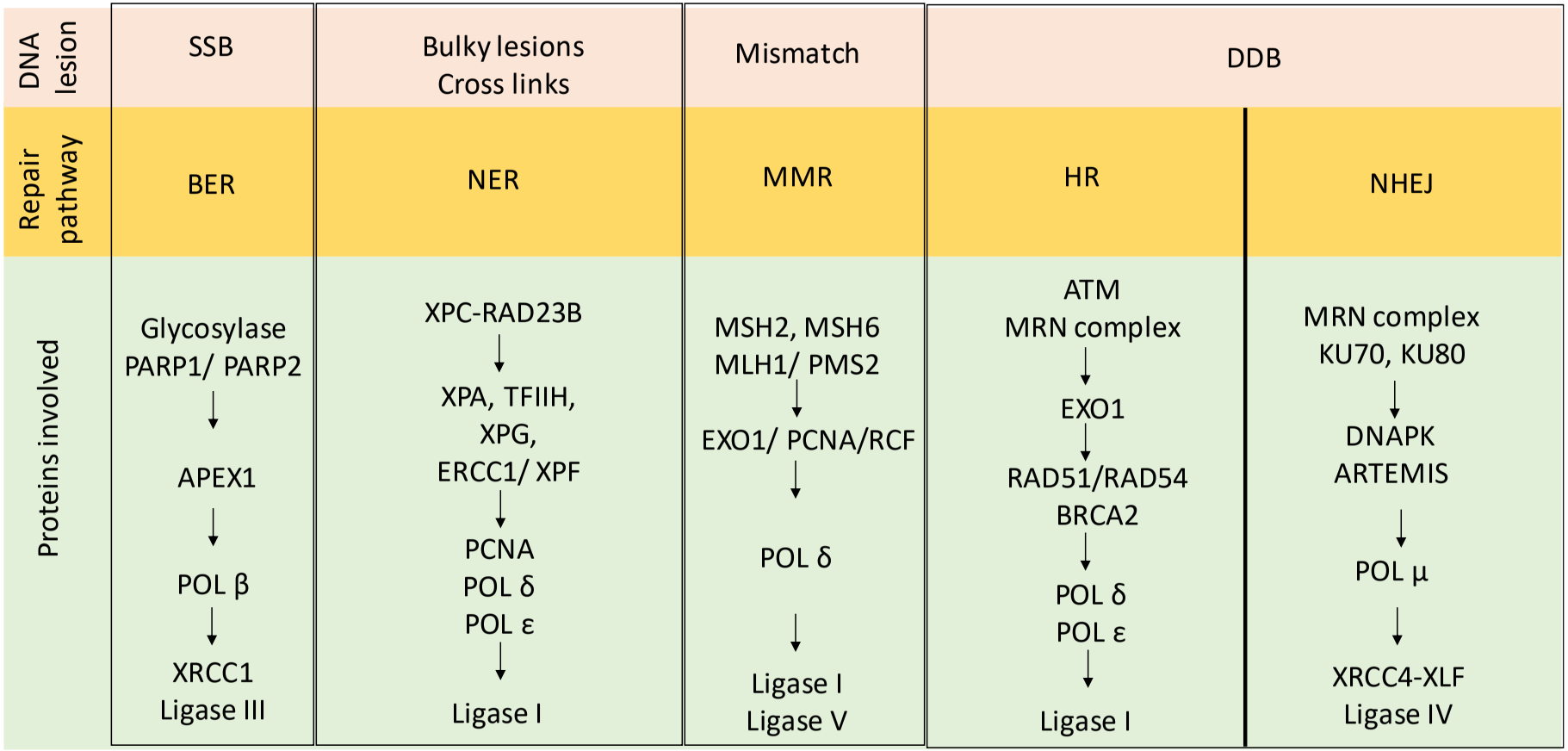

Figure 1.2 Summary of DNA repair pathways

1.2.4 γH2AX: a marker of DSBs

H2AX protein

DNA is wrapped around histone proteins (H2A/B, H3 and H4). The H2A protein has multiple variants including H2A1/2, H2AX and H2AZ. In humans, H2AX makes up to 10% of H2A protein and is randomly present into nucleosomes. H2AX variant differs from H2A due to a carboxyl tail that contains conserved serine and glutamine residues at positions 139 and 140, respectively (Kuo and Yang 2008).

H2AX phosphorylation

Genomic instability can result from unresolved DNA double strand breaks (DSB) (Crosetto *et al.* 2013). Immediately upon a DSB formation the MRN complex binds to DSBs via NBS1 to recruit ATM (Figure 1.7). ATM phosphorylates H2AX on Serine-139 (Ser^{139}). Through a positive feedback loop, mediator of DNA damage checkpoint protein 1 (MDC1) stimulates MRN to recruit more ATM kinase to phosphorylate H2AX. Phosphorylated H2AX (γH2AX), which can extend up to megabases away from the DNA break, triggers either NHEJ or HR pathways, depending on the stage of the cell cycle. DNA-pk, a component of NHEJ, or ATR, a component of HR, phosphorylate H2AX on Ser^{139} (Bonner *et al.* 2008, Sharma *et al.* 2012). γH2AX functions as a scaffold, recruiting more DNA damage response proteins for the resolution of the break; after or during repair, γH2AX is dephosphorylated by PP2A for an efficient DNA break resolution (Chowdhury *et al.* 2005).

γH2AX is a marker of DSBs

γH2AX can be observed using fluorochrome-conjugated antibodies as foci. The number of foci observed in the nucleus of a cell can be directly associated with the number of DNA breaks present. It has been used as a marker for identifying the efficiency cytotoxic drugs and anti-cancer agents (Kuo and Yang 2008).

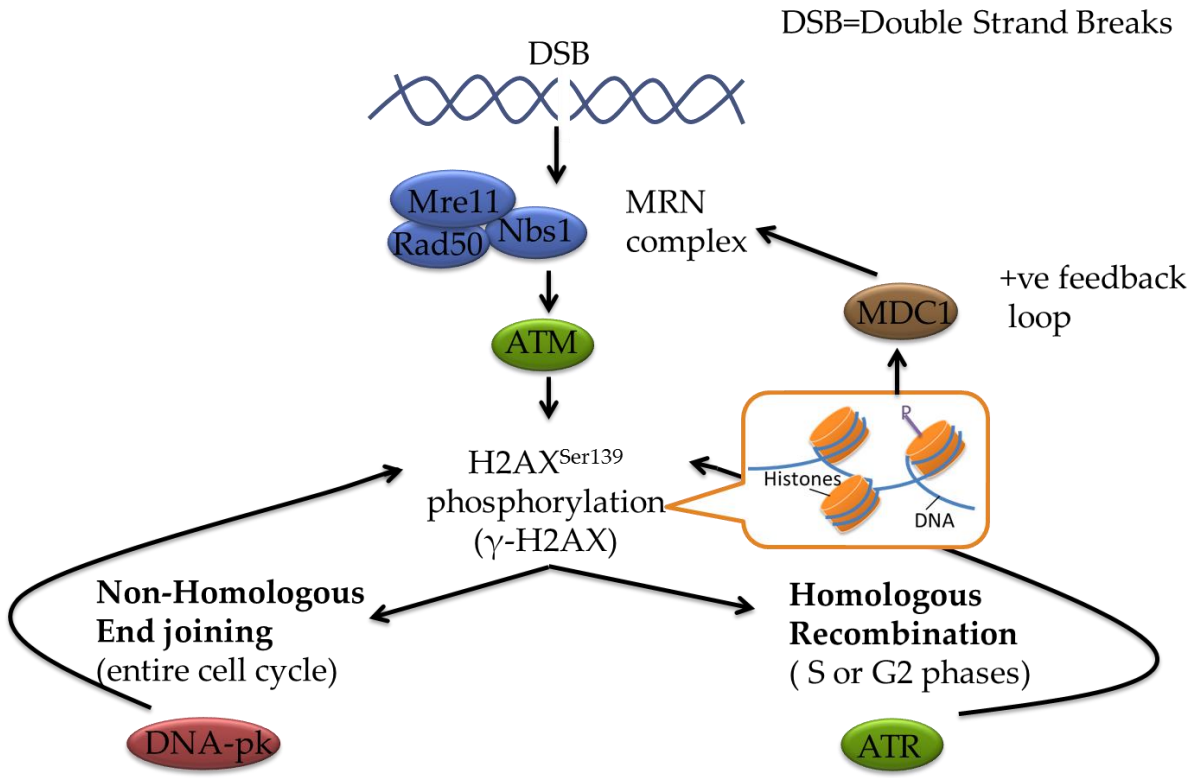

Figure 1.7 DSB induce H2AX phosphorylation.

A single DSB can lead to the phosphorylation of H2AX which extends up to 2 megabases of chromatin and can be identified as discrete nuclear foci using antibodies (Fernandez-Capetillo *et al.* 2004). The repair of the break results in the dephosphorylation of γH2AX (Bonner *et al.* 2008).

Apc deficiency and Wnt signalling activation induce DNA damage.

In 2001 two groups demonstrated chromosomal instability and spindle aberrations in embryonic stem cells derived from *Apc*$^{Min/+}$ mice. In addition, they showed that APC is involved in chromosomal segregation through its phosphorylation by spindle assembly checkpoint proteins BUB1 and BUBR1 (Fodde *et al.* 2001; Kaplan *et al.* 2001). Truncating mutations of APC interfere with the normal microtubule plus-end attachment on the kinetochore of chromosomes, resulting in inappropriate chromosome congression at metaphase, which in turn leads to abnormal chromosomal segregation (Green and Kaplan 2003; Green *et al.* 2005). *APC* loss within human osteosarcoma fibroblastic cells (U2OS) and human colon cancer cells (HCT116) resulted in compromised mitotic spindle checkpoints, including decreased association of BUB1 and BUBR1 proteins to the kinetochore and reduced apoptosis, which resulted in tetraploidy and polyploidy (Dikovskaya *et al.* 2007). Wnt signalling activation by either APC truncations or β-CATENIN activating mutations in intestinal polyps and ES cells resulted in increased number of anaphase bridges, which is a marker for chromosomal instability (CIN)Aoki *et al.* 2007).

Reed *et al.* (2008) have shown using an *AhCreApc*$^{fl/fl}$ mouse model, that *Apc* deficiency within intestinal cells increased *H2AX* mRNA expression, which suggests that there is an increased requirement in *Apc* null cells for H2AX production. Moreover, Méniel *et al.* (2015) have shown that *Apc* deficiency within the liver induced the DNA damage checkpoint proteins p53 and p21 due to increased levels of DSBs, as quantified by IHC markers γH2AX and RAD51. Increased histone expression is coupled with DNA replication (Lyons *et al.* 2016); hence, after *Apc* deficiency, one of the effects of Wnt signalling activation is increased proliferation which partly explains the increase in *H2AX* mRNA levels. However, some histone proteins can also be transcribed independently of the cell cycle, including the H2AX variant (Lyons *et al.* 2016). A reason for this replication-independent expression of H2AX could be that cells need to replace γH2AX with newly synthesised H2AX proteins, during DNA repair *via* chromatin remodelling (Chowdhury *et al.* 2005).

Apc deficiency and Wnt signalling activation result in excess cell division. Increased proliferation may contribute to increased DNA damage simply due to increase in the number of replication stress. Nonetheless, a study by DiTullio *et al.* (2002) showed that despite the fact that normal colonic epithelium has a higher proliferative index compared to lung and melanocytic preneoplastic and neoplastic lesions, γH2AX or phospho-CHK2 IHC stainings were comparably low, indicating no increase in DNA damage due to increased proliferation (Gorgoulis *et al.* 2005). Thus, although increase in total H2AX levels, as a result of cell synthesis, might vary between tissues, phosphorylation of H2AX is unaffected by total H2AX levels and it is induced

mainly in the presence of DNA damage; however, cell-division-independent H2AX transcription might serve as an alternative mechanism to the dephosphorylation of γH2AX, by which cells use to mark the resolution of a DNA break.

Oncogene activation (including MYC, CYCLIN E, MOS, CDC25A, and E2F1) is usually present in preneoplastic lesions (Bartkova *et al.* 2006; Di Micco *et al.* 2006; Denko *et al.* 1994; Halazonetis *et al.* 2008; Bartkova *et al.* 2005). Furthermore, activation of c-MYC, a main target gene of the Wnt pathway, has been demonstrated to induce DNA damage in resting cells, showing that c-MYC-activity dependent DNA damage induction is not always due to DNA replication defects (Vafa *et al.* 2002). In addition, the same study showed that c-MYC activation altered metabolism, causing the production of ROS without inducing apoptosis. Lastly, approximately 10 times more c-MYC-activated cells treated with IR were able to enter S-phase compared to non-c-MYC activated cells, which suggests that c-MYC activation can override DNA damage checkpoints. Consequently, Wnt signalling activation, either through *Apc* mutations, β-CATENIN activation or c-MYC expression and activation, can all lead to increased DNA damage that in turn could lead to genomic instability.

1.3 Intestinal Tumourigenesis

1.3.1 Intestinal Cancer in Humans

Incidence

Worldwide statistics show that 14.1 million people were diagnosed with some type of cancer in 2012. It is estimated that by 2030 this will increase by 63% (Ferlay *et al.* 2015). Colorectal cancer (CRC) is the third most commonly diagnosed cancer and the fourth most common cause of cancer death worldwide (Cancer Research UK 2016a and b). Better screening methods and enhanced awareness could be among the reasons that the last decade has seen a 12% drop in bowel cancer mortality rates in the UK (Cancer Research UK 2015). Despite this fact, only 56-57% of patients survive 10 years after diagnosis (Cancer Research UK 2016a).

Environmental risk factors

Environmental risk factors encompass cultural, social and lifestyle elements. Multiple studies of migrants and their 1st generation offspring have shown that geographic factors associated with community populations clearly affect CRC incidence (Marley and Nan 2016). Migrants moving from low-risk to high-risk countries, for instance from southern Europe to Australia, have an increased risk of CRC compared to the population which remain in their country of origin (Boyle and Langman 2000). Moreover, within the population of a country, urban residents consistently have higher incidence than rural residents (Haggar and Boushey 2009).

In 1975, it was demonstrated that there is a strong correlation between red meat consumption and CRC incidence in women from 23 countries (Armstrong and Doll 1975). It was hypothesised and then proven that high animal fat intake increased the CRC risk (Willett *et al.* 1990; Beyaz *et al.* 2016). In addition, increased fruit and vegetable consumption was shown to be protective against CRC due to the presence of dietary fibre (Boyle and Langman 2000). Physical activity is equally important as proven by epidemiological studies, nonetheless, obesity was not consistently positively correlated with increased CRC incidence (Boyle and Langman 2000). 12% of colorectal cancer deaths are attributed to smoking due to the carcinogens found in tobacco (Haggar and Boushey 2009). Finally, high alcohol consumption is another factor that contributes to colorectal malignancy *via* multiple ways; for example, through its carcinogenic metabolite acetaldehyde, or the generation of reactive oxygen species (ROS) (Haggar and Boushey 2009).

Genetic risk factors and predisposition

Most CRC cases are caused by sporadic mutations, 80% of which occur in the *Adenomatous Polyposis Coli* (*Apc*) gene (Kinzler and Vogelstein 1996), whilst less than 6% are due to hereditary mutations (National Cancer Institute 2016). CRC hereditary mutations are divided in the polyposis and non-polyposis syndromes. Hereditary polyposis syndromes account for less than 5% of all CRC (Al-Sohaily *et al.* 2012). Two main polyposis syndromes include familial adenomatous polyposis (FAP) and *MYH*-associated polyposis (MAP). FAP syndrome is caused by an autosomal dominant germline mutation of the *Apc* gene that leads to the formation of 100 to 1000 colorectal adenomatous polyps in FAP patients, by the age of 20 (Al-Sohaily *et al.* 2012). MAP is an autosomal recessive syndrome provoked by bi-allelic mutation of the *mutY-homolog* (*MYH*) gene, a component of the base excision repair (BER) pathway (Al-Sohaily *et al.* 2012). In MAP patients, *Apc* somatic mutations occur frequently, some of which progress to tumour formation through loss of heterozygosity (LOH; Al-Sohaily *et al.* 2012). The number of adenomatous polyps varies between MAP patients, from ten to a few hundred and at the age of 48, 60% are diagnosed with CRC (Mork and Vilar 2016).

Less common hereditary polyposis syndromes include: Peutz-Jeghers, an autosomal dominant disorder caused by germline mutation in *liver kinase B1* (*LKB1*), gene resulting in hamartomatous polyps; Juvenile Polyposis, a rare autosomal dominant syndrome with germline mutations in *bone morphogenetic protein receptor, type IA* (*BMPR1A*) and SMAD family 4 (*SMAD4*); Cowden syndrome or PTEN hamartoma tumours characterised by *phosphatase and tensin homolog deleted on chromosome ten* (*PTEN*) germline mutations; and lastly, hereditary mixed polyposis, an autosomal dominant disorder with characteristic mutations in *BMPR1A,* or *gremlin-1* (*GREM1*) genes (Mork and Vilar 2016; Al-Sohaily *et al.* 2012).

The most common hereditary CRC syndrome, accounting for 2-3% of CRC cases, is hereditary non-polyposis colorectal cancer (HNPCC, sometimes referred to as Lynch syndrome) which is an autosomal dominant condition caused by germline mutations in DNA mismatch repair (MMR) pathway genes. (Al-Sohaily *et al.* 2012; Mork and Vilar 2016). These are predominantly mutL homolog-1 (MLH1), mutS homolog-2 and-6 (MSH2 and MSH6) and Postmeiotic Segregation Increased, S. Cerevisiae, 2 (PMS2; Al-Sohaily *et al.* 2012; Mork and Vilar 2016). Mutation of MMR genes fuels the accumulation of more mutations due to microsatellite instability (MSI; Jass *et al.* 2002). The age of CRC onset in Lynch syndrome patients is around 45 years old (Jasperson *et al.* 2010). Nevertheless, patients with MAP or Lynch tumour predisposition syndromes have better survival rates than sporadic CRC patients (Mork and Vilar 2016).

It is worth mentioning that individuals with first degree relatives diagnosed with non-syndromic CRC (or familial CRC) have a 2-4 fold higher risk of developing CRC compared to the general population and this might be attributed to a combination of environmental and genetic factors (Armelao and de Pretis 2014; Johns and Houlston 2003).

CRC subtypes

In 2014 the Colorectal Cancer Subtyping Consortium (CCSC) was formed to identify a consensus among the molecular subtypes of CRC described by independent groups, based on a large scale study of 4000 CRC samples, mainly of stage II and III. These consensus molecular subtypes (CMS) were enriched for major genetic and epigenetic characteristics, expression of signalling pathways and clinical traits. The subtypes are described in Table 1.1 (Dienstmann 2014; Rodriguez-Salas *et al.* 2017).

Table 1.1 Consensus molecular subtypes of CRC

	%	Pathways Involved & other characteristics	Genomic Instability	Mutations	Clinical traits	Survival/ tumour recurrence
CMS1	14	Immune activation and infiltration	MSI	Tumour Hypermutations; *BRAF*	Older age at diagnosis; females; Right-sided tumours	Intermediate/ rare recurrence
CMS2	41	strong WNT pathway activation	High CIN, MSS	*TP53; EGFR* amplification/ overexpression	Left-sided tumours	Better/ NS
CMS3	38	moderate WNT pathway activation; enrichment for multiple metabolism signatures	Low CIN; higher prevalence of CIMP	30% hypermutated; *KRAS, PIK3CA; IGFBP2* overexpression	No preference in anatomic location	Intermediate/ NS
CMS4	20	Mesenchymal features; Activation of TGF-β, angiogenesis, matrix remodelling and complement-mediated inflammation	CIN/ MSI heterogeneous	NOTCH3/VEGFR2 overexpression	Younger age at diagnosis; tend to occur in stages III and IV	Worse/ tend to recur
CMS5	17	No clear assignment				

MSI= microsatellite instability, MSS= microsatellite stable, CIN= chromosomal instability, CIMP = CpG island methylator phenotype, NS= not specified

1.3.2 Multi-step carcinogenesis of the intestine

Fearon and Vogelstein (1990) have described a sequence of mutational events required for adenoma to carcinoma transition. This model was formulated after a mutational profile study was performed in CRC samples of various stages, which suggested the requirement of 4-5 sequential mutations that inactivate tumour suppressor genes or activate oncogenes in a preferential sequence, to give rise to colorectal tumourigenesis (Figure 1.8) (Fearon and Vogelstein 1990). More than 20 years since the proposal of this model, recent studies still support this step-wise model of tumourigenesis, which is also known as the 'Chromosomal Instability' mechanism of carcinogenesis (Pino and Chung 2010).

Initiation of colorectal neoplasia

Intestinal crypt hyperplasia and formation of aberrant single crypt lesions initiate benign adenoma development. FAP syndrome has provided the evidence that *APC* gene mutation is one of the important initiators of adenoma formation (Kinzler and Vogelstein 1996). FAP patients, who have only one fully functional *APC* allele, usually develop 100 to 1000 colorectal adenomatous polyps by the age of 20 (Al-Sohaily *et al.* 2012). APC is usually referred to as the gatekeeper to intestinal tumourigenesis because dysfunction of this protein leads to Wnt signalling activation (Morin *et al.* 1997). The majority of CRC have Wnt signalling hyperactivation. *Apc* gene mutation is an early event in colorectal tumourigenesis and 60% of colorectal carcinomas and adenomas have an *APC* gene mutation (Powell *et al.* 1992). B-CATENIN (*CTNNB1)* oncogenic activating mutations are also found in 48% of all CRC but mutually exclusively compared to *Apc* gene mutations (Morin *et al.* 2016) (Sparks *et al.* 1998). Although both *Apc* and *Ctnnb1* gene mutations are equivalently capable of initiating adenoma formation, β-CATENIN mutations are less effective in driving progression of adenoma to carcinoma when compared to *Apc* mutations (Samowitz *et al.* 1999). This highlights the importance of other functions of APC (cell-adhesion, migration, cytoskeletal organization and chromosomal stability) in the progression of CRC. Of note, both *Apc* and β-CATENIN mutations result in increased Chromosomal Instability (CI). Wnt signalling activation leads to the phosphorylation of CDC2 (Cdk1), which inhibits its activity and therefore allows the progression through the G2/M phase of the cell cycle, suppressing mitotic arrest and apoptosis (Aoki *et al.* 2007). Consequently, cell-adhesion, migration, cytoskeletal organization could be the link between APC (but not β-CATENIN) and adenoma progression. Another, less common, initiating mutation and component of the Wnt pathway is *Axin-2* which encodes a negative regulator of the pathway (Liu *et al.* 2000).

Progression of adenoma to carcinoma

The transition of benign adenomas to malignant tumours occurs by sustained hyperproliferaton of abnormal cells and blocked differentiation which encourage tumour mass growth and ultimate transformation of the normal tissue anatomy. Further progression encompases submucosal invasion and ultimately metastasis. Multiple gene and protein expression alterations have been associated with progression of colorectal adenomas; however, it is unknown whether they cause or are the result of adenoma transformation. According to Fearon and Vogelstein (1990), the next events occurring after Wnt signalling activation, include Kirsten-Ras (K-Ras) oncogene activation, loss of chromosome 18q, and impaired expression of the p53 tumour suppressor (Figure 1.8).

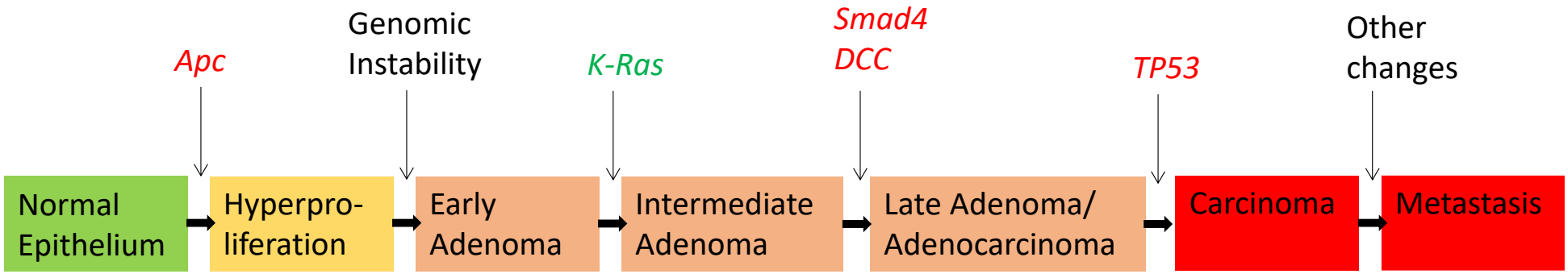

Figure 1.8 Multi-step tumourigenesis of theintestinal epithelium

Fearon and Vogelstein (1990) proposed that intestinal cancer formation occurs after a step-wise accumulation of mutations in the *Apc*, *K-ras*, *Smad4*, *DCC* (Deleted in CRC), *TP53* genes which create a genomically unstable environment. Inactivation of tumour suppressor genes and activation of oncogenes are shown in red and green, respectively.

1.3.3 Mouse models for the study of CRC

The first mouse models studying CRC

The first written report of an experimental study on colon carcinogenesis in rodents was in 1928 by Carl Krebs. Those early CRC models used carcinogenic substances such as polycyclic aromatic hydrocarbon (methylcholanthrene) 4-aminodiphenyl and 3,2-dimethyl-4-aminodiphenyl or even radioactive yttrium to induce the development of gastrointestinal cancer (Lorenz and Stewart 1940; Lisco *et al.* 1947; Walpole *et al.* 1952). When a population study of Guamanians showed the potential carcinogenic nature of hydrozines, found in consumed cycad flour, 1,2-dimethylhydrazine (DMH) and azoxymethane (AOM) were used in rodents to induce CRC and at that period this was the most common CRC rodent model being used (Laqueur *et al.* 1963). However, the genetic background of each mouse strain altered the outcome of carcinogen-induced tumours (Rowlatt *et al.* 1969; Nambiar *et al.* 2003). It was also noticed that even aged untreated C57BL mice developed sporadic tumours within the gastrointestinal tract (Rowlatt *et al.* 1969).

Genetically engineered models with germline and conditional non-inducible alleles

APC mouse models

An important mouse model that recapitulates the adenoma to carcinoma progression and loss of heterozygosity (LOH) observed in FAP patients is the *Apc*$^{Min/+}$ mouse model (Min stands for Multiple Intestinal Neoplasia; Luongo *et al.* 1994; Ichii *et al.* 1992). *Apc*$^{Min/+}$ mice were developed during a mutagenic study using *N*-ethyl-*N*-nitrosourea coupled with phenotypic screening. In these mice, a nonsense mutation caused an APC truncation at 850aa (Moser *et al.* 1990; Su *et al.* 1992). *Apc*$^{Min/+}$ mice develop a large number (~30) of spontaneous benign adenomas within the small intestine but less often within the colon (Moser *et al.* 1990). Subsequently, other *Apc* deficient genetically engineered mice were developed. Homozygosity for the *Apc* mutation led to embryonic lethality, but heterozygosity resulted in multiple adenomas whose number differed depending on the *Apc* mutation. Among them are the *Apc*$^{\Delta 716/+}$ and the *Apc*$^{1638N/+}$ mice (Fodde *et al.* 1994; Oshima *et al.* 1995). These models underscored the importance of WNT/β-CATENIN activation in colorectal cancer development.

Overexpression of β-CATENIN

Other non-inducible models included the overexpression of an activated form of β-CATENIN under the *Calbindin D9K* promoter linked to the enhancer of the *Aldolase B* gene. Those mice had intestinal dysplastic lesions but also polycystic kidney disease due to tissue- non-specific activation of β-CATENIN (Romagnolo *et al.* 1999).

The Cre-LoxP system

The Cre-LoxP system is employed for the deletion, insertion, translocation and inversion of DNA at specific sites; therefore, it is used extensively for the manipulation of the mouse genome to generate models for disease (Sauer 1998). This system is naturally used by P1 bacteriophages to circularize their DNA into plasmids and to unlink interlinked plasmids during bacterial replication, ensuring the passage of their DNA to the daughter bacterial cells (Oberdoerffer *et al.* 2003). The two components of the Cre-LoxP system are the Cre (cyclization recombination) site-specific DNA recombinase and LoxP (locus of X-over in P1 bacteriophages) a 34bp sequence which is recognized by Cre recombinase (Sternberg and Hamilton 1981; Abremski and Hoess 1984). Recombination occurs between two LoxP sites of the same or opposing DNA strand orientation; the former resulting in 'targeted' site excision (or floxing out), whereas the latter in its inversion (Oberdoerffer *et al.* 2003). Therefore, using the Cre-LoxP system, whole gene or specific parts of a gene can be knocked-out, site-specific mutations can be introduced and transgenes can be activated, when a floxed 'STOP' silencing cassette preceding the target gene is present (Sauer 1987; Orban *et al.* 1992; Albert *et al.* 1995; Oberdoerffer *et al.* 2003). Lastly, spatio-temporal regulation of this system can be achieved through Cre recombinase expression and activity regulation (Sauer 1998).

Promoter-coupled Cre expression

Cre-LoxP mouse models of intestinal tumourigenesis have been generated using different tissue-specific promoters such as *Fabpl-Cre*, *Villin-Cre* and *AhCre*. The first model, *Fabpl-Cre*, allows Cre recombinase expression in the small and large intestinal epithelial cells, as well as in the ureter and bladder epithelial cells beginning from embryonic day 13.5 (Saam and Gordon 1999). Two groups generated the *Villin-Cre* mouse model, independently, in which Cre recombinase was switched on at 12.5 days post coitum (dpc) and it was found to be expressed in intestinal epithelial cells and in kidney proximal tubule epithelial cells (Pinto *et al.* 1999; Madison *et al.* 2002).

Constitutive and tissue-specific study of MMR components

To replicate the CRC syndromes associated with inactivation of the mismatch repair (MMR) system, various mouse models were generated; one of which was the *Villin-Cre* mediated constitutive deficient in two important MMR components, MUTS or MUTL (*Msh* or *Mlh,* respectively). This model had microsatellite instability (inability of correcting DNA replication mistakes occurring in DNA areas with repeats of two or three nucleotides) in the intestinal epithelium and developed intestinal tumours after *Apc* gene inactivation (Nandan and Yang 2010).

Genetically engineered models with inducible recombination of conditional alleles

Cre-expressing adenovirus

Tissue specific APC deficiency was the next step in CRC experimental studies, allowing the development of models which resembled better sporadic clinical cases. These genetically modified mouse models were based on the Cre-LoxP system, targeting Cre-dependent excision of exon 14 of from the *Apc* gene, causing a frameshift mutation at codon 580 (Apc^{580S}). In the absence of Cre recombinase activity, $Apc^{580S/580S}$ mice were phenotypically normal. Upon anal infection with Cre-expressing adenovirus, homozygous deletion of exon 14 was achieved, causing the formation of multiple rectal adenomas within 3 months (Shibata *et al.* 1997).

Inducible promoters

Spatiotemporally regulated Cre recombinase activity has been achieved using a tamoxifen-dependent Cre recombinase under the control of the *Villin* (*Villin-*Cre^{ERT2}) or *Lgr5* (*Lgr5-*Cre^{ERT2}) promoters. The *Villin-*Cre^{ERT2}mouse model expresses Cre recombinase in the epithelial cells of the small and large intestines and the kidneys (El Marjou *et al.* 2004). The *Lgr5-*Cre^{ERT2} mouse model targets $LGR5^{+}$ cells including the CBC stem cells of the small and large intestines (Barker *et al.* 2007), as well as fetal mammary stem cells and adult mammary gland myoepithelial cells close to the nipple (Trejo *et al.* 2017) . The third commonly used inducible model, *AhCre,* places Cre recombinase under the control of the cytochrome P-450 promoter, but transcriptional activity is only up-regulated in the presence of lipophilic xenobiotics, such as β-naphthoflavone. *AhCre* $Ctnnb1^{fl/fl}$ mice have been used to assess the effects of β-CATENIN deficiency in many organs such as liver, intestine, pancreas, gallbladder, oesophagus, and stomach (Ireland *et al.* 2004).

Tamoxifen-induced Cre activation for Apc gene knockout.

Using the *Villin-*Cre^{ERT2} $Apc^{fl/fl}$ mouse model Andreu *et al.* (2005) showed that *Apc* loss along the crypt-villus axis leads to crypt expansion through increased proliferation, apoptosis, prevention of migration and differentiation and commitment to Paneth-secretory lineage. Although *Apc* loss within the post-mitotic cells present in the villi resulted in nuclear beta-CATENIN, there was no increase in proliferation and there were no other characteristics of transformation. In contrast, Barker *et al.* (2009) using the *Lgr5-*Cre^{ERT2} $Apc^{fl/fl}$ mouse model, showed that loss of *Apc* within the crypt base columnar (CBC) stem cells, expressing the LGR5 receptor, was responsible for their transformation and macroadenoma formation within 3-4 weeks. *Apc* loss within the transit-amplified cell compartment, using the *Ah-Cre* $Apc^{fl/fl}$ mouse model, could only give rise to microadenomas that rarely progressed into macroadenomas even 30 weeks later. Both studies

highlighted the importance of *Apc* gene as a gatekeeper in suppressing tumourigenesis and also the importance of target cell populations.

Combinatorial approaches

Finally, different combinations of gene mutations and/or deficiencies have been used to achieve invasive and metastatic tumours in mice based on the genetic model of CRC by Fearon and Vogelstein (1990). For example, *Tgfbr2* (the TGFβR-II receptor) null mice, developed CRC and metastasis only when crossed with mice expressing oncogenic *Kras* (Trobridge *et al.* 2009). Similarly, *Smad3*$^{-/-}$ mice developed metastatic colorectal adenocarcinomas within 4-6 months of age (Zhu *et al.* 1998). Since 50% of CRC exhibit activating mutations in *RAS* genes, multiple studies have been carried out to investigate the effects of activated K-RAS using the different intestinal tissue-specific promoters described above. Some of the studies have demonstrated the formation of aberrant crypt foci and adenocarcinomas, whereas K-ras activating mutations driven by the *Fabpl*-Cre promoter resulted in colon dysplasia (Janssen *et al.* 2002; Tuveson *et al.* 2004)

1.4 Cancer Treatment

The stage and severity of cancer dictates the type of treatment course that a patient should undergo. To date, CRC therapies include surgery, chemotherapy, radiotherapy and biological treatments.

1.4.1 CRC disease stage assessment

The extent of the disease for each case is assessed by contrast-enhanced computer tomography (CT). Magnetic resonance imaging (MRI), or in some cases endorectal ultrasound, is used to determine the tumour and lymph node staging, as well as the potential area of surgical margins to assess the possibility of local recurrence.

Tumour resection and pre-operational treatment

Patients with tumours with a potential resection margin and no lymph node metastasis, are considered as low risk of recurrence and could be cured after surgery alone. The distance between the macroscopic tumour and the resection, the surgical margin, is dependent on the position of the tumour. US guidelines state that the surgical margins of proximal and distal tumours should be ≥ 5cm which will allow the resection of the tumour with its associated vascular and lymphatic vessels (Nelson *et al.* 2001; Beasley *et al.* 2017). Nonetheless, even <1cm surgical margins can be decided on, for instance when the tumour is close to the anal sphincter (Kuvshinoff *et al.* 2001; Andreola *et al.* 2001). However, when the tumour size exceeds the accepted surgical margins or there is involvement of lymph nodes or an extramural vascular invasion, preoperative radiotherapy or chemotherapy could be used with an interval to allow tumour shrinkage, as these cases are considered moderate to high risk of recurrence (Poston *et al.* 2011).

Post-operative therapy

Adjuvant chemotherapy is considered for high risk stage II and III CRC to prevent local or systemic recurrence. For many years, the standard adjuvant treatment for this CRC stage was the combination of 5- fluorouracil (5-FU), a thymidylate synthase inhibitor, and folinic acid (LV), which helps longer retention of 5-FU within the body. However, recent evidence showed that monotreatment with capecitabine (pro-drug of 5-FU), or FOLFOX increase cancer-free and overall survival compared to 5-FU/LV alone. FOLFOX is the combined treatment of both oxaliplatin (a platinum alkylating agent which forms inter and intra-strand DNA cross-links inhibiting DNA synthesis) and 5-FU/LV (Eggington *et al.* 2006).

Advanced or metastatic CRC therapy

10-25% of CRC patients with resected primary tumours are diagnosed with liver metastasis, half of which also have extrahepatic (pulmonary, distant nodal, peritoneal) secondary tumours (Sheth and Clary 2005). Indication of metastatic disease is assessed by CT, MRI and 18-fluorodeoxyglucose (^{18}FDG) positron emission tomography (PET) in order to proceed to surgical removal of metastasis where possible, and/or chemotherapy (Poston *et al.* 2011). Chemotherapy options for advanced and metastatic CRC include (Poston *et al.* 2011):

a) FOLFOX as first-line treatment, followed by irinotecan, a topoisomerase II inhibitor.
b) FOLFOX as first-line treatment, followed by triple combination of 5-FU/LV/irinotecan (FOLFIRI).
c) Combination of Capecitabine with Oxaliplatin as first-line treatment followed by FOLFIRI as second-line treatment.

A phase III clinical trial in metastatic CRC patients showed that TAS-102, a combination of tipiracil hydrochloride and trifluridine, could increase the median overall and progression-free survival compared to placebo (Mayer *et al.* 2015). Trifluridine is a deoxyuridine analogue which blocks DNA replication. Tipiracil hydrochloride prevents enzymatic degradation of trifluridine (Mayer *et al.* 2015). Therefore, under NICE recommendations, TAS-102 could be used as a third-line CRC therapy (National Institute for Health and Care Excellence 2016).

Cytotoxic therapies can result in numerous side effects in other organs of the body. Basic research in intestinal tumourigenesis has made it possible to develop more targeted therapies that interfere with vital biochemical pathways or block mutated proteins that are essential for the survival and growth of cancer cells (Vanneman and Dranoff 2012). It is hoped such targeted therapies will target the tumour cells more effectively but with fewer side effects.

1.4.2 Biological agents used in metastatic CRC treatment

Targeted therapies include monoclonal antibodies or small molecule inhibitors (Hagan *et al.* 2013). Cetuximab for example, is a monoclonal antibody that inhibits the function of epithelial growth factor receptor (EGFR) and is used for the treatment of liver metastasis when used in combination with chemotherapy (Van Cutsem *et al.* 2009).

Panitumumab is another antibody based targeted therapy for metastatic CRC with wt *K-RAS* or *N-RAS*, which blocks the extracellular domain of the EGFR and hence its activation. It is given in combination with FOLFLOX or, in cases where there is disease progression even after chemotherapy treatment, it is given as a monotherapy (Giusti *et al.* 2009). Gefitinib, a small molecule which binds to the adenosine-triphosphate (ATP) pocket of the EGFR tyrosine kinase and inhibits its kinase activity, is also employed in the treatment of CRC (Rahman *et al.* 2014).

Various kinase inhibitors are used for the treatment of stromal gastrointestinal tumours which are sarcomas of the gastrointestinal tract arising from activating mutations of *c-KIT* and less commonly platelet-derived growth factor receptor alpha (*PDGFRA*; Linch *et al.* 2013). These include: Imatinib [tyrosine kinase inhibitor targeting ABL which is involved in chronic myelogenous leukemia, and the receptors KIT (CD117) and PDGFR (platelet-derived growth factor receptor; Lee and Wang 2009), Sunitinib (broad spectrum tyrosine kinase inhibitor) and Regorafenib (multi-kinase inhibitor; Pray 2008; Sutent 2007; Ettrich and Seufferlein 2014).

1.4.3 Nuclear medicine for cancer diagnosis and treatment

Cancer diagnosis using nuclear medicine

Nuclear medicine is used for the diagnosis of cancer stage, treatment planning and follow-up to assess the efficiency of a therapy (Eary 1999). Some of the most commonly used nuclear medicine scans include: bone scans, fluorodeoxyglucose-18 (18F-FDG) scan, thyroid scans, multigated acquisition (MUGA) scans and Gallium scans (uses summarised in Table 1.2). The scans work by using a radiotracer, which is essentially a radionuclide, that is administered to a patient, and tracked by specialized equipment detecting the pattern of radioactivity emitted from the examined patient. The scans are performed by Single Photon Emission Computed Tomography (SPECT) and positron emission tomography (PET), two nuclear imaging techniques whose radioactivity detection system defers. SPECT imaging is performed by a camera that rotates 360^{o} around the body, detecting γ-rays released from it and creating a series of pictures depicting the source of radiation in the body. PET scans are used to indirectly detect positron emitting radionuclides through pairs of photons (γ-rays) that are released in opposite directions when a positron encounters a free electron inside the body. The pair of photons reaches the ring-shape detector which slowly moves over the body to create an image-map of the body under examination (Rahmim and Zaidi 2008).

The interpretation of the site of the radioactivity emission is usually carried out by accompanied computer tomography (CT) scans, which use the X-ray energy emission pattern formed by the differences in radiological density of each tissue (the ability of each tissue to absorb X-rays) and computer processing in order to generate cross-sectional images of the body. These can also be used to generate three-dimensional (3D) X-ray images, which are more informative in terms of tissue topology. The combined information of the radioactivity pattern and the site of the body from which it is emitted are very informative. However, patients are exposed to more radiation (Lawrence *et al.* 2008) and there is a limit for tumour-size detection. Small tumours cannot be easily distinguished from the background radioactivity levels; for instance, 4mm is the lowest size to acquire good resolution when using PET scanners; this corresponds to the detection of

tumours with a volume of 0.2 ml (7 mm diameter) in 5:1 tumour-to-blood (T/B) ratio (Erdi 2012). Table 1.2 lists the indications of nuclear medicine in oncology as reviewed by Eary (1999).

The dependency of cancer cells on excess use of glycolysis (the Warburg effect) is the underlying rationale for ^{18}F-FDG-PET scanning. Although, many studies have shown that ^{18}F-FDG-PET imaging has a higher sensitivity (98%) than CT scans (91%) for tumour detection (Staib *et al.* 2000), it is not usually used for primary CRC tumour diagnosis (Brush *et al.* 2011). NICE recommendations, instead, indicate the use of ^{18}F FDG-PET for the detection of extrahepatic CRC metastasis (National Institute for Health Care and Excellence 2014).

Table 1.2 Indications of nuclear medicine in cancer

Scan type	Radiotracer	Indications
Bone scan	^{99m}Tc-methylenedi-phosphonate	Staging of bone metastasis from primary prostate, breast, lung and other cancers; and follow-up
Sestamibi scan	^{99m}Tc-sestamibi	Localisation of breast cancer in cases which remain non-diagnosed after conventional diagnostic tests; localisation of thyroid cancer in iodine-blocked patients or those with non-iodine-avid metastases.
Thallium scan	^{201}Tl chloride	Localisation of viable tissue by testing blood flow, particularly in brain tumour, osteosarcoma
Gallium scan	^{67}Ga chloride	Staging and treatment response in lymphoma and Hodgkin's disease
Metaiodoben-zylguanidine (MIBG) scan	^{131}I or ^{123}I labelled MIBG	Localisation of neuroendocrine tumours that take up norepinephrine
Octreotide scan	^{111}In-octreotide	Localisation of tumours with somatostatin receptors (e.g. pancreatic tumours, carcinoid tumours, medullary thyroid cancer, neuroblastoma)
FDG PET	^{18}F-FDG	Staging and follow-up of lung, colorectal, breast, head and neck, testicular cancers as well as lymphomas and melanoma

Monoclonal antibodies	^{111}In or ^{99m}Tc labelled tumour antibodies	To stage cancer and determine presence of tumour antigen (e.g. in lung, colorectal, and prostate cancers)

Radioimmunoconjugates (RIC) used in cancer

Monoclonal antibodies (mAbs) and monoclonal antibody-based therapeutics are employed against cancer. They are designed to bind specifically to highly expressed molecules on cancer cells, or their microenvironment (Goldenberg 2007). Antibody radiolabelling allows the imaging of its distirubtion within the body through non-invasive SPECT and PET scans. Some of the radionuclides used for mAb labelling are: Zirconium-89 (^{89}Zr), Indium-111 (^{111}In) and Copper-64 (^{64}Cu). Specifically, ^{89}Zr fits well the serum –half life of the mAb due to its 3.3 days of half-life allowing the clearance of non-bound circulating RIC prior to imaging and better tumour visualization (Moek *et al.* 2017).

A review by Moek *et al.* (2017) reported 24 RICs (described in Table 1.3) approved by the U.S. Food and Drug Administration (FDA) or the European Medicines Agency (EMA) for their use in clinical or pre-clinical trials. Most radiolabelled drugs were developed based on already approved antibodies used in the treatment of cancer. Examples include: a) trastuzumab, a drug used in breast cancer treatment because it recognizes and blocks the human epidermal growth factor receptor 2 (HER2) which is usually overexpressed in tumours; and b) cetuximab which binds the epidermal growth factor receptor-1 (EGFR1) and is mainly upregulated in CRC. Some of the uses of RIC include:

a) Detection of tumour lesions, and their position, that cannot be detected by conventional imaging techniques such us CT scans.
b) Assessment of tumour saturation by the mAb- based anti-cancer treatment.
c) Assessment of intrapatient tumour heterogeneity and relate to likelihood of their response to treatment.
d) Selection of patient and treatment according to RIC uptake results (i.e. identifying the expression levels of target molecules) .
e) In the case of bispecific antibodies (see BiTes in Table 1.3), they are used as an immunotherapy to attract cytotoxic T-cells onto cancer cells.

Table 1.3 Clinical trials on cancer patients using radiolabelled monoclonal antibodies or antibody based radio-tracers (Moek et al. 2017)

Target	Tracer name	Tracer structure	Patient population
Tumor			
A33	^{124}I-huA33	mAb	CRC
CA6	^{64}Cu-B-Fab	Fab fragment	Breast or ovarian cancer
CA9	^{124}I-girentuximab	mAb	RCC
	^{89}Zr-girentuximab	mAb	RCC
CEA	^{89}Zr-AMG 211	BiTE	Gastrointestinal adenocarcinoma
CD20	^{89}Zr-ibritumomab tiuxetan	mAb	NHL
CD44	^{89}Zr-RG7356	mAb	CD44-positive solid tumor
EGFR (HER1)	^{89}Zr-cetuximab	mAb	CRC, HNSCC, stage IV cancer
	^{89}Zr-panitumumab	mAb	CRC, NSCLC, sarcoma, urothelial carcinoma
EphA2	^{89}Zr-DS-8895a	mAb	EphA2-positive cancer
HER2	^{64}Cu-trastuzumab	mAb	Breast or gastric cancer
	^{68}Ga-HER2-Nanobody	Nanobody	Breast cancer
	^{68}Ga-trastuzumab-Fab	Fab fragment	Breast cancer
	^{89}Zr-trastuzumab	mAb	Breast cancer
HER3	^{64}Cu-patritumab	mAb	Solid tumors
	^{89}Zr-GSK2849330	mAb	HER3-positive solid tumors
	^{89}Zr-lumretuzumab	mAb	HER3-positive solid tumors
MSLN	^{89}Zr-MMOT0530A	mAb	Ovarian or pancreatic cancer
PIGF	^{89}Zr-RO5323441	mAb	GBM
PSCA	^{124}I-A11	Minibody	Bladder, pancreatic, or prostate cancer
PSMA	^{89}Zr-J591	mAb	GBM, prostate cancer
STEAP1	^{89}Zr-MSTP2109A	mAb	Prostate cancer
Microenvironment			
PD-1	^{89}Zr-pembrolizumab	mAb	NSCLC, melanoma
PD-L1	^{89}Zr-atezolizumab	mAb	Bladder cancer, NSCLC, TNBC
TGFβ	^{89}Zr-fresolimumab	mAb	Glioma
VEGF-A	^{89}Zr-bevacizumab	mAb	Breast cancer, glioma, MM, NET, NSCLC, RCC

Risks and benefits of low-dose radioactivity exposure

In contrast to the benefits of using low-dose radioactivity, potential risks are not well defined, with conflicting evidence. Clinical studies have demonstrated the benefits of using low-dose radioactivity in diagnosis of CRC. PET/CT scans were proven to change the staging of 30% of CRC patients and the treatment plan of 1/3 of those (Petersen *et al.* 2014). Moreover, the use of molecular markers to assist radionuclide imaging procedure was found to be even more sensitive in CRC metastasis detection compared to MRI and CT scans (83.6% and 88.2%, respectively; Boykin *et al.* 1999; Rohren *et al.* 2002; Sahani *et al.* 2005).

The potential risks associated with low-dose radioactivity were introduced by Muller based on his collaborative work with Raychaudhuri (1939-1940) which showed that γ-rays induced irradiation dose rates of 0.01 roentgen (R)/min or 0.09 millisieverts (mSv)/min and that doses as low as 400 R (equivalent to 3.73 Sv) could cause genetic alternations (Muller 1941). Hence, Muller suggested the linear no-threshold dose (LNTD) hypothesis which predicts that doses even lower than 400 R, are harmful proportionally to dose, and that they accumulate over time.

However, multiple studies followed that contradict this LNTD hypothesis. Natural occurring background radiation varies in different places on earth, ranging from 1-260 mSv/year (Ghiassi-Nejad *et al.* 2002). For comparison, a CT scan alone or combined with F-FDG PET/CT deliver doses of 10 and 14 mSv, respectively. Nonetheless, there was no association between cancer or childhood deaths and varying background radiation dose exposures, which is inconsistent to the LNTD hypothesis (Dobrzyński *et al.* 2015). Another study from atomic-bomb survivors showed that lower than 180 milligrays (mGy; equivalent to 180 mSv) acute dose exposure, did not increase the risk of solid-cancer mortality; in some cases, it was even beneficial, reducing cancer risk (Ozasa *et al.* 2011; Sasaki *et al.* 2014). Different levels of irradiation dose exposure could trigger mechanisms such as evolutionary adaptation to irradiation, DNA repair mechanisms and/ or elimination of damaged cells (Dauer *et al.* 2010). These studies suggest that there is a lower threshold at which the linear dose to mutation accumulation cannot be applied.

A statistically significant increase in cancer risk has not been associated with exposure to less than 100mSv doses therefore, based on the report of Biological Effects of Ionizing Radiation (BEIR) VII, the US National Academy of Sciences defines low-radiation doses as those <100mSv (Council 2006). The following paragraphs were dedicated in giving examples of studies pertinent to the use of nuclear diagnosis and the associated risks, if any, in increasing cancer incidence. One of these studies showed that radiation exposure from CT scans on fetuses and children increased their risk in developing cancer, probably due to increased cell division related to their developmental stage, as well as the longer life expectancy compared to an adult, which increases the opportunity for radiation-related cancers to occur (Stewart *et al.* 1956; Frush *et al.*

2003). However, diagnostic 0.8-1Gy (0.8-1Sv) doses of ^{131}I in thyroid does not show any increase in thyroid cancer risk even when given at an early age (11 years old; Hamilton *et al.* 1984).

Different diagnostic methods however, were correlated with increased cancer incidence. For instance, there was strong association between dose-response and increased breast cancer incidence in patients having fluoroscopic diagnosis (live X-ray imaging) of tuberculosis (Howe and McLaughlin 1996). Limited data from a case-control study suggests that there is an increased risk of chronic myeloid leukemia associated with gastrointestinal radiography and multiple spinal X-rays (Pogoda *et al.* 2011). In a study carried out in the U.S., a strong link was shown between numbers and types of X-ray diagnostic tests and chromosomal translocations in the peripheral blood of radiologic technologists (Sigurdson *et al.* 2008). Overall, more data need to be obtained for low-dose radiation exposure in relation to increased cancer risk. Nevertheless, these studies are difficult to be done, due to the fact that the radiation-related excess cancer risk at low doses cannot be easily extrapolated from the background level variation which would require multiple year studies involving millions of people (U.S. Food & Drug Administration 2017).

Radioimmunoconjugates (RIC) in CRC diagnosis

Radionuclide-labelled monoclonal antibodies are commonly termed radioimmunoconjugates or RICs. To date, none of the clinically-tested RICs are currently in use for the diagnosis of primary or metastatic CRC. OncoScint®, a radiotracer identifying the tumour-associated glycoprotein-72 (TAG-72), was approved by the U.S. Food and Drug Administration (FDA) in 1992 but not by the European Medicines Agency (EMA) for the detection of CRC and ovarian cancer as a diagnostic agent (Animal Cell Technology Industrial Platform 2013). CEA-scan, a radiotracer which identifies the carcinoembryogenic antigen (CEA), was approved in 1996 by both the FDA and the EMA; however, it was withdrawn from the EU market in 2005 for commercial reasons (European Medicines Agency 2005). HumaSPECT®, a [^{99m}Tc] labelled mAb against cytokeratin tumour-associated antigen, was EMA approved in 1998 for the detection of CRC recurrence and/or metastasis in patients with histologically proven carcinoma. In 2003, it was withdrawn from the market in EU, as its registration has not been renewed by the marketing authorisation holder (European Medicines Agency 2004).

Pre-clinical and Clinical trials

Many pre-clinical and clinical trials have been performed using RICs against various antigens that are found to be overexpressed in tumour cells such as: VEGF, CEA, CA 19-9, TAG-72 and EGFR. Table 1.3 summarises some of the studies that have been carried out since the 1980's in

identifying the appropriate immunoscintigraphy (the procedure that makes use of radioactively labelled antibody) for the detection of CRC-related tumours.

Table 1.4 Pre-clinical and clinical studies of immunoscintigraphic detection of CRC associated tumours

Scan type	Radiotracer	Aim	Diagnostic sensitivity, specificity or accuracy	Pre-clinical or clinical	Reference
γ-camera	^{131}I labelled 791T/36 (mAb against an osteogenic-sarcoma cell line, 791T)	Tumour detection CRC	10/11 patients with primary and/or secondary CRC turmours were accurately detected.	Clinical	(Farrands *et al.* 1982)
PET	^{64}Cu-DOTA-bevacizumab	Imaging and biodistribution of VEGF to correlate with tumour accumulation in CRC xenografts	Correlation (ρ = 0.81, *P* = 0.004) between VEGF expression in tumours with radiotracer accumulation	Pre-clinical	(Paudyal *et al.* 2011)
SPECT	^{131}I or ^{111}In labelled anti-CEA F(ab')2	Immunoscintigraphy of 1^{o} and metastatic CRC	96/121 known lesions detection (abdominal, pelvic and lymph node lesions but not liver metastasis) change in administration route increased liver metastasis detection.	Clinical	(Riva *et al.* 1989)
SPECT	^{111}In labelled mAb anti-TAG-72	Immunoscintigraphy for the detection of primary or recurrent tumours.	69% Sensitivity, 77% specificity. In comparison with CT immunoscintigraphy has greater sensitivity for the detection of pelvic tumours (74% vs 57%, P = .035) and extrahepatic abdominal tumours (66% vs 34%, P < 0.001). CT was more sensitive in identification of liver metastases (84% vs 41%, P < 0.001).	Clinical	(Collier *et al.* 1992)
SPECT	^{99}mTc labelled BW 431/26	Diagnosis and follow-up	Primary tumour identification (n = 65), sensitivity was	Clinical	(Lind *et al.*

	intact anti-CEA antibody	patients	95%, specificity 91%. For the diagnosis of early recurrences (n = 76) had 94% sensitivity and 86% specificity. Overall sensitivity of immunoscintigraphy in patients with suspected colorectal carcinomas and early recurrences was 95%, with 88% specificity.		1991; Hertel *et al.* 1990)
SPECT	^{99}mTc labelled BW 431/26 intact anti-CEA antibody	Diagnosis and follow-up patients	Immunoscintigraphy had an overall sensitivity of 70.0%, 37.5% for primary tumours 75.0% for recurrences and 100% for distant metastases	Clinical	(Vieira *et al.* 1993)
SPECT	^{99}Tcm labelled BW 431/26 anti-CEA antibody	Follow-up CRC patients	Differentiation of tumour recurrence vs scar tissue. On evaluation of 40 lesions, the radiotracer had a sensitivity and accuracy of 80%. On a patient basis had 83% sensitivity, 100% specificity and 87% accuracy.	Clinical	(Lacic *et al.* 1999)
SPECT	^{99}mTc labelled anti-CEA antibody	Diagnosis of recurrent CRC	78% sensitivity and 90% specificity for immunoscintigraphy in extrahepatic abdominal and pelvic disease. CT scans was more accurate than immuoscintigraphy for detecting liver and lung metastasis.	Clinical	(Fuster *et al.* 2003)
PET	^{64}Cu-DOTA-cetuximab	Selection of patients with EGFR positive tumours, monitor therapeutic efficacy of EGFR treatment,	Imaging EGFR-positive tumours	Pre-clinical	(Cai *et al.* 2007)
	^{89}Zr-DOTA-cetuximab		Selection method for cetuximab treatment in patients with wt RAS metastatic CRC (6/10 patients with tumour uptake)	Clinical	(Menke-van der Houven

		optimization of dosage of cetuximab treatment			van Oordt *et al.* 2015)
SPECT	Imacis 1: combination of (111 MBq ^{131}I) mAb CA 19-9 F (ab') $_2$ and mAb anti CEA F (ab') $_2$	Detection of metastasis and recurrence of colorectal carcinoma based on CAE and CA 19-9 expression	Generally, sensitivity of immunoscintigraphy was 97%, specificity 82%, positive predictive value 92%, negative predictive value 93%, and accuracy 92%	Clinical	(Artiko *et al.* 2011)
	Indimacis 19-9: ^{111}In-DTPA-CA 19-9 F (ab') $_2$				
	Oncoscint CR 103: (site-specific modification of the mAb B72.3) ^{111}In labelled TAG-72				

Cancer therapy using nuclear medicine

Radiotherapy is one of the main therapies approved by the NICE for the treatment of CRC. It is currently used:

- pre-operatively for the reduction of the tumour size, making it possible for resection of tumours that cannot initially be excised with sufficient margins.
- post-operatively as an adjuvant therapy for the elimination of remaining cancer cells.
- to palliate the symptoms of advanced and metastatic cancer due to intestinal blockage, or infiltration through pelvic structures (Janjan *et al.* 2002).

IR is usually administrated using external beam. Brachytherapy, an internally administered IR, is usually used for rectal tumours, because it avoids exposure of the skin and other abdominal tissues, thereby minimising some side effects. Radioembolization, which is the radioisotope injection into blood vessels from which tumours retrieve nutrients, and radiofrequency ablation of tumours through the generation of heat from medium frequency alternating current, are also used (American Cancer Society 2017).

Clinical trials

Some clinical trials have been conducted using radionuclides alone or conjugated to a monoclonal antibody (mAb), for the treatment of advanced and/or metastatic CRC. A systematic review carried out by Rosenbaum *et al.* (2013) showed that radioembolization with ^{90}Y, either as a monotherapy or combined with chemotherapy, could increase survival in 50% of the patients with unresectable and chemorefractory liver lesions for more than 12 months. Currently, at the University of California in San Francisco a combination radioembolization therapy with TAS-102 and ^{90}Y resin microspheres (phase I clinical trial) is being tested in patients with chemo-refractory CRC liver metastasis (ClinicalTrials.gov 2016).

A phase I clinical trial has been attempted in the past using a radiolabelled anti-CEA antibody. Patients were screened with ^{111}In-DTPA cT84.66 [a mouse/human chimeric anti-CEA antibody derived from the parental murine mAb T84] to identify CEA-expressing tumours; positive patients were then treated with ^{90}Y-DOTA-cT84.66. In this study, there was a dose-limiting haematopoietic toxicity observed with this treatment. In addition, the highest antibody uptake and tumour doses were observed in small nodal lesions, suggesting that ^{90}Y-DOTA-cT84.66 may be best applied in cases of minimal tumour burden (Wong *et al.* 2006).

Although some other clinical studies have been completed, no results have yet been published. Examples of these studies include:

- the use of ^{90}Y-DOTA-anti-CEA mAb M5A in combination with chemotherapy and bevacizumab for CRC metastatic patients (ClinicalTrials.gov 2015)
- the treatment of advanced CRC patients with ^{131}I- humanized antibody (huAb) A33 (glycoprotein highly expressed in colon tumours) (Barendswaard *et al.* 1998; ClinicalTrials.gov 2013).

^{111}In -anti- γH2AX-TAT characteristics

^{111}In makes a highly potent radionuclide thanks to emission of short-range Auger electron (Cornelissen *et al.* 2012). Auger electron emission triggers a cluster of ionization events in the scale of nanometres (O'Donoghue and Wheldon 1996; Spitz and Hauer-Jensen 2014) causing irreparable local DNA damage.

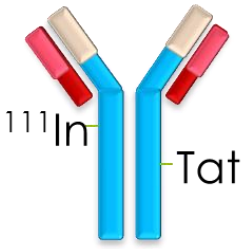

Figure 1.9 Anti-γH2AX RIC structure.

An anti-γ-H2AX antibody modified with a Tat peptide for nuclear localization and conjugated with a radioisotope (^{111}In).

^{111}In is an electron capture (EC) nuclide (100% of its decay occurs via EC), with a radioactive half-life of 2.8047 days which, upon capture of its orbital electrons, forms ^{111}Cadmium (^{111}Cd) nuclide in an excited state. ^{111}Cd is stabilized by emission of 171.3 (90%) and 245.4 (94%) kilo electron-volts (keV) γ-rays and X-rays of 23 keV (68%). Some of the atomic disintegrations of the ^{111}Cd nucleus expel orbital electrons, with energies 145 and 219 keV (8% and 5%, respectively), by internal conversion, resulting in X-ray emission. K and L Auger electrons can then be ejected from the X-ray emission with energies of 19 and 3keV respectively (in 16% and 100% of atomic disintegrations, respectively) (Perkin Elmer 2010).

Auger electrons

Auger electrons have a low kinetic energy with a subcellular range of a few nanometers (nm) to a few micrometers (µm). The different DNA condensation states, such as chromatin fibres, nucleosomes and double stranded DNA, are within this range. Thus, if the source of Auger electrons happens to be close to or within the nucleus, this could lead to DNA damage. Howell

et al. (1990) showed that Auger electrons are as capable as α-positron-emitting radionuclides at causing biological damage when incorporated into DNA.

Auger electrons do not have the potential of γ-, x-rays or α-, β-positrons in causing ionization events to a whole organ. Intracellularly, however, they can affect structures that may be irreversibly damaging to the cell. The survival of the cell is dependent on the extent of damage to DNA integrity caused by Auger electrons (Baverstock and Charlton 1988; Hofer 1996). An *in vitro* study by McLean *et al.* (1989) showed that differences in cellular localization of ^{111}In can affect cell survival. Extracellular ^{111}In-chloride caused damage at a rate of about 6.1 X 10^{-12} Gy/decay, whereas intracellular introduction of high specific activity ^{111}In (0.389 Bq/cell; 2.9 X 10^4 Gy/decay) stopped cell division whilst low (0.075 Bq/cell; 7.2 x10-4 Gy/decay) to moderate (0.204 Bq/cell; 4.5 X 104 Gy/decay) activities did not. The surviving fraction of cells treated internally with ^{111}In could divide and redistribute ^{111}In to their daughter cells, as indicated by reduction of radioactivity in cells post mitotic phase (McLean *et al.* 1989). However, it remains unclear whether these cells had repaired any possible DNA damage caused by low or medium activity exposure to ^{111}In prior to division; the opposite could imply that there is an increased possibility of DNA damage accumulation in the daughter cells.

Internalization, retention and γH2AX affinity

^{111}In-anti-γH2AX-TAT Ab (Figure 1.9) enters a cell and its nucleus irrespective of the expression of γH2AX due to its antibody and TAT associated properties. TAT peptide (GRKKRRQRRRPPQGYG) has cationic charge as it is rich in arginine and lysine which facilitate the cell membrane and nuclear penetration (Drin *et al.* 2003). The mechanism is not clear, however multiple studies have suggested that TAT peptides are enclosed in endosomes post cellular membrane internalization (Brooks *et al.* 2005; Ferrari *et al.* 2003; Fittipaldi *et al.* 2003). In agreement with these, a study by Cornelissen *et al.* (2007) showed that cellular and nuclear importation of ^{111}In-anti-mIgG-TAT was decreased by 3-fold and 2-fold respectively after inhibition of lysosomal acidification. TAT contains a nuclear localization signal containing domain of the HIV-1 transactivator of transcription (TAT) which has proven to be capable of penetrating nuclear membranes using importins (Cornelissen *et al.* 2008).

A competition radioimmunoassay (RIA) was performed by Cornelissen *et al.* (2011) to assess the affinity of ^{111}In-anti-γH2AX-TAT for γH2AX. Unlabelled DTPA-anti-γH2AX-TAT and anti-γH2AX had similar affinity for γH2AX. Moreover, fluorochrome conjugated anti-γH2AX-TAT but not fluorochrome conjugated anti-IgG-TAT could co-localise with γH2AX foci *in vitro* at 2h post treatment whilst both were also present on the cell membrane and cytoplasm (Cornelissen *et al.* 2011). At 24h there was a complete nuclear internalization and γH2AX foci colocalization

only by fluorochrome-conjugated anti-γH2AX-TAT. γH2AX foci exist even 23h post irradiation in the presence of either fluorochrome conjugated anti-γH2AX-TAT or fluorochrome conjugated anti-IgG-TAT which implies that DNA damage repair pathways are not altered in the presence of the fluorochrome conjugated anti-γH2AX-TAT. Furthermore, the localization of fluorochrome conjugated anti-γH2AX-TAT is specific to the site of γH2AX induction determined by Cornelissen *et al.* (2011) through the slit-irradiation technique.

The pharmacokinetics of ^{111}In-DTPA–anti-γH2AX-TAT or isotype control (^{111}In-DTPA–mIgG-TAT) Ab in a cell were also addressed by Cornelissen *et al.* (2012). RICs were incubated for 0-4h with 4Gy irradiated or sham-irradiated MDA-MB-468 cells. At 10h ^{111}In-DTPA–anti-γH2AX-Tat or ^{111}In-DTPA–mIgG-Tat were mostly eliminated from the sham-irradiated cells reaching 20%. Only ^{111}In-DTPA–mIgG-Tat had similar fate in irradiated cells reaching background levels at 10h ($T_{1/2}$ elimination half-life= 0.23 ± 0.09 h). Significantly higher was ^{111}In-DTPA–anti-γH2AX-TAT retention in irradiated versus sham-irradiated cells (half-life 27.71 ± 11.01h vs. 1.81 ± 0.87h, respectively; P = 0.0076, F test), indicating the specificity ^{111}In-DTPA–anti-γH2AX-TAT retention in γH2AX-induced cells. As determined by Cornelissen *et al.* (2012) the percentage of ^{111}In remaining internalized in MDA-MB-468 cells at 4h after 1h of exposure to ^{111}In-DTPA-anti-γH2AX-Tat (0.5μg/mL, 0-6MBq/μg) with or without 10 Gy IR was proportional to the specific activity of the RIC.

^{111}In -anti- γH2AX-TAT for imaging DNA damage in vivo

^{111}In has a well-developed radiochemistry and available Ab labelling chelators such as diethylenetriaminepentaacetic acid (DTPA) and 1,4,7,10-Tetraazacyclododecane-1,4,7,10-tetraacetic acid (DOTA), due to its various applications in patient diagnosis. Some of the imaging applications of ^{111}In include labelling of platelets, leukocytes, octreotide, anti-CD20 Ab and capromab pendetide, which are used for the diagnosis of thrombus formation, inflammation, neuroendocrine tumours, lymphoma and prostate cancer, respectively (Peters *et al.* 1984; Lewis *et al.* 2014; Jamar *et al.* 1995; Knox and Levy 2015; Petronis *et al.* 1998).

Initially, ^{111}In-anti-γH2AX-TAT Ab was developed to image DNA damage and more specifically DSBs *in vitro* and *in vivo* (Cornelissen *et al.* 2011). Imaging DSBs is useful as they are the most dangerous form of DNA damage. Moreover, the number of DSBs and their persistence in the cell reflects the likelihood of cell death (Banáth *et al.* 2010). DNA damage and cell death are two important factors on which many anti-cancer treatments depend on. *In vivo* imaging of superficial tumour DNA damage could be carried out by fluorescence imaging after intravenous (i.v.) injection of a fluorochrome (Cy3)-conjugated anti-γH2AX-TAT Ab. However, this technique could not be used for tumours positioned deep inside the body due to light retention by

overlying tissues; therefore, they used the γ-rays of ^{111}In labelled anti-γH2AX-TAT Ab to image the DSBs of these tumours using SPECT imaging (Cornelissen *et al.* 2011).

A study was conducted by Cornelissen *et al.* (2011) to assess the *in vivo* pharmacokinetics of ^{111}In-DTPA-anti-γH2AX-TAT, described in this paragraph. MDA-MB-468 xenografts bearing mice were injected with bleomycin (10 μg/mouse) or IR (10 Gy) and subsequently injected (10 μg, 1 MBq/μg) intravenously with ^{111}In-DTPA-anti-γH2AX-TAT or ^{111}In-DTPA-mIgG-TAT. SPECT-CT imaging was carried out at 24, 48 and 72h post RIC injection (Figure 1.10 A). Volume of interest analyses for tumours (Figure 1.10 B) showed that ^{111}In-DTPA-anti-γH2AX-TAT had higher uptake in treated tumours at each time point compared to ^{111}In-DTPA -mIgG-TAT. In addition, ^{111}In-DTPA-mIgG-TAT could not distinguish between treated and untreated tumours; whereas, both bleomycin and IR tumour treatment resulted in significantly increased uptake of ^{111}In-DTPA-anti-γH2AX-TAT compared to control, which implies that tumours had higher DNA damage content. Even 72h post RIC treatment, ^{111}In-DTPA-anti-γH2AX-TAT was retained within the bleomycin treated tumours, as DNA damage was not resolved compared to IR tumours. Increased γH2AX foci induction was positively correlated to increased ^{111}In-anti-γH2AX-TAT uptake (Spearman r=0.9; p=0.042) confirmed by biodistribution assays from harvested tissue and SPECT-CT imaging (Cornelissen *et al.* 2011) confirming the fact that ^{111}In-DTPA-anti-γH2AX-TAT exerts its specific to tumour uptake due to increased levels of γH2AX.

Generally, ^{111}In-DTPA-anti-γH2AX-TAT and ^{111}In-DTPA -mIgG-TAT biodistributions were comparable for normal tissues at all time points (i.e. 2, 24, 48, 72h; Table 1.4; Cornelissen *et al.* 2011). This was due to the fact that ^{111}In-anti-γH2AX-TAT Ab has a non-specific mode of cellular internalization, hence isotype control RIC (^{111}In-anti-IgG-TAT), could also internalize into tumours, probably due to the enhanced permeability and retention (EPR) effect usually characterising uptake into tumours.

Whilst ionizing events from γ-, X-photons and Auger electrons are capable of damaging macromolecules, the small quantities of radioactivity used in imaging procedures (as opposed to therapeutic doses) are not expected to cause significant cell or DNA damage. As a proof, the specific activity of 1MBq/μg of ^{111}In-anti-γH2AX-TAT used for *in vivo* imaging has not been shown to decrease cell survival when used *in vitro* on MDA-MB-468 breast cancer cell line (Cornelissen *et al.* 2011).

^{111}In -anti- γH2AX-Tat as a radiosensitizer

Cornelissen *et al.* (2012) have demonstrated that ^{111}In-anti-γH2AX-TAT RIC can also be used as a radiosensitizer when labelled with high-enough specific activities (>3MBq/μg), taking advantage of the Auger electron emission for the amplification of the DNA damage signal caused by DNA

damaging agents (Kersemans and Cornelissen 2010). In their study, they showed that IR (4Gy or 10Gy) or bleomycin (20μg/mL) treatment of two breast cancer cell lines (MDA-MB-468 and 231-H2N), used to induce γH2AX formation, when followed by treatment with 6MBq/μg of ^{111}In-anti-γH2AX-TAT, resulted in 2-fold increase in γH2AX foci number and 10-fold increase in the cytotoxic effect of these DNA damaging agents, whereas combination treatment with the isotype control RIC had no effect on cell survival. Hence, the specific activity of ^{111}In-anti-γH2AX-TAT was a critical variable in the amplification of DNA damaging agent-induced cytotoxicity.

The damage caused by high specific activities of ^{111}In-anti-γH2AX-TAT was the result of ionization events from ^{111}In decay which generated oxidised purines whose number increased in combination treatment with IR. In MDA-MB-468 cells, the combination of 4Gy IR with ^{111}In-anti-γH2AX-TAT increased purine oxidisation but did not generate more pyrimidine oxidisation or AP-sites compared to control. Furthermore, ^{111}In-anti-γH2AX-TAT alone could also generate oxidised purines compared to control though fewer than when combined with IR (Cornelissen *et al.* 2012). In contrast, ^{111}In-mIgG-TAT alone or IR combined could not significantly increase the number of oxidised purines or pyrimidine, or AP-sites (Cornelissen *et al.* 2012).

γH2AX foci spatial distribution in 231-H2N cells has been also studied by Cornelissen *et al.* (2012). Specifically, γH2AX foci grouping tendency was estimated by spatial descriptive statistics using Ripley's-K value (Kiskowski *et al.* 2009). This demonstrated that combination treatment of a genotoxic agent with ^{111}In-anti-γH2AX-TAT, but not the isotype control, generated γH2AX foci in groups with ~1 μm average diameter, independent of the foci number/cell, compared to genotoxic agent alone (Cornelissen *et al.* 2012)**.** Therefore, γH2AX foci clustering in combination treatment with ^{111}In-anti-γH2AX-TAT was a result of the ionization events from the specific antibody rather than due to the increased foci number/ cell, which provides additional evidence of the amplification of already existing DSB.

The *in vivo* results were even more promising showing that the combination of the RIC along with 10Gy IR in breast cancer xenograft-bearing mice resulted in a 20-fold decrease in tumour growth (Cornelissen *et al.* 2012). It was demonstrated that tumour growth rate was significantly reduced following just one dose of 10 Gy IR combined with ^{111}In-anti-γH2AX-TAT (10μg/mouse, 6MBq/μg) compared to untreated mice or each treatment alone. Non-radiolabelled anti-γH2AX-TAT or ^{111}In-mIgG-TAT combined with IR did not significantly decrease tumour growth rate compared to IR alone. Moreover, all treatments were proven to be well tolerated by the mice with no significant weight loss (Cornelissen et al. 2012).

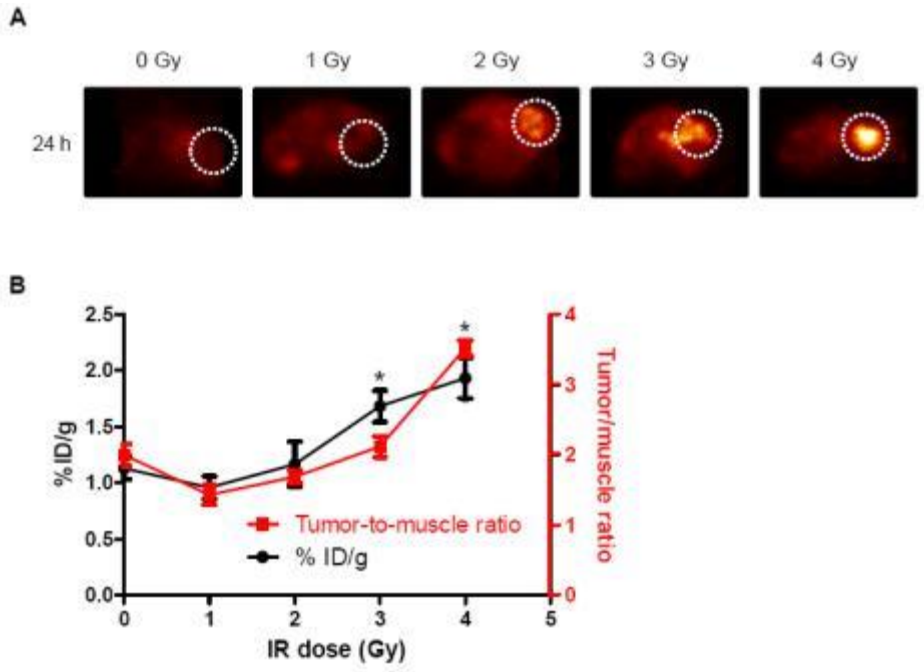

Figure 1.10 γH2AX induction within tumours by IR is correlated to the percentage of uptaken 111In-anti-γH2AX-TAT.

MDA-MB-468 tumours (circled) of xenograft bearing mice were sham-irradiated or irradiated with 1-4Gy 1h before ^{111}In-DTPA -anti-γH2AX-TAT injected (10 µg, 1 MBq/µg). (A) SPECT-CT transverse images through the tumour are shown. (B) Radioactivity uptake within the tumour is expressed as %ID/g or as tumour to muscle ratio (Cornelissen *et al.* 2011).

Table 1.5 Biodistribution data comparing ^{111}In-DTPA-anti-γH2AX-TAT and ^{111}In-DTPA -mIgG-TAT (Cornelissen et al. 2011)

	Control		Bleomycin		IR (10 Gy)	
%ID/g	**^{111}In-mIgG-Tat**	**^{111}In-anti-γH2AX-Tat**	**^{111}In-mIgG-Tat**	**^{111}In-anti-γH2AX-Tat**	**^{111}In-mIgG-Tat**	**^{111}In-anti-γH2AX-Tat**
Blood	3.61 ± 0.30	3.04 ± 0.77	3.29 ± 0.32	3.19 ± 0.26	3.43 ± 0.77	3.69 ± 0.52
Tumour	2.62 ± 1.02	3.58 ± 0.41	2.39 ± 1.07	6.86 ± 0.71	2.27 ± 0.42	2.56 ± 0.36
Muscle	0.47 ± 0.23	0.41 ± 0.08	0.53 ± 0.02	0.30 ± 0.27	0.48 ± 0.14	0.37 ± 0.03
Stomach	0.27 ± 0.07	0.35 ± 0.04	0.26 ± 0.13	0.39 ± 0.24	0.28 ± 0.08	0.44 ± 0.08
Small Intestine	0.80 ± 0.05	0.84 ± 0.03	0.78 ± 0.06	0.92 ± 0.24	0.72 ± 0.04	0.79 ± 0.12
Large Intestine	0.54 ± 0.02	0.64 ± 0.14	0.52 ± 0.02	0.68 ± 0.13	0.52 ± 0.07	0.59 ± 0.05
Spleen	1.05 ± 0.07	1.03 ± 0.51	1.08 ± 0.07	2.05 ± 0.15	0.98 ± 0.45	2.02 ± 0.18
Liver	4.24 ± 0.55	4.10 ± 0.33	4.00 ± 0.75	4.20 ± 0.52	4.50 ± 0.58	4.60 ± 0.64
Kidneys	5.19 ± 0.61	4.72 ± 0.59	5.48 ± 0.28	4.89 ± 0.21	5.00 ± 1.18	4.88 ± 0.32
Heart	1.71 ± 0.24	1.38 ± 0.23	1.69 ± 0.69	1.43 ± 0.21	1.64 ± 0.18	1.38 ± 0.07
Lungs	2.21 ± 0.08	1.85 ± 0.25	1.95 ± 0.22	1.93 ± 0.20	2.22 ± 0.37	2.00 ± 0.25

1.5 Aims and objectives

Based on the anti-tumour effects of ^{111}In-anti-γH2AX-TAT radioimmunoconjugate (RIC) in amplifying the effects of DNA damaging agents, the hypothesis of this project was that the DNA damage caused endogenously after *Apc* loss and excess Wnt signaling activation will be enough to attract ^{111}In-anti-γH2AX-TAT RIC. The usage of high enough specific activity ^{111}In-anti-γH2AX-TAT RIC could potentially amplify endogenous DNA damage, thereby increasing apoptosis and ultimately reducing tumourigenesis.

Key aims of this project were, first, to quantify γH2AX levels in *Apc*-deficient intestinal dysplasia and tumours of transgenic mouse models, as well as in *ex vivo* intestinal organoids derived from these mouse models and human tumours. Second, this project aimed to use low specific activity RIC treatment to image intestinal lesions *in vivo,* and subsequently assess its effects on DNA damage, cell death and proliferation. Although initially being part of the project aims, the investigation of the ^{111}In-anti-γH2AX-TAT RIC potential in amplifying *Apc*-deficiency-associated DNA damage has not been possible.

2. Materials and Methods

2.1 Experimental animals

All animal procedures and experiments were conducted in accordance with the UK Animals (Scientific Procedures) Act 1986, under the authority of Home Office project and personal licenses following local ethical review and in accordance with the ARRIVE guidelines.

2.1.1 Transgenic constructs and animals

Mouse models with a Cre-LoxP conditional allele of the *Apc* gene were used. Mice carrying LoxP (locus of cross over in P1 bacteriophages) sequences in the introns flanking exon 14 of APC ('flanked by LoxP sites' or floxed; abbreviated fl; Shibata *et al.* 1997) were crossed with mice that express Cre (causes recombination) recombinase under a tissue specific promoter. The initiation of transcription of the promoter triggers the expression of the Cre recombinase and the excision of the flanked region of DNA (Kühn and Torres 2002). The *Vil*Cre^{ER}*Apc*$^{fl/fl}$ model expresses Cre^{ER}, a fusion protein of Cre recombinase connected to a mutated ligand-binding domain of human estrogen receptor (ER) under the *Villin* (*Vil*) promoter which is expressed in the mouse intestinal enterocytes (Crosnier *et al.* 2006; El Marjou *et al.* 2004). Similarly, the *Lgr5*Cre^{ER}*Apc*$^{fl/fl}$ model expresses Cre^{ER} under the control of the *Lgr5* promoter, which is expressed in intestinal stem cells (Barker *et al.* 2007). ER fusion proteins are normally present in the cytoplasm where they bind to chaperones (Hayashi and McMahon 2002). Tamoxifen, an antagonist of estrogen, binds the ER fusion protein and disrupts its interactions with chaperones allowing Cre^{ER} to translocate into the nucleus, where the modified Cre recombinase can recombine the floxed gene (Chen *et al.* 2007; Hayashi and McMahon 2002).

2.1.2 Experimental procedures

All experimental procedures were carried out on mice that were at least 10-weeks old. Administration of solutions was either *via* intraperitoneal injection using 1 ml syringe (BD Plastipak) and 25G needle (BD Microlance 3), or *via* oral gavage, using 1 ml syringe (BD Plastipak) and bulb tipped gastric gavage needle (Harvard apparatus).

Injection of Tamoxifen

Mice carrying the *Vil*Cre^{ER} or *Lgr5*Cre^{ER} transgene were administrated Tamoxifen to induce Cre recombination. Tamoxifen powder (Sigma-Aldrich) was mixed in corn oil (Sigma-Aldrich) at a concentration of 10 mg/ml by heating up to 80^{o}C while being stirred continuously. Aliquots were stored at -20^{o}C. Before each procedure, aliquots were thawed and kept warm at 80^{o}C until prior to the administration. The remaining tamoxifen solution was re-frozen, but thawed out for up to three times only, in order to avoid tamoxifen degradation. The induction of *Villin*CreER

mice was carried out by three intraperitoneal administrations of 80 mg of tamoxifen per kg of mice, at least 3h apart (but in a single day). *Lgr5*CreER mice were orally gavaged with tamoxifen once daily for four days (80mg/kg).

2.1.3 Polymerase Chain Reaction (PCR) genotyping

Genotyping of the animals was performed by PCR using extracted DNA from ear biopsies, both at weaning and also confirmed at death. PCR primers were selected from either previous publications or designed through Primer3 software (http://fokker.wi.mit.edu/primer3/input.htm). Primer specificity was confirmed by Basic Local Alignment Search Tool (BLAST) software against the Ensembl sequence database (http://www.ensembl.org/Multi/Tools/Blast) before being synthesised by Sigma Genosys.

DNA extraction from ear biopsies

Ear biopsies were stored at -20°C in 1.5 ml eppendorf tube until processed. Tissue digestion was facilitated by incubation in 250 µl of Cell Lysis Buffer (5 Prime; ThermoFisher Scientific) including 0.4 mg/ml Proteinase K (Roche) overnight at 37°C with agitation. Addition of 100 µl of Protein Precipitation Solution (5 Prime; ThermoFisher Scientific) and subsequent mixing by inversion, precipitated the protein. Following centrifugation at 13000 rcf for 10 min, the resulting supernatant, containing the DNA, was transferred to a 1.5 ml eppendorf tube containing 250 µl of isopropanol. The solution was mixed and centrifuged at 13000 rcf for 15 min to pellet the DNA. Supernatant was discarded carefully, before pellets were air dried for 1h and dissolved in PCR-grade water (Sigma-Aldrich).

Generic PCR genotyping protocol

PCR reactions were mixed in thin-walled 0.2 ml strip tubes or thin-wall 96-well plates (Alpha Laboratories) using a multichannel pipette with filtered pipette tips. In individual wells, 2.5 µl of either PCR-grade water (Sigma-Aldrich) or purified genomic DNA from an ear biopsy were added to 47.5 µl of prepared master-mix (seeTable 2.1) The 96-well plates were then covered with aluminium foil seals (StarLab) or the caps of the strip tubes were closed, always ensuring that there were no bubbles in the mixture. The reactions were run using GS1 (G-Storm) thermal cycler using the conditions shown in Table 2.2. Primer sequences and sizes for each transgene and LoxP-targeted *Apc* Allele amplification are outlined in Table 2.3 and examples of the genotyping results are depicted in Figure 2.1. Cre and LacZ transgenes were run together in a single PCR reaction. Note that the Lgr5-Cre transgene was run using 2 reverse primers and one forward primer to identify both WT and mutant bands simultaneously.

2.1.3.1 *Visualization of PCR products*

PCR products were separated by agarose gel electrophoresis. 5 µl of DNA loading dye (50% Glycerol (Sigma-Aldrich), 50% distilled water (dH_2O), 0.1% [w/v] Bromophenol Blue (Sigma-Aldrich)) were added to the PCR products and mixed by pipetting. The samples, as well as DNA ladder (Promega) were loaded onto 2% agarose gel (4 g agarose (Eurogentech), 200 ml 1X Tris Borate-EDTA (TBE) buffer (National Diagnostics), 10 µl of 10 mg/ml ethidium bromide (Sigma) or 10 µl Safeview (NBS Biologicals)). Gels were run in 1X TBE at 120V for approximately 30min and then visualised under UV light using GelDoc UV Transilluminator (BioRad). GelDoc software (BioRad) was used to capture the images.

Table 2.1 Genotyping PCR reaction mixture

	Cre	ApcLoxP	Lgr5-Cre	Villin-Cre
PCR reaction components:				
DNA extract	2.5 µl	2.5 µl	2.5 µl	2.5 µl
Master Mix:				
PCR-grade H_2O (Sigma-Aldrich)	31.7 µl	31.7 µl	31.6 µl	31.7 µl
GOTaq PCR Buffer (5X, Promega)	10 µl	10 µl	10 µl	10 µl
Magnesium Cloride (25 mM, Promega)	5 µl	5 µl	5 µl	5 µl
dNTPs (25 mM, ThermoFisher Scientific)	0.4 µl	0.4 µl	0.4 µl	0.4 µl
Forward Primer (100 mM, Genosys; Sigma-Aldrich)	0.1 µl	0.1 µl	2 x 0.1 µl	0.1 µl
Reverse Primer (100 mM, Genosys; Sigma-Aldrich)	0.1 µl	0.1 µl	1 x 0.1 µl	0.1 µl
Taq Polymerase	0.2 µl	0.2 µl	0.2 µl	0.2 µl
Taq Polymerase Brand	GOTaq	DreamTaq	DreamTaq	GOTaq
Total Reaction Volume	50 µl	50 µl	50 µl	50 µl

Table 2.2 PCR thermal cycler conditions

Cycling conditions (Time; Temperature)	Cre	ApcLoxP	Lgr5-Cre	Villin-Cre
Initial denaturation	3 min; 95 °C	3 min; 95 °C	3 min ; 95 °C	2.5 min ; 95 °C
Cycle number	30	40	40	35
Step 1 (Denaturation)	30 sec; 94 °C	30 sec; 95 °C	30 sec; 94 °C	30 sec; 94 °C
Step 2 (Annealing)	30 sec; 55 °C	30 sec; 60 °C	30 sec; 58 °C	30 sec; 62 °C
Step 3 (Elongation)	1 min; 72 °C	1 min; 72 °C	30 min; 72 °C	1 min; 72 °C
Final Extension	5 min; 72 °C	5 min; 72 °C	5 min; 72 °C	5 min; 72 °C
Hold	∞; 10 °C	∞; 10 °C	∞; 10 °C	∞; 10 °C

Table 2.3 Primer sequences and band sizes

Name	Forward primer	Reverse primer	Product size
Cre	TGA CCG TAC ACC AAA ATT TG	ATT GCC CCT GTT TCA CTA TC	1000 bp
ApcLoxP	GTT CTG TAT CAT GGA AAG ATA GGT GGT C	CAC TCA AAA CGC TTT TGA GGG TTG ATT C	WT at 226 bp; Targeted at 314 bp
Lgr5-Cre^{ER}	CTG CTC TCT GCT CCC AGT CT	ATA CCC CAT CCC TTT TGA GC	WT at 298bp;
		GAA CTT CAG GGT CAG CTT GC	Targeted at 174bp
Villin-Cre^{ER}	CAA GCC TGG CTC GAC GGC C	CGC GAA CAT CTT CAG GTT CT	Targeted at 220bp

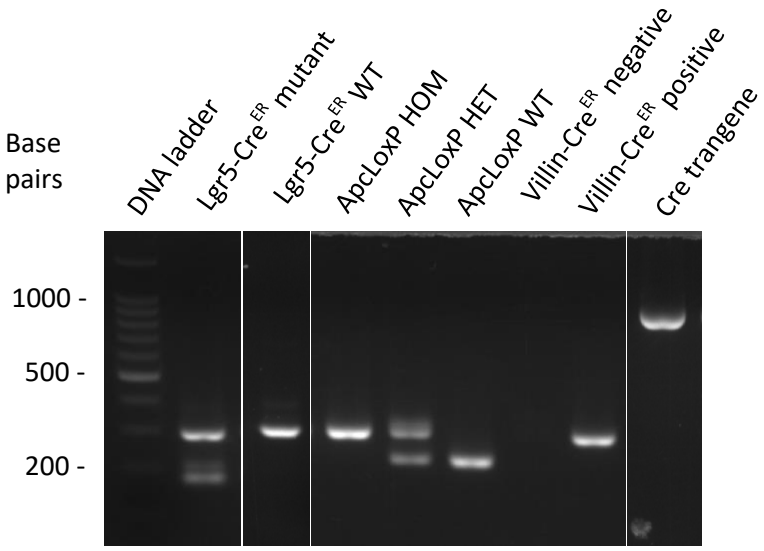

Figure 2.1 Genotyping band sizes

2.2 Tissue harvesting and processing

Experimental animals were culled by cervical dislocation according to schedule-1 of the Animals (Scientific Procedures) Act 1986. Tissue was immediately harvested after humane killing of an animal to avoid degradation of RNA and protein or alteration of the phosphorylation status of phospho-proteins.

2.2.1 Tissue harvesting

Dissections were carried out using a micro-dissection kit in a designated area. The abdominal fur was dampened with 70% ethanol and the skin together with the peritoneal muscle wall were cut open using one incision at the bottom of the ventral mid-line and two longitudinal incisions stemming from this incision towards the upper abdominal sides. Kidney, spleen and a small part of liver were removed before disconnecting the small intestine from the stomach at the pyloric junction to the beginning of the caecum. The large intestine including the anus was separated from caecum. The contents of both small and large intestines were flushed out using a syringe (BD Plastipak) filled up with cold tap water, unless otherwise specified. Both small and large intestines were opened longitudinally on a flat surface exposing the intestinal epithelium (Figure 2.2). A small piece (0.5 – 2.0 cm) of small and large intestine and dissected tumours were placed in separate eppendorf tubes and immediately snap-frozen on dry ice to be stored at -80°C until processed for RNA or protein extraction. Using forceps, the side from the pylorus junction of the small intestine was rolled inside towards the end of small intestine; similarly, the large intestine closer to caecum was rolled inside towards the anus. The gut-rolls were pierced through by a 23G syringe needle (BD Microlance), to hold the required shape for fixing.

Figure 2.2 Longitudinal incision of the small intestine.

2.2.2 Tissue fixation

The dissected tissues for immunohistochemical analysis were immersed in 10% neutral buffered formalin (Sigma-Aldrich) and quick-fixed for 24 h at 4°C. 24h later tissues were either paraffin embedded or kept in 70% ethanol at 4°C until processed.

2.2.3 Tissue processing for light microscopy

Processing of fixed-tissue

Fixed-tissues were transferred to a cassette (ThermoFisher Scientific) and passed through an automated processor (Leica TP1050) which dehydrated the tissues by immersing them into increasing alcohol gradients (70% ethanol for 1 h, 95% ethanol for 1 h, 2 x 100% ethanol for 1.5 h each, 100% ethanol for 2 h) and 2 x 2 h soaking in xylene. Subsequently, liquid paraffin covered the tissues 3 x for 1 h each.

Sectioning of paraffin embedded tissue

A microtome (Leica RM2135) was used to cut 5 µm sections of the paraffin embedded tissue, which were then placed on Poly-L-Lysine (PLL) coated slides to be incubated at 58°C for 24 h. The sections were then stained by Haemotoxylin and Eosin (H&E; see section 2.3) or by immunohistochemistry (see section 2.4).

2.3 Histological analysis

2.3.1 Haematoxylin and eosin staining of tissue sections

Paraffin embedded fixed tissue on PLL slides was dewaxed and rehydrated (section 2.4.1) before immersion in Mayer's Haemalum (R.A. Lamb; ThermoFisher Scientific) stain for 5 min. The slides were then washed for 5 min under running tap water, before staining in 1% Eosin solution for 2 min (R.A. Lamb; ThermoFisher Scientific) and briefly washed in water for 15 sec.

2.3.2 Quantitative histological analysis of H&E sections

Images of the stained sections were taken with a Leica MC170-HD camera, attached to an Olympus BX41 light microscope, using Leica software. Otherwise, a ZEISS slide-scanner was used for automatic imaging through ZEN software under 20 x magnification.

Scoring of crypt length

All epithelial cells from the base of the crypt until the crypt-villus junction (isthmus) were counted. The average number of crypt cells per mouse was quantified after scoring 50 half-crypts from each section.

2.4 Immunohistochemical staining (IHC)

2.4.1 Dewaxing and rehydrating tissue sections

Paraffin embedded fixed tissue sections were dewaxed twice for 10 min in xylene (ThermoFisher Scientific). Subsequently, the sections were rehydrated by immersing in a gradient of decreasing ethanol (ThermoFisher Scientific) concentration (2 x 3 min in 100%

ethanol, 1 x 3 min in 95% ethanol, 1 x 3 min in 70% ethanol). The slides were then transferred in dH_2O before the antigen retrieval process.

2.4.2 Antigen retrieval

The antigen retrieval step was used to partially revers the formalin-mediated cross-linking of the amino acids, which changes the conformation of, or masks, the epitopes. This step involved heating the slides in 10 mM sodium citrate buffer, pH 6.0, (Sigma-Aldrich) unless otherwise specified (Table 2.4). The heating procedure was either performed in a water bath or using a pressure cooker. The water bath procedure involved immersing the slides for 20 min in citrate buffer which had been gradually heated up to 99.9 ^{o}C in a Coplin jar (R.A. Lamb; ThermoFisher Scientific). For the pressure cooker method, citrate buffer, was heated up for 10 min in a pressure cooker inside a microwave at full power (1000 W). The slides were placed in the citrate buffer and further heat was applied at full power for approximately 5min, so that maximum pressure was reached inside the cooker. Subsequently, the power of the microwave was lowered to 400W to keep heating the citrate buffer at high pressure for 15 min. Slides were left to cool to room temperature (rt) for 20-30 min, before a brief wash in dH_2O and 3 x 5 min washes in either 1X PBS or 1X TBS with 0.1% (v/v) Tween-20 (Sigma-Aldrich; Table 2.4).

2.4.3 Blocking endogenous peroxidase activity

To avoid non-specific staining due to endogenous peroxidase activity, the sections were immersed in hydrogen peroxide solution (H_2O_2) (Sigma-Aldrich) inside a Coplin jar (R.A. Lamb; ThermoFisher Scientific). Table 2.5 shows the incubation times of the different H_2O_2 concentrations used, after dilution of the 30% (v/v) H_2O_2 in dH_2O or PBS, for each primary antibody used. H_2O_2 was then removed and washing buffer added to wash the slides for 3 x 5 min.

2.4.4 Blocking non-specific antibody binding

Non-specific binding of antibodies on tissue epitopes with neutral side-chain amino acids via hydrophobic interactions could lead to unwanted background (unspecific) staining. Normal serum (DAKO; Agilent) is used to minimise the non-specific binding of antibodies due to hydrophobic interactions. The serum used was from the same species as those in which the secondary antibody was developed. After the blocking step for endogenous peroxidase activity, sections were circled with a hydrophobic pen (DAKO; Agilent) before they were placed in a humidified chamber. 70 µl of normal serum diluted in washing buffer (blocking serum) was added to each section. Slides were covered with parafilm to ensure hydration of the sections and equal distribution of the buffer throughout the section. The incubation time and normal serum dilutions for each primary antibody used are indicated in Table 2.5.

2.4.5 Primary Antibody

Parafilm was removed after incubation of sections with normal serum buffer. 70 µl of primary antibody diluted in blocking serum, as indicated in Table 2.5 were added on each section and subsequently covered with a new piece of parafilm to be incubated for a period of time, as designated in Table 2.5. The slides were subsequently washed 3 x 5 min in washing buffer in a Coplin jar (R.A. Lamb; ThermoFisher Scientific).

2.4.6 Secondary Antibody

The secondary antibody was chosen to recognize antibodies made from the species in which the primary antibody was produced in. Slides were placed back in the humidified chamber and sections were covered with 70 µl of secondary antibody and subsequently covered with parafilm to be incubated as per Table 2.5. The slides were washed 3 x 5 min in washing buffer in a Coplin jar. When a signal amplification step was required a biotinylated secondary antibody (Vector laboratories) was used. Otherwise, a Horseradish peroxidase (HRP) conjugated secondary antibody (DAKO; Agilent), was added. Table 2.5 shows the details of the type of secondary antibody used and the incubation time.

2.4.7 Signal amplification

A signal amplification step was included for certain primary antibodies, listed in Table 2.5, where the HRP-conjugated secondary antibodies were not suitable. As indicated by manufacturer's instructions, the Avidin-Biotin Complex reagent (Vectastain ABC kit, Vector laboratories) was prepared 30 min before application. In a humidified chamber, 70 µl of the reagent were applied on sections and the slides were covered with parafilm. The slides were washed 3 x 5 min in washing buffer in a Coplin jar.

2.4.8 Signal visualisation using DAB

The presence of a biomarker was detected using the addition of 3,3'-diaminobenzidine (DAB) (Envision+ Kit, DAKO; Agilent). The peroxidase activity of the HRP-conjugated secondary antibody or of the HRP-Avidin-Biotin complex on the secondary antibody oxidises DAB to generate an insoluble brown precipitate. Diluted DAB (made in the ratio 1 drop of chromogen in 1 ml of DAB substrate) was added to the slides for 5-10 min. Slides were then washed for 5 min in dH_2O.

2.4.9 Counterstaining, dehydration and tissue mounting

Slides were placed in a slide-rack and submerged in Mayers Haemalum (R.A. Lamb; ThermoFisher Scientific) for 30 sec to 1 min. After counterstaining, the slides were washed in running tap water for 3 min. The slides were then dehydrated in an increasing gradient of ethanol (ThermoFisher Scientific) (1 x 3 min 70%, 1 x 3 min 95%, 2 x 3 min 100%) and finally 2 x

5 min in xylene (ThermoFisher Scientific). Two drops of DPX mounting solution (R.A. Lamb; ThermoFisher Scientific) were placed on each slide and a coverslip (ThermoFisher Scientific) was applied.

Table 2.4 Washing buffer stock solutions

Buffer	Grams of solute/ 1L dH_2O	Chemical Substance	Manufacturer
10X PBS (pH 7.4)	14.4	Sodium Phosphate Dibasic anhydride (Na_2HPO_4)	Sigma-Aldrich
	80	Sodium Chloride (NaCl)	Sigma-Aldrich
	2	Potassium Chloride (KCl)	Sigma-Aldrich
	2.4	Potassium Phosphate Monobasic (KH_2PO_4)	Sigma-Aldrich
10X TBS (pH 7.6)	8.8	Tris base $NH_2C(CH_2OH)_3$	ThermoFisher Scientific
	88	Sodium Chloride (NaCl)	Sigma-Aldrich

Table 2.5 Antibody-specific conditions for immunohistochemical staining

Primary antibody (species)	Manufacturer	Antigen retrieval	Peroxidase Block	Serum Block	Wash Buffer	Primary antibody incubation	Secondary antibody	Signal amplification
Anti-β-catenin (mouse)	BD Transduction Labs #610154	Citrate buffer, Water bath, 20 min	1.5% H2O2 in dH_2O, 20 min, RT	10% Normal Rabbit Serum (NRS) in TBS/T, 45 min, RT	3 x 5 min TBS/T	1:200 in 10% NRS, o/n, 4°C	Envision + HRP-conjugated anti-mouse (DAKO; Agilent), 30 min, RT	N/A
Anti-Cleaved Caspase-3 (rabbit)	Cell Signalling Technology #9661	Citrate buffer, Pressure cooker-microwave, 15 min	3% H2O2 in dH_2O, 10 min, RT;	5% Normal Goat Serum (NGS) in PBS/T, 1h, RT	3 x 5 min TBS/T	1:200 in 5% NGS, 2 days, 4°C	Biotinylated anti-rabbit (Vector Laboratories), 1:200 in 5% NGS, 30 min, RT	ABC Kit (Vector Laboratories)
Anti-γH2AX (mouse)	Millipore #05-636	Citrate buffer, Pressure cooker-microwave, 15 min	1.5% H2O2 in PBS, 15 min, RT	5% Normal Goat Serum (NGS) in PBS/T, 1h, RT	3 x 5 min PBS/T	1:2000 in 5% NGS, o/n, 4°C	Biotinylated anti-mouse (Vector Laboratories), 1:200 in 5% NGS, 30 min, RT	ABC Kit (Vector Laboratories)
Anti-Ki67 (rabbit)	Abcam #16667	Citrate buffer, Pressure cooker-microwave, 15 min	0.5% H2O2 in dH_2O , 20 min, RT	20% Normal Goat Serum (NGS) in TBS/T, 1h, RT	3 x 5 min TBS/T	1:50 in 20% NGS, o/n, 4°C	Biotinylated anti-rabbit (Vector Laboratories),	ABC Kit (Vector Laboratories)

							1:200 in 5% NGS, 30 min, RT	
Anti-pS1981-ATM (mouse)	Rockland #200-301-500	Citrate buffer, Solution 1.96mM citric acid and 9.35mM sodium citrate in	10% H2O2 in dH_2O, 10 min, RT;	5% Normal Goat Serum (NGS) in PBS/T, 1h, RT	3 x 5 min PBS	1:500 in 5% NGS, o/n, 4°C	Envision + HRP-conjugated anti-mouse (DAKO; Agilent), 30 min, RT	N/A

2.4.10 Quantification of histological traits by the use of cell specific stains

Stainings were quantified from the bottom of the crypt to the crypt-villus border either manually or automatically (see section 2.9). Per cohort, the average of the mean number of positive cells per mouse within a cohort was calculated.

γH2AX staining was used as a DNA damage marker and both the overall number and staining intensity (low, medium or high) of γH2AX staining were quantified. Staining intensity was considered to be indicative of the DNA damage level. Quantification of γH2AX staining in *Lgr5Cre^{ER}Apc$^{fl/fl}$* lesions was performed as in Figure 2.3. DSBs in dividing cells were identified using RAD51 staining. Cells with nuclear RAD51 foci (RAD51 positive or RAD51^{+}) were quantified. Phospho-Serine1981 (pSer^{1981}) ATM nuclear staining was indicative of DSB formation.

Cleaved Caspase-3 staining was used to mark apoptotic cells and localization of beta-catenin staining was used to mark Wnt signalling activity. Nuclear β-catenin staining was considered to indicate canonical Wnt signalling pathway activation. Ki67 staining was used as a marker of proliferation.

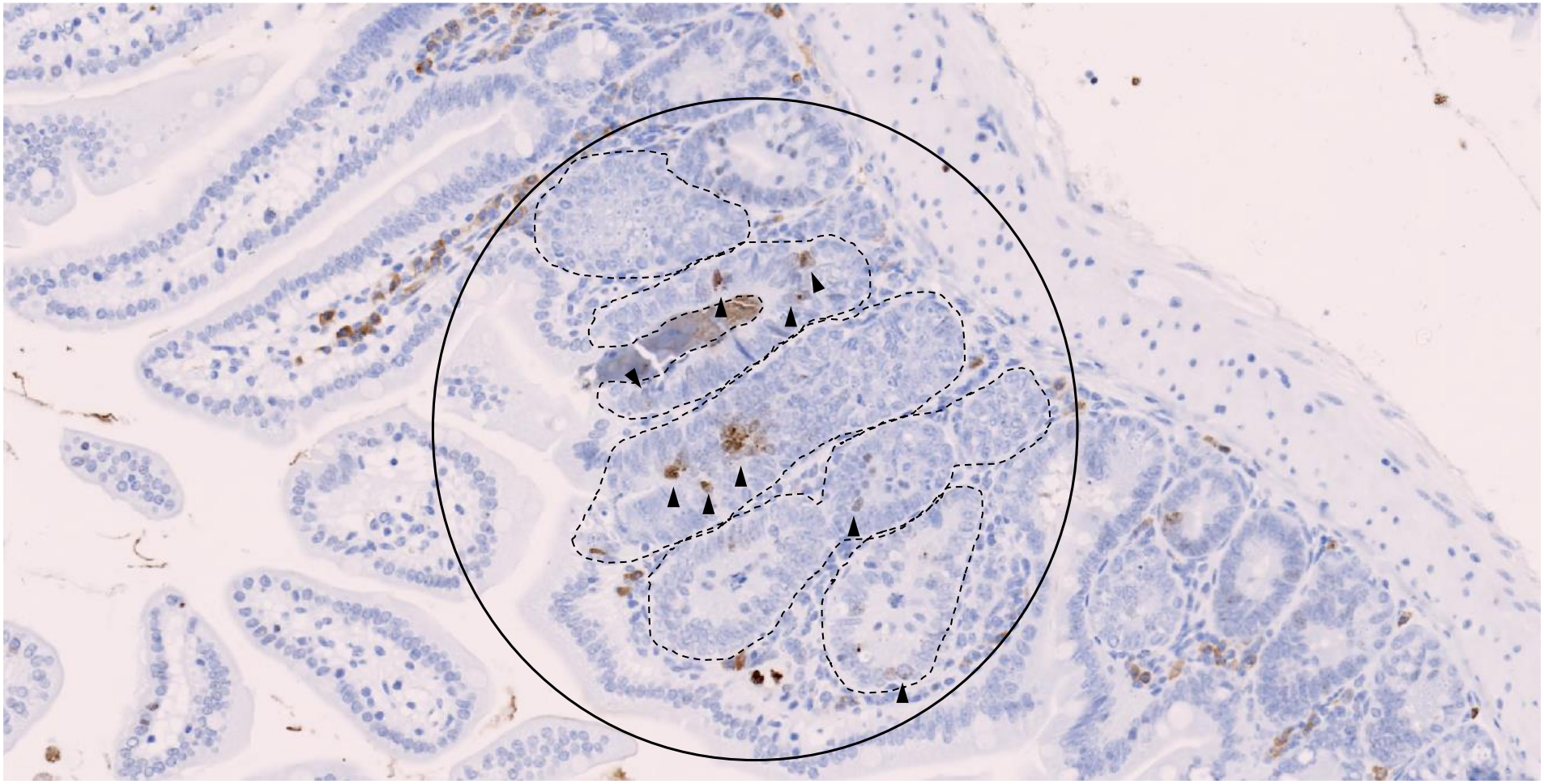

Figure 2.3 Example of γH2AX quantification in the Lgr5Cre^{ER}Apc$^{fl/fl}$ lesions.

IHC staining for γH2AX on paraffin sections of 24h 10% formalin fixed intestinal rolls of 50 days p.i. *Lgr5Cre^{ER}Apc$^{fl/fl}$*. Irregular shapes within the lesion (encircled) shows neoplastic epithelial cells. Arrows indicate γH2AX positive cells.

2.5 Radioimmunoconjugate (RIC) treatment

DNA double strand breaks (DSB) were targeted *in vivo* by ^{111}In-DTPA-anti-γH2AX-TATprobes. All procedures involving radioactive material were performed in designated areas controlled for radioisotope usage and storage and were conducted by our collaborator Dr. James Knight in the group of Dr. Bart Cornelissen at Oxford University.

2.5.1 Synthesis of RIC

^{111}In-DTPA-anti-γH2AX-TAT and ^{111}In-DTPA-anti-IgG-TAT probes were synthesised as described by Cornelissen *et al.* (2011). The γH2AX antibody purchased from Merck cross-reacts with mouse γH2AX and is specific to a synthetic phospho-peptide which includes the Human H2AX Ser^{139} phosphorylation site. γH2AX antibody (Merck Millipore), or mouse serum IgG (Sigma-Aldrich) were dissolved in 0.1M 2-(N-morpholino) ethanesulfonic acid. TAT-peptide (GRKKRRQRRRPPQGYG) was incorporated by N-(3-dimethylaminopropyl)-N'-ethylcabodiimide/ N-hydroxysuccinimide (EDC/NHS; Pierce Biotechnology) activation. Incubation of 5-fold molar excess of TAT for 2 h at rt allowed TAT incorporation. Sephadex G50 gel filtration columns (SEC; Sigma-Aldrich) were used to remove unconjugated TAT resulting in 5:1 ratio of Tat:IgG. Incubation of anti-γH2AX-TAT with isocyanatobenzyl-DTPA (p-SCN-Bn-DTPA) (Macrocyclics), an activated metal ion chelator, formed DTPA-anti-γH2AX-TAT. Unconjugated p-SCN-Bn-DTPA was removed by G50 gel SEC. An appropriate volume of ^{111}In chloride ($^{111}InCl_3$) was added to Bn-DTPA-anti-γH2AX-TAT for 1 h at rt to form ^{111}In-DTPA-anti-γH2AX-TAT of 1MBq/µg specific activity (e.g 20 MBq of $^{111}InCl_3$ in 20 µg of antibody).

2.5.2 Assessing RIC purity

RIC purity was assessed by instant thin layer chromatography (iTLC). On one side of each iTLC strip (Agilent) a 12 mm spot was drawn by pencil. As control, 1MBq of $^{111}InCl_3$ was dissolved in 0.1M citrate buffer (pH 5.5). 2 µl of reaction mixture or control were placed on each iTLC strip spot and allowed to dry. iTLC strips were placed in 50ml Falcon tubes (Corning) with 750 µl of 0.1M citrate buffer (pH 5.5) so that citrate buffer was absorbed up to 1-2cm from the top. Strips were removed, allowed to dry and then wrapped with cling film to prevent contamination. Strips were placed in an autoradiography cassette and image plane (IP) film (Kodak), which had been previously placed in a light box for 5 min, was placed on top. Film was exposed to iTLC strips for 2 min. IP film was placed on the Cyclone phosphor imager, which is covered with photostimulable phosphor crystals (BaFBr:Eu^{2+}) of a europium (Eu) -activated barium fluorohalide compound, to determine radiochemical purity (Van Kirk *et al.* 2001). The radioactivity from a sample are able to eject Eu^{2+} electrons converting them into Eu^{3+} which become traped in bromine crystal vacancies. Light exposure of the crystals reverts the

excitation event allowing Eu^{3+} to return to its ground state by releasing light. Intensity of the light emission is detected quantitatively and spatially. The signal is digitally converted into a histogram of light units and migrating distance. The amount of detected signal (hence radioactivity) is proportional to the radiolabelled sample and different sample components have differential distribution when carried by liquid citrate buffer. Thus, different peaks indicate different radioactive conjugates or free radioisotopes. Therefore, if RIC purity was lower than 95% then the reaction mixture was run through G50 gel SEC to achieve >95% radiochemical purity. RIC was eluted with an appropriate volume of 1X PBS (Gibco) so that each mouse could receive 5MBq in ~100 µl (maximum 200 µl allowed injected volume).

2.5.3 Administration of RIC

All experimental procedures were carried out on mice of at least 6 weeks of age. Mice were restrained (Harvard apparatus) and their tails placed in warm (30-35 ºC) water for 2 min to dilate the tail veins for easier solution administration. RIC administration was conducted *via* intravenous tail injection using 1 ml syringe (BD Plastipak) and 25G needle (BD Microlance 3).

2.5.4 SPECT-CT (Single Photon Emission Computed Tomography - Computed Tomography) *in vivo* imaging.

24 h post RIC administration, mice were anaesthetised with 5% isoflurane (Piramal) through an anaesthetic machine (Harvard apparatus). Mice were then transferred into the scanner. To maintain the unconscious state of the animals, 2.5 – 3.5% isoflurane was provided to each mouse while a heat pad maintained their body temperature at 37°C. *In vivo* imaging of RIC localization in the *VilCre^{ER} Apc$^{fl/fl}$* mice was carried out by nanoScan SPECT-CT preclinical scanner (Mediso). Nucline (Mediso) software was used for the acquisition of the images. Due to scheduled replacement of the imaging instrument, *Lgr5Cre^{ER} Apc$^{fl/fl}$* mice were imaged via VECTor-CT SPECT/PET-CT preclinical scanner (MILabs) and pmod (PMOD Technologies LLC) software was used for the imaging processing.

2.5.5 *Ex vivo* Biodistribution studies

Detailed quantification of the radioactivity in each organ was assessed by a biodistribution assay. Mice were euthanised, using a schedule 1 protocol, immediately after SPECT-CT imaging. Each tissue (large intestine including caecum, 15 cm of proximal small intestine, distal small intestine, blood, heart, lung, liver, spleen, stomach, pancreas, kidney, muscle, skin and fat) was rinsed twice in H_2O and placed on a tissue to drain excess H_2O. Each tissue was weighed and placed in round bottom tubes (Corning) that were read by a γ-counter (Perkin Elmer). γ-counter data was analysed by Prism-5 (GraphPad) using 1-way ANOVA analysis.

2.6 Intestinal stem cell *ex vivo* enrichment

2.6.1 Intestinal crypt isolation

Small intestine was harvested as described in section 2.2.1 (Figure 2.4a) but with some protocol alterations. Using a syringe (BD Plastipak) filled with ice-cold HBSS (Gibco) including 1:50 Penicillin and Streptomycin (Pen-Strep) (10 000 U/ ml) (Gibco), the contents of the intestine were flashed out. Subsequently, a longitudinal incision along the length of the intestine was made to expose the epithelial side of the intestine (Figure 2.4b). Only 15-20 cm of the proximal intestine including the duodenum and jejunum were further processed. Villi and mucus were scraped off gently using a coverslip (Fisher Brand; Figure 2.4c). The scraped intestine was cut into 5 mm pieces (Figure 2.4d) which were collected in 25 ml of Pen-Strep enriched HBSS (Gibco) and kept on ice for up to 45min.

Processing the proximal intestinal pieces

Samples were processed 20 - 45 min after collection under sterile conditions in a Class II Biological Safety cabinet (Thermo Scientific). Tube were gently inverted three times before HBSS was removed using a 25 ml Strippet (Costar). Tissue pieces were washed three more times using 15 ml Pen-Strep enriched ice cold HBSS (Gibco) or until HBSS was relatively clear. After removal of most of the HBSS the tissue was incubated for 5 min at room temperature (rt) in 10 ml of 8mM EDTA (Sigma) in HBSS (Gibco) kept at rt. Vigorous shaking of the tube for 1 min released any residual epithelial cells from villi that have not been removed by scraping and they were discarded. Then intestinal pieces were incubated in 10 ml of fresh 8mM EDTA (Sigma) in ice-cold HBSS (Gibco) for 30 min. Vigorous shaking for 1 min allowed detachment of the crypts and the suspension was collected in a separate 50 ml falcon tube. An equal volume of DMEM/F12 (Gibco) with 1X Glutamax (Gibco) was added to the crypt suspension and kept on ice. 10 ml of HBSS were added to the tissue and vigorously shaken for 1 min to be pooled with the already collected suspension. The last step was repeated and the collected cryptsuspension was centrifuged at 650 - 700 rpm for 5 min. The supernatant was discarded as it contained mostly epithelial cells of the villi. Crypts were resuspended in 10 ml of DMEM/F12 (Gibco) and passed through a 70 µm cell strainer (Falcon).

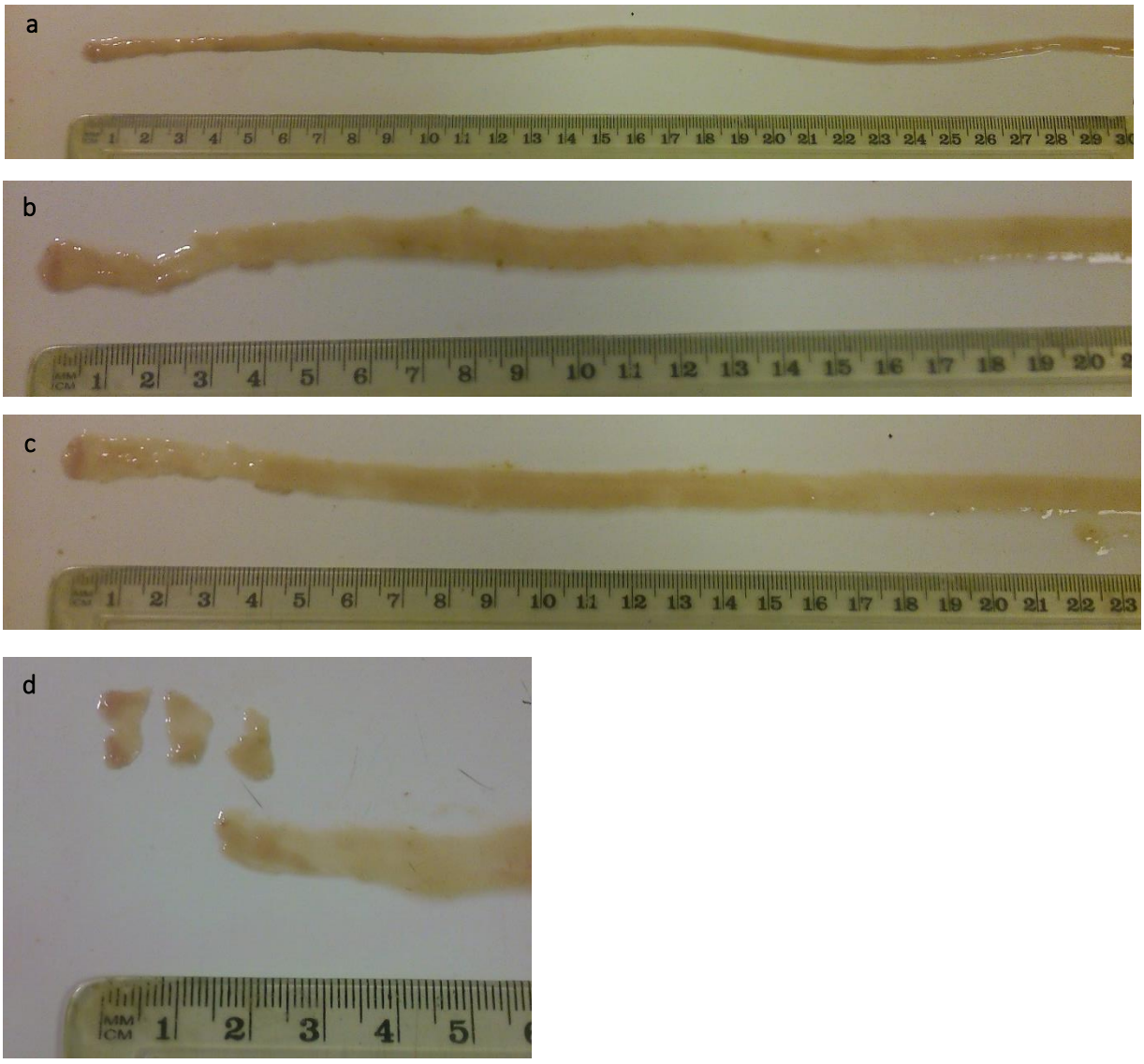

Figure 2.4 The Isolation and process of the small intestine.

a) The intestinal tube was flushed and b) cut longitudinally to expose the epithelium. c) Using a coverslip, the villi were scraped off. d) The intestine was then cut in 5mm pieces in order to be processed for crypt isolation.

Quantifying the crypt number

Three lines of 10 µl crypt suspension were laid on a petri dish (Corning) to quantify the crypt number under bright field microscope (Olympus BX41) as indicated by Figure 2.5. The average of the crypt number from each 10 µl sample was calculated as well as the total crypt number.

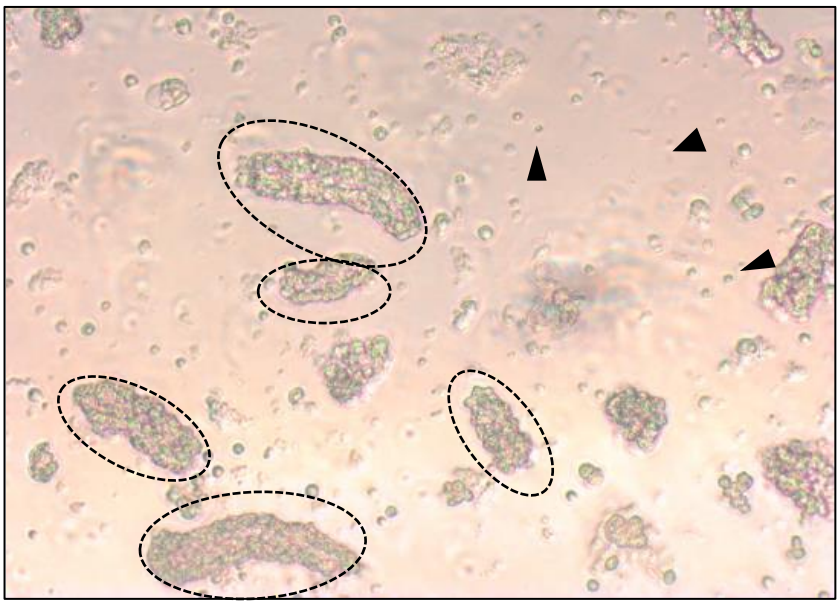

Figure 2.5 Crypt quantification.

Bright field image of 10x magnification. Crypts are encircled in dashed line. Arrows show the presence of lymphocytes in the preparation.

Seeding crypts

Crypts were seeded in an extracellular protein matrix (Matrigel) to support their three-dimensional (3D) structure. 200 - 500 crypts were seeded in 50 µl of ice-cold Matrigel in the middle of a well in a 24-well plate (Corning), pre-warmed at 37°C for minimum 10 min. To allow polymerization of Matrigel, the crypt-seeded plate was incubated at 37°C, 5% CO_2 for 20 - 30 min. 500 µl of media (see Table 2.6; detailed medium of each organoid line) was added in the well and incubated at 37°C, 5% CO_2. Media was changed every three days.

Expansion of organoid number

Seven days post intestinal crypt culture or dissociated organoid culture (as described in this section), organoids were mechanically or enzymatically dissociated to expand their numbers.

Mechanical organoid dissociation

The Matrigel embedded organoids were dislodged from the bottom of the well using a 1000P pipette tip, resuspended in the media from the well and transferred to a 15 ml falcon tube (BD

Plastipak). Organoids were resuspended by pipetting up and down 100 times using a 1000P pipette tip and 100 times more using a 200P pipette tip. Organoids were then centrifuged at 900 rpm at rt for 4 min. Media phase was discarded and 1 ml of HBSS (Gibco) was added to further dissociate the organoids by resuspending using the same pipetting protocol or until suspension became homogeneous. The suspension was centrifuged at 1100rpm at rt for 4 min to discard the media phase. Depending on how dense the culture was before passage, triturated organoids were seeded in up to 1:5 dilution in Matrigel.

Enzymatic organoid dissociation into single cells.

The media was removed and the well (of a 24-well plate) was washed with 200 µl 1X PBS (Gibco). PBS was removed and 300 µl of TrypLE Express (Gibco) was added. A 1000P pipette tip was used to detach and disperse the Matrigel and the plate was returned back to the incubator. 6 min later, the dissociated Matrigel was further resuspended using a 1000P pipette until it became homogeneous. An equal volume of FBS (Gibco) was added to exhaust TrypLE's action. The suspension was collected in a 15 ml falcon tube (BD Plastipak) and topped up to 5 ml with HBSS (Gibco). Equal volumes (100 µl) of cell suspension and Trypan blue (Gibco) were mixed and 10 µl of the mixture loaded at each side of a haemocytometer (Weber Scientific) to quantify live cell number. An appropriate volume of cell suspension was centrifuged at 1600 rpm for 5 min and, after supernatant removal, 4000 cells per 10 µl Matrigel were seeded in each well of a 96-well plate with glass bottom (Cellvis), pre-warmed at 37^{o}C for at least 10 min. The plate was returned to the incubator (37^{o}C, 5% CO_2) for 20 - 30 min before 100 µl of media per well (see Table 2.6) was added. Cell cultures were incubated at 37^{o}C with 5% CO_2 and media was changed every three days.

2.7 Imaging organoids by whole mount Immunofluorescence

Organoids grown in Matrigel (section2.6) in a glass bottom 96-well plate (Cellvis) were fixed and stained in their wells. Images of organoids at different plane (z) levels were captured under 20 x magnification by confocal imaging (Zeiss LSM-710) and ZEN software. All reagents used, (see Table 2.7) were at rt and incubations were carried out at 37^{o}C.

2.7.1 Organoid fixation and immunostaining

The organoid media was removed and wells were washed with 100 µl of 4% PFA (Sigma) in 1X PBS (Gibco). Organoids were incubated for 30 min in 100 µl of fresh 4% PFA, washed 3 x with 100 µl of 100 mM Glycine (Sigma), the last wash being 10 min before it was replaced by blocking buffer for an o/n incubation. The next day, wells were rinsed 2 x with 100 µl of washing buffer followed by an o/n wash. Organoids were then incubated o/n with 100 µl of mouse anti-γH2AX antibody (1:900 dilution; Millipore). Primary and secondary antibodies were diluted in

the washing buffer. After washing the wells as previously, organoids were incubated o/n with 100 µl of AF488 conjugated anti-mouse secondary antibody (1:200 dilution; Invitrogen). Wells were rinsed as previously and DNA was stained by a 30 - 60 min incubation with 100 µl of 20µg/ml DAPI (Sigma) in the washing buffer. Wells were washed 2 x before imaging.

Table 2.6 Crypt culture medium

Crypt culture medium		
Constituents:	**Company**	**Final dilution/concentration**
Advanced DMEME/F12	Gibco	1X
Glutamax	Gibco	1:100
1M Hepes buffer Solution	Gibco	10mM
Pen/Strep	Gibco	1:100
Gentamycin	Sigma	1:500
N2 supplement	Invitrogen	1:100
B27 supplement, retinoic acid free	Invitrogen	1:50
Fungizone	Invitrogen	1:500
Human recombinant noggin	Peprotech	100ng/ml
Human recombinant EGF	Sigma	50ng/ml
Human recombinant R-spondin 1	R & D systems	665ng/ml

Table 2.7 Whole mount IF reagents

Components	Company
100mM Glycine in 1xPBS	Sigma
IF buffer in 1xPBS:	
0.1% w/v BSA	Invitrogen
0.2% v/v TritonX-100	Sigma-Aldrich
0.05% v/v Tween 20	Sigma-Aldrich
IF blocking in 1xPBS:	
1% w/v BSA	Invitrogen
3% Normal Goat serum	DAKO
0.2% v/v TritonX-100	Sigma-Aldrich
0.05% v/v Tween 20	Sigma-Aldrich

2.8 Cytometric analysis of extracted intestinal epithelial cells

2.8.1 Single cell extraction from intestinal crypts

Intestinal Crypt Isolation was performed as in section 2.6.1, without the inclusion of antibiotics, and all reagents and equipment were kept at 4°C, unless otherwise stated. Up to 30cm of intestine was processed per mouse. Intestinal crypts were isolated as per section 2.6.1. After discarding the supernatant, containing mostly single epithelial cells from the villi, the crypt pellet was further enzymatically dissociated into single cells using 3ml of TrypLE (Thermofisher Scientific) per 20cm harvested intestine supplemented with 0.01mM of ROCK inhibitor (Y-27632; Sigma-Aldrich) to avoid death of the anchorage-dependent cells after their detachment from the surrounding extracellular matrix (anoikis). Enzymatic digestion was performed at 37°C for 10min with 15 sec of vigorous shaking every 2min. An equal volume of FBS was added to stop the enzymatic digestion. The suspension was topped up to 10 ml with HBSS and passed through a 40 µm cell strainer (Falcon). Cell number was determined by haemocytometer as per section 2.6.1 (Figure 2.6). 0.2 - 0.4 x 10^6cells / sample were spun down in eppendorf tubes at 1500 rpm for 5 min. The cell pellet was washed with PBS and re-centrifuged as before.

2.8.2 Sequential extracellular and intracellular cell staining

The staining procedure was performed in the dark to avoid photobleaching and the cells were kept on ice until FACS analysis. The cell pellet was vortexed in 100 µl of staining buffer (to stain extracellular epitopes) and incubated for 25min. 1ml of FACS buffer was added, the sample was centrifuged at 500 rcf for 5 min and the supernatant was removed. The cell pellet was then vortexed in 200 µl of fixation buffer and incubated for 12 min. After centrifugation at 500 rcf for 5 min the supernatant was removed and the pellet was vortexed in 200 µl of permeabilization buffer and incubated for 15 min (to make intracellular epitopes accessible). After 10 min centrifugation at 300 rcf, the cell pellet was vortexed in 1 ml of washing buffer and centrifuged again at 500 rcf for 5 min. The pellet was then vortexed with 100 µl of staining buffer and incubated in the dark for 30 min after which it was vortexed with 1ml of FACS buffer and again centrifuged at 500 rcf for 5min. The last step was repeated once before the cell pellet was vortexed with 200 µl of washing buffer. Reagents used are listed in Table 2.8.

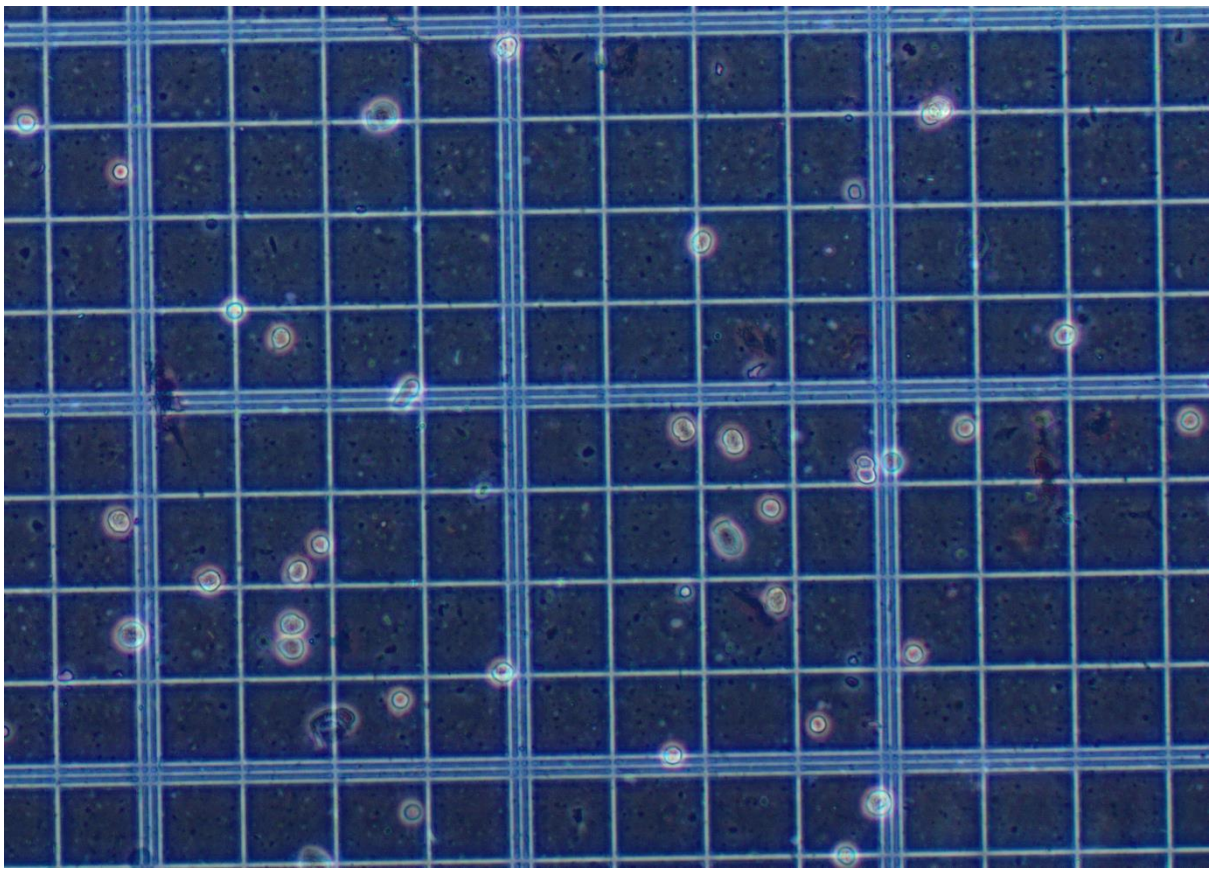

Figure 2.6 Crypt enzymatic digestion into single cells.

Enzymatically digested crypt cells were stained with Trypan blue and the percentage of viability was determined using a haemocytometer. After the enzymatic digestion, most crypt cells are in singlets or doublets.

Table 2.8 Constituents of FACS staining

Extracellular Staining	
Reagent	**Constituents**
FACS buffer	2% FBS (Gibco) in PBS (Gibco)
Staining buffer	Conjugated Antibody (Biolegend) in FACS buffer
Intracellular Staining	
Reagent	**Constituents**
Fixation buffer	4% PFA (Sigma) in PBS (Gibco) or 1% PFA in PBS (Thermo Scientific)
Permeabilization buffer	0.1% Triton (Sigma-Aldrich) with 2% BSA (Sigma) in PBS (Gibco)
Washing buffer	0.1% Triton (Sigma-Aldrich) in PBS (Gibco)
Staining buffer	Conjugated Antibody (Biolegend) in permeabilization buffer
FACS buffer	2% BSA (Sigma) in PBS (Gibco)

2.8.3 FACS analysis

Cells were passed through a 40µm strainer (Falcon) into 5ml Falcon tubes (BD Falcon) and kept on ice until FACS analysis on the BD LSRFortessa Cell Analyzer. The isotype and antigen-specific stained samples were analysed to set the voltages and determine the cut-off for positive staining. Debris was excluded from gates on the forward scatter area (FSC-A) / side scatter area (SSC-A), and the live cells were further gated to exclude doublets by using FSC-Height (FSC-H) / FSC-A (Figure 2.7). Unstained samples, isotype controls, or 'fluorescence minus one' (FMO) were used to gates for positive staining (Figure 2.8).

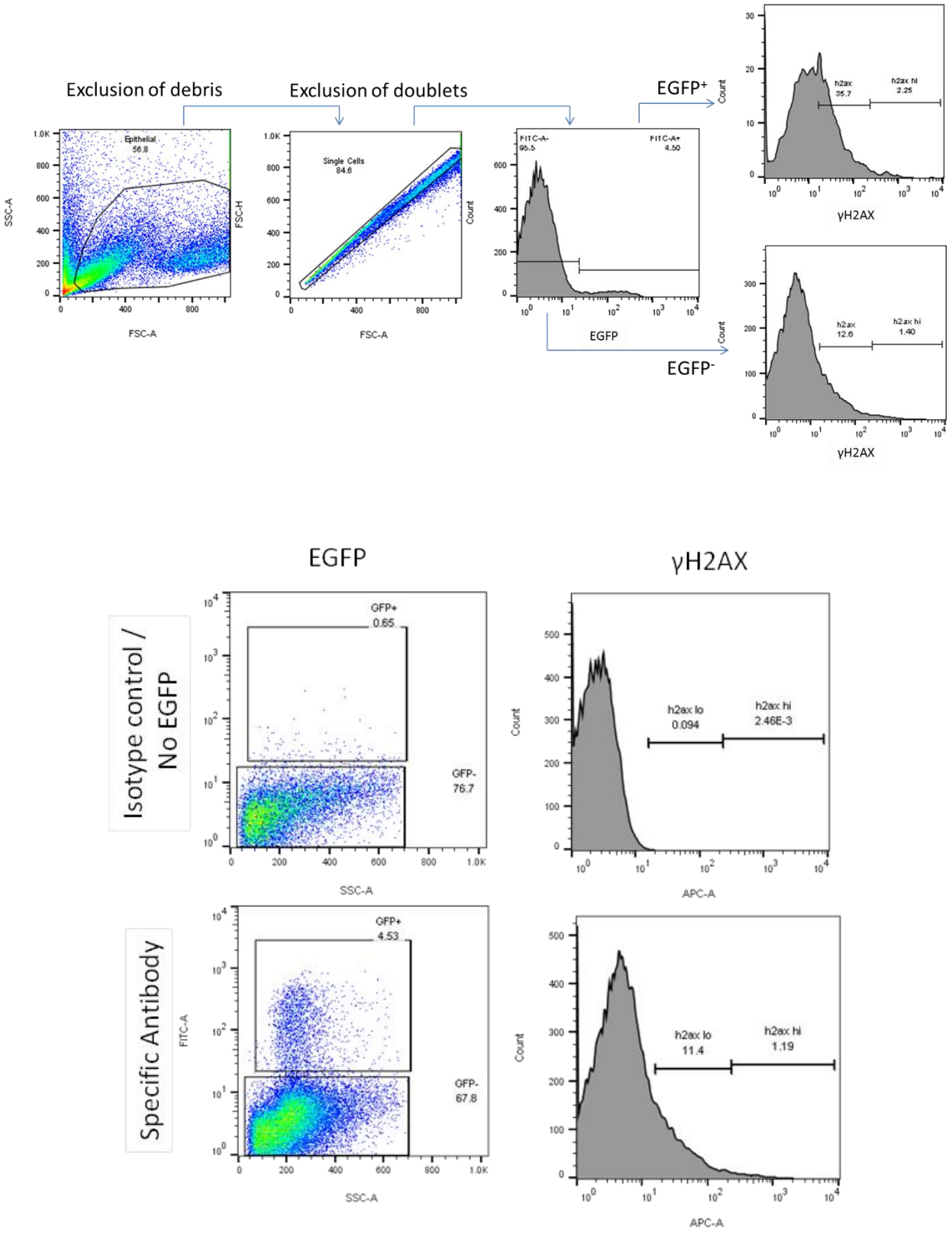

Figure 2.8 Gating strategy for antigen-specific stained cells.

Schematic representation of the gating strategy used. (b) Background fluorescence of cells stained with a fluorochrome-conjugated isotype control antibody instead of the specific antibody, was used to guide the selection of positive cell populations. Samples without EGFP signal i.e. cells not derived from LGR5-EGFP knockin mice were used to gate the EGFP positive cells.

2.9 Development of scripts for automatic quantification of immunohistochemical (IHC) stainings.

ImageJ Macro Language (IJM) was used to create programmes that would automatically score IHC images in order to avoid the subjective scoring that accompanies manual quantification and to increase the speed of image analysis.

The aim was to quantify only the brown nuclei within the intestinal crypts excluding the lamina propria and the vili. The brown (DAB) staining was first separated from the blue (haematoxylin staining) and then the total number of nuclei (blue) were identified and tabulated after segmentation of the edges of nuclei that touched other nuclei. The number of brown areas that colocalized with blue staining (i.e. DAB positive nuclei) was then identified and tabulated. Hence, the number or percentage of positive cells within the crypt were calculated.

The following section describes the series of steps undertaken to automatically quantify the DAB positive nuclei within the crypt.

2.9.1 Macro used for scoring on IHC images.

Selection of field of view and image extension.

IHC images were acquired by Zeiss Slide Scanner at 20x magnification using the brightfield option. The images were then processed using the ZEN software by zooming 100% into the scanned tissue section, selecting the field of view showing a whole crypt and then creating image from view. Images were saved as TIFF (.tif) in order to preserve most of their features.

Manual elimination of unwanted tissue structures.

The images were opened with Fiji. Manually, the crypts were selected by drawing around each of them. Everything else apart from the crypt was cleared. Then the black background was pool-filled with white which is translated into “intensity signal = 0”. The image (Figure 2.9) was saved with the extension “_clear.tif”.

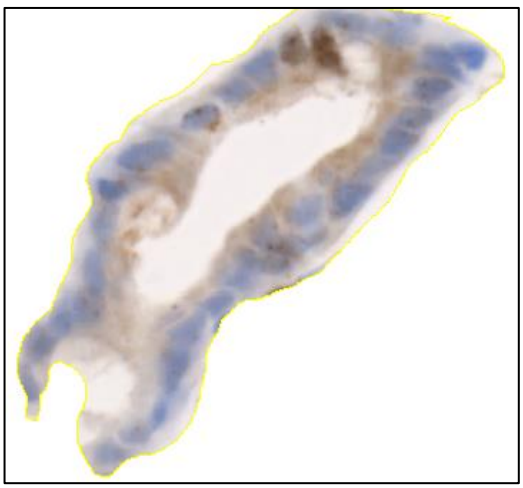

Figure 2.9 Selection of crypts from a field of view.

Separating the haematoxylin staining from the DAB staining.

The "_clear.tif" image was opened in Fiji and using colour deconvoloution with H&E DAB as an option, the Red, Green and Blue (RGB) colours were separated into three different images as in Figure 2.10.

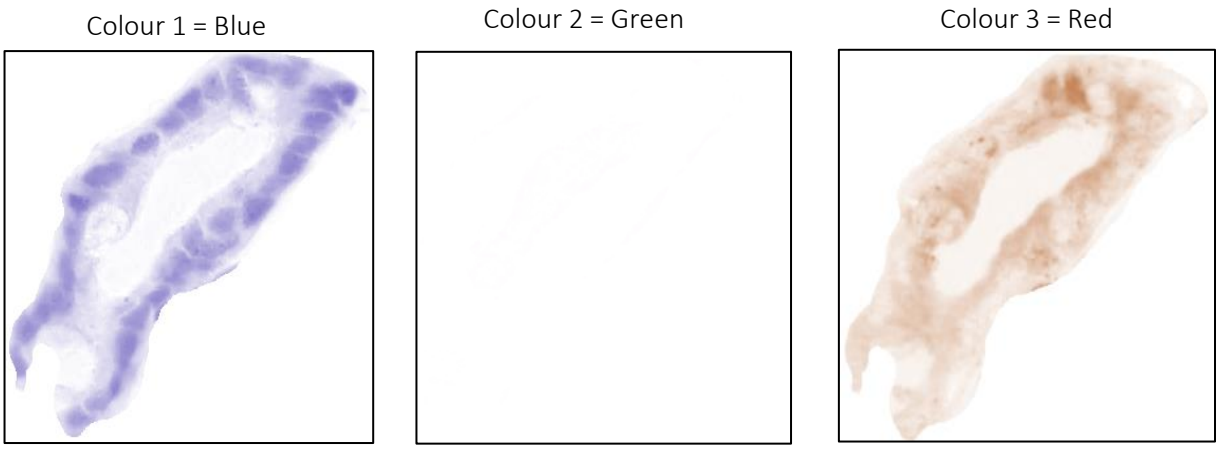

Figure 2.10 Colour deconvolution using Fiji's H&E DAB option.

Creating a mask for identification of the nuclei.

To identify the nuclei the background signal was decreased by increasing the brightness and contrast (B&C) of the Colour 1 image within the range of 0-185 (Figure 2.11).

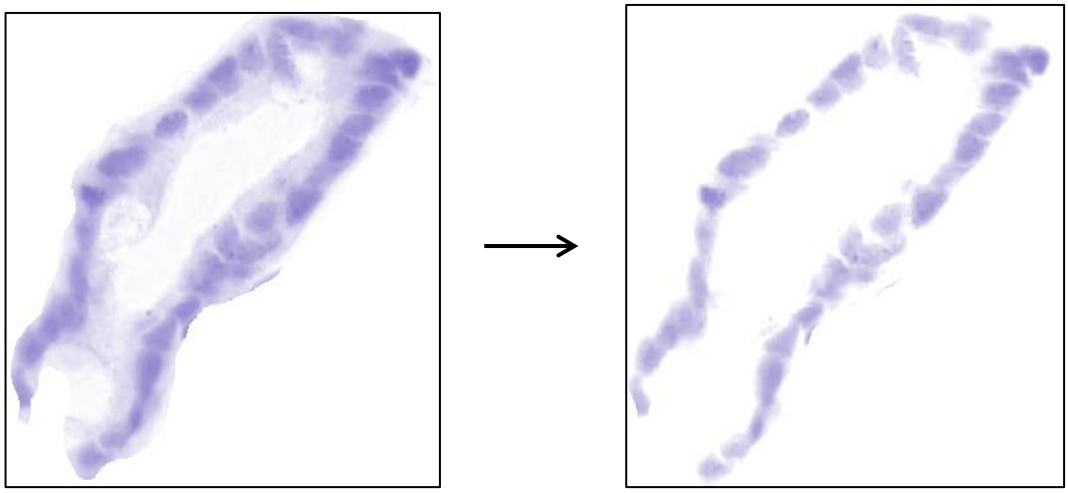

Figure 2.11 Increased B&C to decrease background signal.

The resulting image was blurred using the smooth option to avoid the discontinuity and segmentation of main structures (Figure 2.12).

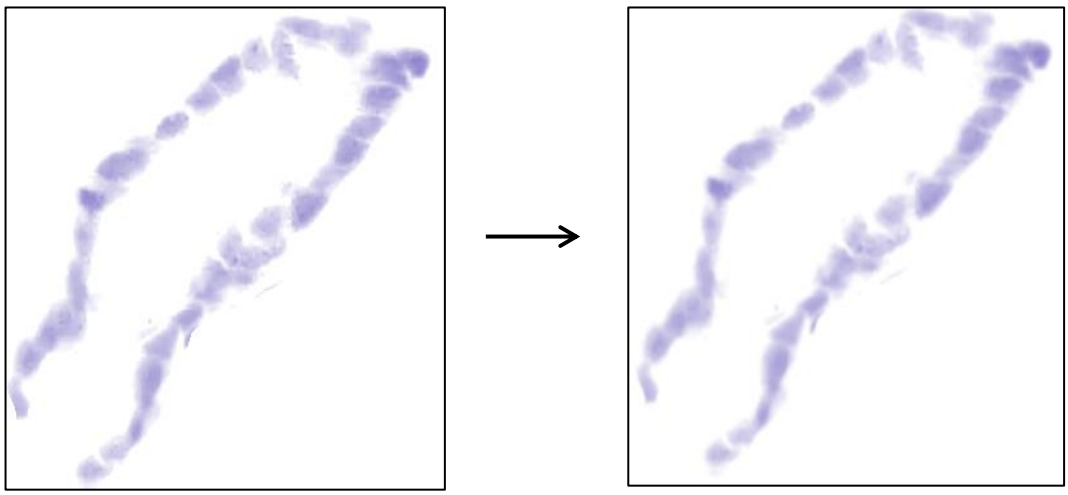

Figure 2.12 Image blurring.

Otsu's clustering-based thresholding iterates through all the possible threshold intensity signal values in order to identify the optimum threshold that separates the foreground from the background pixels into black (255) and white (0), respectively (Otsu 1979). This threshold was applied using the intensity range (0-212) in order to convert the greyscale image into binary (0 and 255) (Figure 2.13).

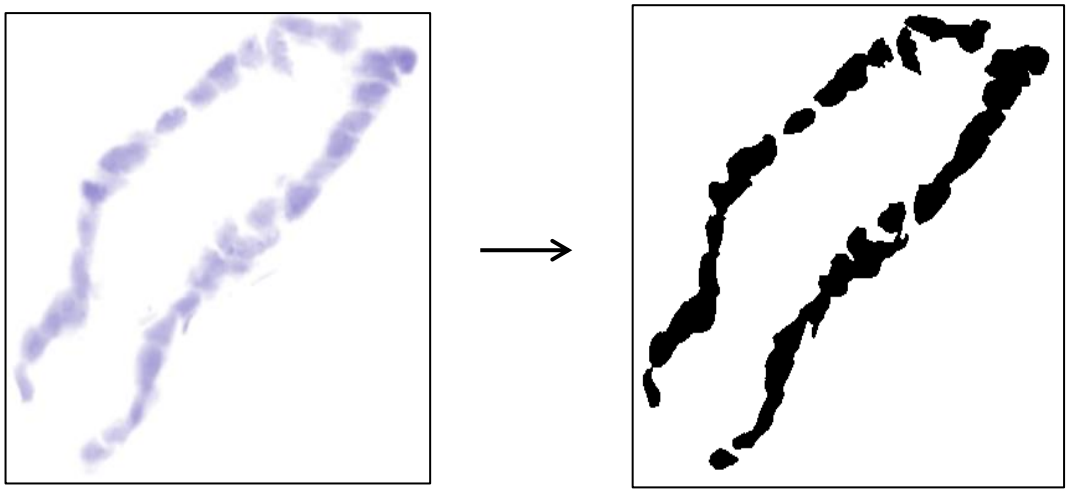

Figure 2.13 Otsu thresholding to convert the greylevel into binary image.

In order to distinguish better the boundaries of each object, the erode option was applied therefore the pixel size of the objects in the foreground shrinks (Figure 2.14).

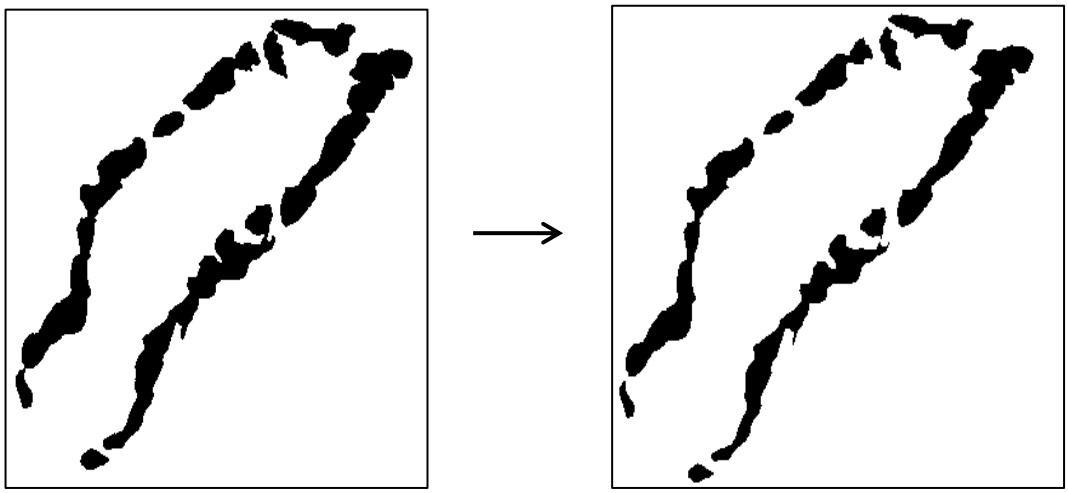

Figure 2.14 Erosion applied for more distinguishable object boundaries.

Next step was to remove the noise from the objects' boundaries. Therefore, the median filtering was used by which the centre pixel value of a square window with a radius of 2 pixels was replaced by the median value of its surrounding pixels (Figure 2.15).

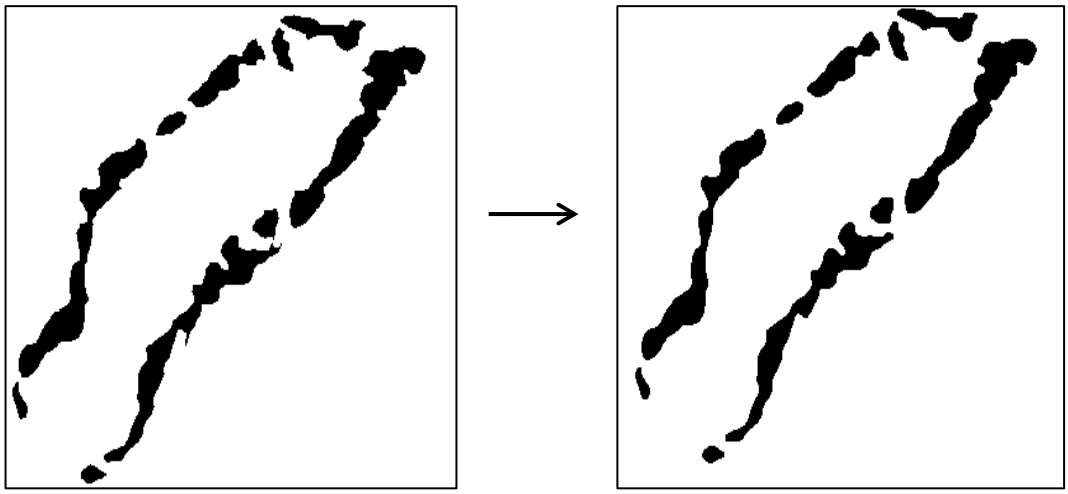

Figure 2.15 Median filtering to remove the noise from the foreground boundaries.

Smaller objects on the foreground were converted to background using the "open" option (Figure 2.16).

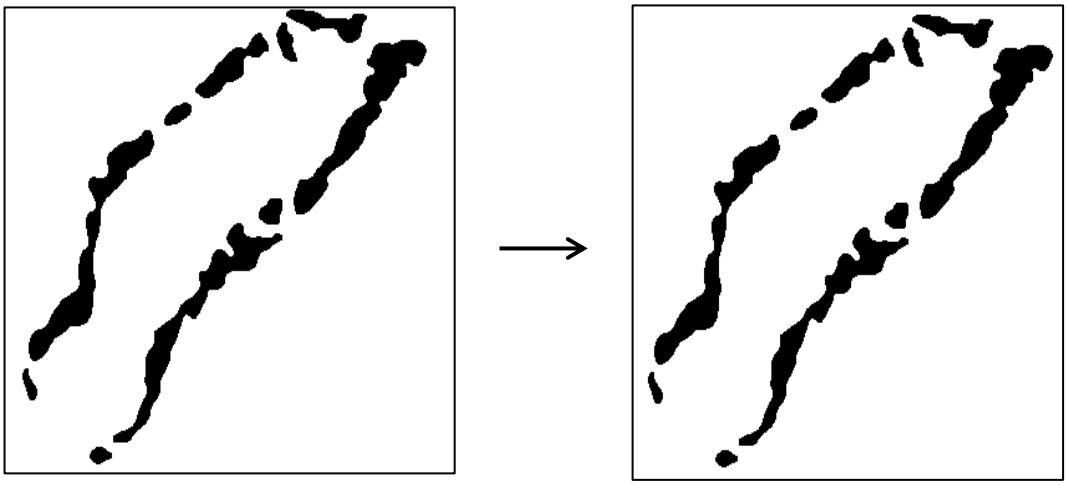

Figure 2.16 Morphological noise removal

Image dilation was then applied to expand the size of an object and smooth the object boundaries and to close holes and gaps (Figure 2.17). This was performed using the MorphoLib plugin.

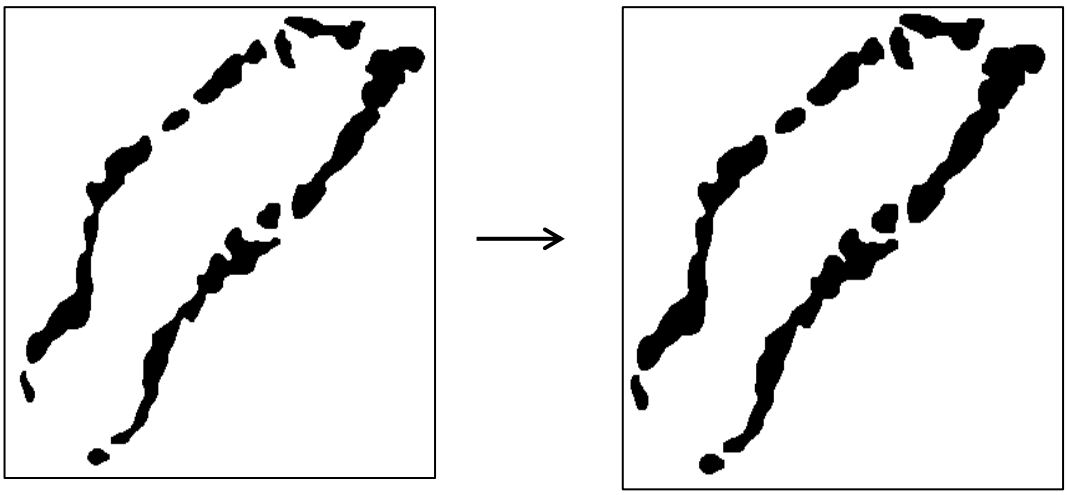

Figure 2.17 Image dilation

To separate objects touching each other the Watershed method was applied that creates a distance map from the centre of an element to its edges (Figure 2.18). Filling that "topological

map" with imaginary water results in "Watersheds". Where they meet, a “dam” is drawn to separate the elements.

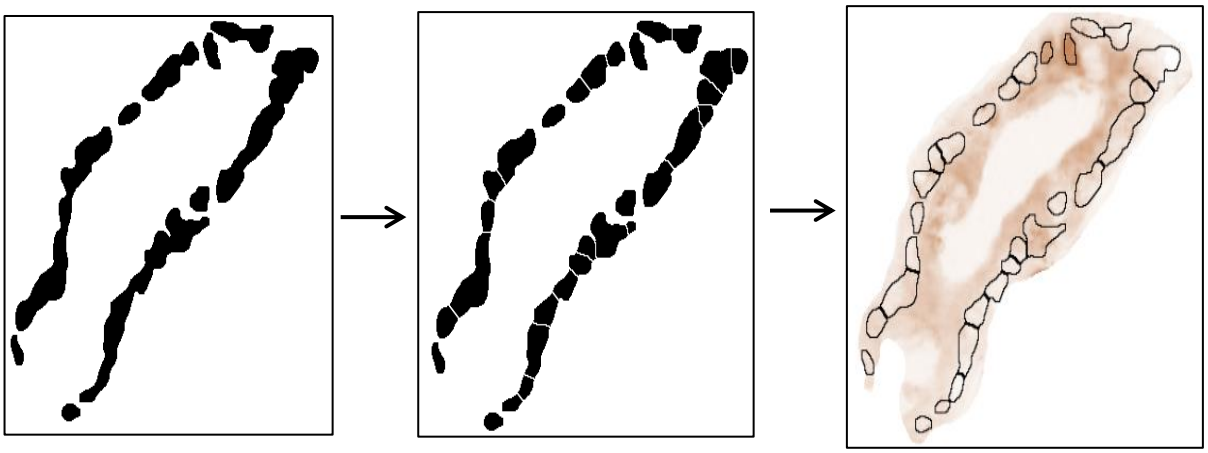

Figure 2.18 Separating the elements using watershed.

Identifying the DAB stained cells.

The image indicated as Colour 3 which corresponded to the red colour and therefore DAB stain was used in order to identify the positively stained areas. Therefore, Otsu thresholding was applied (Figure 2.19).

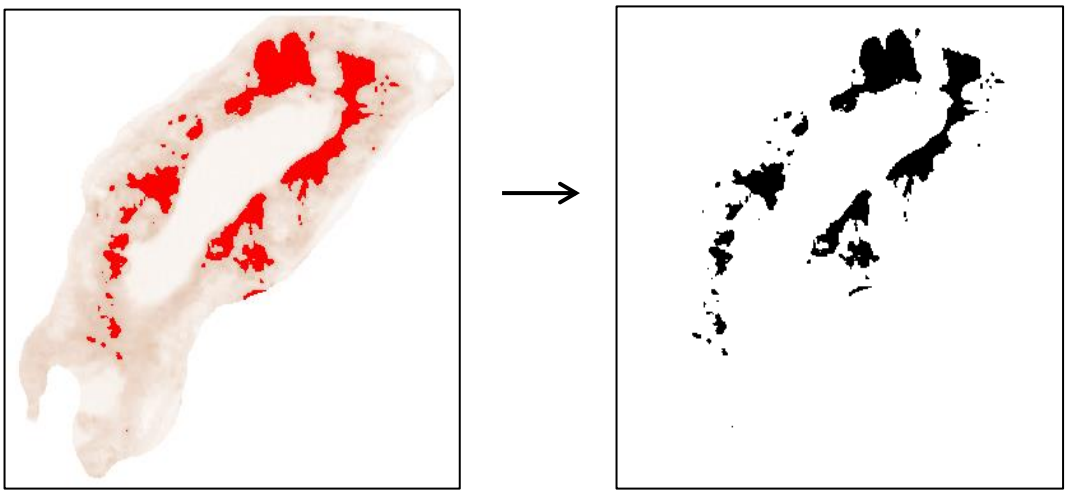

Figure 2.19 Identification of γH2AX stained areas including background signal.

Overlapping the nuclei mask on the thresholded Colour 3 image enabled the identification of the positive cells, and allowed non-specific staining to be excluded (Figure 2.20).

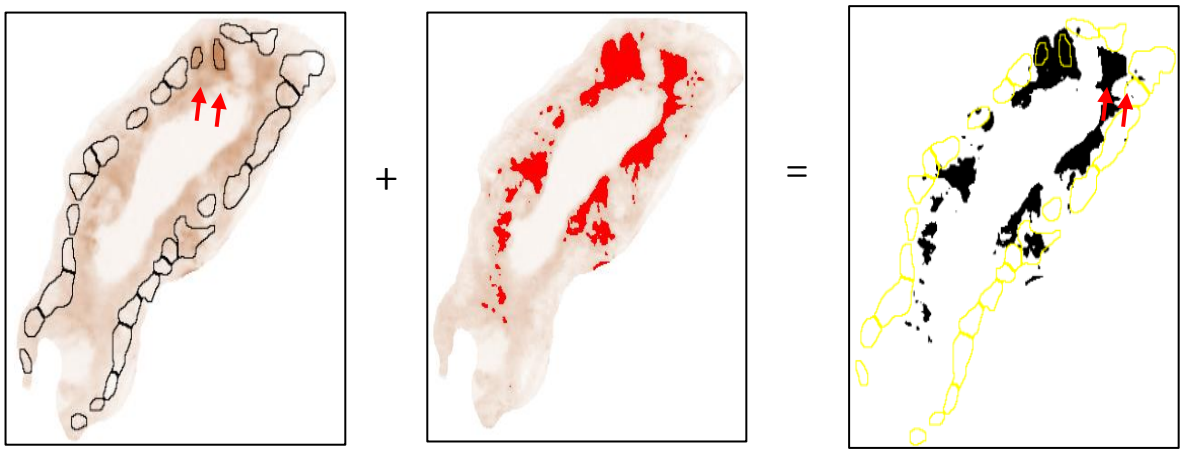

Figure 2.20 Identifying the cells that are positive for γH2AX.

Application of the nuclei mask over the Colour 3 image allows identification of positive nuclei shown with red arrow.

Using this overall approach for each input image, ROIs were generated for the selected positive cells, (in this case each ROI = a nucleus) and their staining intensity was measured and tabulated in an excel spreadsheet. The described steps were automatically performed using a Macro script that I have written (see Appendix). Subsequently, the tabulated data were manually assessed and represented using GraphPad.

2.9.1 Comparing manual versus automatic staining quantification

IHC analysis was conducted either manually or automatically using an in-house written macro script, created accordingly for the identification of each surrogate marker. The accuracy of the macro script staining quantification was compared to manual counting for each surrogate marker. Depicted in Figure 2.21 is the manual and automatic quantification for γH2AX, cleaved caspase-3, Ki67 staining in different samples. Automatic quantification of γH2AX and Ki67 in some of the samples was significantly different from the results of manual quantification. Whereas, for cleaved caspase-3 the automatic counting reflects the manual counting. Therefore, automatic quantification was only used for the quantification of cleaved caspase-3 only when specified under the figure.

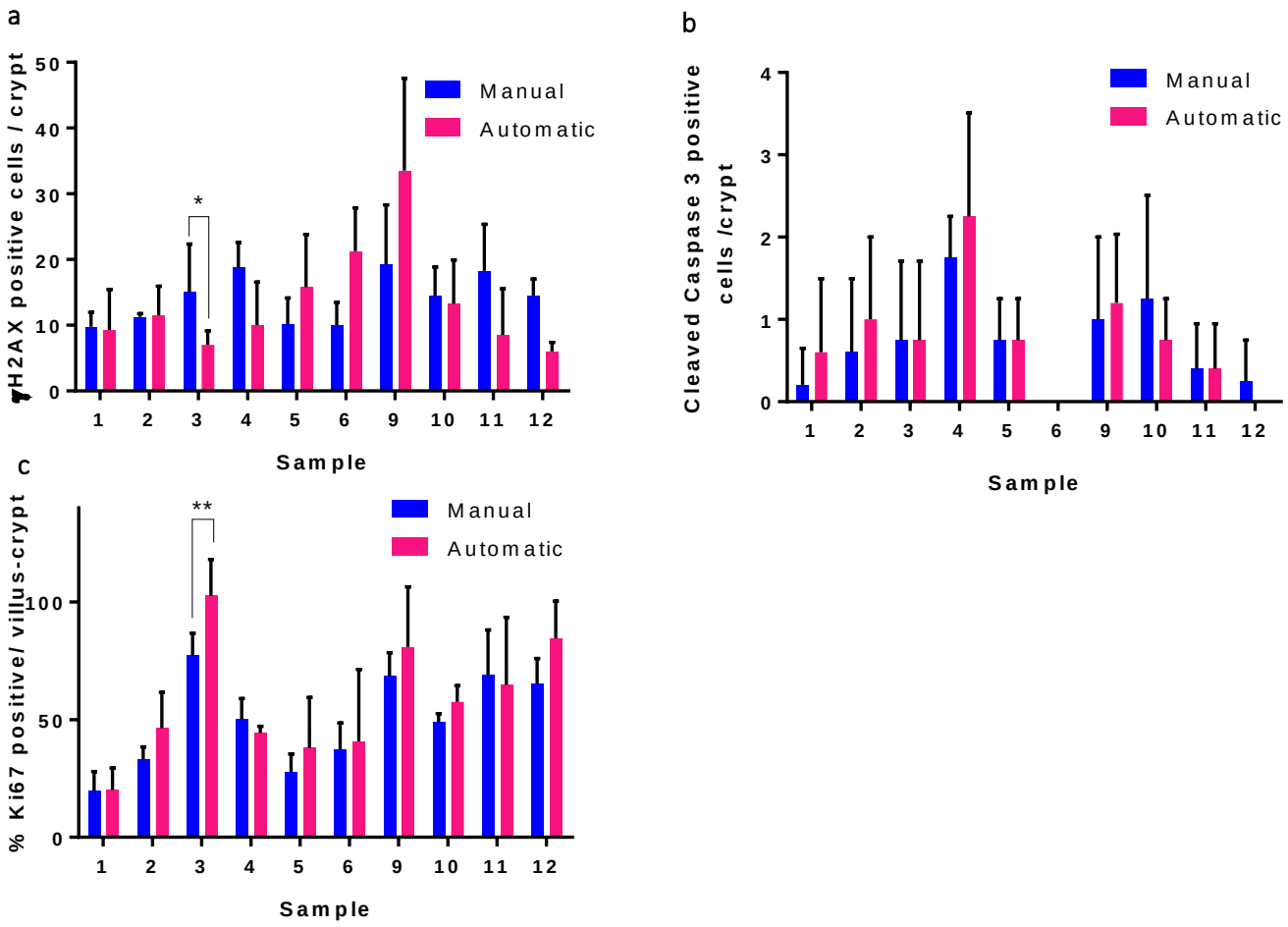

Figure 2.21 Comparison between manual and automatic methods of IHC counting.

IHC analysis of a sample of multiple crypts or crypt-villi was performed for (a) Ki67, (b) γH2AX and (c) Cleaved Caspase-3 markers. Analysis was conducted both by manual counting and automatically, using a macro script that had been created uniquely for each marker. Any significant differences between the methods of counting excluded the automatic counting as a suitable method for analysis of that particular marker. Mann-Whitney two-tailed test was used, *p=0.0286, ** p=0.0062.

2.10 Statistical Analyses

Statistical analyses were performed using GraphPad Prism version 6.00 for Windows, (GraphPad Software, La Jolla California USA).

Mann-Whitney test

The unpaired Mann-Whitney test was used to assess the statistical significance between the distribution of unrelated groups whose data sets did not follow Gaussian distribution. (GraphPad Software n.d.).

ANOVA

One-way ANOVA was used to compare, simultaneously, more than two unpaired groups whose samples follow Gaussian distribution. Brown-Forsythe test was used to identify differences in standard deviation between groups. Dunnet's multiple comparison was used after ANOVA analysis in order to correct for obtaining false significantly different results by chance due to multiple independent comparisons (GraphPad Software n.d.).

Comparisons with *p*-values less than 0.05 were considered significantly different.

3. *Apc* status influences the DNA damage repair pathway, both directly and indirectly

3.1 Introduction

One of the hallmarks of malignant cells is genomic instability (Negrini *et al.* 2010). DNA damage usually occurs spontaneously, *via* endogenous products of cellular processes or exogenous factors such as IR (Hoeijmakers 2009). Thus, cells employ various mechanisms to repair each type of DNA lesion, as unrepaired DNA damage may ultimately lead to the development of cancer. As an example, Lynch syndrome, one of the familial CRC syndromes, causes instability in microsatellite DNA sites due to germline mutations in DNA MMR pathway proteins (Jasperson *et al.* 2010). However, not all familial or sporadic CRC are initially driven by deficient DNA repair.

Studies have shown that oncogene activation can induce DNA damage by stalling and collapsing DNA replication forks (Halazonetis *et al.* 2008). Frequently mutated genes in CRC promote genomic instability (Rao and Yamada 2013). These include the *Apc* tumour suppressor gene, a negative regulator of the WNT signalling pathway. *Apc* dysfunction contributes to DNA damage; however, it remains unclear the exact mechanism by which this occurs.

DNA damage could stem from (i) the technique used to knockout *Apc* or (ii) the direct effect of APC loss of function. It has been demonstrated that there is an association between APC and efficient chromosomal segregation, *via* direct APC attachment and enhancement of microtubule stability in murine embryonic stem cells (Fodde *et al.* 2001; Kaplan *et al.* 2001) and in the human CRC cell line HCT116 (Green and Kaplan 2003; Green *et al.* 2005). In line with these, *APC* loss within HCT116 contributed to tetraploidy and polyploidy (Dikovskaya *et al.* 2007), whereas its loss within murine embryonic stem cells caused the formation of anaphase bridges, a marker of CIN (Aoki *et al.* 2007). Deficiency in *Apc* inevitably activates WNT signalling, which in turn induces *c-Myc* proto-oncogene transcription. Therefore, based on the evidence for oncogene induced DNA damage, *Apc* deficiency could (iii) indirectly lead to DNA damage (Robinson *et al.* 2009).

DSBs are the most dangerous form of DNA breaks, as genetic information can be lost or altered if not repaired properly, and the free DNA ends which result can lead to genomic rearrangements (Costanzo *et al.* 2009). The two most commonly cited markers of DSBs are γH2AX, pATM and RAD51. ATM is the first protein to be activated upon DSB formation. Similarly, H2AX phosphorylation on Ser139 (γH2AX) is one of the earliest events in response to any type

of DNA damage event and can extend up to ~ 3Mb away from a lesion (Fernandez-Capetillo *et al.* 2004). γH2AX foci are easily detected and visualized by immune-based assays. The number of foci observed in the nucleus of a cell is thought to be directly proportional to the number of DNA breaks present (Sharma *et al.* 2012). Although, the direct relationship between number of DSB and γH2AX foci is yet to be confirmed, γH2AX assays are commonly used to determine DNA damage and its resolution (Löbrich *et al.* 2010).

Whilst γH2AX foci form throughout the cell cycle, RAD51 translocates into the nucleus to form clusters (foci) only during the S-phase of the cell cycle as it is a component of the HR DNA repair pathway which requires sister chromatids for the error-free completion of DNA repair. Thus, γH2AX marks DNA damage in both dividing and non-dividing cells, whereas RAD51 nuclear foci formation only signifies damage in dividing cells. Nonetheless, both markers have been suggested as potential clinical biomarkers to predict patient response to therapies targeting defective DNA (Ivashkevich *et al.* 2012; Stover *et al.* 2016).

Using the *AhCreApc*$^{fl/fl}$ mouse model of intestinal *Apc* deficiency, Reed and colleagues (2008) showed increased *H2AX* mRNA expression in *Apc* deleted cells. However, it has only been shown in the murine liver that *Apc* deficiency induced the DNA damage checkpoint proteins p53 and p21 due to increased levels of DSBs, as quantified by IHC markers γH2AX and RAD51 (Méniel *et al.* 2015). Hence, apoptosis can be induced in p53 wt cells when DNA damage is unrepaired (Norbury and Zhivotovsky 2004).

In this chapter, we visualised and quantified DNA damage in detail in the intestines of mice where *Apc* has been deleted using either the epithelial-specific promoter *VilCre*^{ER}, or the stem cell-specific promoter *Lgr5Cre*^{ER} in order to investigate the hypothesis that *Apc* deficiency leads to DNA damage. The second aspect of this chapter investigates the mechanisms by which *Apc* loss causes DNA damage. We hypothesised that the Cre-LoxP recombination technique, which was used to knockout the *Apc* gene, was partly responsible for the DNA damage signal observed, and that the WNT signalling activation following *Apc* loss, was also involved.

3.2 *Apc* deficiency increases DNA damage levels in the small intestine of an early CRC mouse model (*VilCre^{ER} Apc$^{fl/fl}$*).

3.2.1 *Apc* loss in the *VilCre^{ER} Apc$^{fl/fl}$* mouse model induced by IP tamoxifen injection, increases γH2AX levels in small intestinal crypts.

The investigation of γH2AX levels following *Apc* deficiency was not only necessary for the determination of DSB induction, but also for the quantification of the target protein levels for ^{111}In-anti-γH2AX-TAT RIC, as this project investigates its use as a theranostic agent. Before performing any *in vivo* experiments using the *VilCre^{ER} Apc$^{fl/fl}$* model, it was necessary to characterise the intestinal crypt γH2AX levels following *Apc* deficiency. Mice were injected intraperitoneally with tamoxifen (80mg/kg; 200µl/ 25g) to induce Cre recombinase expression within the small and the large intestine, and mice were killed 1 - 4 days p.i.. Small intestinal rolls were fixed, sectioned and IHC processed and analysed. *Apc* deficiency resulted in previously described crypt-progenitor area expansion (Sansom *et al.* 2004), which was more prominent within the first 15 cm of the small intestine (Figure 3.8). Nuclei were counted starting from the crypt base to the crypt-villi junction, in order to determine crypt cell number within the tissues. As early as day 2 p.i. there was a small but significant increase in the crypt cell number of *Apc*$^{fl/fl}$ mice compared to control (*Apc*$^{+/+}$) mice, which was more prominent at days 3 and 4 p.i., signifying WNT signalling hyperactivation and excess proliferation of crypt epithelial cells (Figure 3.3).

γH2AX levels in crypt epithelial cells of the small intestine were quantified by IHC to assess the kinetics of DSB formation following *Apc* loss (Figure 3.1 and Figure 3.3). IHC staining was assessed for specificity by comparing to staining patterns of an isotype control antibody being detected by an anti-mouse secondary antibody (Figure 3.2). There was no difference at day 1 p.i. between *Apc*$^{fl/fl}$ and *Apc*$^{+/+}$ mice, but at days 2 - 4, overall γH2AX levels were significantly higher in *Apc*$^{fl/fl}$ compared to *Apc*$^{+/+}$ mice (Figure 3.4a). However, normalization of these data to the total number of cells within each crypt showed that there was no difference in the percentage of positive cells between the two genotypes at any of the days p.i. (Figure 3.4b).

γH2AX intensity levels were stratified into low, medium and high (for examples see Figure 3.5) and quantified for the time course of 1 – 4 days p.i.. Figure 3.6 shows the percentage of γH2AX positive cells stratified by staining intensity after normalization to the total number of cells in a crypt. The stratification of γH2AX intensity was used as a relative measurement of DNA damage severity. Generally, the majority of the γH2AX positive cells in either *Apc*$^{+/+}$ or *Apc*$^{fl/fl}$ mice had

low staining intensity throughout the time course. Approximately 5% and 3% of the cells in both groups were stained with medium or high γH2AX, respectively between days 1-3 p.i.. However, at days 3 and 4 p.i., *Apc*$^{fl/fl}$ mice had significantly increased high γH2AX intensity levels compared to *Apc*$^{+/+}$ mice; although medium γH2AX intensity levels followed a similar pattern the results were not significantly different.

IHC quantification is represented in two ways in this chapter. Column bar plot representation (e.g. Figure 3.4) shows the average value of all crypts per mouse within the group, whereas in a dotted plot (e.g. Figure 3.12), each dot represents the value for each quantified crypt within a group of mice. The initial experiments performed by IP injection of tamoxifen were represented as a column bar plot based on the traditional way our group represented IHC quantifications. Whilst column bar plots depict clearer the differences between each group of mice, when the number of animals used for each group was less than 4, no non-parametric statistics could show any significant difference between groups that appeared to be significantly different. Hence, subsequent analysis of data from oral gavaged *VilCre*^{ER} mice or IP injected *AhCre* mice (section 3.3) was represented on a dot plot because statistics could be applied on the average quantification of crypts within a group rather than per mouse.

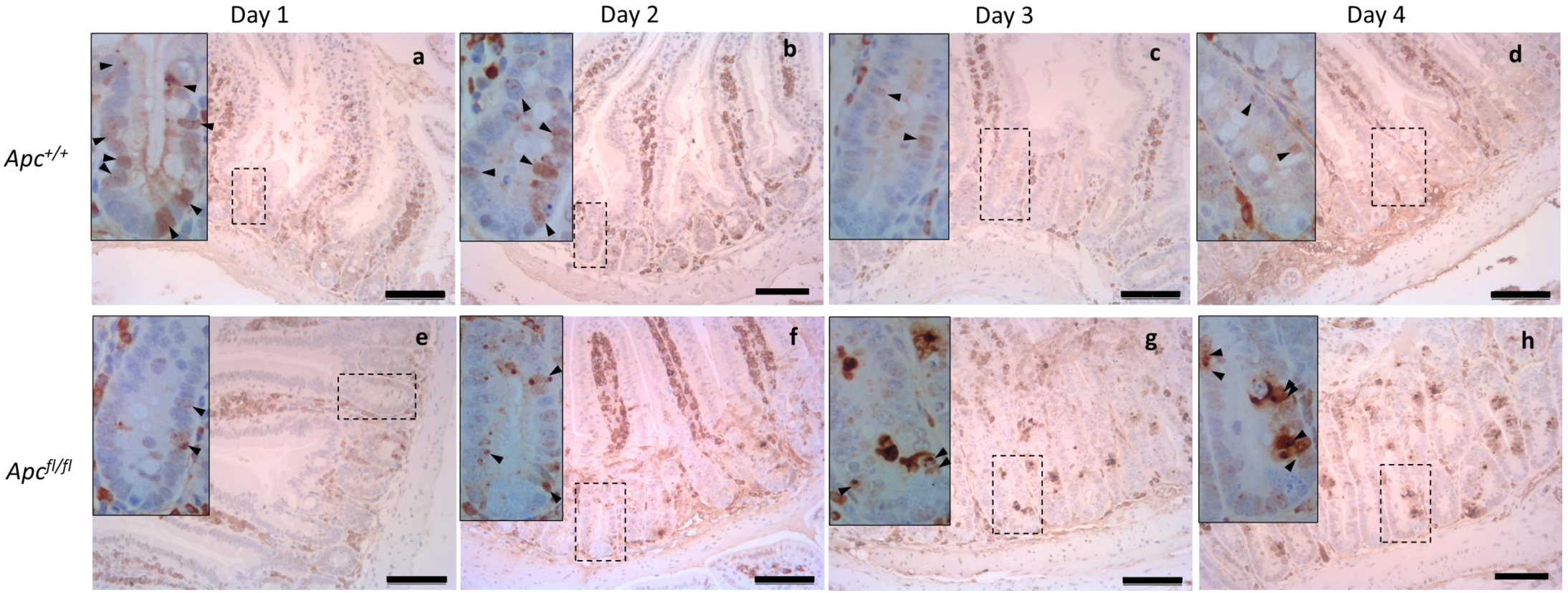

Figure 3.1 Immunohistochemical analysis for the identification of γH2AX levels in VilCre^{ER}Apc$^{fl/fl}$ and VilCre^{ER}Apc$^{+/+}$ mice over a time course of 4 days.

Bright field images of histological sections of the small intestine from *VilCre^{ER} Apc$^{+/+}$* (a - d) and *VilCre^{ER} Apc$^{fl/fl}$* (e - h) mice, 3 days post oral induction. Brown stained nuclei indicate γH2AX positive cells; non-specific staining due to anti-mouse secondary antibody binding on mouse B-cells of lamina propria. On day 3 p.i. (c) an abnormal crypt-villi structure was formed in *Apc$^{fl/fl}$* which is more prominent on day 4 p.i. (d). Bright field images; scale bar = 100 µm; *n* = 3 or 4 mice per group.

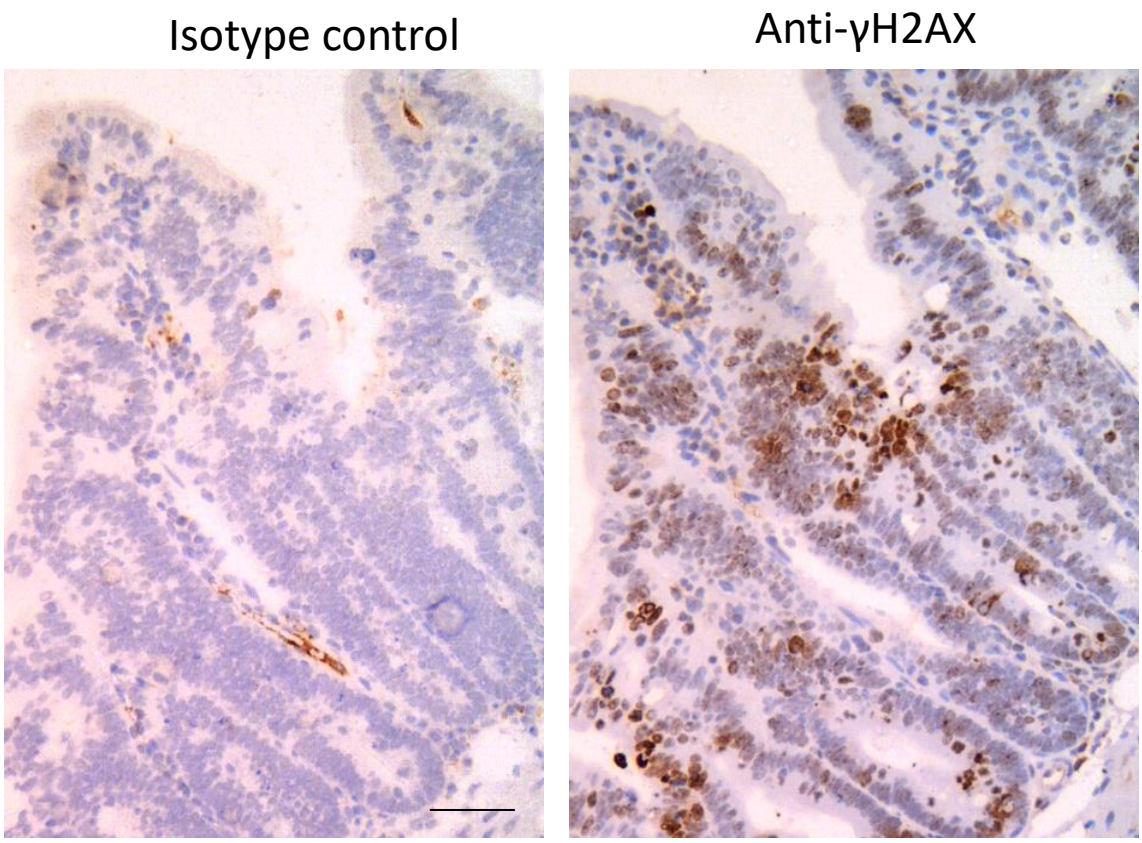

Figure 3.2 Specific and unspecific IHC staining of the mouse anti-γH2AX antibody in the small intestine.

IgG1 (isotype control) and γH2AX stainings were performed on small intestinal sections of the same *VilCre*^{ER} *Apc*$^{fl/fl}$ mouse (*n* = 1; not serial sections) 4 days post IP injection with 80mg/kg of tamoxifen. Scale bar = 50µm.

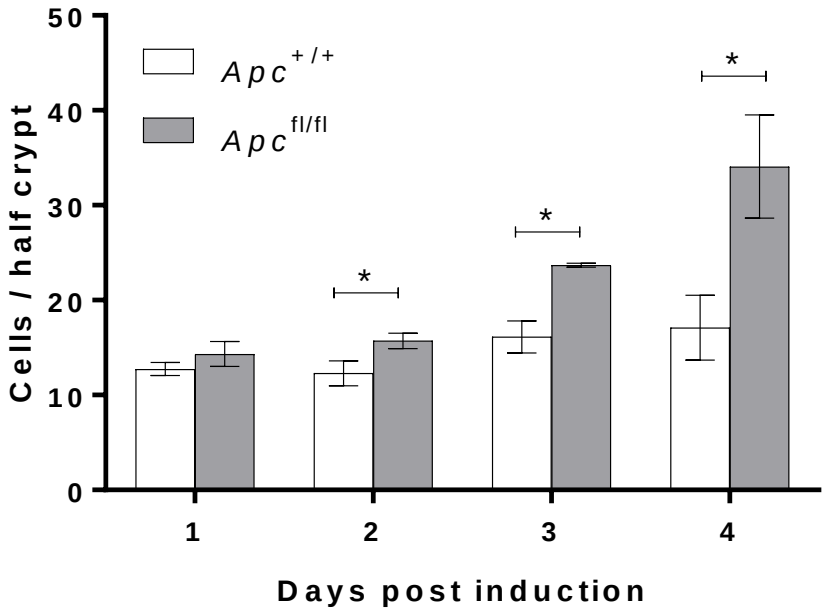

Figure 3.3 Increased crypt cell number after induction of the VilCre^{ER}Apc$^{fl/fl}$ mouse model.

VilCre^{ER}Apc$^{fl/fl}$ and *VilCre^{ER}Apc$^{+/+}$* mice were induced with 80mg/kg of tamoxifen by IP injection. IHC analysis in the small intestine of mice was performed for samples taken at different days post Induction. Total number of cells per half crypt section ±SD in *VilCre^{ER}Apc$^{fl/fl}$* and *VilCre^{ER}Apc$^{+/+}$* mice are shown. One-tailed Mann-Whitney test was performed, *$p \leq 0.05$; n = 3 or 4 mice per group.

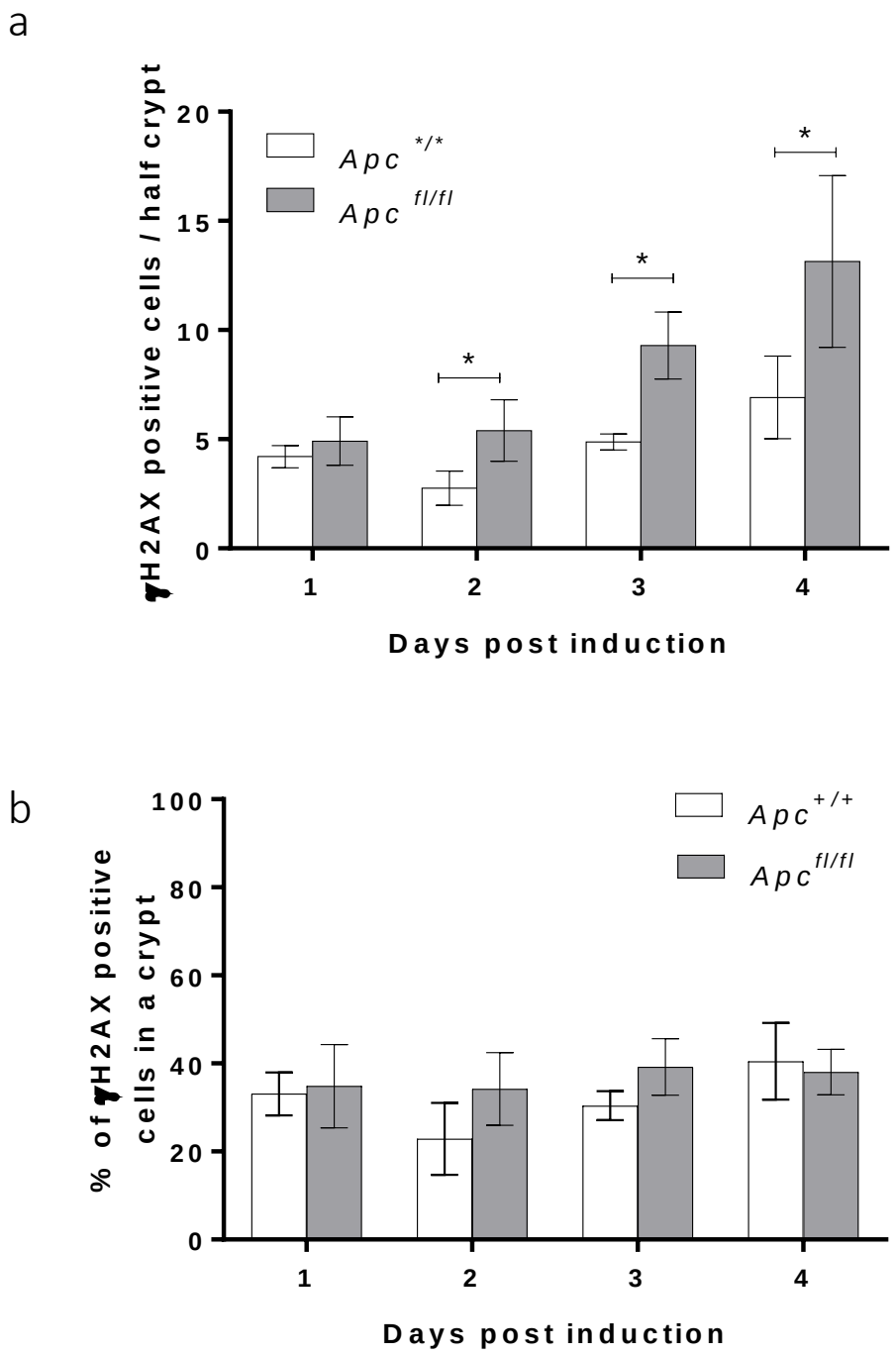

Figure 3.4 Increased γH2AX levels in small intestinal crypts after induction of the VilCre^{ER}Apc$^{fl/fl}$ mouse model.

*Vil*Cre^{ER}*Apc*$^{fl/fl}$ and *Vil*Cre^{ER}*Apc*$^{+/+}$ mice were induced with 80mg/kg of tamoxifen by IP injection. IHC analysis in the small intestine of mice was performed for samples taken at different days post induction. (a) Overall γH2AX levels per half crypt small intestinal sections of *Vil*Cre^{ER}*Apc*$^{fl/fl}$ and *Vil*Cre^{ER}*Apc*$^{+/+}$ mice. Mean values of 50 half crypts per mouse ± SD are shown (n = 3 or 4 mice per group; One-tailed Mann-Whitney test, *$p \leq 0.05$). (b) The percentage of overall γH2AX levels per crypt are shown after normalization to the total number of cells within half crypt section. $p \geq 0.05$

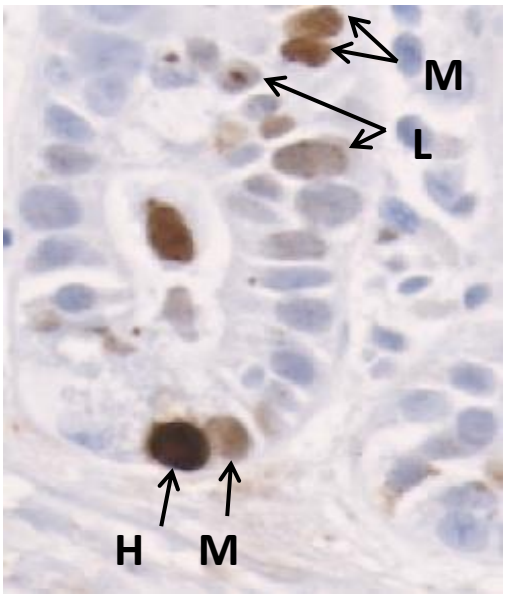

Figure 3.5 Quantification method for different γH2AX intensities in the small intestine of the early Wnt signalling deregulation mouse model.

IHC staining for γH2AX on paraffin sections of 24h 10% formalin fixed intestinal tissue of *VilCre^{ER}Apc$^{fl/fl}$* mice. Arrows indicate the different level of γH2AX intensity. H = High, M = Medium, L = Low staining intensities.

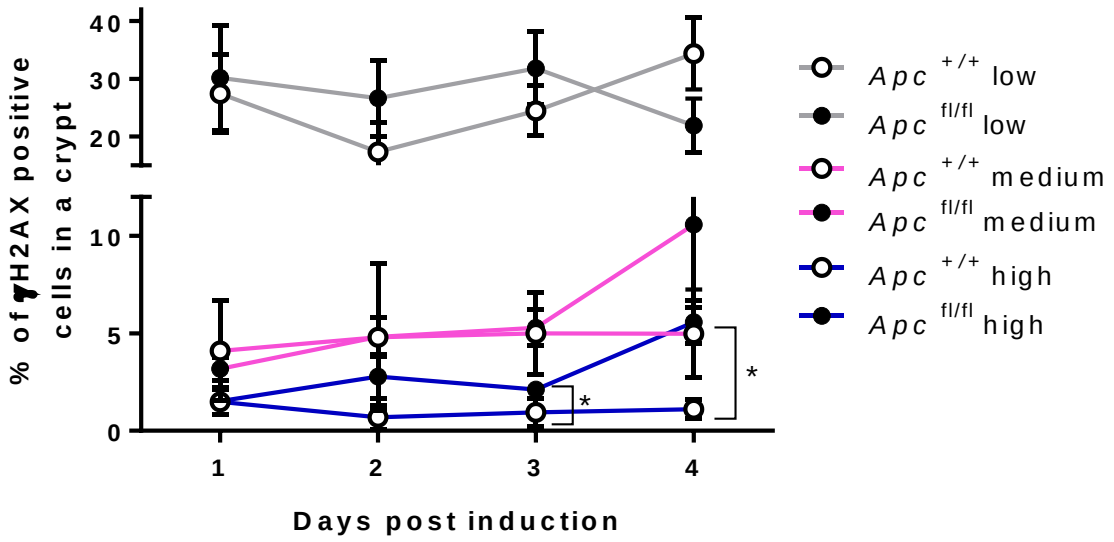

Figure 3.6 Increased γH2AX intensity levels in small intestinal crypts at days 3 and 4 post induction of the VilCre^{ER}Apc$^{fl/fl}$ mouse model.

*Vil*Cre^{ER}*Apc*$^{fl/fl}$ and *Vil*Cre^{ER}*Apc*$^{+/+}$ mice were induced with 80mg/kg of tamoxifen by IP injection. IHC analysis in the small intestine of mice was performed for samples taken at different days p.i.. The percentage of stratified quantification of γH2AX intensities per crypt section of *Vil*Cre^{ER}*Apc*$^{fl/fl}$ and *Vil*Cre^{ER}*Apc* $^{+/+}$ mice is shown. 50 half crypts per mouse were quantified and the measurements were converted to percentage per crypt ±SD (n = 3 or 4 mice per group; One-tailed Mann-Whitney test; *$p \leq 0.05$). Error bars = ± SD.

3.2.2 Differences in γH2AX levels in intestines from *VilCre*^{ER} *Apc*$^{fl/fl}$ mice induced with tamoxifen by IP injection or oral gavage

The experiment described in the previous section was performed in Cardiff premises. To overcome the unexpected adverse effects of IP corn-oil injection, we investigated whether tamoxifen administration by oral gavage could be used as an alternative administration route. Changes in tamoxifen pharmacokinetics and mode of administration could affect recombination efficiency and therefore γH2AX levels. Therefore, as crypt length following induction shows the extent of *Apc* deficiency and therefore reflects *Apc*$^{fl/fl}$ recombination levels (Feil *et al.* 2009), we compared crypt cell number following either IP or oral tamoxifen administration in *VilCre*^{ER} *Apc*$^{fl/fl}$ and *VilCre*^{ER} *Apc*$^{+/+}$ mice at day 3 p.i. and found no significant difference between administration routes in either genotype (Figure 3.7 a), despite the fact that oral administration resulted in more variable crypt length compared to IP injection. Crypt length at day 2 p.i. in IP-injected mice was also scored and compared to crypt length in day 3 oral-administered mice in order to assess whether recombination following oral gavage was occurring with similar efficiency to IP injection despite the differences in tamoxifen pharmacokinetics.

Quantification of γH2AX staining in the crypts at day 3 p.i showed that levels were higher in both genotypes following IP injection in comparison to oral gavage (Figure 3.7 b). Levels were similar for day 3 post oral administration and day 2 after IP injection (Figure 3.7 b). Detailed γH2AX intensity analysis (Figure 3.7 c) showed that at day 3 post oral tamoxifen administration, there were significantly more cells showing high γH2AX intensity in *Apc*$^{fl/fl}$ mice compared to both IP-administered groups. In *Apc*$^{+/+}$ mice, at both days 2 and 3 after IP injection there were significantly more cells showing medium γH2AX intensity compared to orally-administered mice, where intensity was almost exclusively low. Generally, *Apc*$^{+/+}$ mice administered with tamoxifen by oral gavage had almost no cells with medium or high γH2AX intensities which is consistent with the phenotype present in wild-type tissue (Figure 3.23a). However, administration of tamoxifen by IP injection in *Apc*$^{+/+}$ mice showed that there were cells with medium and high γH2AX intensities in the intestinal crypts. This could possibly be attributed to the administration route per se. IP injections cause abdominal inflammation in some extend (Hubbard *et al.* 2017) due to a) the penetration through the skin into the abdominal cavity and b) the deposit of a non-sterile liquid (tamoxifen in corn oil) into the cavity. This might induce cell stress hence γH2AX (Mah *et al.* 2010); whereas, the technique of oral gavage does not cause any tissue injury and the non-sterile liquid passes through the same route as the non-sterile food given to the mice.

Taking these results together, oral administration of tamoxifen had a similar expansion of the crypt to IP injection, implying similar recombination efficiency, and a similar pattern of γH2AX staining differences between *Apc*$^{+/+}$ and *Apc*$^{fl/fl}$ crypts, albeit IP injection generally resulted in higher γH2AX staining levels compared to oral gavage. Hence, we changed the induction protocol for the *VilCre*^{ER} *Apc*$^{fl/fl}$ mouse model in order to perform the *in vivo* experiments in Oxford.

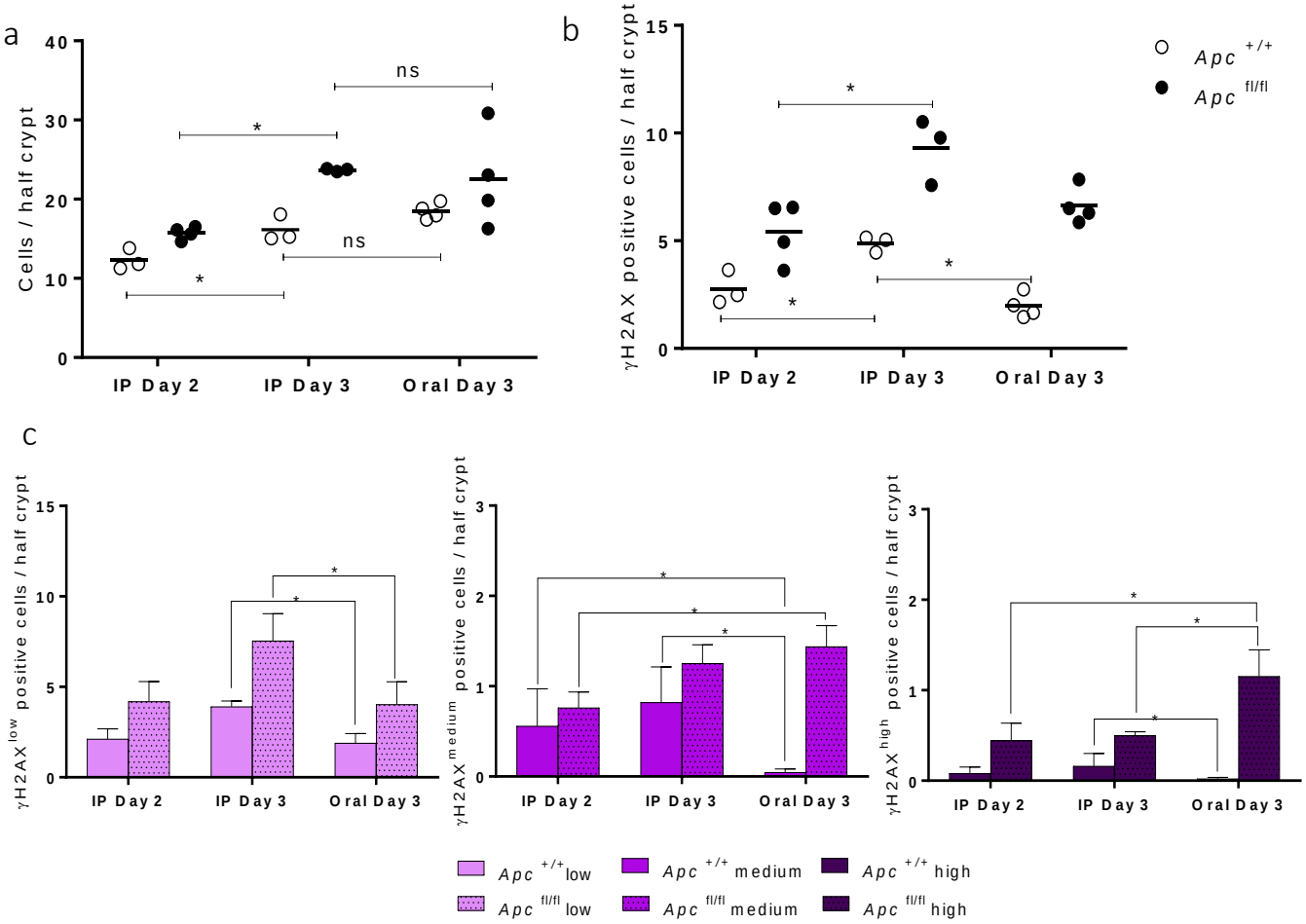

Figure 3.7 Comparison of γH2AX levels following oral gavage or IP administration of tamoxifen in the VilCre^{ER} *Apc*$^{fl/fl}$ *mouse model.*

Tamoxifen was administered to *VilCre*^{ER} *Apc*$^{fl/fl}$ and *VilCre*^{ER} *Apc*$^{+/+}$ mice orally by gavage or by IP injection. (a) Total number of crypt cells scored from γH2AX IHC. (b) Quantification of IHC staining for overall γH2AX positive cells per half crypt, at days 2 and 3 post IP injection and day 3 post oral administration of tamoxifen (both 10mg / kg; 3 times in a day). Each dot represents the mean value of 50 half crypts per mouse (n = 3 or 4 mice per group; $p \leq 0.05$. (c) Stratified quantification of γH2AX low, medium and high intensities are given. Average ±SD of 50 half crypts per mouse are shown (n = 3 or 4 mice per group). One tailed Mann-Whitney U-test; *$p \leq 0.05$.

3.2.3 *Apc* loss in the *VilCre^{ER} Apc$^{fl/fl}$* mouse model induced by oral gavage of tamoxifen, increases γH2AX levels in small intestinal crypts.

Similar to the results obtained by IP injection, were the results obtained for mice 3 days after oral gavage, using the same regime (3x in single day of 80mg/kg of tamoxifen; 200µl/ 25g). There was an increase in the number of cells within the crypt zone of *Apc*$^{fl/fl}$ mice, as quantified by the number of nuclei within a crypt section (Figure 3.8, Figure 3.11). Analysis of IHC and IF γH2AX staining showed significantly increased γH2AX overall levels in *Apc*$^{fl/fl}$ mice compared to the *Apc*$^{+/+}$ mice (Figure 3.10a and Figure 3.11b, respectively). Stratification of γH2AX staining intensity showed that the percentage of cells with medium and high staining intensities was significantly higher in *Apc*$^{fl/fl}$ mice compared to *Apc*$^{+/+}$ mice (Figure 3.10b).

Ex vivo intestinal crypt cultures derived from *VilCre^{ER}Apc$^{fl/fl}$* and *VilCre^{ER}Apc$^{+/+}$* intestinal tissue, 3 days after IP injection with tamoxifen (60 mg/kg), gave rise to 3D mini-organs, called organoids, which contained all of the epithelial cell lineages found in the *in vivo* intestinal system (Sato *et al.* 2009). Whole mount immunofluorescence for γH2AX was performed on 3 day old organoids from both genotypes and representative confocal images of maximum projection are shown in Figure 3.12. The images depict the phenotypic differences between *Apc*$^{+/+}$ and *Apc*$^{fl/fl}$ organoids stemming from the inability of *Apc*$^{fl/fl}$ cells to generate differentiated cells (Sansom *et al.* 2004). *Apc*$^{+/+}$ form buds (crypts) which are all linked to the main organoid body (villi) (Sato *et al.* 2009). *Apc*$^{fl/fl}$ organoids form cyst-like structures due to expansion of stem and progenitor cells, similarly to the crypt expansion observed in intestines of the *VilCre^{ER}Apc$^{fl/fl}$* mouse model (Figure 3.1). Quantification of γH2AX positive cells in organoids showed a significant increase in *Apc*$^{fl/fl}$ compared to *Apc*$^{+/+}$ organoids (Figure 3.12b), which was in agreement with the *in vivo* quantification.

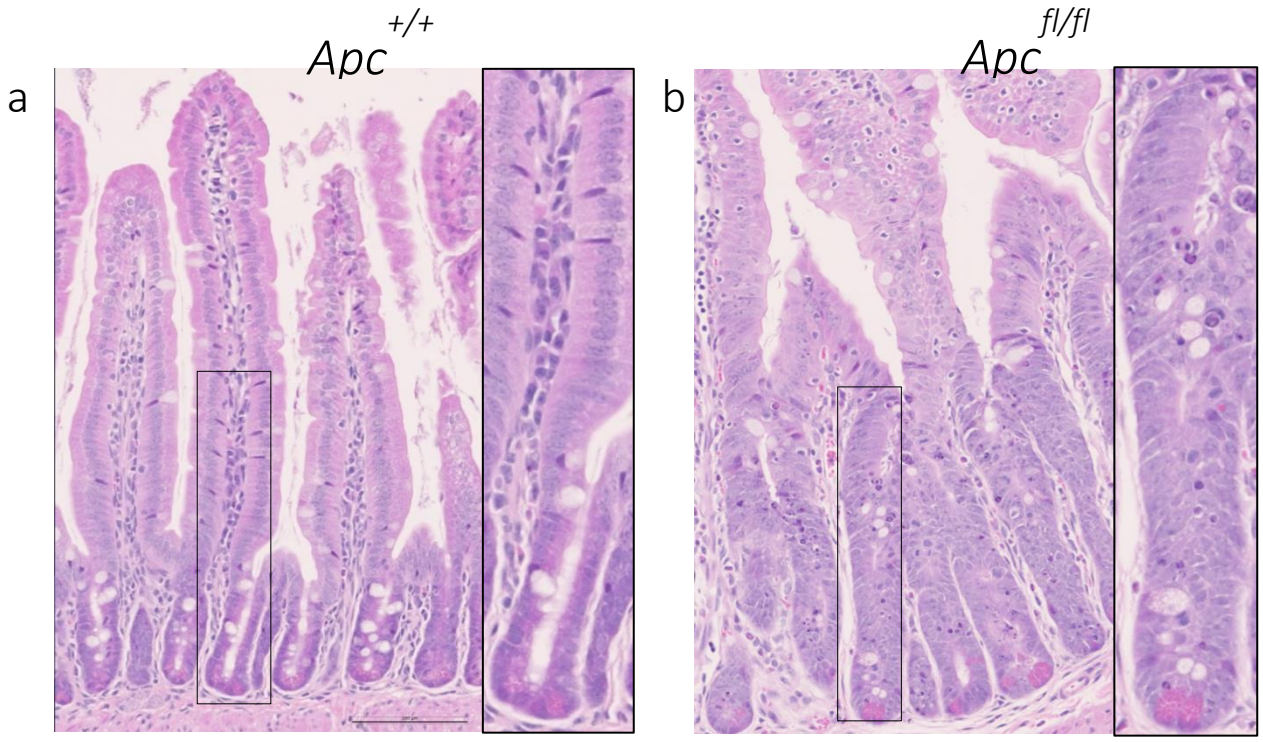

Figure 3.8 VilCre^{ER}Apc$^{fl/fl}$ oral gavage induction with tamoxifen expands the proximal small intestinal crypt compartment.

Representative bright field images of H&E staining of histological sections of the small intestine of (a) *Vil*Cre^{ER} *Apc*$^{+/+}$ and (b) *Vil*Cre^{ER} *Apc*$^{fl/fl}$ mice, 3 days post oral induction. Scale bar = 100 µm; *n* = 4 mice per group.

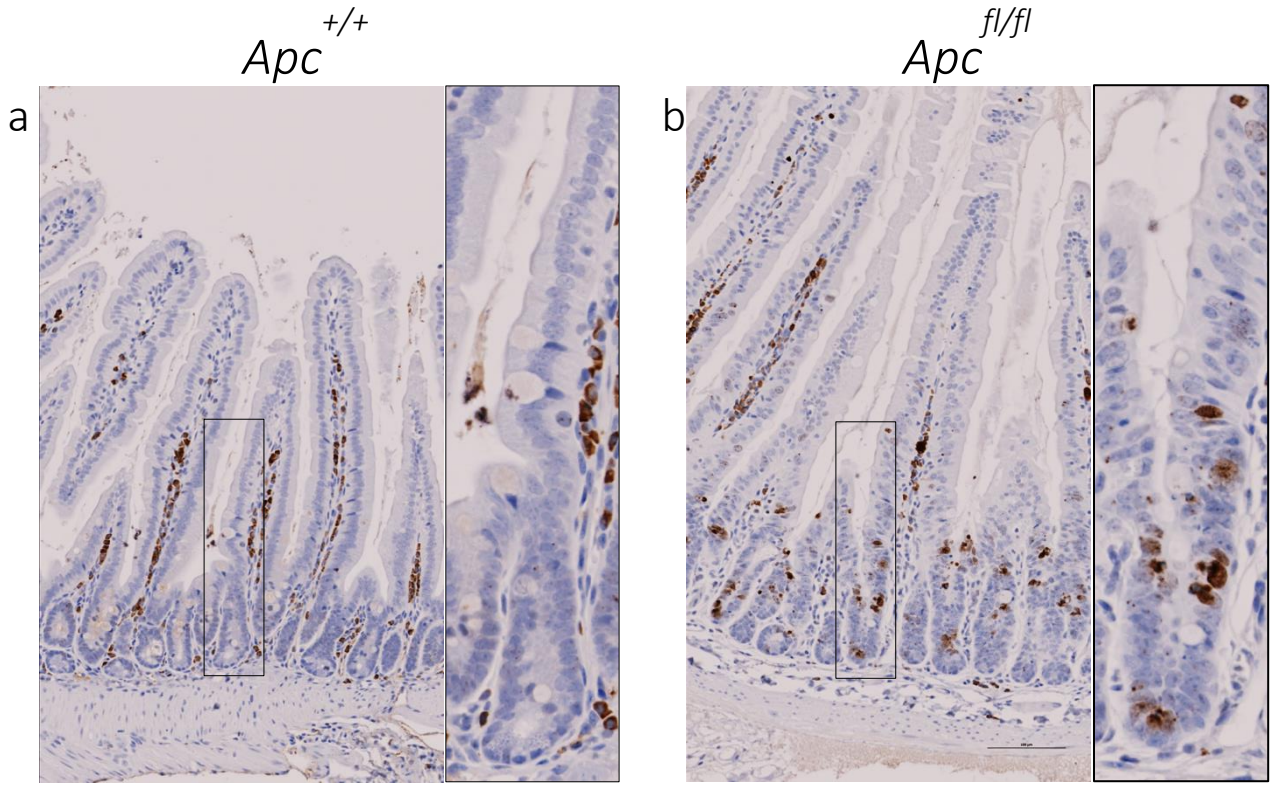

Figure 3.9 VilCre^{ER}Apc$^{fl/fl}$ oral gavage induction with tamoxifen induces γH2AX in the proximal small intestine.

Representative bright field images of histological sections of the small intestine of (a) *Vil*Cre^{ER} *Apc*$^{+/+}$ and (b) *Vil*Cre^{ER} *Apc*$^{fl/fl}$ mice 3 days post oral induction Brown stained nuclei indicate γH2AX positive cells. Scale bar = 100 µm; *n* = 4 mice per group.

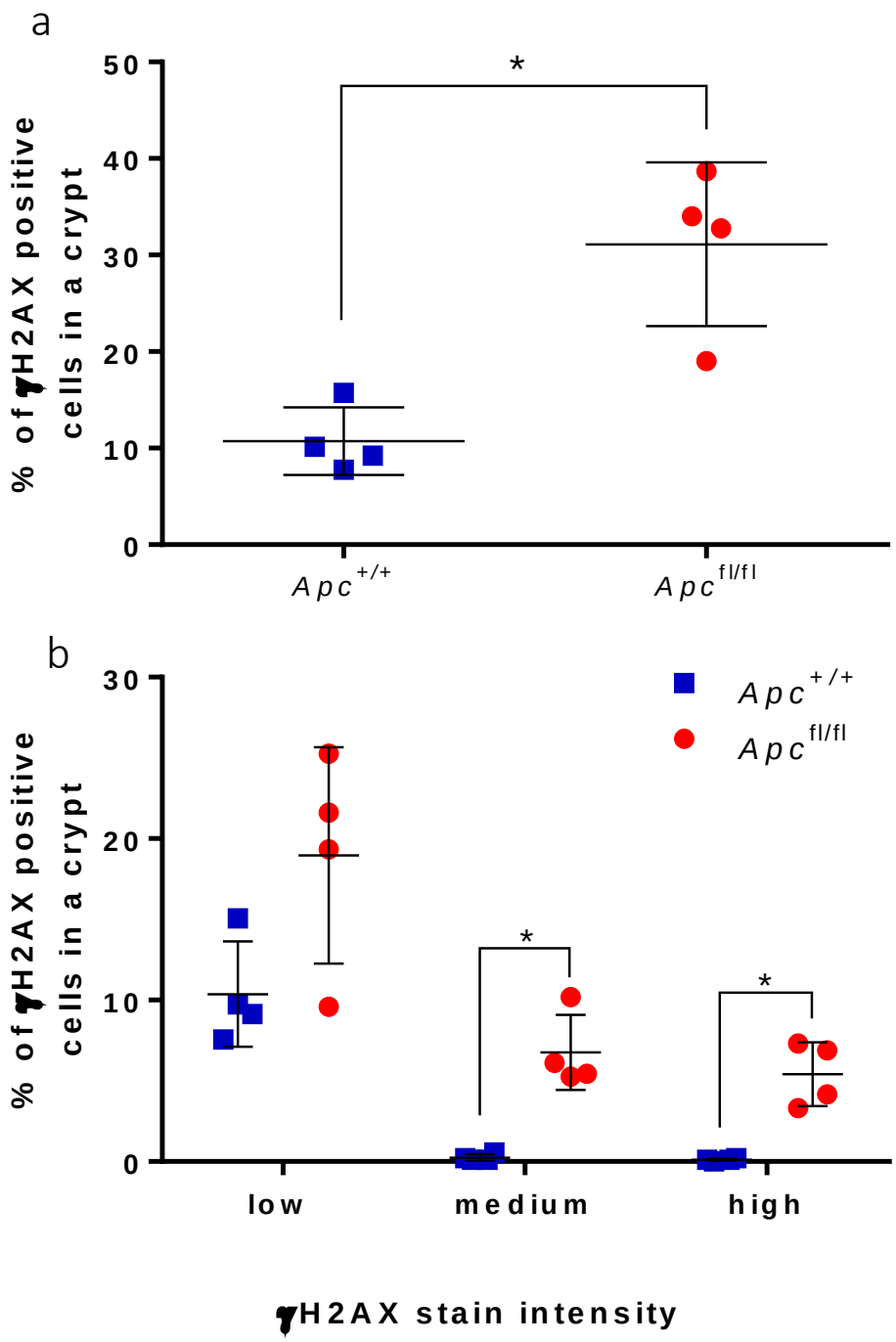

Figure 3.10 Increased crypt cell number and γH2AX levels after induction of the VilCre^{ER}Apc$^{fl/fl}$ mouse model by oral gavage.

*Vil*Cre^{ER}*Apc*$^{fl/fl}$ and *Vil*Cre^{ER}*Apc*$^{+/+}$ mice were induced with 80mg/kg of tamoxifen by oral gavage. IHC analysis in the small intestine of mice was performed for samples taken 3 days p.i.. (a) The percentage of overall γH2AX levels per crypt are shown. Two-tailed Mann-Whitney test was performed; *p = 0.0286. (b) The % of stratified γH2AX levels per crypt section is shown. Two-tailed Mann-Whitney test was performed; * p = 0.0286; n = 4 mice per group. Error bars = ± SD.

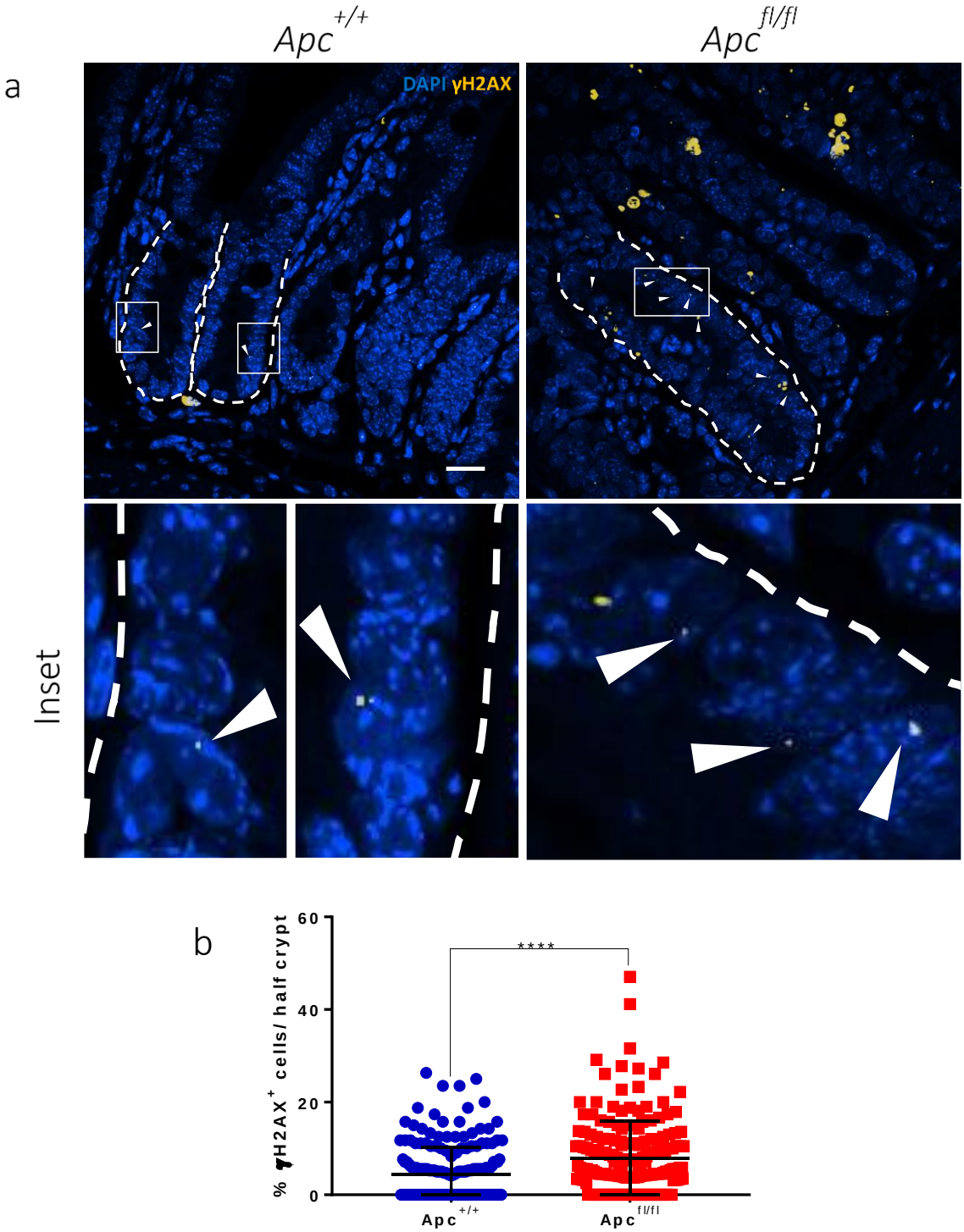

Figure 3.11 Apc deficiency in the murine small intestine increases the number of crypt epithelial cells with γH2AX foci.

(a) γH2AX IF analysis in half crypt sections of the small intestine from *Vil*Cre^{ER}*Apc*$^{+/+}$ and *Vil*Cre^{ER}*Apc*$^{fl/fl}$ mice, 3 days post oral induction with 80mg/kg of tamoxifen. Representative images of γH2AX^{+} cells are shown. Scale bar = 20 µm. (b) Mean percentage of nuclear γH2AX positive cells from >47 half crypt sections / mouse for 4 mice within each group ±SD are shown. Unpaired 2-tailed Mann Whitney test was performed; ****p < 0.0001.

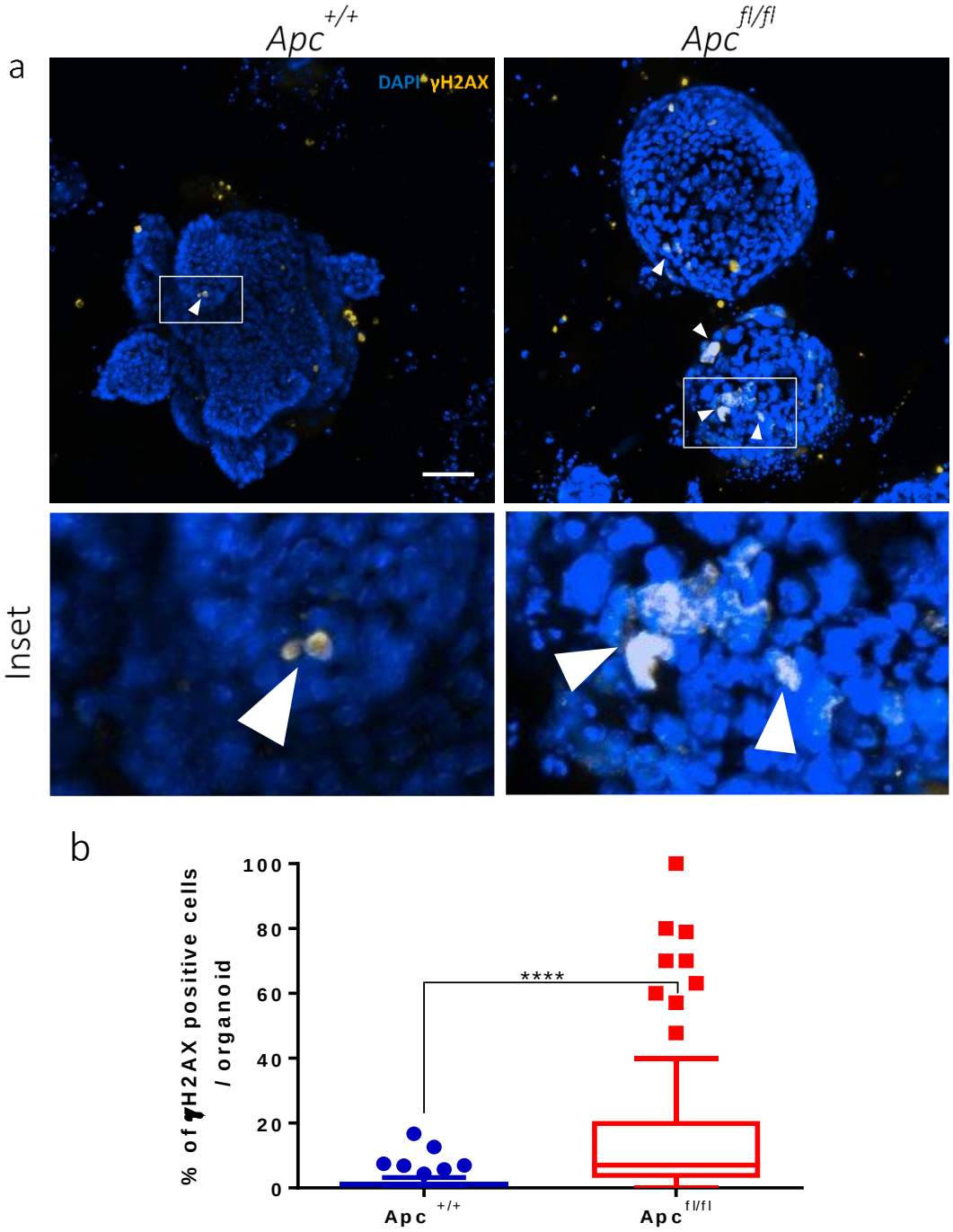

Figure 3.12 Apc deficiency in murine small intestinal organoids increases the number of crypt epithelial cells with γH2AX foci.

(a) γH2AX whole mount IF analysis of organoids derived from small intestinal crypts of *VilCre^{ER} Apc$^{+/+}$* and *VilCre^{ER} Apc$^{fl/fl}$* mice, 3 days post oral induction with 60mg/kg of tamoxifen. Representative maximum projection confocal images are shown. Scale bar = 50 µm. Arrows indicate specific γH2AX positive nuclei. *(b) Percentage of nuclear γH2AX positive cells per organoid ± SD, from 44 wt or 104 Apc$^{fl/fl}$ organoids. Unpaired 2-tailed Mann Whitney test was performed; ****p < 0.0001. Biological replicates: n = 2 and n = 3 for the VilCre^{ER} Apc$^{+/+}$ and VilCre^{ER} Apc$^{fl/fl}$, respectively.*

3.2.4 *Apc* loss in the *VilCre^{ER} Apc$^{fl/fl}$* mouse model increases the number of cells in small intestinal crypts with perinuclear phospho-Ser^{1981} ATM.

ATM (Ataxia Telangiectasia Mutated) is the first protein in the DDR pathway to be activated upon a DSB (So *et al.* 2009). It localizes to the DSB with the help of the MRN complex and is activated by autophosphorylation or trans-phosphorylation at Ser^{1981}. The activated ATM monomer triggers the collective responses necessary for the resolution of the DNA break, as well as controlling cell cycle, transcription, apoptosis and cell proliferation (Shiloh and Ziv 2013).

Hence, assessing the presence of activated nuclear ATM was the first step in identifying the presence of DSBs in *VilCre^{ER} Apc$^{+/+}$* and *VilCre^{ER} Apc$^{fl/fl}$* mice (in this chapter referred to as *Apc$^{+/+}$* and *Apc$^{fl/fl}$*) 3 days after oral gavage with 80mg/kg of tamoxifen. Small intestinal sections were fixed and IHC stained with an antibody recognising phospho-Ser^{1981} ATM (pATM). We hypothesised that *Apc* loss induces DSB; hence we expected nuclear localization of the phosphorylated ATM, similarly to observations made by other studies following irradiation of melanoma and fibroblast cells (Zhang *et al.* 2016). Unexpectedly, nuclear, perinuclear or both patterns of pATM staining were observed, in epithelial cells of both *Apc$^{+/+}$* and *Apc$^{fl/fl}$* crypts (Figure 3.13). The majority of stained cells had perinuclear staining pattern which sometimes extended towards the cytoplasm.

As Figure 3.13 suggests, the number of total pATM cells (independent of staining localization) was higher in the small intestine of the *Apc$^{fl/fl}$* mice compared to the *Apc$^{+/+}$* mice. However, this was a result of excess proliferation and cell accumulation in crypts, as normalization of the pATM positive cell number to the total cell number of crypts showed that there was no significant difference in percentage of positive cells between the two groups (Figure 3.14a). The few cells with nuclear pATM staining were significantly higher in the *Apc$^{+/+}$* crypts compared to *Apc$^{fl/fl}$*, whereas the opposite was observed for cells with both nuclear and perinuclear pATM staining (Figure 3.15 a-c).

Usually, staining for pATM was observed at +3 cell positions of the *Apc$^{+/+}$* crypt base, whereas positions +1 to +4, +7 and +8 of *Apc$^{fl/fl}$* crypts more often accommodated perinuclear pATM positive cells (Figure 3.14b). The described crypt positions were mostly accommodated by cells with perinuclear pATM staining.

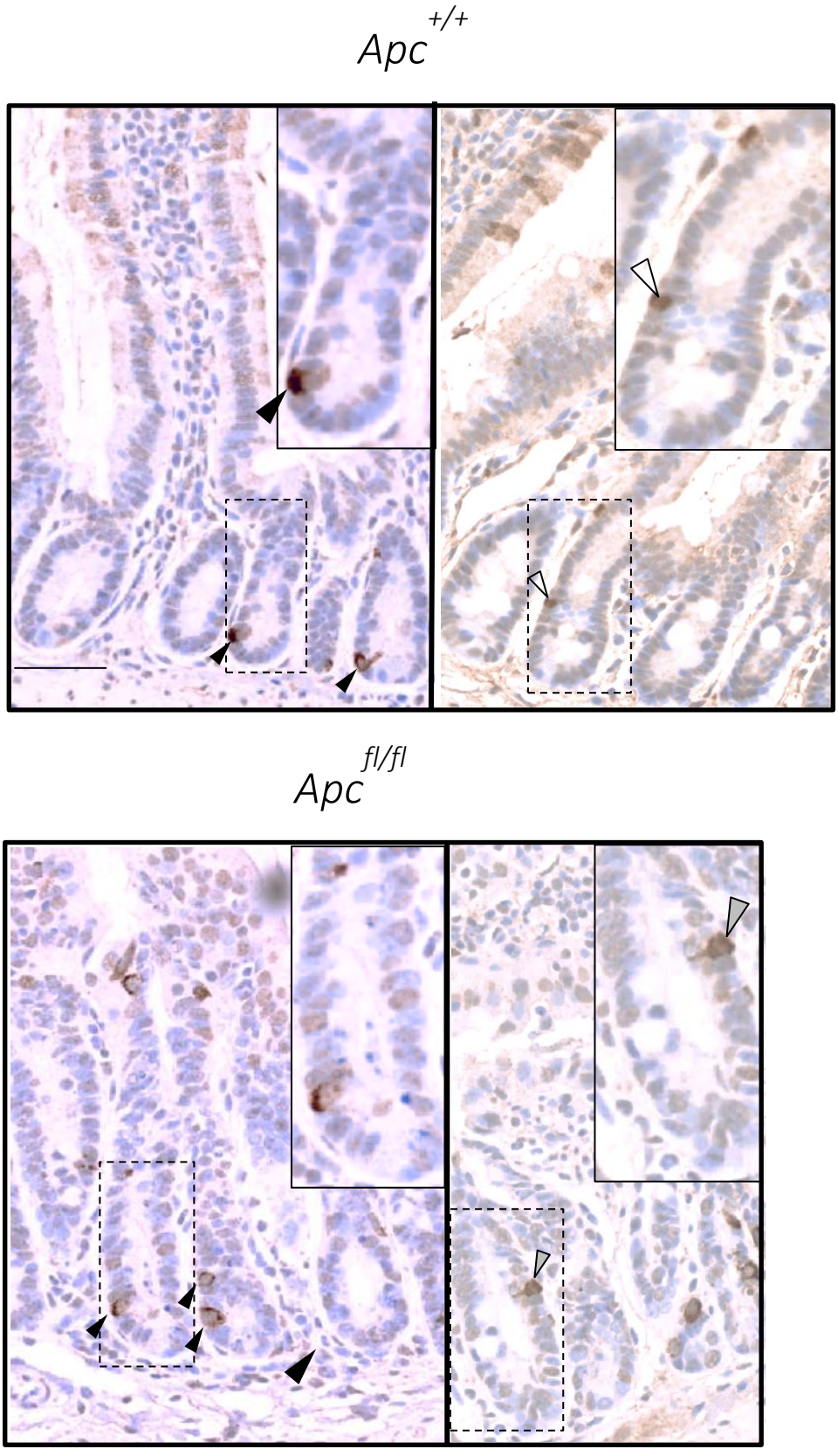

Figure 3.13 pATM staining in the VilCre^{ER} Apc$^{+/+}$ and VilCre^{ER} Apc$^{fl/fl}$ mouse models.

pATM IHC staining in the small intestine of *VilCre^{ER} Apc$^{+/+}$* and *VilCre^{ER} Apc$^{fl/fl}$* mice 3 days post oral induction. Bright field images; scale bar = 50 µm; Arrow heads showing ► perinuclear (sometimes cytoplasmic), ▻ nuclear or ► both perinuclear (sometimes cytoplasmic) and nuclear staining.

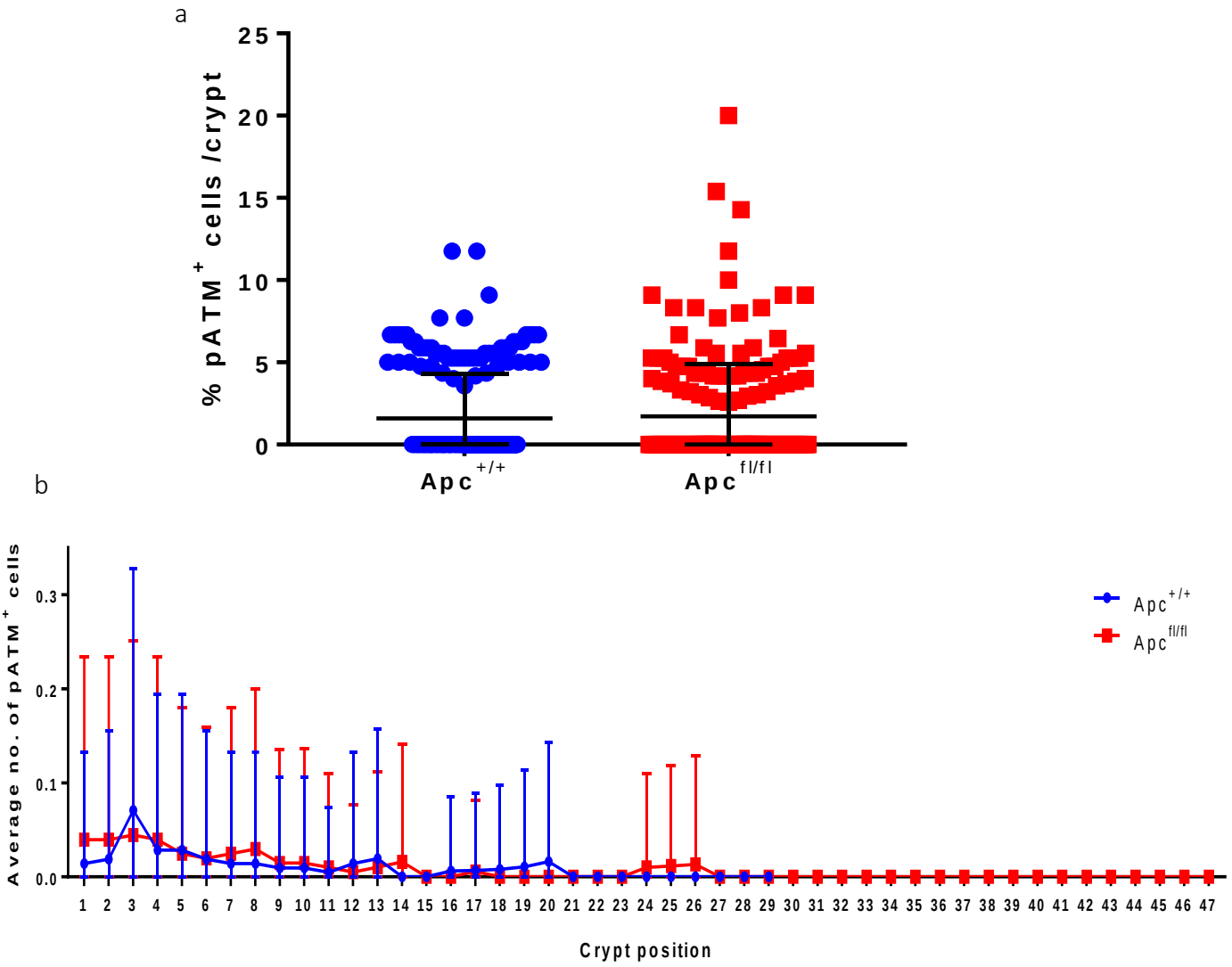

Figure 3.14 pATM IHC staining quantification in the small intestine

(a) Percentage of cells with pATM IHC staining in small intestinal crypts of *VilCre^{ER} Apc$^{+/+}$* and *VilCre^{ER} Apc$^{fl/fl}$* mice, 3 days post oral induction by tamoxifen (212 and 205 crypts, respectively; biological replicates n = 4 per group). Two-tailed Mann Whitney U-test was performed; NS; $p \geq 0.05$.

(b) Average number of pATM positive cells per crypt position (starting from the crypt base) in the small intestine. Error bars show ±SD.

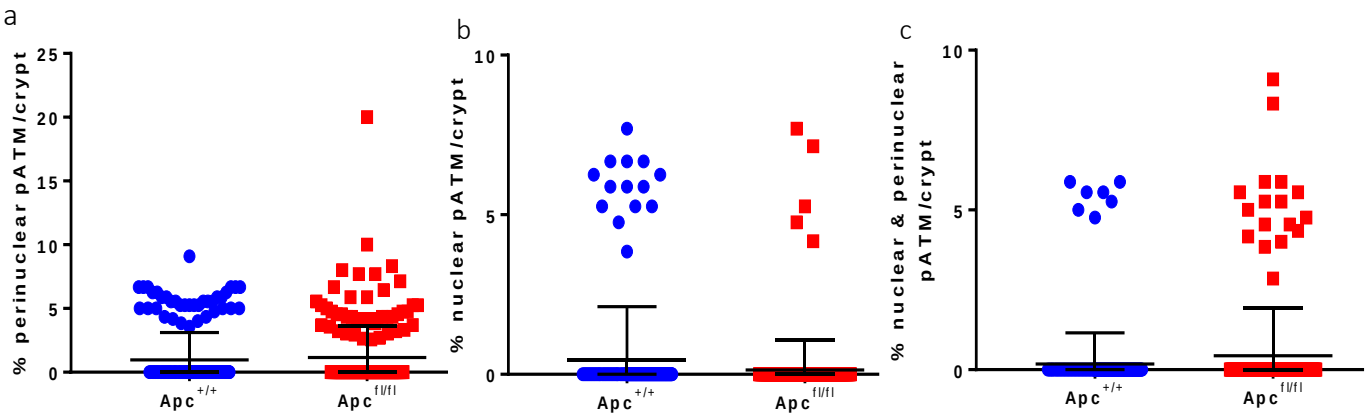

Figure 3.15 Perinuclear, nuclear or combined pATM IHC staining quantification in the small intestine

Percentage of cells with (a) perinuclear, (b) nuclear, or (c) both perinuclear and nuclear pATM IHC staining in small intestinal crypts of *VilCre^{ER} Apc$^{+/+}$* and *VilCre^{ER} Apc$^{fl/fl}$* mice, 3 days post oral induction by tamoxifen (212 and 205 crypts, respectively; biological replicates n = 4 per group). Two-tailed Mann Whitney U-test was performed; *$p < 0.05$. Error bars show ±SD

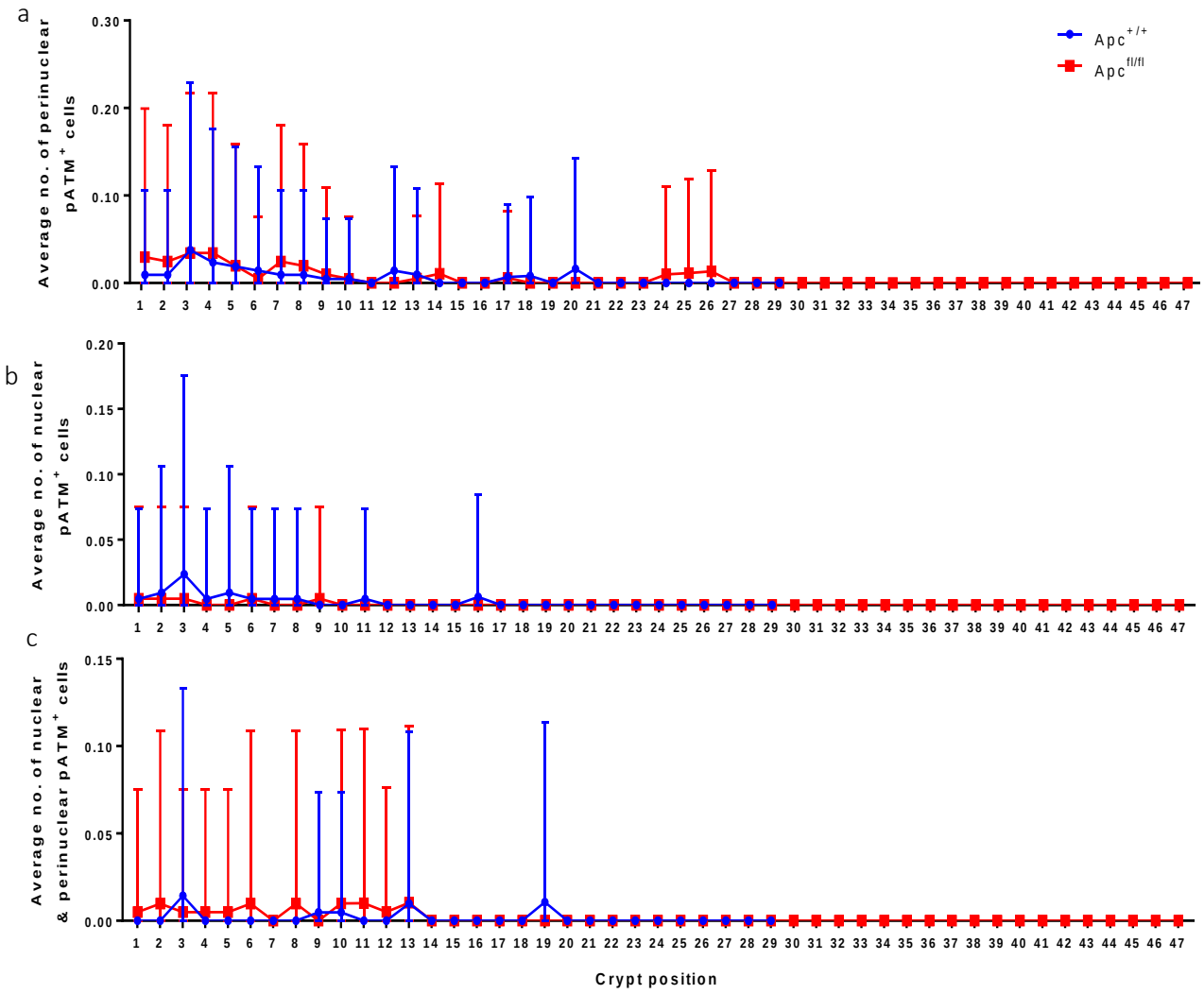

Figure 3.16 Position of perinuclear, nuclear or combined pATM IHC staining quantification in the small intestine

Average number of cells with (a) perinuclear, (b) nuclear or (c) both perinuclear and nuclear pATM staining per crypt position (starting from the crypt base) in the small intestine. Error bars show ±SD; n = 4 per group.

3.2.5 *Apc* loss in the *VilCre^{ER} Apc$^{fl/fl}$* mouse model increases the number of cells with nuclear RAD51 foci in small intestinal crypts.

Next, we investigated whether the HR pathway was activated to repair DSBs formed after *Apc* loss, which could signify that DSB were generated in proliferating cells. Similarly, to γH2AX, RAD51, a HR component, clusters on DSB in the cell nucleus, and can be detected by immunofluorescence as nuclear foci. RAD51 IF staining was performed on fixed small intestinal sections from *Apc*$^{+/+}$ and *Apc*$^{fl/fl}$ mice, 3 days p.i. by oral gavage with 80mg/kg of tamoxifen (Figure 3.17 a). Quantification of the percentage of RAD51^{+} cells within a section of a crypt showed significantly increased levels in *Apc*$^{fl/fl}$ mice compared to control mice (Figure 3.17 b), indicating that the HR pathway is employed after DSB formation mediated by *Apc* loss. γH2AX and RAD51 co-IF staining was also performed and quantified (Figure 3.18); cells with γH2AX and RAD51 co-stained foci were significantly higher in *Apc*$^{fl/fl}$ mice compared to *Apc*$^{+/+}$ mice.

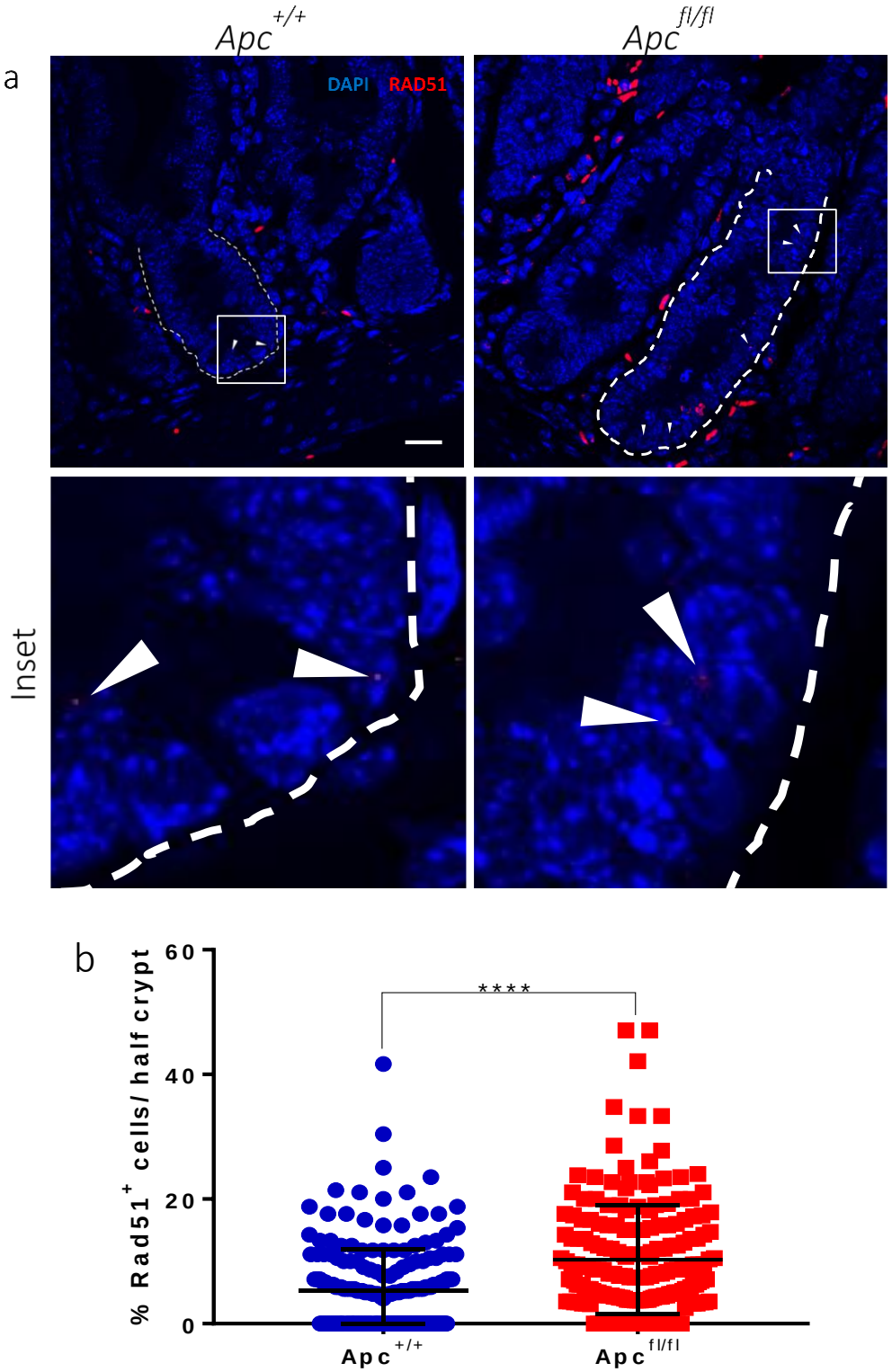

Figure 3.17 Apc deficiency in the murine small intestine increases the number of crypt epithelial cells with RAD51 foci.

(a) RAD51 IF analysis in half crypt sections of the small intestine from *VilCre^{ER}Apc$^{+/+}$* and *VilCre^{ER}Apc$^{fl/fl}$* mice, 3 days post oral induction with 80mg/kg of tamoxifen. Representative images of RAD51^{+} cells are shown. Dotted lines surround a crypt. Arrows indicate nuclei with RAD51 foci. Scale bar = 20 µm. (b) Mean percentage of nuclear RAD51 positive cells from >47 half crypt sections / mouse for 4 mice within each group ± SD are shown. Unpaired 2-tailed Mann Whitney test was performed; ****p < 0.0001.

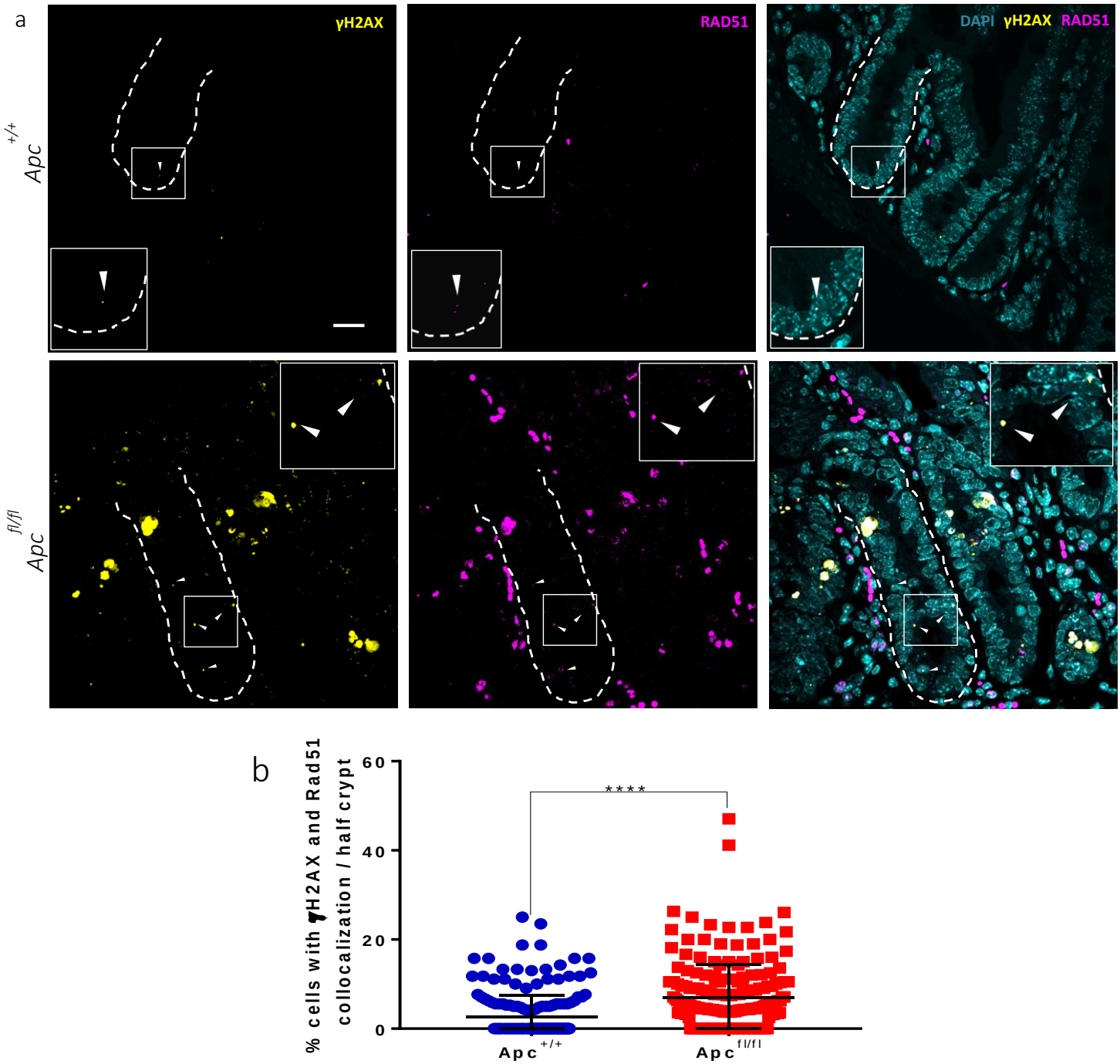

Figure 3.18 Apc deficiency in the murine small intestine contributes to significantly increased number of crypt epithelial cells with DSB induced during cell replication.

(a) RAD51 and γH2AX IF staining quantification in half crypt sections of the small intestine from *VilCre^{ER} Apc$^{+/+}$* and *VilCre^{ER} Apc$^{fl/fl}$* mice, 3 days post oral induction with 80mg/kg of tamoxifen. Representative images of double-positive Rad51^{+}γH2AX^{+} cells are shown. Scale bar = 20 μm.

(b) Percentage of double-positive Rad51^{+}γH2AX^{+} cells in a section of a half crypt are shown based on IF staining. Mean percentage of >47 half crypt sections / mouse for 4 mice within each group ±SD are shown. Unpaired 2-tailed Mann Whitney test was performed; ****p<0.0001.

3.2.6 *Apc* loss in the *VilCre^{ER} Apc$^{fl/fl}$* mouse model increases the apoptotic index of small intestinal crypts.

We quantified the levels of apoptosis within the intestine to assess whether there was a correlation with the levels of DNA damage, indicating that high levels of DNA damage were possibly eliminated by apoptosis. Hence, active caspase-3, the surrogate marker for apoptosis, was stained by IHC (Figure 3.19). Quantification showed that at days 3 and 4 p.i. there was a significant increase in apoptotic cells per half crypt section in *VilCre^{ER} Apc$^{fl/fl}$* compared to *VilCre^{ER} Apc$^{+/+}$* mice which was not a result of excess proliferation that lead to crypt expansion (Figure 3.19a and b).

Phenotypically, some high intensity γH2AX positive cells resembled cells undergoing apoptosis, as they were round/circular, similarly to the pyknotic nucleus of apoptotic epithelial cells, and usually situated towards the apical side of the epithelium close to the lumen (Figure 3.20). To further analyse this, a linear regression analysis was performed between the independent IHC quantifications for γH2AX^{high} and cleaved caspase-3-expressing cells of the crypt, from non-serial sections as shown in Figure 3.21. There was no significant correlation between the number of γH2AX^{high} and active caspase-3 positive cells of the crypt for *Apc*$^{+/+}$ mice at days 1 - 4 p.i., however for the *Apc*$^{fl/fl}$ group of mice there was.

Studies have shown that apoptotic cells are characterised by a γH2AX pan-nuclear staining pattern, resembling our IHC staining, as opposed to H2AX foci (Bonner *et al.* 2008; Solier and Pommier 2014). To investigate whether this occurs in both human and murine intestinal cancer, whole mount IF co-staining for active caspase-3 and γH2AX was performed in spheroids from a human CRC cell line (HCT116) and organoids derived from induced *Vil*Cre^{ER} *Apc*$^{fl/fl}$ mice (Figure 3.22). Apoptotic bodies and condensed nuclei positive for active caspase-3 staining showed this pan-nuclear γH2AX staining, whereas nuclei with individual γH2AX foci did not have concurrent active caspase-3 staining. It is important to note that not all γH2AX^{high+} cells also express active caspase-3.

Quantification of the % of cleaved caspase-3 positive cells in *Vil*Cre^{ER} *Apc*$^{fl/fl}$ or *Vil*Cre^{ER} *Apc*$^{+/+}$ mice-derived organoids showed no significant difference (Figure 3.23 a and b). Hence, the rate by which cells undergo apoptosis in those two different genotypes was unaffected *ex vivo*.

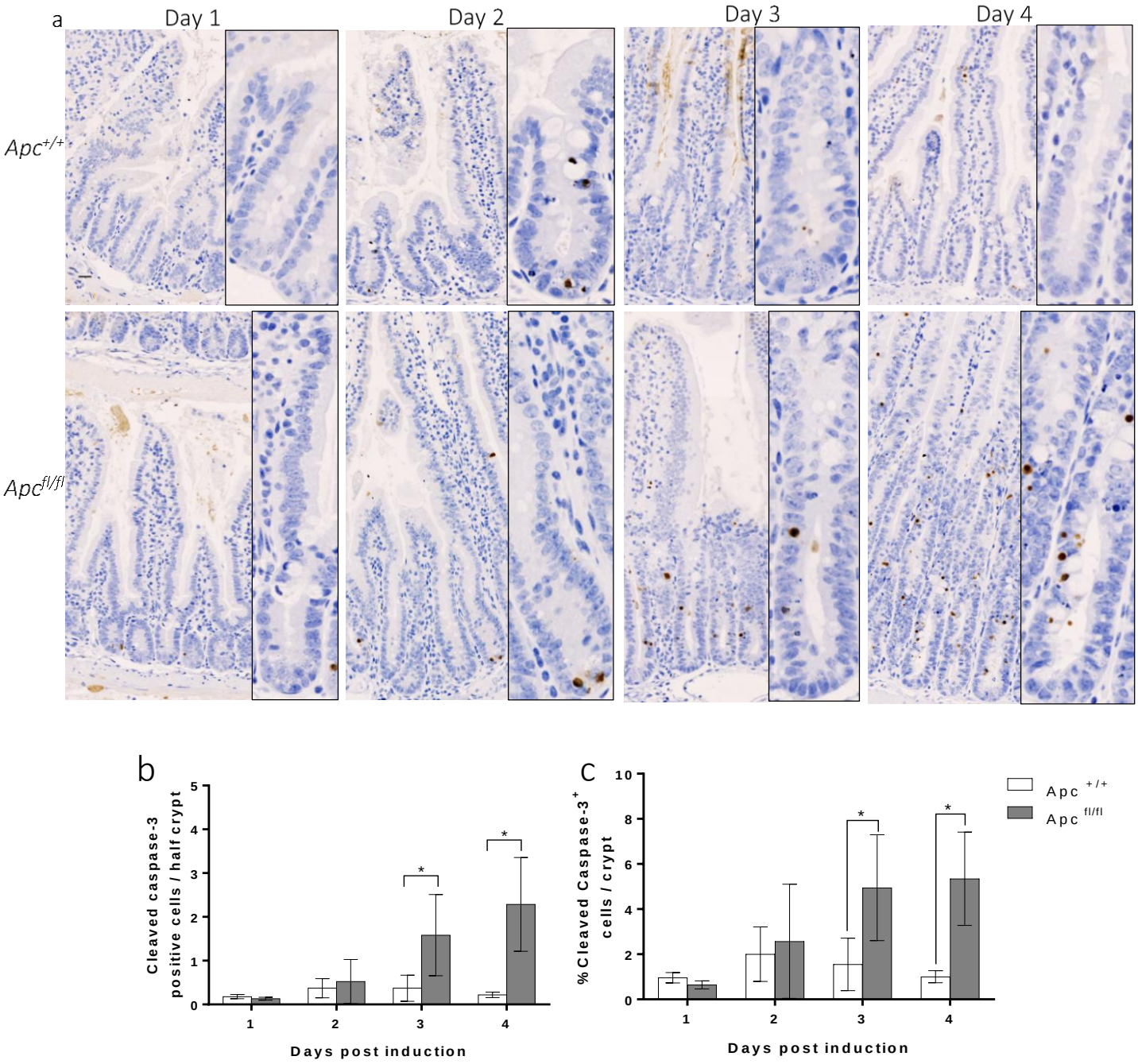

Figure 3.19 Increased apoptotic cells post induction of VilCre^{ER}Apc$^{fl/fl}$ mice.

(a) IHC analysis of cleaved caspase 3 in *VilCre^{ER}Apc$^{fl/fl}$* and *VilCre^{ER}Apc$^{+/+}$* mice 1 to 4 days post IP injection. Brown cells indicate positive cells. (b) Mean number of active caspase-3 positive cells in a crypt section. Mean values of 50 half crypts per mouse are shown ± SD. (c) Percentage of cleaved caspase 3 positive cells in a crypt section after normalization to total number of cells in a crypt section. Unpaired 1-tailed Mann-Whitney test was performed; *$p \leq 0.05$ (n = 3 or 4 mice per group); scale bar = 20 µm

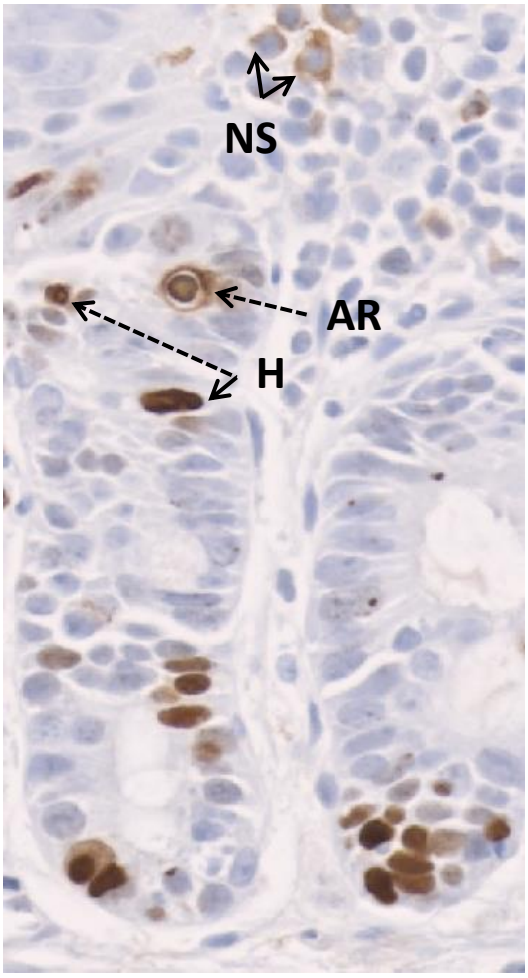

Figure 3.20 Some high γH2AX intensity cells are apoptotic.

IHC staining for γH2AX on paraffin sections of 24h 10% formalin fixed intestinal tissue of *VilCre^{ER}Apc$^{fl/fl}$* mice. Dotted arrows indicate γH2AX^{high} cells that resemble apoptotic cells. AR = Apoptotic ring, H = High staining intensity and NS = Non-specific staining.

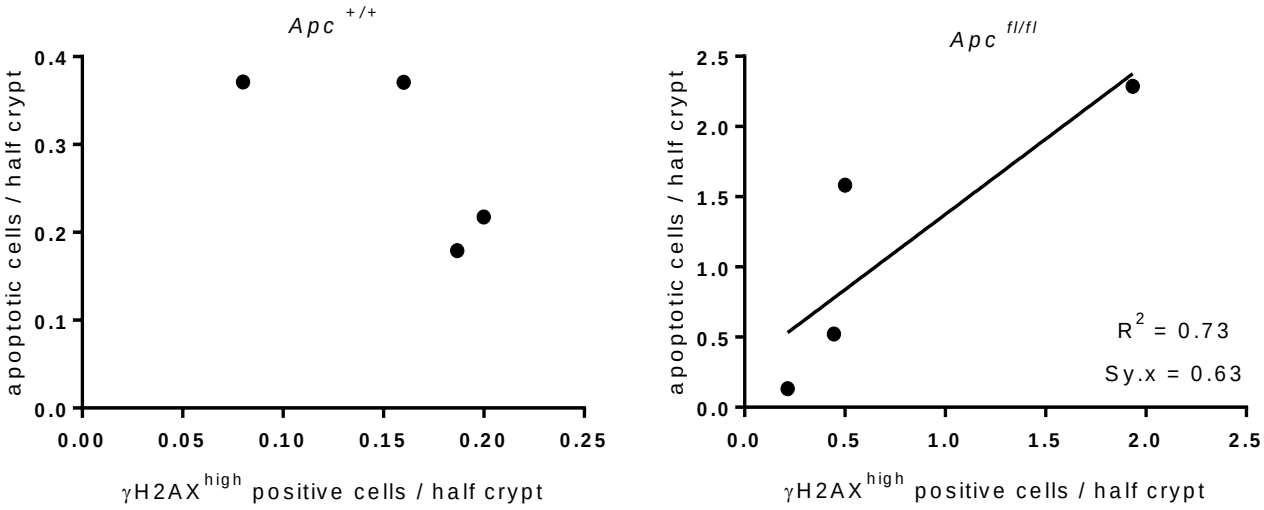

Figure 3.21 Correlation between γH2AX^{high} staining intensity and apoptosis in VilCre^{ER}Apc$^{fl/fl}$.

Linear regression analysis between the number of active caspase-3 and γH2AX^{high} positive cells / half crypt in the *VilCre^{ER}Apc$^{fl/fl}$* and *VilCre^{ER}Apc$^{+/+}$* mice for a course of 4 days p.i.. Points represent the mean values of each marker in each group of mice (> 50 half crypts / mouse, for *n* = 3 or 4 mice per group) for days 1 – 4 p.i.. One-tailed Spearman correlation test was performed. There was no correlation between the two markers for *VilCre^{ER}Apc$^{+/+}$* mice, as opposed to *VilCre^{ER}Apc$^{fl/fl}$* mice; * $p = 0.04$, SD of the residuals (Sy.x) = 0.63.

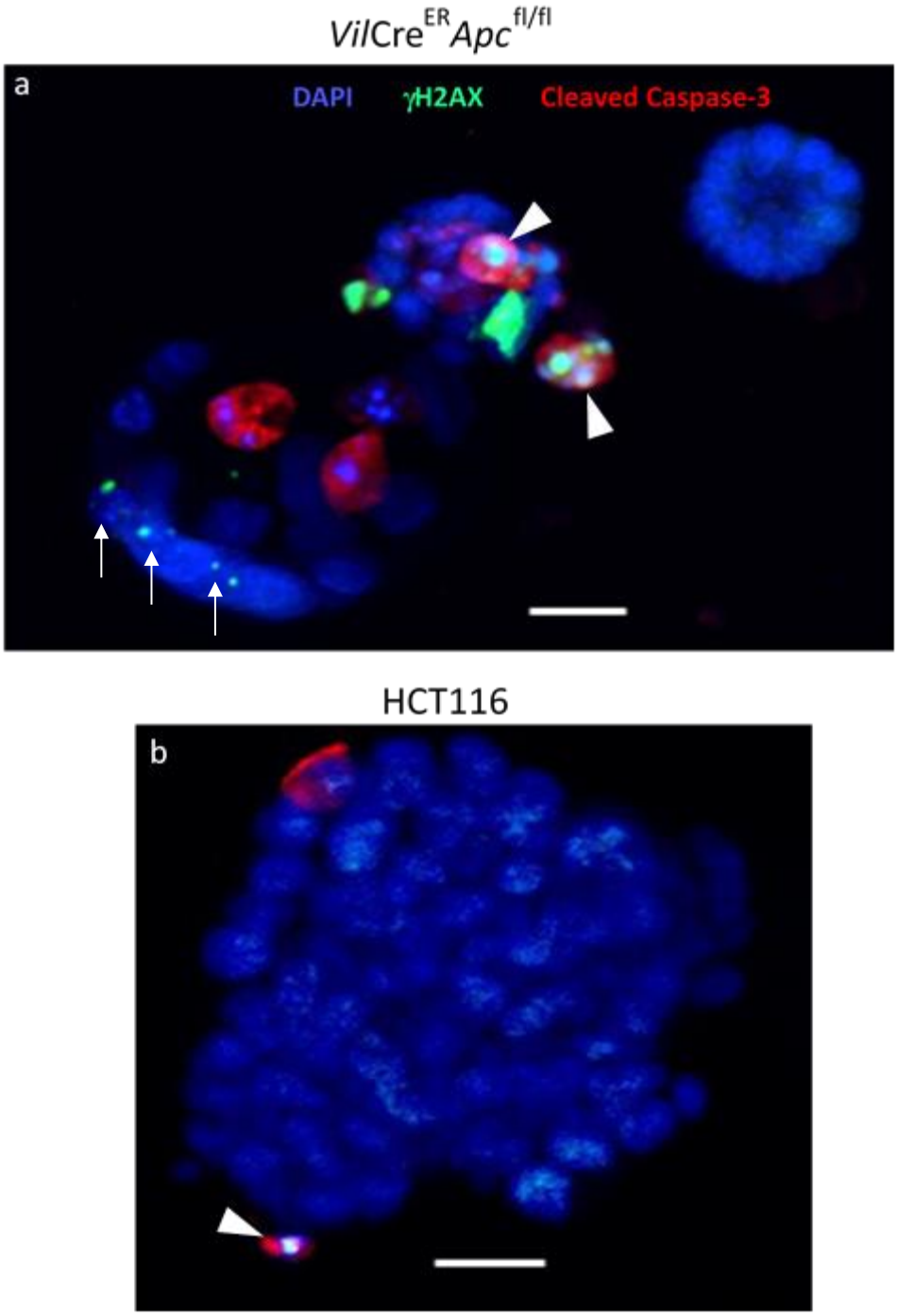

Figure 3.22 Colocalization of active caspase-3 with panuclear γH2AX staining

Whole mount immunofluorescence in (a) *Vil*Cre^{ER}*Apc*$^{fl/fl}$ and (b) HCT116 cell line-derived organoids, double-stained with fluorochrome-conjugated antibodies against cleaved caspase-3 (red) and γH2AX (green). DAPI (blue) was used for DNA staining. Maximum projection confocal images are shown. Arrow heads indicate cells co-stained with active caspase-3 and pan-nuclear γH2AX whereas small arrows show γH2AX foci. Scale bars, 20 µm.

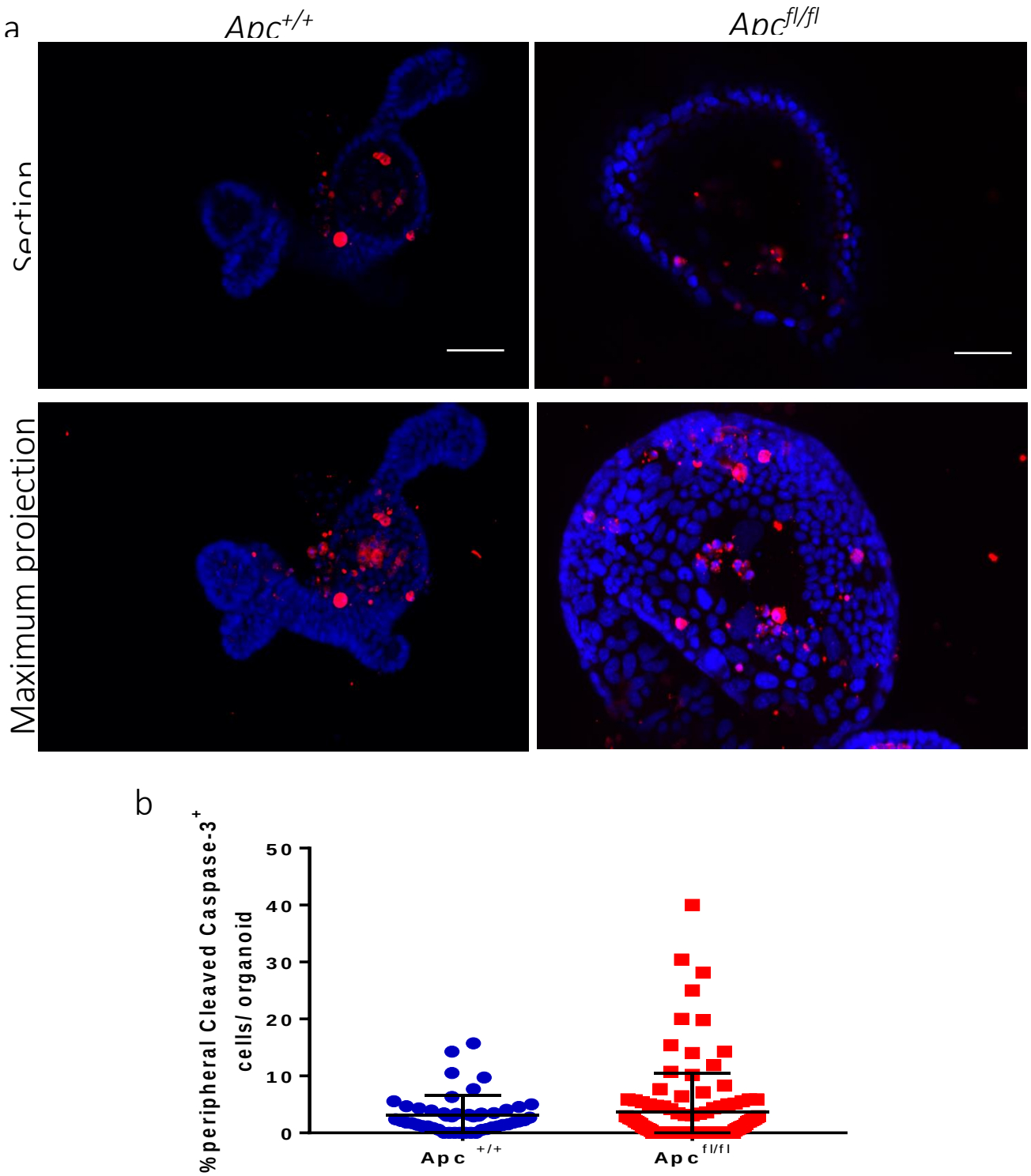

Figure 3.23 Apoptosis in VilCre^{ER}Apc$^{fl/fl}$ mouse derived organoids ex vivo.

Whole mount IF for apoptosis (cleaved caspase-3) in *VilCre^{ER} Apc$^{+/+}$* and *VilCre^{ER} Apc$^{fl/fl}$*, mice derived organoids, 3 days post seeding. (a) Representative sections and maximum projection images are shown. Scale bar = 50 µm (b) Percentage of peripheral cleaved caspase-3 positive cells per organoid was quantified. Mean percentage of 44 or 104 organoids / *VilCre^{ER} Apc$^{+/+}$* or *VilCre^{ER} Apc$^{fl/fl}$*, mouse respectively ± SD is represented with a horizontal line. Unpaired 2-tailed Mann Whitney test was performed; NS; $p > 0.05$. Biological replicates: n = 2 and n = 3 for the *VilCre^{ER} Apc$^{+/+}$* and *VilCre^{ER} Apc$^{fl/fl}$*, mice derived organoids, respectively.

3.3 Investigating the mechanisms by which *Apc* deficiency contributes to DNA damage

3.3.1 Recombination alone causes DNA damage

It was necessary to analyse whether the increase in DSBs following *Apc* loss was at least partly due to the Cre-LoxP-mediated recombination that was used to knockout exon 14 of the *Apc* gene. To investigate this, we induced *VilCre^{ER}*, *VilCre^{ER} Apc $^{fl/fl}$* and *VilCre^{ER} LacZ$^{fl/fl}$* mice with tamoxifen (80mg/kg) by oral gavage. The induction of the latter resulted in recombination of the *loxP* sites flanking the exogenous gene *LacZ,* which induced Cre-mediated recombination without excision of the *Apc* gene. 3 days p.i. mice were culled and the intestinal tissue was collected and fixed. Overall, induced *VilCre^{ER} LacZ$^{fl/fl}$* mice had a healthy intestinal structure similar to *VilCre^{ER}* mice, whereas *VilCre^{ER} Apc $^{fl/fl}$* mice had an expanded crypt area, as described in chapter 3. γH2AX IHC staining of small intestinal sections was performed and quantified (Figure 3.24). The percentage of γH2AX positive cells was similar but significantly higher in *VilCre^{ER} LacZ$^{fl/fl}$* mice when compared to *VilCre^{ER}*; but much higher in *VilCre^{ER} Apc $^{fl/fl}$* mice (Figure 3.24 b). Less than 9% of the *VilCre^{ER}* intestinal cells of the crypt have a background level of low γH2AX intensity, whereas cells with medium and high γH2AX intensity were rarely present (Figure 3.24 c - e). Induced *VilCre^{ER} LacZ$^{fl/fl}$* mice had significantly higher numbers of cells with medium and high γH2AX intensities, whereas *VilCre^{ER} Apc $^{fl/fl}$* mice had significantly more cells with low, medium and high γH2AX levels when compared to *VilCre^{ER} LacZ$^{fl/fl}$*. This data suggests that recombination of any gene would cause an increase in the number of γH2AX positive cells in the mouse small intestine, but deletion of the *Apc* gene causes the majority of the increased γH2AX expression in this model.

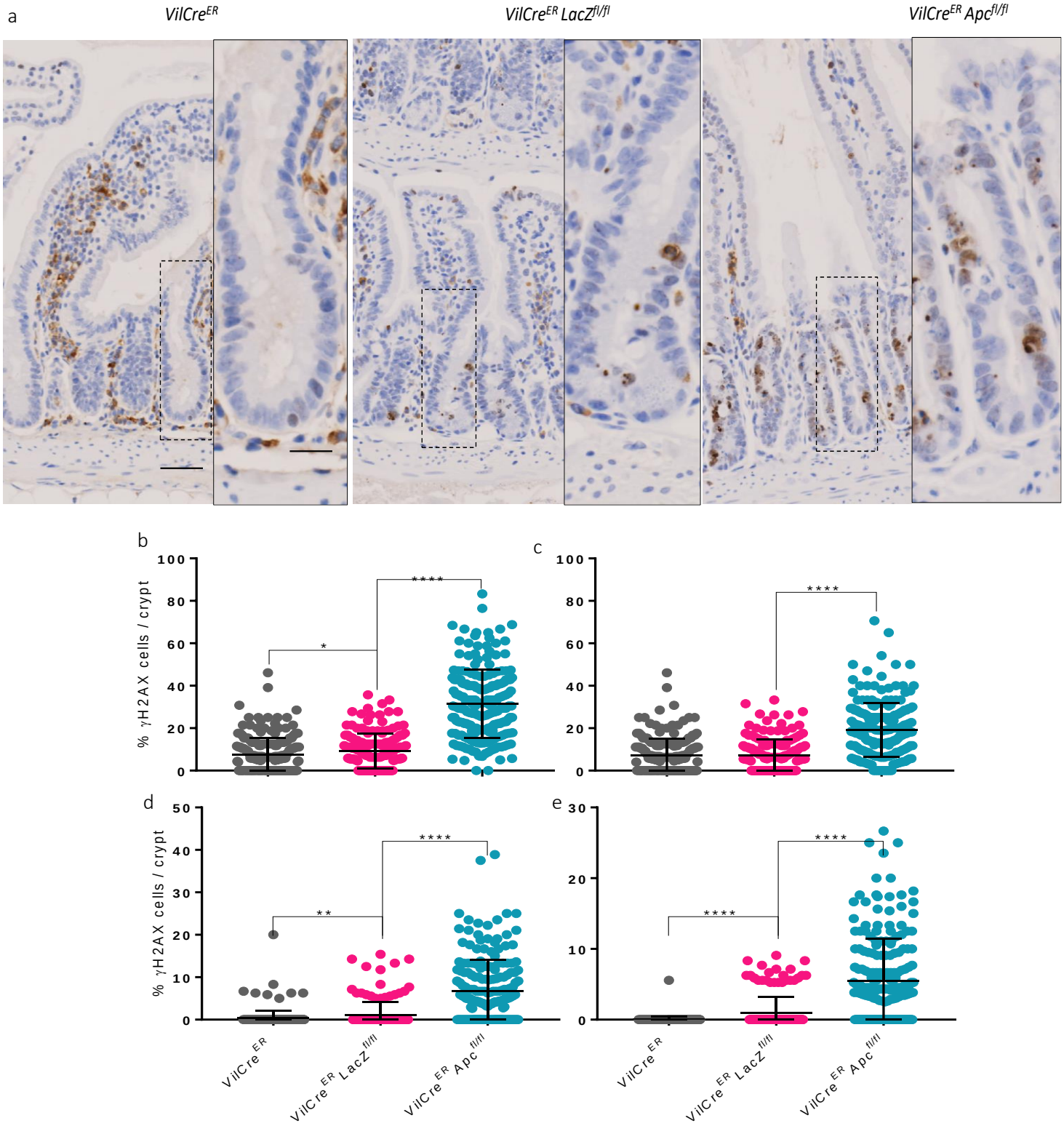

Figure 3.24 Apc loss induces higher DNA damage than LoxP site recombination alone in the small intestine

(a) Representative pictures of γH2AX staining performed on small intestinal sections of *VilCre*^{ER} (*n* = 4), *VilCre*^{ER} *LacZ*$^{fl/fl}$ (*n* = 3) and *VilCre*^{ER} *Apc*$^{fl/fl}$ (*n* = 4) mice, 3 days post oral induction with 80mg/kg of tamoxifen; scale bar = 50µm, inset scale bar = 20µm. (b – e) % of γH2AX positive cells per half crypt section are shown for (b) total, (c) low, (d) medium and (e) high γH2AX intensity cells. % of >50 half crypts per mouse ± SD are shown. Kruskal-Wallis multiple comparisons test was performed; *$p \leq 0.05$, **$p \leq 0.01$ and **** $p \leq 0.0001$.

3.3.2 Is *Apc* loss-induced DNA damage Wnt-driven?

Following the demonstration that *Apc*-deficiency in the *VilCre^{ER} Apc $^{fl/fl}$* mouse model causes increased γH2AX levels in cells of small intestinal crypts, we wanted to know whether this due to WNT signalling activation or *Apc* loss itself, possibly through its involvement in chromosomal segregation (K B Kaplan *et al.* 2001; Green and Kaplan 2003; R Fodde *et al.* 2001). In order to do this, we used archived intestinal samples from mice where Cre recombinase was expressed using the cytochrome P450 promoter (*AhCre)* instead of the *Villin* promoter. *AhCre Apc$^{fl/fl}$*, *AhCre Myc$^{fl/fl}$* and *AhCre Apc$^{fl/fl}$Myc$^{fl/fl}$* mice were induced with 3 doses of 80mg/kg of β-napthoflavone (βNF) each in a day and culled 4 days p.i.. Small intestinal tissue was fixed and IHC stained for γH2AX (Figure 3.25 a). Overall, induced *AhCre Myc$^{fl/fl}$* mice had a healthy intestinal structure, whereas *AhCre Apc $^{fl/fl}$* mice had an expanded crypt area, as previously described (Sansom *et al.* 2004), and similar to the phenotype of induced *VilCre^{ER} Apc $^{fl/fl}$* mice, as described in chapter 3. The intestinal structure of *AhCre Apc$^{fl/fl}$Myc$^{fl/fl}$* mice resembled those of wt, as previously described (Sansom *et al.* 2007). Levels of γH2AX were counted and the percentage of total cells with γH2AX positivity was similar for both *AhCre Apc$^{fl/fl}$* (n=4) and *AhCre Myc$^{fl/fl}$* mice (n = 1), whereas combined loss of *Apc$^{fl/fl}$* and *Myc$^{fl/fl}$* (n=3) resulted in less γH2AX positive cells (Figure 3.25 b). Crypts from *AhCre Apc$^{fl/fl}$Myc$^{fl/fl}$* mice had more cells with medium and high γH2AX intensities compared to *AhCre Apc$^{fl/fl}$*, and more cells with low γH2AX intensity when compared to *AhCre Myc$^{fl/fl}$* crypts. The latter had significantly less cells with medium γH2AX intensity than *AhCre Apc$^{fl/fl}$* crypts. The comparisons of γH2AX percentage in *AhCre Apc$^{fl/fl}$* or *AhCre Apc$^{fl/fl}$Myc$^{fl/fl}$* crypts with *AhCre Myc$^{fl/fl}$* might not be reliable because only one *AhCre Myc$^{fl/fl}$* mouse was analysed.

An alternative way to investigate whether activation of the WNT signalling pathway contributes to increased γH2AX levels and numbers of γH2AX positive cells, was to use the *AhCre β-catenin$^{fl/fl}$* and *AhCre Apc $^{fl/fl}$β-catenin$^{fl/fl}$* mouse models. We used archived samples from mice induced with 80mg/kg of βNF. 3 days p.i. mice were culled and small intestinal tissue was collected, fixed and IHC processed for γH2AX (Figure 3.26a). Intestinal structures in both genotypes were comparable to wt. However, quantification of γH2AX staining in crypts of the small intestine showed that combined deficiency of *Apc $^{fl/fl}$* and β-*catenin$^{fl/fl}$* contributed to approximately 2-fold increase in the percentage of γH2AX positive cells compared to *β-catenin$^{fl/fl}$* deficiency alone. This was a result of significant increase in the percentage of cells with low and medium γH2AX staining intensities. Unfortunately, there were no historical samples available to compare this data with *AhCre Apc$^{fl/fl}$* mice at 3 days p.i..

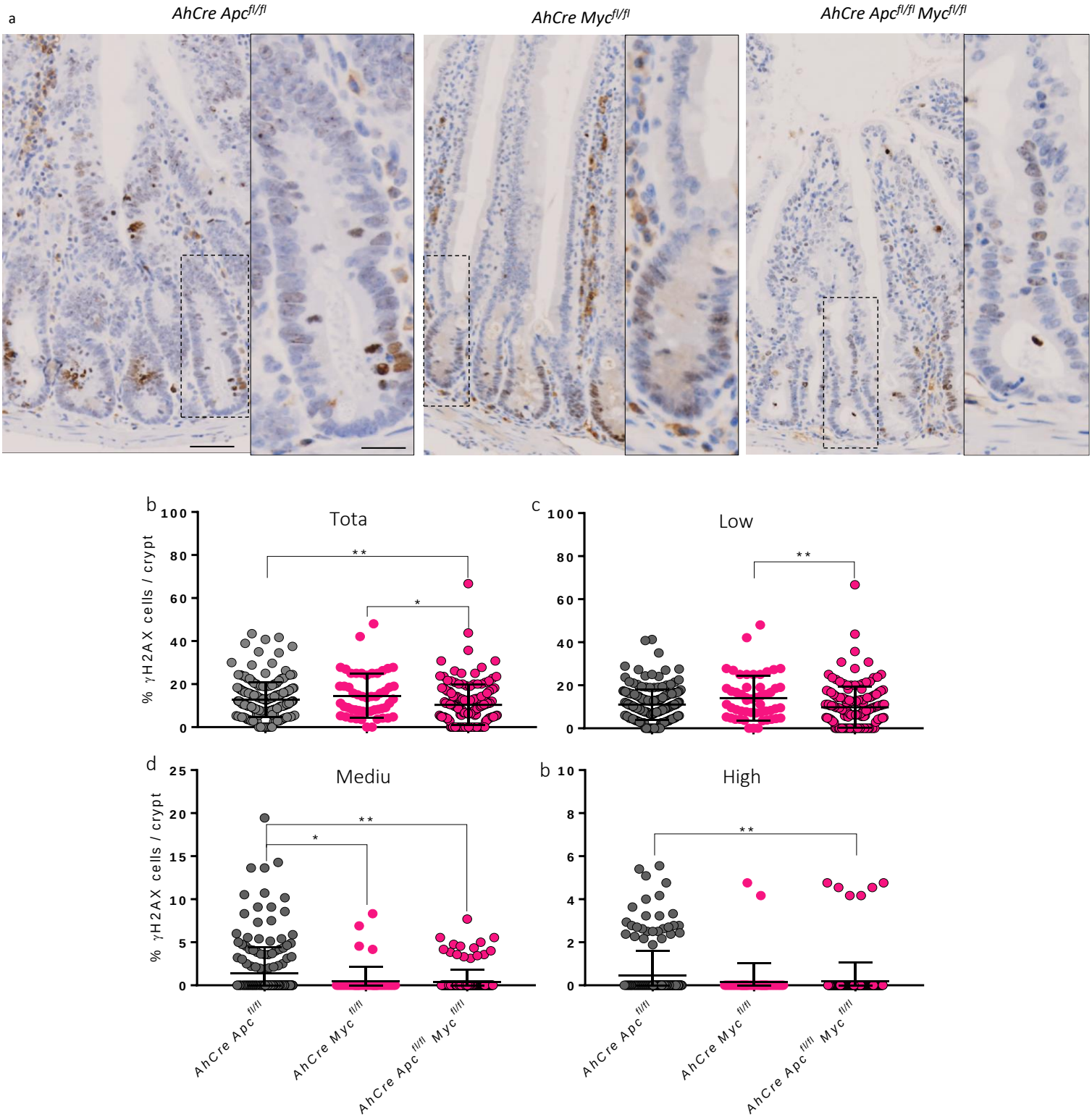

Figure 3.25 Apc loss-related γH2AX increase partly contributed to increased c-Myc.

(a) γH2AX staining was performed on small intestinal sections of *AhCre Apc*$^{fl/fl}$ (n = 4), *AhCre Myc*$^{fl/fl}$ (n = 1) and *AhCre Apc*$^{fl/fl}$ *Myc*$^{fl/fl}$ (n = 3) mice 4 days post IP injection with 80 mg / kg of β-napthoflavone (βNF); scale bar = 50μm, inset scale bar = 20μm. (b – e) % of γH2AX positive cells per half crypt section are shown: (b) total, (c) low, (d) medium and (e) high γH2AX intensity cells. % of >50 half crypts per mouse ± SD are shown. Kruskal-Wallis multiple comparisons test was performed; *p≤0.05 and **p≤0.01.

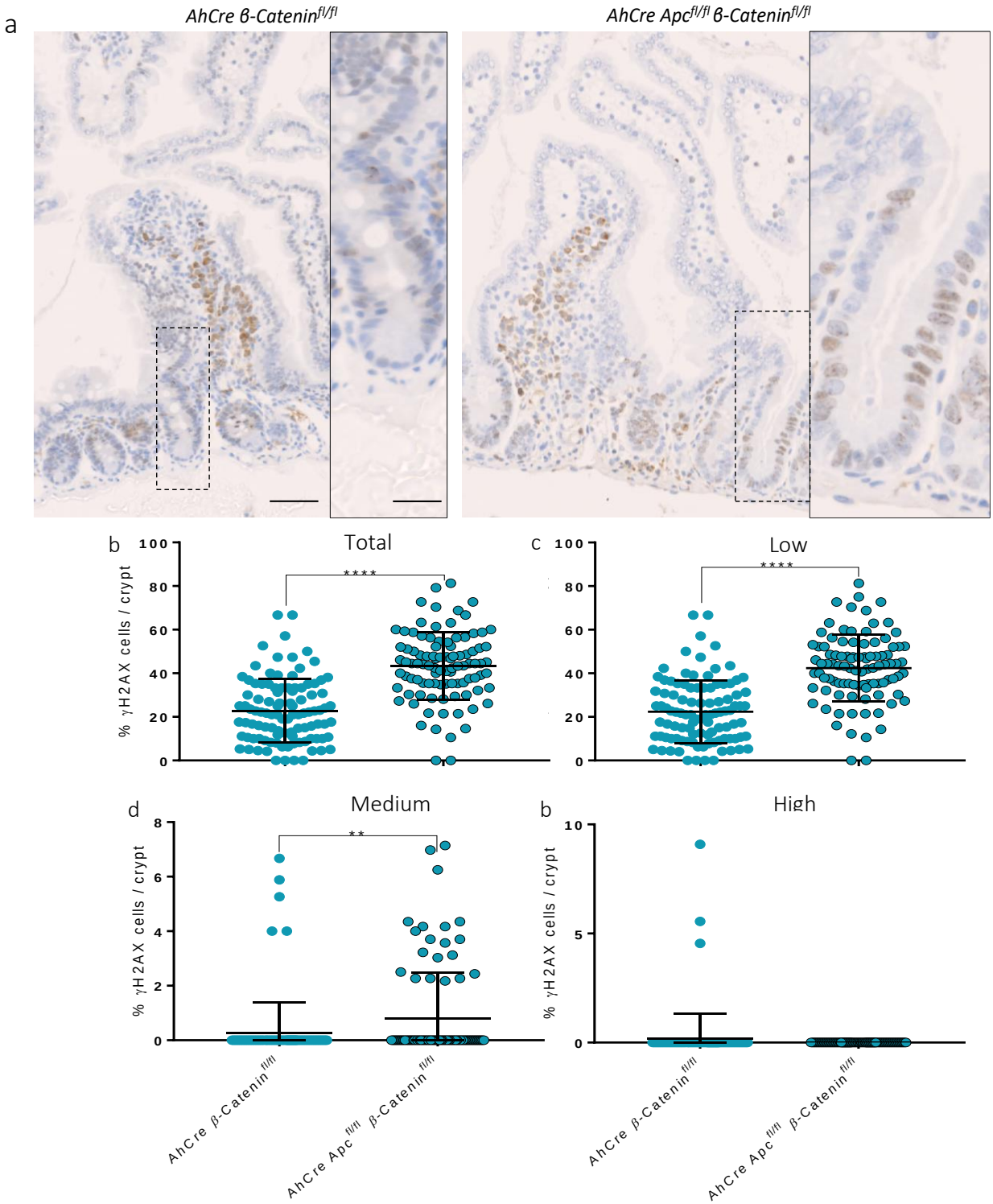

Figure 3.26 Deficiency of both β-Catenin and Apc contribute to higher γH2AX levels compared to β-Catenin deficiency alone.

(a) γH2AX staining was performed on small intestinal sections of *AhCre β-Catenin*$^{fl/fl}$ (n = 2) and *AhCre Apc*$^{fl/fl}$ *β-Catenin*$^{fl/fl}$ (n = 2) mice, 3 days post ost IP injection with 80 mg / kg of β-napthoflavone (βNF); scale bar = 50µm, inset scale bar = 20µm. (b – e) % of γH2AX positive cells per half crypt section are shown: (b) total, (c) low, (d) medium and (e) high γH2AX intensity cells. % of >50 half crypts per mouse ± SD are shown. Two-tailed Mann-Whitney test was performed; **p≤0.01, **** p≤0.0001)

3.3.3 LGR5⁺ intestinal stem cells often have higher γH2AX levels compared to non-stem cells

To investigate further the γH2AX levels of the LGR5⁺ stem cell population in *Apc*-proficient and -deficient small intestines, we used the *Lgr5-EGFP VilCre^{ER}Apc$^{fl/fl}$* mouse model. Single cells isolated from crypts of *Lgr5-EGFP VilCre^{ER}Apc$^{fl/fl}$* and *Lgr5-EGFP VilCre^{ER}Apc$^{+/+}$* mice 4 days p.i., were analysed by FACS, as shown in (Figure 2.6). *Lgr5-EGFP VilCre^{ER}Apc$^{fl/fl}$* mice had approximately 3-fold higher percentage of EGFP positive cells compared to *Lgr5-EGFP VilCre^{ER}Apc$^{+/+}$*, although these data were not significantly different. Subsequently, the percentage of LGR5⁺ cells stained with low or high γH2AX fluorescent intensities were analysed for both genotypes (Figure 3.27). The *Apc*-deficient LGR5⁺ population had significantly more cells with high γH2AX fluorescence and there was also a non-significant trend for more cells with low γH2AX intensities.

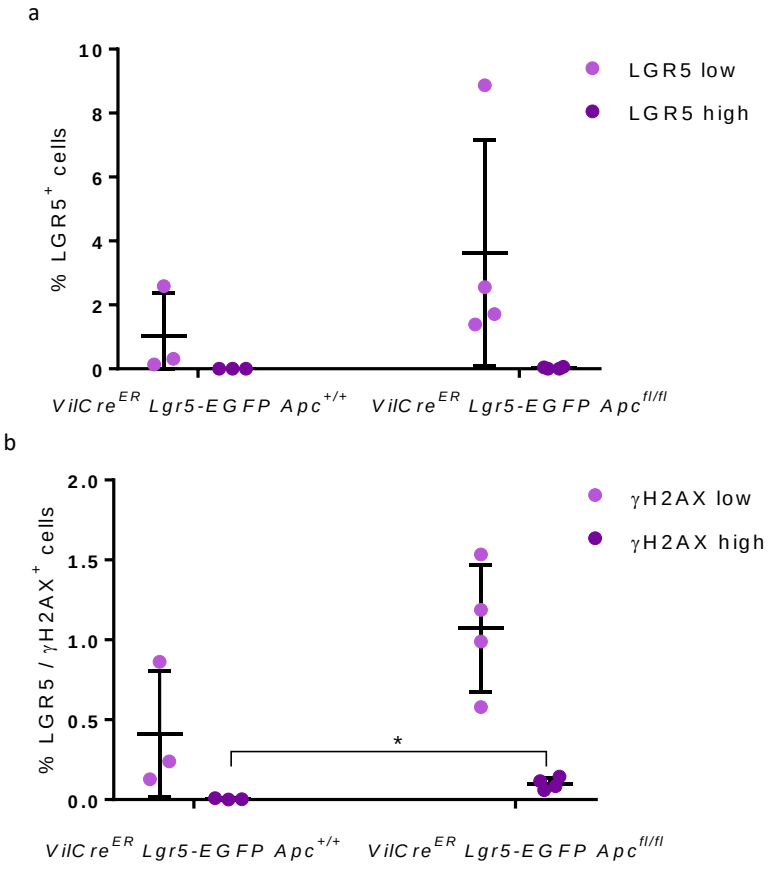

Figure 3.27 γH2AX levels in Apc proficient or deficient LGR5⁺ stem cells.

VilCre^{ER}Lgr5-EGFP Apc$^{+/+}$ and *VilCre^{ER}Lgr5-EGFP Apc$^{fl/fl}$* mice were IP injected with 80mg/kg of tamoxifen for four consecutive days. Mice were sacrificed 4 days post induction and 15 cm of small intestine were isolated. Single cell murine epithelial cells were yielded and intracellularly stained for γH2AX for FACS analysis. (a) % of LGR5-GFP low or high intensity positive cells (b) % of LGR5 and γH2AX double positive cells with low or high γH2AX levels. Error bars indicate SD; *Apc$^{+/+}$* and *Apc$^{fl/fl}$* n = 3 and 4 respectively; One-tailed Mann Whitney test; * $p \leq 0.05$.

3.4 Discussion

Malignant cells are genomically unstable, their genomic instability is usually driven by oncogene activation or tumour suppressor gene dysfunction (Rao and Yamada 2013; Halazonetis *et al.* 2008). Loss of *Apc* leads to DNA damage formation, possibly through c-MYC oncogene activation, that contributes to excessive cell proliferation and replication fork stalling (Robinson *et al.* 2009), or directly through the inability of microtubules to interact with APC for efficient chromosomal segregation (Fodde *et al.* 2001; Kaplan *et al.* 2001; Green and Kaplan 2003; Green *et al.* 2005).

DSBs are the most dangerous form of DNA damage and are recognised by the DDR pathway. ATM is the first mediator of this pathway, is activated immediately upon the formation of a DSB and directly contributes to the phosphorylation/ activation of other components of the DDR pathway, including H2AX and CHK1. Activated CHK1 halts cell cycle progression and also activates RAD51, a component of the HR DNA repair pathway. ATM, γH2AX and RAD51 are used as DSB markers; ATM and γH2AX detect cells with DSB formed throughout the cell cycle, whereas RAD51 is only activated in those generated during cell division (Wang *et al.* 2014).

Previous studies in both embryonic stem cells and HCT116 human colon cancer cells have demonstrated the importance of APC in chromosomal segregation by its attachment to the microtubule spindle and chromosomal segregation (Fodde *et al.* 2001; Kaplan *et al.* 2001; Green and Kaplan 2003; Green *et al.* 2005). Two studies have also provided evidence that *Apc* loss contributes to DNA damage *in vivo*. Reed *et al.* (2008) used the *AhCreApc*$^{fl/fl}$ mouse model to show that *Apc* deficiency increased *H2AX* mRNA expression in intestinal cells, while Méniel *et al.* (2015) used the same model to show that *Apc* deficiency induced the DNA damage checkpoint proteins p53 and p21 in the mouse liver, due to increased levels of DSBs, as quantified by IHC for γH2AX and RAD51.

In this chapter, our aim was to investigate in detail the *in vivo* effects of *Apc* loss within the murine intestinal epithelium with respect to DNA damage markers, to provide the necessary background information for targeting such damaged cells with an anti-H2AX antibody. We used *VilCre*^{ER}*Apc*$^{fl/fl}$ and *Lgr5Cre*^{ER} *Apc*$^{fl/fl}$ mice to induce *Apc* deficiency in the small intestinal epithelium and in the intestinal LGR5^{+} stem cells, respectively, in order to visualize and quantify DNA damage using ATM, γH2AX and RAD51 DSB markers and to determine the levels of apoptosis caused upon *Apc* loss. The hypothesis was that *Apc* loss in the murine intestinal epithelium would contribute to DNA damage, either directly or indirectly.

3.4.1 Intestinal *Apc* deficiency increases endogenous DNA damage levels in the small intestine of dysplastic (*VilCre^{ER} Apc$^{fl/fl}$*) CRC mouse model.

Nuclear ATM activation has been linked with DDR and senescence (Pospelova *et al.* 2009; Pankotai *et al.* 2009), whereas cytoplasmic staining has been associated with ROS-induced ATM activation (Kozlov *et al.* 2016). Perinuclear phospho-Ser^{1981}ATM staining was previously observed in a study where irradiated cells were treated with hypertonic medium which inhibited DSB rejoining (Reitsema *et al.* 2005). Before describing the data relevant to pATM staining, it is important to note that IHC staining was performed without the negative control to test for non-specific binding of the anti-mouse secondary antibody on the sections; hence, the significance of this part of data should be taken with caution.

The majority of crypt cells with pATM staining had perinuclear staining regardless of the genotype (Figure 3.15 a). The reason for this particular localization remains unknown; however we can hypothesize that the sequestration of pATM away from the DNA can affect the resolution of DNA breaks. The few nuclear pATM stained crypt cells were significantly higher in *Apc$^{+/+}$* crypts compared to *Apc$^{fl/fl}$* (Figure 3.15 b), which could signify that either *Apc$^{+/+}$* cells have more DNA damage compared to *Apc$^{fl/fl}$*, which is unlikely according to the literature (Fodde *et al.* 2001; Kaplan *et al.* 2001) or that *Apc$^{fl/fl}$* cells might not be able to efficiently use pATM for the recognition and repair of possible DNA damage. In contrast to these speculations is the fact that, *Apc$^{fl/fl}$* crypts had significantly higher percentage of cells with both nuclear and perinuclear staining compared to *Apc$^{+/+}$* (Figure 3.15 c). Nonetheless, more experiments need to be performed in order to identify the protein levels of pATM in cells of each staining pattern (nuclear, perinuclear or both), from both genotypes, and their efficiency in repairing DNA damage. In addition, due to the low frequency of cells with nuclear or both nuclear and perinuclear staining in the small intestinal crypts, a higher number of crypts (> 50 half crypts/ mouse) should be quantified in order to clarify the importance of these staining patterns.

VilCre^{ER}Apc$^{+/+}$ crypt cells with pATM staining, mainly perinuclear, predominantly resided in +3 cell positions from the crypt base (Figure 3.14), which could mark a specific cell population of the crypt. In contrast, *VilCre^{ER}Apc$^{fl/fl}$* crypts had a different and broader pattern of predominantly perinculear pATM cell positioning (usually at +1 to +4, +7 and +8 crypt cell positions). This could be due to the expansion of the crypt area and the decrease in the ability of cells to differentiate (Sansom *et al.* 2004) which reiterates the results of abnormal tissue homeostasis and cell migration along the crypt-villus axis and increase the likelihood of *Apc$^{fl/fl}$* cells to outcompete *Apc$^{+/+}$* cells (Suijkerbuijk *et al.* 2016).

Apc loss in the intestinal epithelium of the *VilCre^{ER}Apc$^{fl/fl}$* mouse model (induced by IP injection) increased the number of cells with γH2AX, hence DNA DSB, as early as 2 days p.i. and up to 4 days p.i. (which is the average life span of this mouse model; Figure 3.4a). Total crypt cell number was higher due to increased proliferation of pre-neoplastic *Apc$^{fl/fl}$* cells throughout the time course (Figure 3.3); hence, the increase in the number of cells with γH2AX staining was attributed to the overall increase in the crypt cell compartment (Figure 3.4b). Although the percentage of total γH2AX positive cells remained unchanged regardless of the genotype or day p.i., the extent of DNA damage (measured by low, medium or high γH2AX intensity) on days 3 and 4 p.i. by IP injection was significantly higher in *VilCre^{ER}Apc$^{fl/fl}$* compared to *VilCre^{ER}Apc$^{+/+}$* mice, which was most probably caused by direct or indirect effects of APC loss and not by increased crypt cell number (Figure 3.6).

It was necessary to identify the day post induction that resulted in similar, high levels of γH2AX following oral administration in order to adjust the animal experiment performed at Oxford accordingly. IHC counting of γH2AX within the proximal small intestine showed that on day 3 p.i. there were similar, but not the same, numbers of γH2AX-positive cells within the crypt following either gavage or IP injections. Albeit IP injection generally resulted in a slightly higher γH2AX staining levels compared to oral gavage, the latter technique resulted in the further separation of γH2AX staining levels between the two groups (*Apc$^{+/+}$* and *Apc$^{fl/fl}$*; Figure 3.7 c). Hence, when tamoxifen was administered in mice by oral gavage, the percentage of γH2AX positive cells at day 3 p.i. was significantly higher in *Apc*-deficient cells compared to *Apc*-proficient cells (Figure 3.10).

Furthermore, IHC staining intensity can be used only as a semi-quantitative approach because it cannot be directly related to the extent of DNA damage and it is very difficult to identify foci. Using IF and the nuclear γH2AX foci quantification (Figure 3.11), it was demonstrated that there were significantly increased numbers of cells with γH2AX foci in IP-induced *VilCre^{ER}Apc$^{fl/fl}$* mice compared to *VilCre^{ER}Apc$^{+/+}$*, supporting the interpretation that oral induction of recombination is magnifying differences between the *Apc$^{fl/fl}$* and *Apc$^{+/+}$* models which are already present, rather than having a different biological effect.

γH2AX^{+} cell number quantification in *VilCre^{ER}Apc$^{+/+}$* and *VilCre^{ER}Apc$^{fl/fl}$* derived intestinal organoids recapitulated the *in vivo* results (Figure 3.12, Figure 3.10a and Figure 3.11). This suggested that the increase in the number of cells with DNA damage in organoids was not a result of DNA DSB formation at LoxP sites being recombined by Cre activity, because the loxP flanked *Apc* exon was recombined *in vivo,* and also because the *VilCre^{ER}Apc$^{fl/fl}$* organoid culture media did not allow the growth of non-recombined *VilCre^{ER}Apc$^{fl/fl}$* cells, due to lack of R-

SPONDIN, which supports WNT signalling activation and cell survival. Therefore, cells growing under these conditions must already have recombined the loxP-flanked exons prior to plating. Although Cre recombinase is expressed continuously, it could not create new DNA breaks in recombined cells with a single remaining loxP site while growing in culture. Hence, the agreement between *in vivo* and *ex vivo* results, imply that *Apc*-deficiency contributes to increase in DNA damage.

Apc-deficient cells employ the HR pathway to repair at least a portion of the DSBs caused in dividing cells, as evidenced by an increase in $RAD51^+$ crypt cells (Figure 3.17). Moreover, apoptosis is one of the biological processes which is disturbed after APC loss of function, which hyperactivates WNT signalling and leads to c-MYC induced expression of pro-apoptotic proteins (Askew *et al.* 1991; Dang 1999). APC is also linked to aberrant mitotic spindle formation and polyploidy (Dikovskaya *et al.* 2007) which might lead to aberrant mitosis and mitotic catastrophe-induced apoptosis through a p53-independent mechanism (Merritt *et al.* 1997). Unrepaired DNA damage can also lead to cell death by apoptosis *via* p53 (Rogakou *et al.* 2000). Our data showed that apoptosis is induced in *Apc*-deficient cells on days 3 and 4 p.i. (Figure 3.19),as previously described (Sansom *et al.* 2004), and that γH2AX pan-nuclear staining could mark apoptotic cells (Figure 3.22), as demonstrated in previous studies (Bonner *et al.* 2008; Solier and Pommier 2014). Due to the fact that this mouse model has a short lifespan we could not assess whether the apoptotic index in those organoids eventually reverts back to basal levels. Interestingly, apoptosis in *ex vivo* growing organoids was independent of *Apc* status (Figure 3.23), probably because *Apc*-proficient organoids were constantly supplied by R-SPONDIN which kept the WNT signalling pathway levels high. This could imply that apoptosis in wt organoids *in vitro* was artificially elevated because of the need to add R-SPONDIN. Another possible explanation for this results could be the fact that apoptosis induction in *Apc*-deficient cells requires the cooperation of the immune system, which is absent from the cell culture system; therefore, *Apc*-deficient organoids might have artificially low apoptosis in culture. Lastly, a combination of both could also explain these results.

3.4.2 Investigating the mechanisms by which *Apc* deficiency contributes to DNA damage

Apc-deficient small intestine had more $LGR5^+$ stem cells than *Apc*-proficient intestine, because normal intestinal cell differentiation was abolished (Sansom *et al.* 2004). Moreover, *Apc*-deficient $LGR5^+$ stem cells were more prone to DNA damage when compared to normal $LGR5^+$ stem cells.

To exclude the possibility that increased DSBs in crypt cells following *Apc* loss was due to the Cre-LoxP recombination itself, we knock-out the exogenous *LacZ* gene using the *VilCre^{ER} LacZ$^{fl/fl}$* mouse model. This resulted in more crypt cells with DNA damage, often at higher levels, as indicated by more intense γH2AX staining, compared to wt (*VilCre^{ER}*; Figure 3.24). However, the number of cells with DNA damage was significantly lower than in *Apc*-deficient intestine, which indicates that although recombination itself induces some level of DNA damage 3 days p.i. in the *VilCre^{ER} Apc$^{fl/fl}$* mice, additional high levels of damage are caused by deficiency of the particular gene, *Apc.* Interestingly, even wt cells had a background percentage of crypt cells positive, mainly, for low levels of DNA damage (< 9%), which is probably due to the rapid turnover of cells within this tissue (Darwich *et al.* 2014) as well as general repair of endogenous damage. It is worth noting that *VilCre^{ER}Apc$^{fl/fl}$*-derived intestinal organoids after 2 passages had retained the increased DNA damage levels when compared to wt (Figure 3.10) suggesting that *Apc*-deficiency, and not only recombination of loxP sites, contributes to the increase in DNA damage.

Our next step involved examining whether this increase was a result of WNT signalling activation or due to *Apc* gene loss itself, which is known to be involved in chromosomal segregation (Green and Kaplan 2003; R Fodde *et al.* 2001; K B Kaplan *et al.* 2001). This was assessed in two ways; the first combined deficiency of *Apc* and *c-Myc*, a target gene of the WNT signalling pathway, which restored the *Apc* loss-associated crypt-progenitor like phenotype (Figure 3.25a; Sansom *et al.* 2007) and reduced the percentage of cells with medium or high levels of DNA damage (Figure 3.25 b). This may imply that DNA damage is a result of WNT signalling pathway activation and, more specifically, of *c-Myc* transcription, either through excess proliferation and replication fork collapse (Robinson *et al.* 2009) or generally through oncogene-mediated DNA damage formation (Halazonetis *et al.* 2008).

The second approach combined *Apc* and *β-catenin* deficiency. β-CATENIN is the essential regulator of transcription of canonical WNT signalling target genes, hence even in the absence of functional APC, the absence of β-CATENIN does not allow activation of the canonical WNT pathway. Therefore, combined deficiency of *Apc* and *β-catenin* contributed to approximately a 2-fold increase in the number of γH2AX positive cells compared to *β-catenin* deficiency alone. These results can be interpreted as *Apc*-deficiency contributing to an additional increase in DNA damage on top of that caused by *β-catenin* loss. Due to the fact that both APC and β-CATENIN are involved in chromosomal segregation through mitotic spindle attachment and protection from genomic instability (R Fodde *et al.* 2001; Aoki *et al.* 2007), it might be expected that

combined deficiency of both would increase damage when compared to single *β-catenin* deficiency.

On the other hand, this data contradicts the result of combined *c-Myc* and *Apc* deficiencies, with regard to increased DNA damage through canonical WNT signalling activation. Nevertheless, *c-Myc* transcription can be activated through other pathways besides canonical WNT signalling, such as PI3K/AKT and MAPK (Zhu *et al.* 2008). Also, it is not yet explored whether non-canonical WNT signalling can activate *c-Myc* transcription, as most work has been done on cytoskeleton and cell movements rather than target gene expression (Wallkamm *et al.* 2016).

3.5 Summary

The hypothesis that *Apc* deficiency drives DDR was supported by γH2AX nuclear accumulation in *Apc*-deficient dysplastic crypts. *Apc*-deficient cells employ the HR pathway, evidenced by increased number of RAD51 positive cells, to repair at least a portion of DSBs caused in dividing cells. Although the Cre-LoxP recombination technique used to excise *Apc* in *VilCre^{ER} Apc$^{fl/fl}$* mice induced some DNA damage, the majority was caused by deficiency of the *Apc* gene, most likely generated through WNT signalling pathway activation and more specifically, by *c-Myc* transcription. However, we cannot eliminate the possibility that increased DNA damage by *Apc*-deficiency is also caused by APC loss of function related to microtubule spindle binding and chromosomal segregation (Green *et al.* 2005; K B Kaplan *et al.* 2001).

This chapter showed evidence that *Apc*-deficient murine LGR5$^+$ stem cells had more DNA damage than wt, which led to the hypothesis that tumours originating from *Apc*-deficient LGR5$^+$ stem cells would also have increased DNA damage levels. This study is described in chapter 5.

4. *Apc* status influences the DNA damage repair pathway in the tumour CRC mouse model (*Lgr5Cre^{ER}Apc$^{fl/fl}$*)

4.1 Introduction

Although the *VilCre^{ER}Apc$^{fl/fl}$* mouse model is useful in studying the effects of *Apc* deficiency in the intestine due to the rapid transformation of a large part of the tissue and the intense dysplastic phenotype that follows loss of the gene (chapter 3), it does not reflect the random sporadic tumourigenic events occurring in patients initiated by transformation of a single cell (Barker *et al.* 2009). Therefore, the *Lgr5Cre^{ER}Apc$^{fl/fl}$* tumour mouse model was also used, as *Apc* deficiency can be induced specifically in the intestinal stem cell compartment, leading to adenoma formation which is more clinically relevant (Barker *et al.* 2009). This model allows the investigation of different developmental stages of cancer, i.e. from early/dysplastic up to small and large adenoma formation. In this chapter, we visualised and quantified DNA damage in detail in the intestines of mice where *Apc* has been deleted using the stem cell-specific promoter *Lgr5Cre^{ER}* in order to investigate the hypothesis that *Apc* deficiency leads to DNA damage.

4.2 DNA damage levels in *Apc*-deficient tumour CRC mouse model (*Lgr5Cre^{ER}Apc$^{fl/fl}$*)

4.2.1 Wnt signalling activation in lesions of the *Lgr5Cre^{ER}Apc$^{fl/fl}$* mouse model

To investigate γH2AX levels upon *Apc* deficiency in the intestinal stem cell compartment, IF and IHC analyses were performed in this model prior to and after tumour formation. WNT signalling activation can be observed by IHC for nuclear β-catenin. Therefore, to track WNT signalling hyperactivation occurring post *Apc* deletion in the intestinal stem cell compartment, mice were culled at various time points (days 4 – 6, 9, 12, 15, 27, 33) after induction. Small and large intestines were stained for β-catenin, as shown in Figure 4.1 and Figure 4.2, respectively. At days 4 and 5 there were single cells positive for nuclear β-catenin in both small and large intestines (Figure 4.1 a and b respectively). At days 6 and 9 clusters of nuclear β-catenin positive cells were present in otherwise phenotypically normal intestinal structures (Figure 4.1 c and d respectively). From day 12 p.i. small lesions were present which were positive for nuclear β-catenin and at days 27 and 33 larger lesions (adenomas) were also visible (Figure 4.1 e - h).

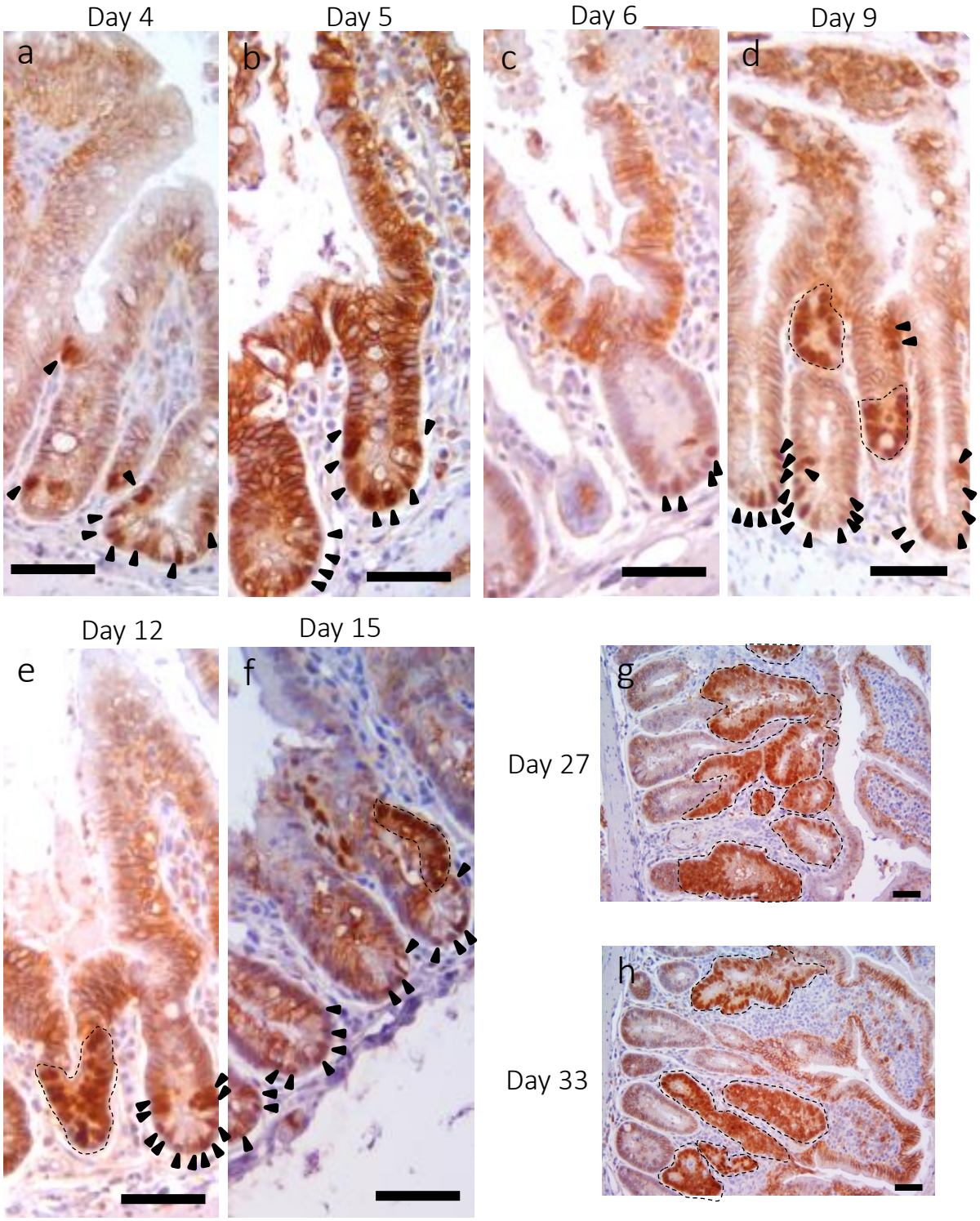

Figure 4.1 Immunohistochemical staining for β-catenin in the Lgr5Cre^{ER} Apc$^{fl/fl}$ small intestine over a time course post induction.

Paraffin sections of 24h 10% formalin-fixed small-intestinal rolls were immunostained. Brown stain indicates β-catenin presence; nuclear stain signifies stabilised β-catenin and WNT targeted gene transcription. Images captured under bright field microscope, scale bar = 50µm, n = 1 for each time-point.

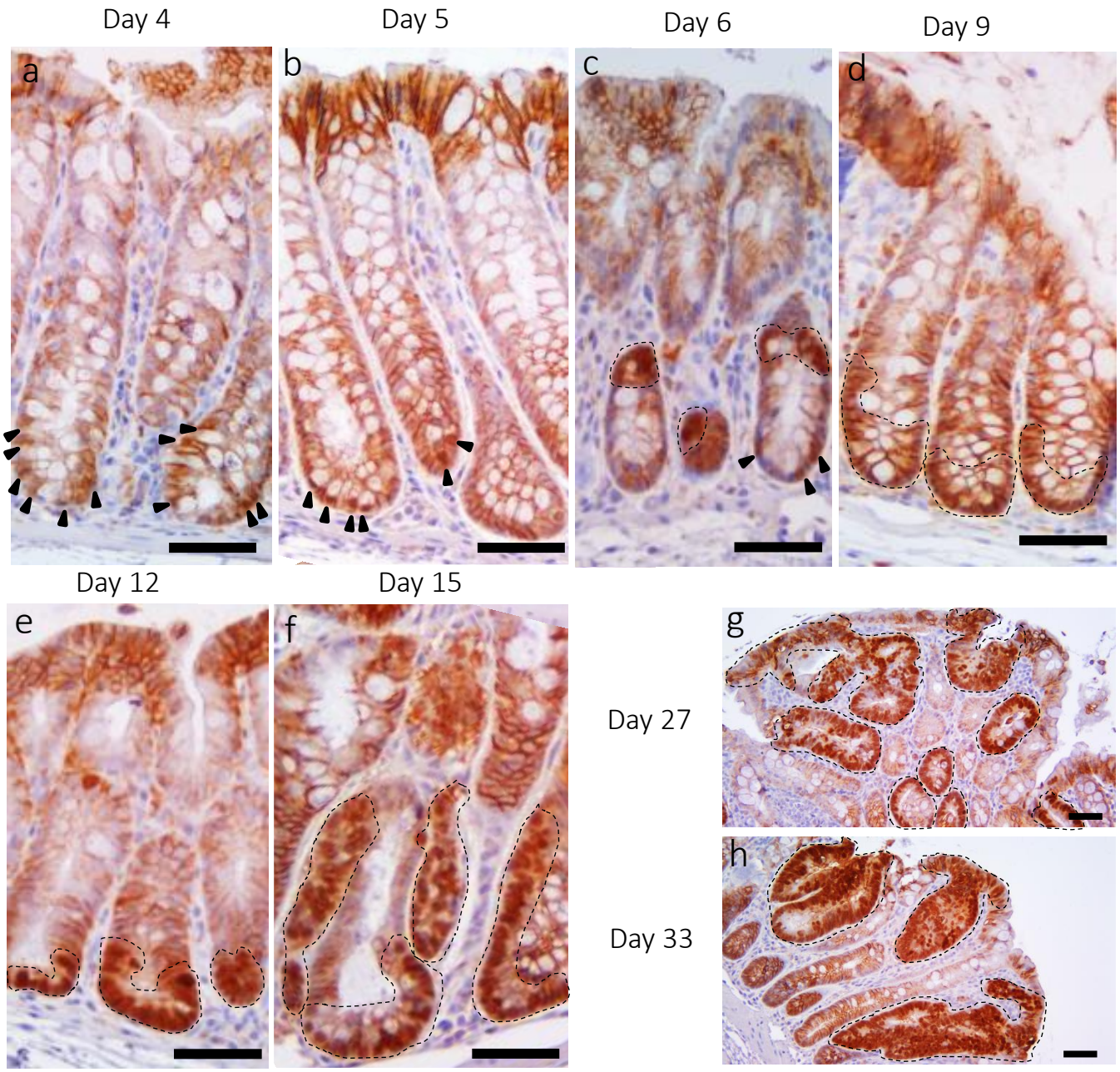

Figure 4.2 Immunohistochemical staining for β-catenin in the Lgr5Cre^{ER} Apc$^{fl/fl}$ large intestine over a time course post induction.

Paraffin sections of 24h 10% formalin fixed large-intestinal rolls were immunostained. Brown stain indicates β-catenin presence; nuclear stain (arrowheads) signifies stabilised β-catenin and WNT targeted gene transcription. Images captured under bright field microscope, scale bar = 50µm, n = 1 for each time-point.

4.2.2 Quantification of γH2AX levels in lesions of the *Lgr5Cre^{ER}Apc$^{fl/fl}$* mouse model

Early after *Apc* deficiency, the levels of DNA damage within the small intestine were quantified. *Lgr5Cre^{ER}Apc$^{fl/fl}$* mice were orally administered with tamoxifen (80mg/kg for 4 days) and humanely killed at days 0, 5, 6 and 9 p.i.. Small intestinal sections were stained for γH2AX (Figure 4.3) by IF in order to identify any small differences in the cell number with γH2AX foci, as γH2AX positive cells were more discretely stained when identified using this technique compared to IHC. Although more biological replicates will be required to fully validate the IF pattern for days 5 and 9 p.i., there is an indication that more γH2AX foci are observed in the crypts early post induction compared to non-induced (day 0 p.i.) samples.

Quantification of γH2AX positive cells was carried out as in Figure 2.3 for single crypt lesions, microadenomas, small adenomas and large adenomas of the small and large intestines (Figure 4.4). Small and large intestines of mice 50 days p.i., had 11.9±3.6% and 8.7±4.0% of γH2AX positive cells/ lesion, respectively (Figure 4.5 a). Generally, small intestines had a significantly higher % of γH2AX positive cells in single crypt lesions and microadenomas when compared to the large intestines. γH2AX percentage was proportional to the stage of the lesion, being higher in more advanced compared to early lesions (Figure 4.5 b). In the small intestine, large adenomas had significantly higher levels of γH2AX positive cells compared to single crypt lesions. Similarly, in the large intestine, small and large adenomas had significantly higher percentage of γH2AX positive cells compared to microadenomas. In phenotypically normal crypts of the small and large intestine there were only 3±2 or 1±1 γH2AX positive cells, respectively (9±6% and 2±3% of γH2AX positive cells/ crypt; Figure 4.6 a and b). In the small intestine, the percentage of γH2AX positive cells in large adenomas was significantly higher compared to phenotypically normal crypts, whereas in the large intestine, phenotypically normal crypts have significantly lower percentage of γH2AX positive cells compared to the rest of lesions.

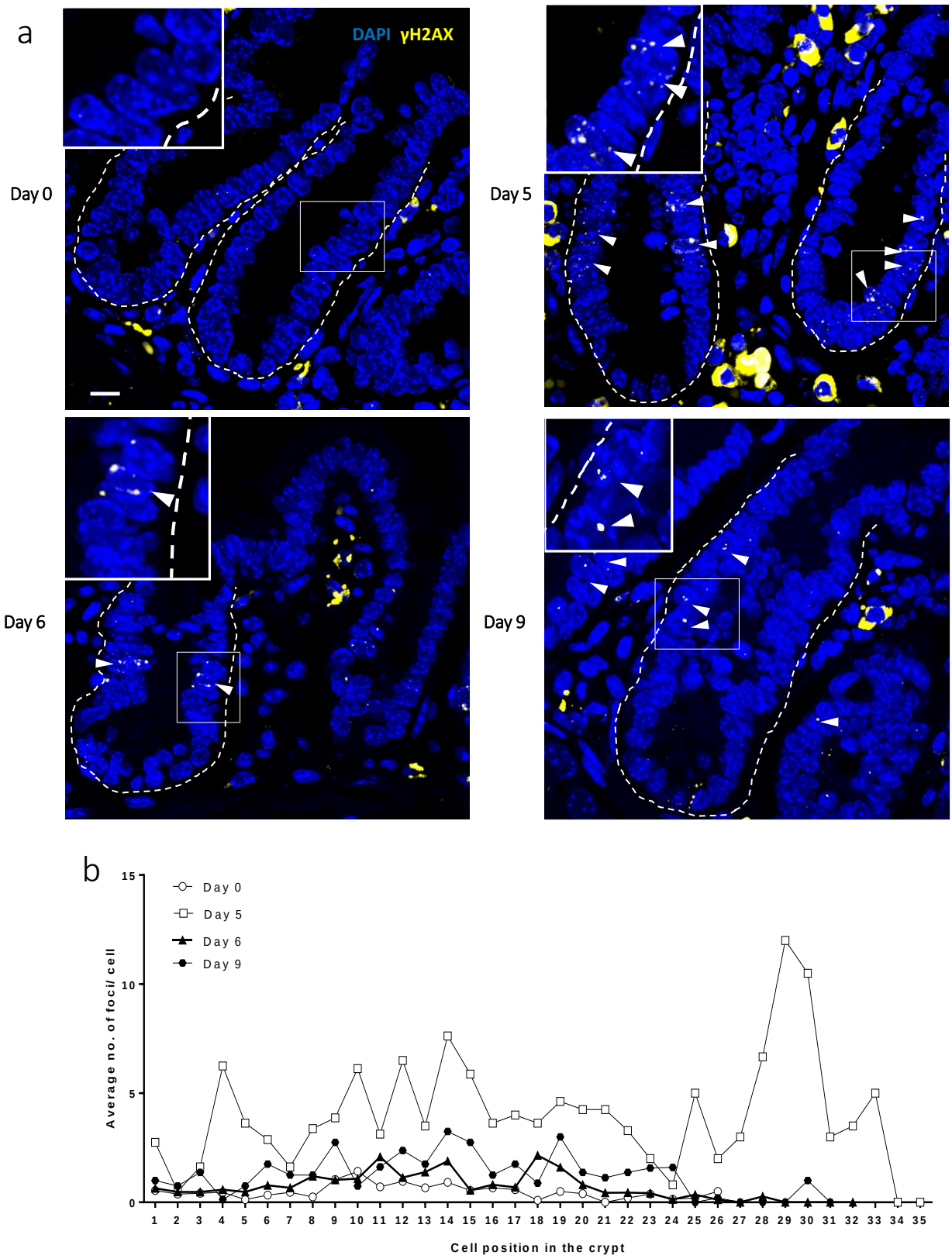

Figure 4.3 DDR response early after Cre-induced Apc excision in the Lgr5 stem cells of the small intestine.

Lgr5Cre^{ER}*Apc*$^{fl/fl}$ induced with 80mg/kg of tamoxifen for 4 days were killed at days 0, 5, 6 and 9 p.i.. (a) Representative images of γH2AX IF stained sections of the small intestinal gut rolls. Dotted line shows the barriers of the crypt epithelium. Scale bar = 10 µm. (b) Quantification of the average number of foci in a nucleus of crypt epithelial cells according to their position from the base of the crypt (min 4 crypts/ time point). Biological replicates *n* = 4, 1, 3, 1 for days 0, 5, 6, 9 p.i. respectively.

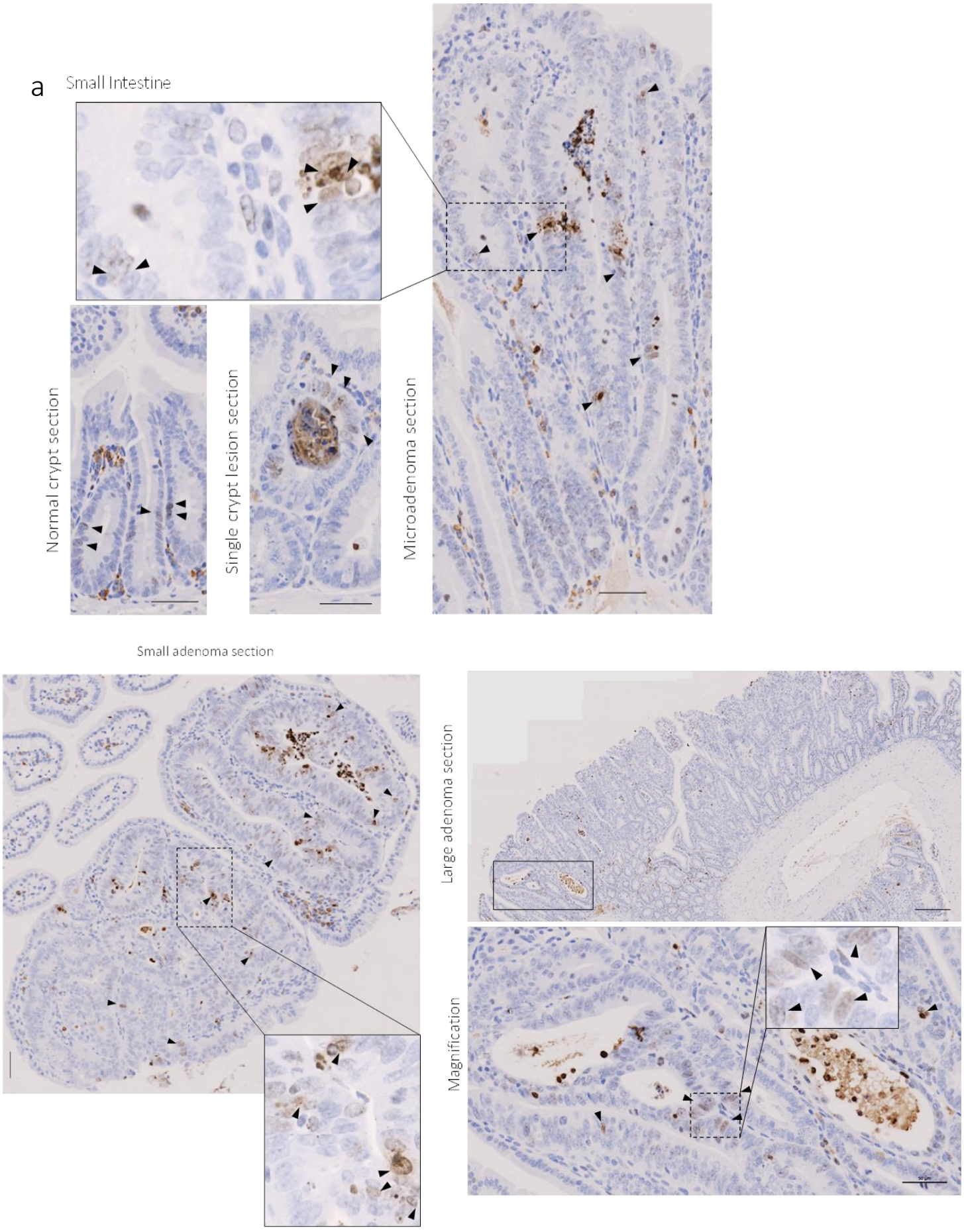

Fiugre 4.4 (b) and figure legend are on the next page.

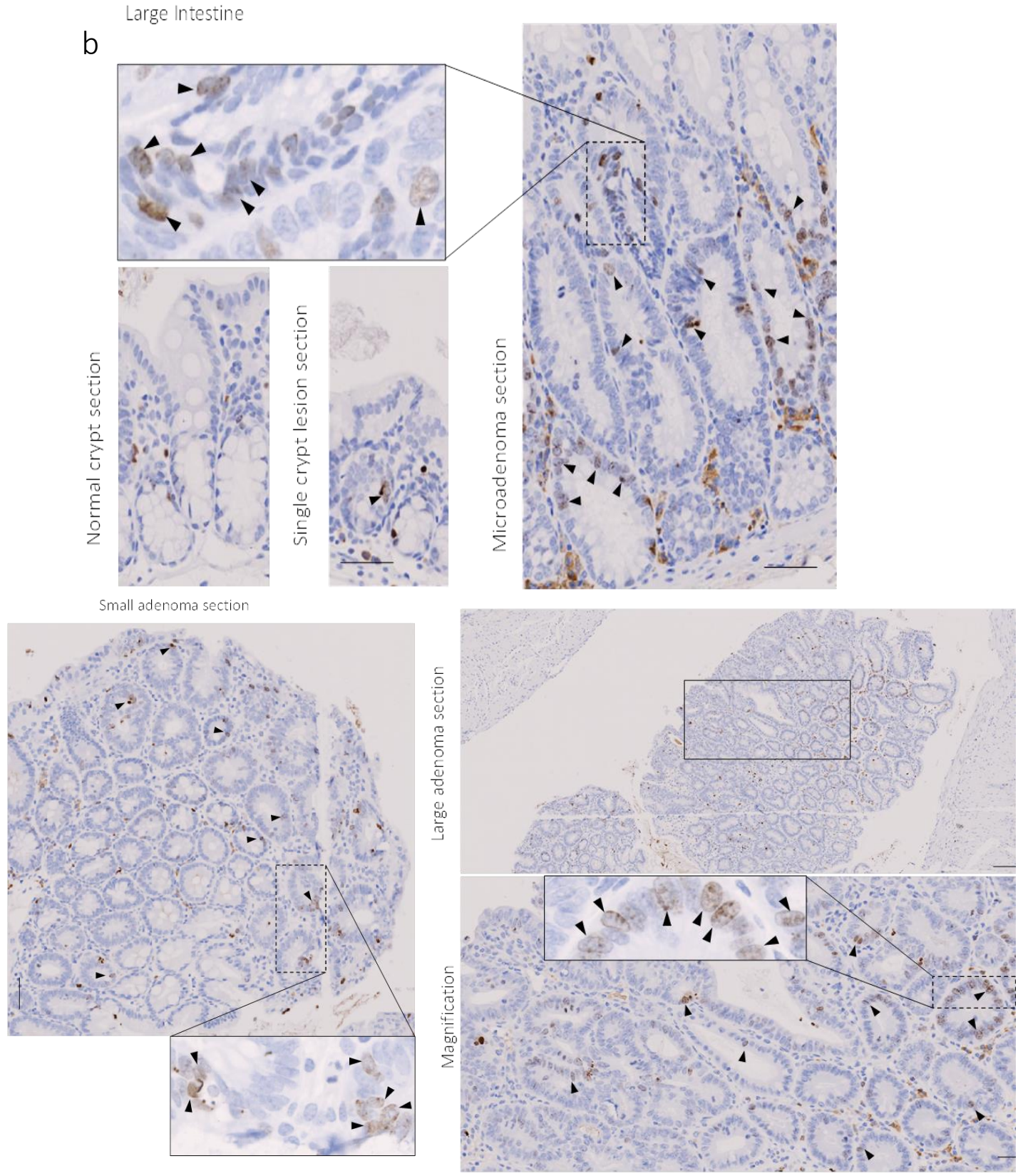

Figure 4.4 Apc deficiency in the murine small and large intestinal LGR5⁺ cells leads to the development of lesions with γH2AX⁺ cells.

γH2AX quantification in the *Lgr5Cre^{ER}Apc$^{fl/fl}$* lesions. IHC staining for γH2AX on intestinal sections of 50 days p.i. *Lgr5Cre^{ER}Apc$^{fl/fl}$*. Representative bright field images of the (a) small and (b) large intestine for each lesion type: (i) normal crypts, (ii) single crypt lesion, (iii) microadenomas, (iv) small adenomas and (v) large adenomas. Scale bars: i – iv = 50 µm, v = 200 µm; arrow heads indicate γH2AX positive cells; biological samples n = 3.

a

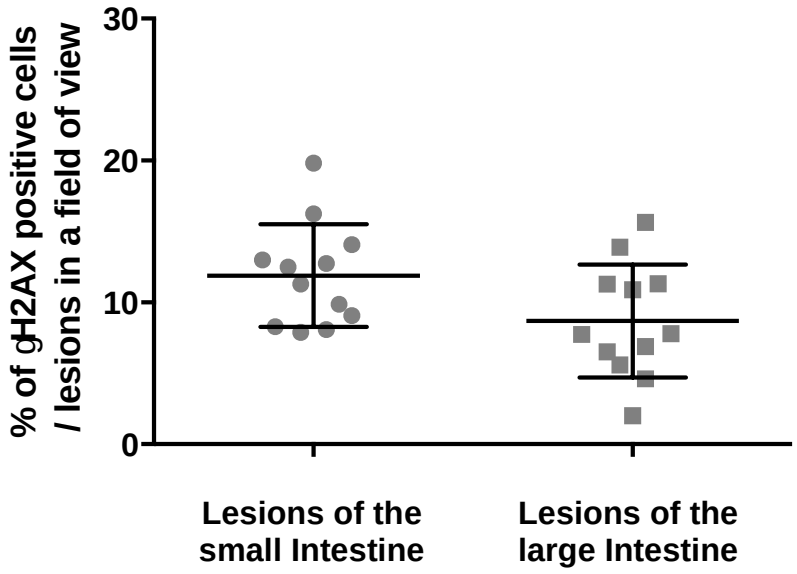

b

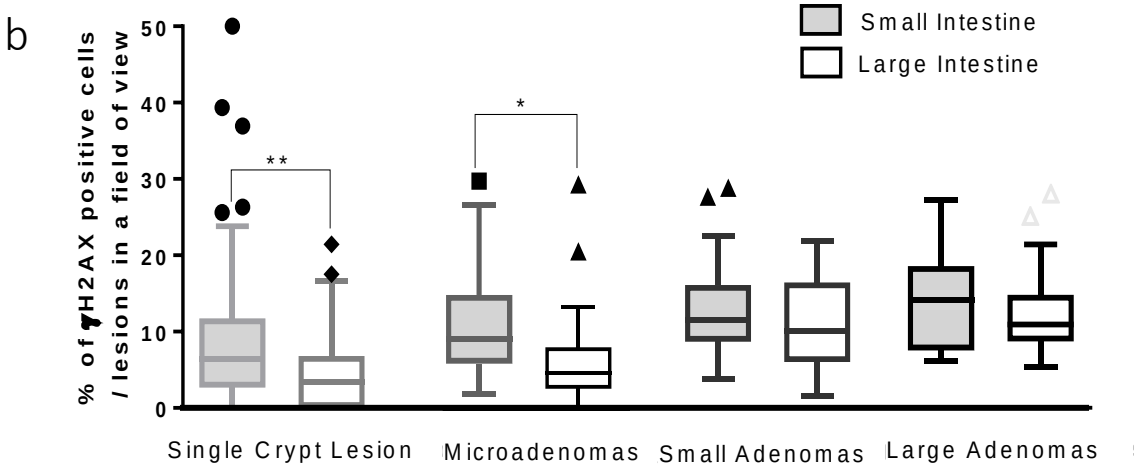

Figure 4.5 Apc deficiency in the murine small and large intestinal LGR5⁺ cells leads to the development of lesions with γH2AX⁺ cells.

(a) Percentage of γH2AX⁺ cells in all lesion types of the small and the large intestine. Normally distributed data analysed using two-tailed T-test; NS; $p > 0.05$.

(b) Tukey-style box and whiskers plot represents the percentage of the average γH2AX cell number in different types of lesions per field of view within the small intestine (single crypt n = 73, microadenoma n = 29, small adenoma n = 27, large adenoma n= 26) and the large intestine (single crypt n = 76, microadenoma n = 42, small adenoma n = 31, large adenoma n= 21). The running mean of the percentage of the average γH2AX cell number within a field of view for each lesion was used to identify the required number of samples to be quantified. Biological samples n = 3. One-way ANOVA multiple comparisons test; *$p < 0.05$, ** $p < 0.005$.

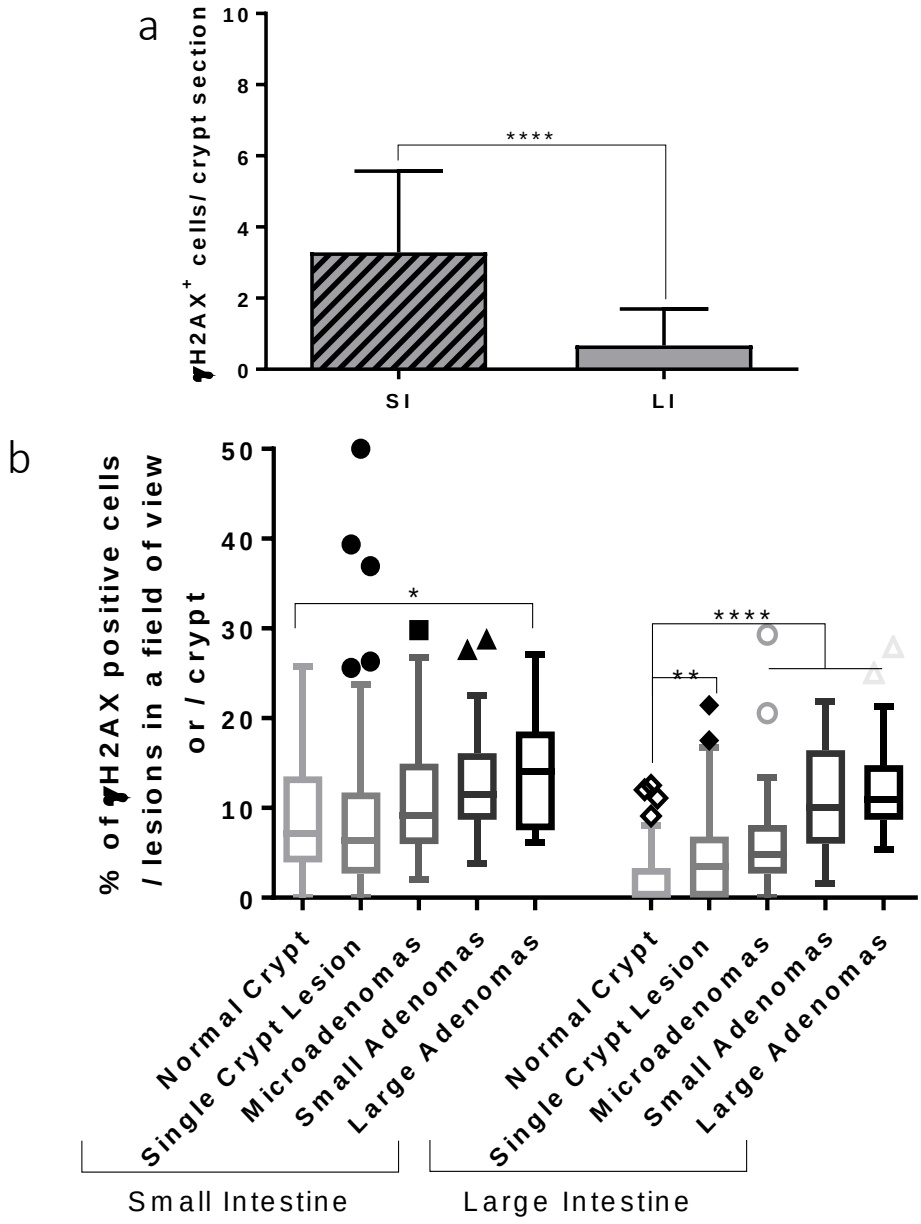

Figure 4.6 γH2AX quantification in the Lgr5Cre^{ER}Apc$^{fl/fl}$ single crypt lesions and phenotypically normal crypts.

γH2AX quantification in the *Lgr5Cre^{ER}Apc$^{fl/fl}$* mouse model in phenotypically normal or dysplastic whole crypt sections of the small and large intestine. γH2AX IHC staining was performed on intestinal sections of *Lgr5Cre^{ER}Apc$^{fl/fl}$* mice, 50 days p.i.. (a) The number of γH2AX positive cells within phenotypically normal whole crypt sections of the small and the large intestine (n = 91 and 87, respectively) is shown. (b) Percentage of the average γH2AX positive cells ± SD in sections of the small intestine (phenotypically normal crypts, n = 91; single crypt lesions, n = 73, microadenoma, n = 29; small adenoma, n = 27; large adenoma, n= 26) and the large intestine (phenotypically normal crypts, n = 87; single crypt, n = 76; microadenoma, n = 42; small adenoma, n = 31; large adenoma, n= 21) are shown. The running mean for both normal and dysplastic crypts was used to identify the required number of crypts to be quantified. Tukey-style box and whiskers plot was used to represent the data. Two-tailed Mann-Whitney test was performed; **** $p < 0.0001$; Biological samples for (a) and (b) n = 3.

4.3 Discussion

This chapter investigated the *in vivo* effects of *Apc* loss within the murine intestinal, to broaden our knowledge in this system in order to design experiments for targeting tumour cells using a radioisotope conjugated anti-γH2AX antibody. We used a more clinically relevant mouse model, *Lgr5Cre*^{ER} *Apc*$^{fl/fl}$, to induce *Apc* deficiency in the intestinal LGR5^{+} stem cells, in order to visualize and quantify DNA damage γH2AX DSB marker. The hypothesis was that *Apc* loss in the murine intestinal epithelium would contribute to DNA damage in tumours.

Increased levels of γH2AX foci in cells of the *Lgr5Cre*^{ER}*Apc*$^{fl/fl}$ mouse model was observed in multiple stages of tumour development. This indicates that DNA damage is not only induced early after *Apc* deficiency (Figure 4.3) but is also present at later stages of tumour development (Figure 4.4). In addition, it was observed that more advanced tumours had higher levels of DNA damage, suggesting that the progression of a lesion allows further cells to acquire DNA damage (Figure 4.6 b). Generally, large intestinal tumours had lower levels of DNA damage compared to those in the small intestine, which might suggest they have different mechanisms for coping with DNA damage. In human patients, sporadic tumours usually occur in the large intestine and less often in the small intestine (Aparicio *et al.* 2014) which suggest different homeostatic functions between small and large intestine.

4.4 Summary

The hypothesis that *Apc* deficiency drives DDR was supported by γH2AX nuclear accumulation in *Apc*-deficient intestinal tumour models. Having determined the key parameters of the system, we subsequently tested the hypothesis that ^{111}In-anti-γH2AX-TAT antibody could be attracted by the endogenous DNA damage signal, γH2AX, present in dysplastic *Apc*-deficient intestinal tissue or intestinal tumours. These studies are described in chapter 5.

5. *In vivo* imaging and characterization of CRC mouse models following low specific activity ^{111}In-anti-γH2AX-TAT

5.1 Introduction

The critical role of APC in intestinal tumourigenesis suppression is well established (Fearon and Vogelstein 1990). One of the crucial studies for establishing the role of APC loss in tumourigenesis was conducted by Sansom *et al.* (2004) using an inducible *AhCre Apc$^{fl/fl}$* transgenic mouse model, which showed that *Apc* loss throughout the intestinal epithelium immediately results in whole intestinal crypt dysplasia. Later it was demonstrated by Barker *et al.* (2009) that *Apc* deletion within LGR5^{+} intestinal stem cells is sufficient to drive tumourigenesis.

In Chapter 3, we demonstrated that *Apc* deficiency either throughout the intestinal epithelium, or specific to intestinal LGR5^{+} stem cells, results in increased DNA damage in dysplastic crypts or intestinal lesions respectively, as indicated by elevated levels of the DSB markers γH2AX and RAD51.

Cornelissen *et al.* (2011) have developed ^{111}In-anti-γH2AX-TAT, an ^{111}In radiolabelled antibody that recognizes the γH2AX DNA damage marker, can penetrate cell nuclei using a NLS- containing peptide (TAT) and can also be tracked *in vivo via* its radioactive emissions. In a breast cancer xenograft mouse model, they imaged *in vivo* γH2AX caused by DNA damaging agents such as IR or bleomycin, using a low specific radioactivity of this RIC, and without significantly increasing the number of γH2AX foci/cell.

This chapter aims to identify the *in vivo* localization pattern of ^{111}In-anti-γH2AX-TAT (RH2AX) in both early CRC and tumour mouse models. We hypothesised that the *Apc* deficient (*Apc*$^{fl/fl}$) intestinal tissue would have higher uptake of the RH2AX compared to controls (RIgG). Relevant biological outputs from the RH2AX-exposed intestinal tissue are also interrogated in this chapter, in order to investigate the effects of the RIC with low specific activity within the tissue.

5.2 Early CRC mouse model

5.2.1 ^{111}In-anti-γH2AX-TAT localization following tamoxifen IP injection

To demonstrate that RH2AX localized at sites of the intestine where DNA damage was generated after *Apc* loss, we used the *VilCre*^{ER} *Apc*$^{fl/fl}$ early WNT signalling deregulation CRC mouse model, due

to the high γH2AX levels present in the small intestine at days 3 and 4 p.i. in this mouse (Figure 3.3). The maximum life span of this model is 5 days p.i. (Johnson and Fleet 2013), hence RIC treatment was performed at day 3 p.i. when γH2AX levels were high. Due to funding and money constraints we could not perform a time course experiment to identify the best possible time point for RIC treatment and SPECT imaging. However, previous work (Cornelissen *et al.* 2011 and 2012) showed that the RIC uptake in irradiated tumours was similar after 24, 48 and 72 h post treatment. Based on the fact that this mouse model has a really short life span post induction, we decided to perform SPECT imaging at 24 h after RIC treatment (day 4 p.i.). All experiments using the RIC were performed in Oxford, using mouse induction protocols first established in Cardiff.

Mice were injected with 80 mg/kg tamoxifen or an equivalent volume of corn oil (vehicle) and 3 days later with the radioactive specific antibody (RH2AX) or its isotype control (^{111}In-anti-IgG-TAT; RIgG). Unexpectedly, IP injection of tamoxifen or corn oil caused health issues when carried out at Oxford, even with the same reagents as used in Cardiff. Injection of corn oil alone caused rapid weight loss and peritonitis to some non-induced mice during the first two days post injection. These mice recovered by day 3 post injection; however, some of the tamoxifen-induced mice had to be culled at this point due to worsening health status.

SPECT images acquired at day 4 p.i. from corn oil-injected mice, show RH2AX accumulation in the heart, liver, nasal glands and throughout the abdomen (Figure 5.1). The latter is presumably due to inflammation from peritonitis, since the RIC is IV-administered and the inflamed sites are likely to accumulate radioactive signal because of higher blood flow. Moreover, free ^{111}In is sequestered by the reticuloendothelial system; for example, neutrophils internalize free ^{111}In, thus some may have been sequestered by the circulating neutrophils that aggregate in areas of inflammation (Castronovo Jr and Wagner Jr 1973; Segal *et al.* 1976). RIgG accumulated in the liver, kidneys, nasal glands, bone joints and abdomen for the same reason. Bone joint accumulation of radioactivity following ^{111}In-immunoconjugate treatment is usually observed when ^{111}In is released from the antibody and binds to transferrin or is engulfed by neutrophils (Castronovo Jr and Wagner Jr 1973; Segal *et al.* 1976).

Tamoxifen-injected (hereafter referred to as $Apc^{fl/fl}$) mice similarly accumulated RH2AX in the heart, liver, nasal glands and abdominal site indicated by an arrow in Figure 5.1 (see Figure A.1 in appendix for the full panel of SPECT images). There were no obvious differences in RH2AX uptake between

Apc$^{+/+}$ and *Apc*$^{fl/fl}$ mice; hence we performed biodistribution assays on the organs, to measure and compare their radioactivity.

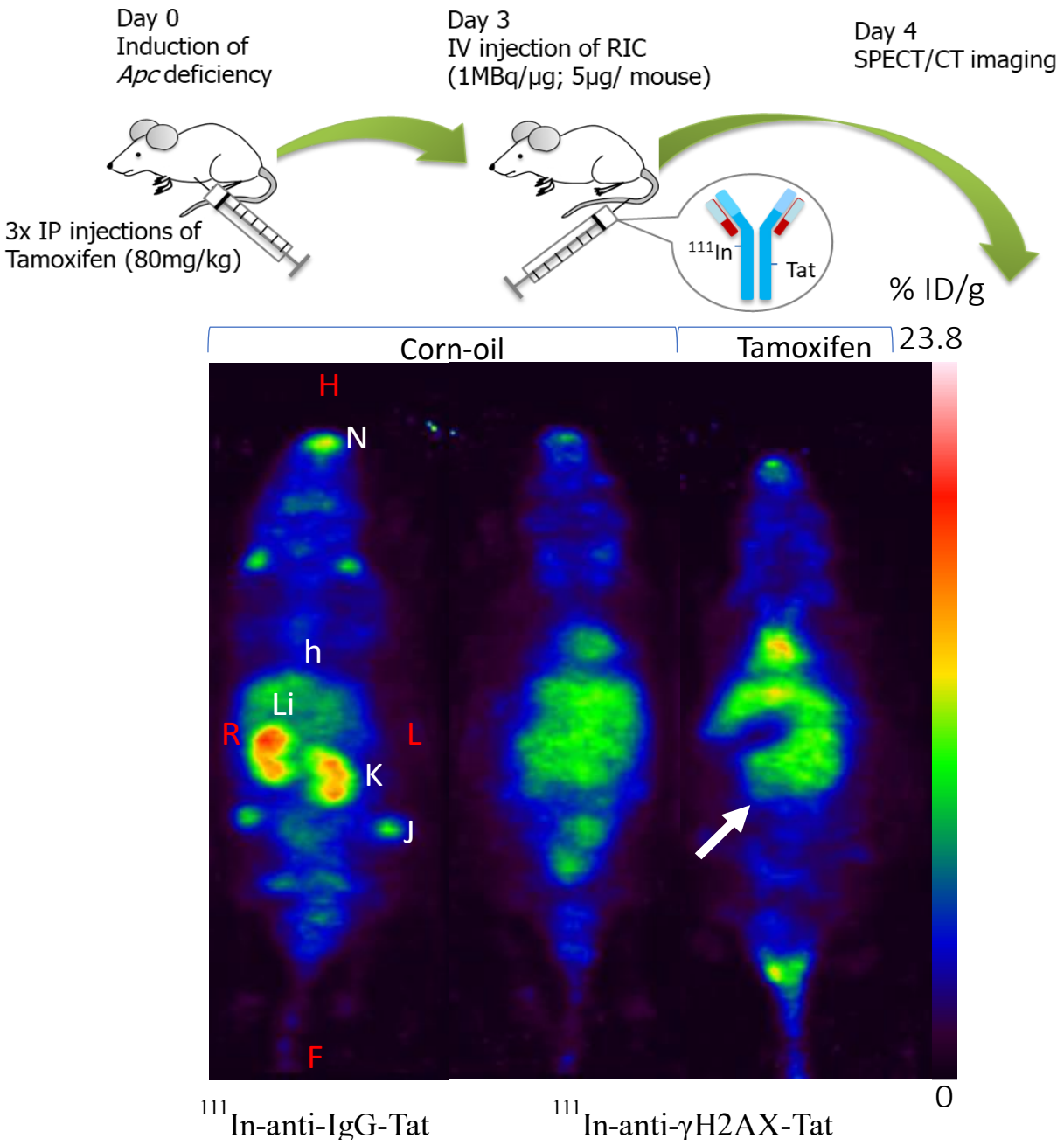

Figure 5.1 In vivo DNA damage imaging in VilCre^{ER} Apc$^{fl/fl}$ mouse model using ^{111}In-anti-γH2AX-TAT.

Tamoxifen (3x 80 mg / kg) or vehicle IP injected *VilCre^{ER} Apc$^{fl/fl}$* mice were treated intravenously with ^{111}In-anti-γH2AX-TAT or ^{111}In-anti-IgG-TAT (1MBq/µg; 5µg/mouse). Tamoxifen injected and ^{111}In-anti-IgG-TAT treated group had to be killed before ^{111}In-anti-IgG-TAT treatment. 24h later mice were scanned by SPECT/CT imaging. Representative maximum projection images showing the percentage of injected dose per gram of tissue (%ID/g) using colour code. White arrow indicates RIC uptake in the abdomen. Mouse orientation is indicated with red letters: H= head, F= feet, R= right, L= left; Organs are indicated with the letters: h=heart, K=kidney, Li=liver, J= bone joints, N= nasal glands; n = 3 for RH2AX treated *Apc$^{+/+}$* and *Apc$^{fl/fl}$* groups and n = 4 for RIgG treated *Apc$^{+/+}$* group.

At 24h post RIC injection, mice were culled after imaging and biodistribution assays performed. Tissue and organ radioactivity is shown in Figure 5.2. In corn oil-administered mice (hereafter referred to as $Apc^{+/+}$) treated with RIgG, radioactivity was > 6% ID/g in blood, liver, spleen, pancreas and kidneys 24h after treatment. Administration of RH2AX in $Apc^{+/+}$ mice resulted in similar biodistribution patterns to the RIgG treated $Apc^{+/+}$ mice, showing > 5% ID/g in blood, liver, spleen, pancreas and kidneys but also within the heart, lung, skin and fat. Whilst high accumulation of RIC in the these tissues/organs is usually observed (Cornelissen *et al.* 2011), high RIC uptake in the skin and fat is uncommon. However, due to the fact that skin and fat samples were collected from the abdominal site it is likely that peritonitis-induced inflammation affected those tissues. Neutrophil engulfment of free ^{111}In could possibly be observed in both RH2AX and RIgG treated mice with peritonitis due to accumulation of the labelled neutrophils in inflamed areas. However, only a very small percentage of ^{111}In is released from the antibody, hence, this could not explain the high radioactivity uptake observed at the abdomen of these mice. Activation of the innate immune system in inflamed organs could explain the intense radioactivity uptake in the abdomen, as it induces ROS production in the surrounding tissues, which in turn activates the DNA damage response, hence H2AX phosphorylation (Martin *et al.* 2011). Thus, RH2AX (but not the RIgG) could accumulate within those tissues. RIC uptake was < 5% ID/g in the stomach and intestines of these two groups. In the $Apc^{fl/fl}$ mice, RH2AX treatment resulted in high accumulation of radioactivity in the same tissues, i.e. blood, heart, lung, liver, spleen, pancreas, kidneys and fat, and medium RH2AX accumulation in the skin; whereas < 2.5% ID/g radioactivity accumulation was observed in the stomach and muscle, respectively. A single radioactivity measurement for each mouse was obtained for full length non-flushed small and large intestines, including caecum. There was no significant difference between the percentage of RIgG uptake in the intestine for both $Apc^{+/+}$ and $Apc^{fl/fl}$ mice (< 5% ID/g) compared to RH2AX uptake in the $Apc^{fl/fl}$ group (~ 5% ID/g). Unfortunately, we could not obtain data for the RH2AX uptake in the $Apc^{+/+}$ group because animals had to be killed due to the health issues described above. Thus, we could not compare the RH2AX accumulation between $Apc^{+/+}$ and $Apc^{fl/fl}$ intestines.

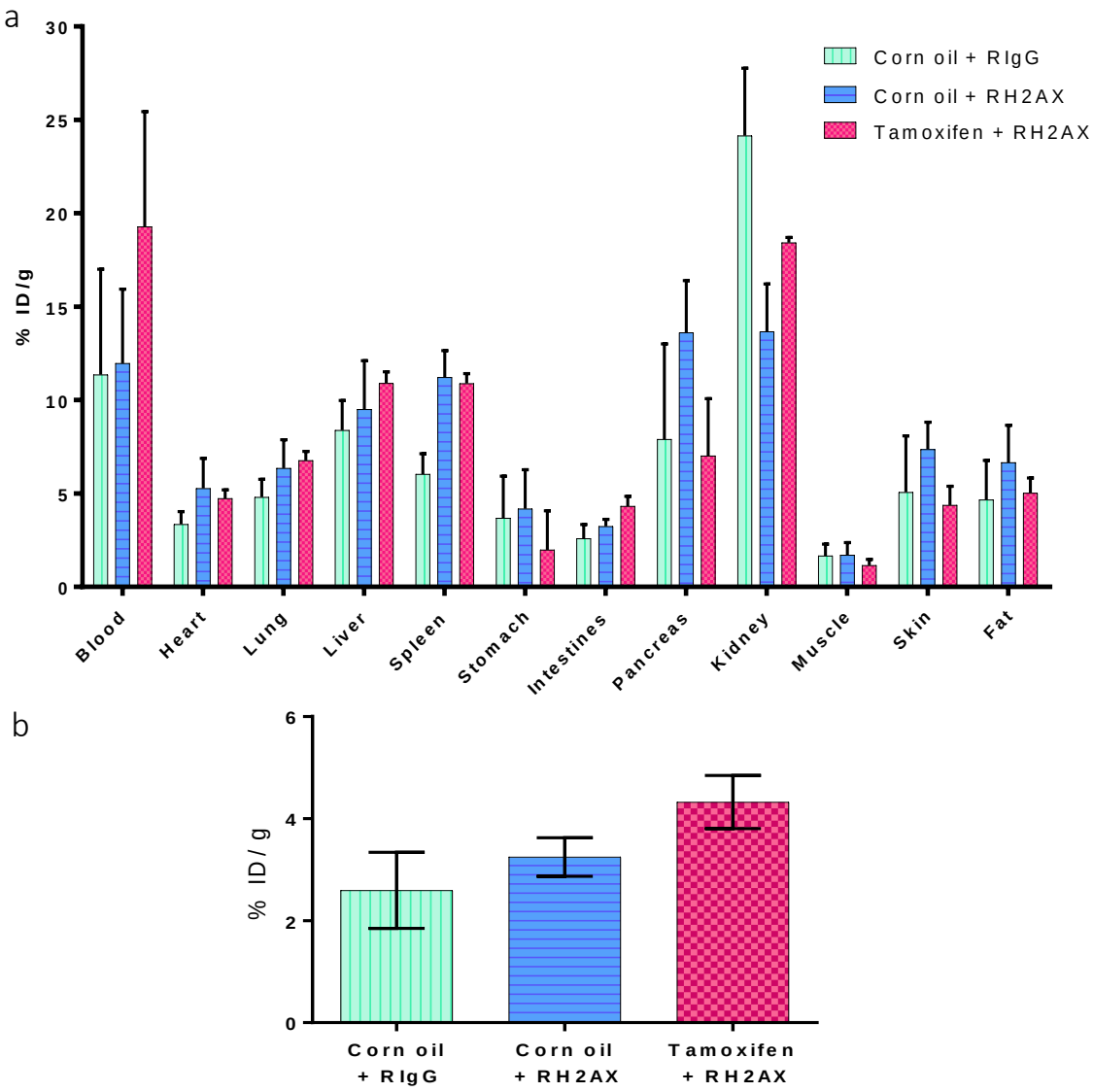

Figure 5.2 Biodistribution analysis in VilCre^{ER} Apc$^{fl/fl}$ mouse model post RIC treatment.

Tamoxifen IP (3x 80 mg/kg) or vehicle injected *VilCre^{ER} Apc$^{fl/fl}$* mice were injected intravenously with ^{111}In-anti-γH2AX-TAT or ^{111}In-anti-IgG-TAT (1 MBq / µg; 5 µg / mouse). 24h later mice were scanned by SPECT/CT imaging and then culled. Organs were removed and passed through a γ-counter to quantify their radioactivity. The average percentage of injected dose per gram of tissue (% ID / g) is shown for (a) all the analysed tissues/organs and (b) specifically for the intestinal tissue (including small and large intestines and caecum). 1-way ANOVA, Tukey's multiple comparisons test was performed; ns $p > 0.05$; n = 3 for RH2AX treated *Apc$^{+/+}$* and *Apc$^{fl/fl}$* groups and n = 4 for RIgG treated *Apc$^{+/+}$* group.

5.2.2 ^{111}In-anti-γH2AX-TAT localization following oral administration of tamoxifen.

To overcome the unexpected effects of IP corn oil administration, and also to generate more widespread γH2AX lesions to provide a greater signal / noise ratio, we next tested the RICs in the oral induction *Vil*Cre^{ER} *Apc*$^{fl/fl}$ model. At day 3 post oral induction of *Vil*Cre^{ER} *Apc*$^{fl/fl}$ mice, experimental (RH2AX) or control (RIgG) RICs were intravenously injected (1MBq/μg; 5μg/mouse) and SPECT-CT scans performed 24h later (Figure 5.3) as previously following IP injection. Maximum projection SPECT images showed a general pattern of RIC accumulation in the heart, liver and sometimes in kidneys, which is normally observed in RIC-based *in vivo* scans (See section 1.4.3 for comparison with previous studies). There was some uptake of RH2AX in nasal and Harderian glands, which was more prominent in the RH2AX-treated *Apc*$^{fl/fl}$ mice (See Figure A.2 for full panel of SPECT images). Importantly, an abdominal pattern of RIC localization was only seen in RH2AX-administered mice, indicated in Figure 5.3 by an arrow.

To further investigate specific RIC uptake in each tissue, mice were killed following imaging and biodistribution assays performed (Figure 5.4 a-c). In *Apc*$^{+/+}$ or *Apc*$^{fl/fl}$ mice injected with RIgG, >5% ID/g of radioactivity accumulated in the blood, and lungs 24h post intravenous injection. Radioactivity uptake in spleen and kidneys of *Apc*$^{+/+}$ and *Apc*$^{fl/fl}$ mice injected with RIgG was <5% ID/g and >5% ID/g, respectively. Administration of RH2AX to *Apc*$^{+/+}$ mice resulted in similar biodistribution in these tissues. Radioactivity uptake of <5% ID/g was observed in the heart, liver and pancreas of all three groups. In *Apc*$^{fl/fl}$ mice treated with RH2AX, >5% ID/g of radioactivity were seen in the same tissues (blood, lung, spleen and kidneys) and liver, as well as medium uptake in the heart. Radioactivity uptake of <2.5% ID/g in *Apc*$^{+/+}$ mice was present in the skin, fat and faeces. *Apc*$^{fl/fl}$ mice had considerably, but not significantly, higher levels (7 to 10-fold increase) of radioactivity in their faeces compared to *Apc*$^{+/+}$ mice, possibly due to crypt dysplasia causing inflamed intestine and diarrhoea. There was a negligible (i.e. <1% ID/g) amount of radioactivity present in the stomach and muscle of all groups of mice. In the distal small intestine, radioactivity was low and similar for all groups. Importantly, however, in the proximal small intestine, *Apc*$^{fl/fl}$ mice treated with RH2AX had significantly higher radioactivity compared to controls (Figure 5.4 c). In the large intestine, radioactivity was also significantly higher in *Apc*$^{fl/fl}$ mice treated with RH2AX compared to *Apc*$^{+/+}$ mice however, this is most probably due to reduced uptake within the corn-oil administrated group rather than due to higher uptake within the *Apc* deficiency.

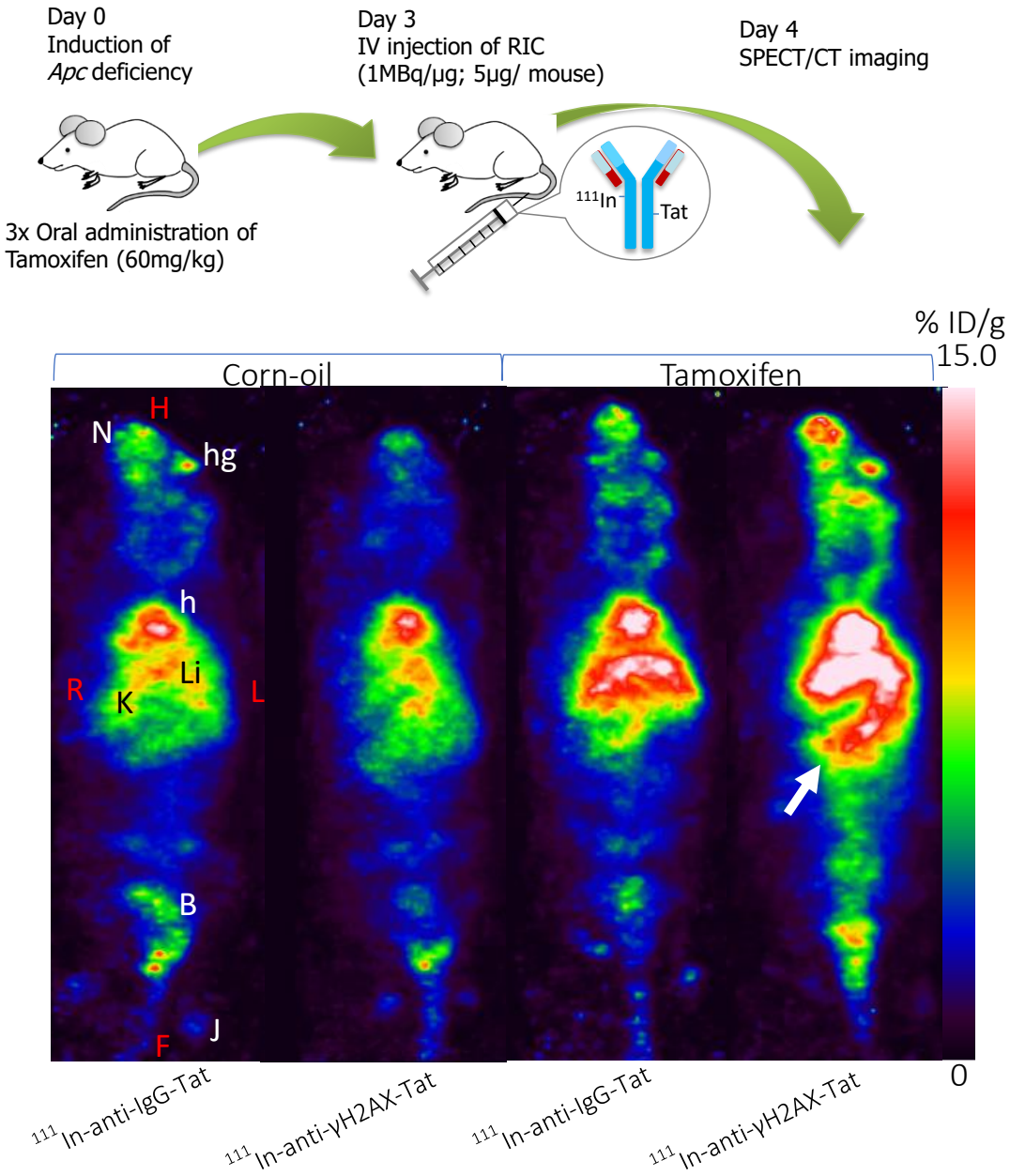

Figure 5.3 Imaging intestinal dysplasia in the VilCre^{ER} Apc$^{fl/fl}$ mouse model using ^{111}In-anti-γH2AX-TAT.

Tamoxifen-induced (3x 60mg/kg) or vehicle gavaged *Vil*Cre^{ER} *Apc*$^{fl/fl}$ mice were injected intravenously 72 hours later with ^{111}In-anti-γH2AX-TAT or ^{111}In-anti-IgG-TAT (1MBq/µg; 5µg/mouse). 24h later, mice were imaged through SPECT/CT imaging. Representative maximum projection images showing percentage of injected dose per gram of tissue (% ID / g) using colour code (n = 3 per group). White arrow indicates RIC uptake in the abdomen. Mouse orientation is indicated with red letters: H= head, F= feet, R= right, L= left; Organs are indicated with the letters: h=heart, K=kidney, Li=liver, J= bone joints, N= nasal glands, hg = Harderian glands, B= bladder.

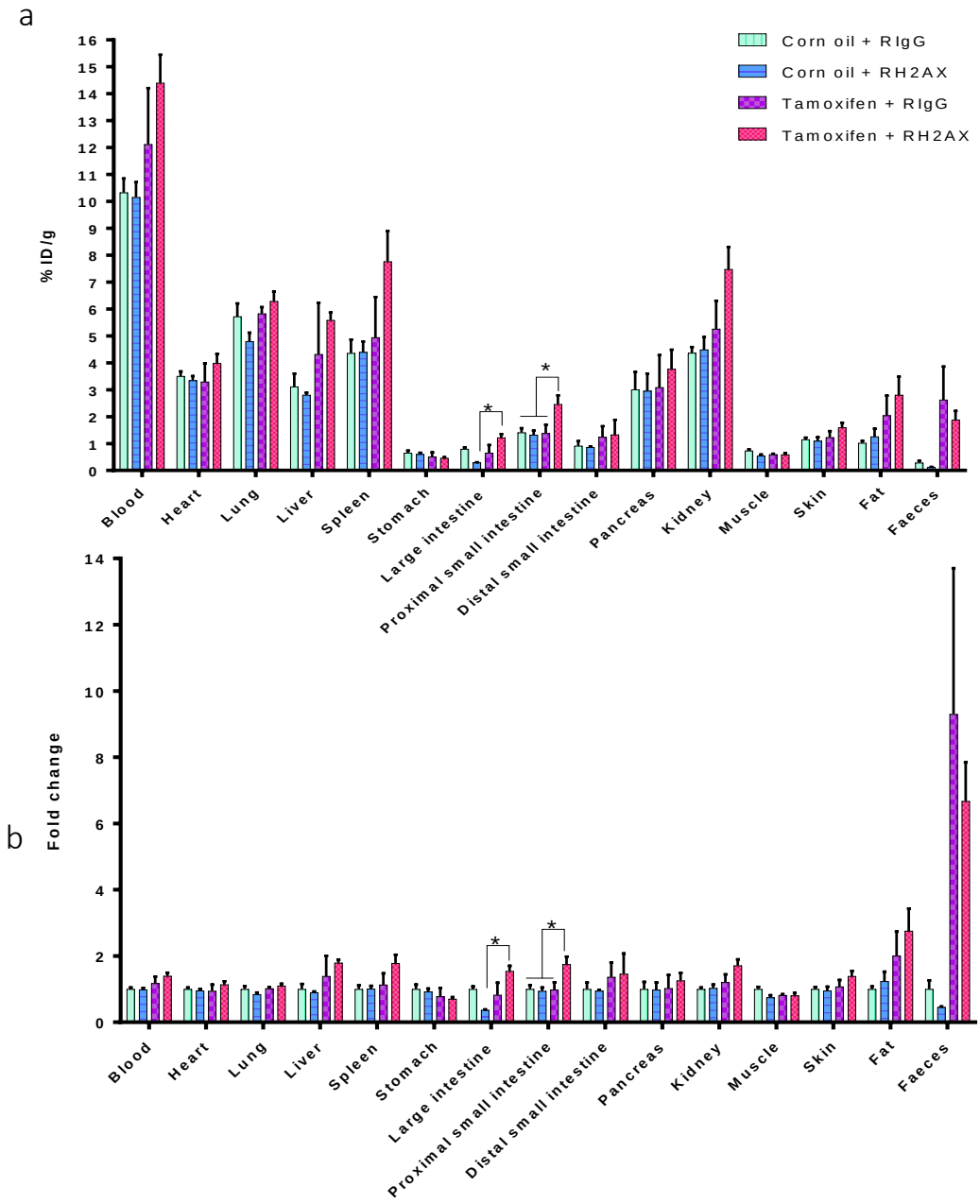

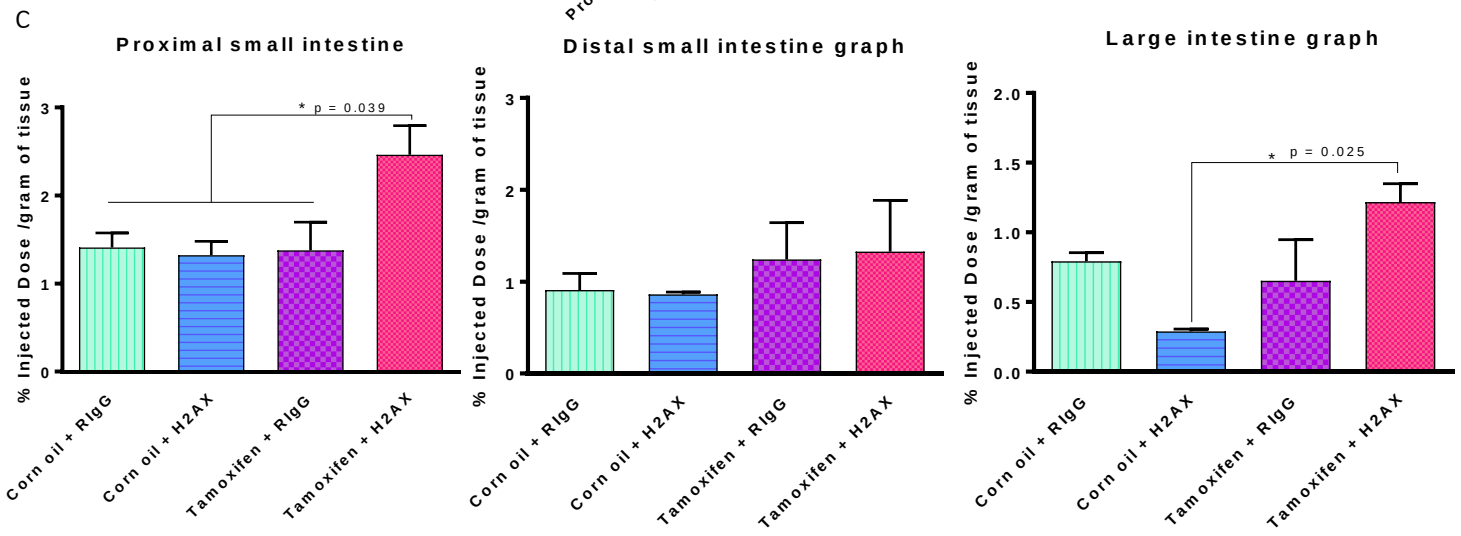

Figure legend on next page.

Figure 5.4 Biodistribution analysis in VilCre^{ER} Apc$^{fl/fl}$ mouse model post RIC treatment.

Tamoxifen induced (3x 60mg/kg) or vehicle gavaged *Vil*Cre^{ER} *Apc*$^{fl/fl}$ mice were injected intravenously with ^{111}In-anti-γH2AX-TAT or ^{111}In-anti-IgG-TAT (1MBq / μg; 5μg / mouse). 24h later mice were imaged through SPECT/CT imaging and then sacrificed. Tissues were harvested and run through a γ-counter to record radioactivity. (a) The average percentage of injected dose per gram of tissue (% ID / g) is shown for all organs that were removed and specifically for (c) the proximal and distal small intestine and large intestine. 1-way ANOVA statistical analysis was performed; $p < 0.05$. (b) Fold change of the % ID/g after normalization to the % ID/g of the Corn-oil + ^{111}In-anti-IgG-TAT group. n = 3 per group.

5.3 Tumour CRC mouse model

Using oral gavage activation in the early CRC mouse model, *Vil*Cre^{ER} *Apc*$^{fl/fl}$, we have shown by *in vivo* SPECT imaging that there was an increased RH2AX uptake in the abdomen of these mice; more specifically biodistribution assays showed that early dysplastic intestinal lesions accumulated significantly higher levels of the RH2AX due to higher expression of the γH2AX DNA damage biomarker. This data has clinical potential for visualising lesions that cannot be identified by normal intestinal screening procedures such as colonoscopy. Next, we asked whether established macroscopic tumours could be imaged, using RH2AX with low specific activity. While imaging macroscopic tumours by RH2AX might have similar sensitivity to current intestinal screening procedures for identifying tumours, an additional benefit of specific uptake of RH2AX within tumours could be as an indicator of the potential for using a higher specific activity RIC as a therapeutic agent.

5.3.1 ^{111}In-anti-γH2AX-TAT localization post oral administration of tamoxifen.

At day 34 post oral induction of *Lgr5*Cre^{ER} *Apc*$^{fl/fl}$ and *Lgr5*Cre^{ER} *Apc*$^{+/+}$ mice, RH2AX or RIgG were intravenously injected (0.5MBq/μg; 5μg/mouse) and SPECT-CT scans performed 24h later (Figure 5.5). The total number of mice induced was 6 per group; SPECT-CT scans were planned to be performed on n = 3 per group and all mice of each group were dissected for the biodistribution assay. However, 6 out of 12 mice induced with tamoxifen had to be killed, due to weight loss, before the end point. Hence, the remaining tamoxifen induced mice were randomly distributed in two groups (n = 3 / group) to be either treated with RIgG or RH2AX. Based on a pilot experiment performed at Cardiff, all mice induced orally by gavage with tamoxifen (80 mg / kg for 4 consecutive days) developed macroscopic tumours at day 34 (data not shown). Whilst all 3 mice induced by tamoxifen and treated with RIgG had tumours, only 1 out of 3 mice treated with RH2AX had tumours. This was only identified after SPECT imaging, during animal dissection.

Maximum projection of SPECT images showed a general pattern of RIC accumulation in the heart and liver. There was a specific accumulation of RH2AX in the abdomen of a *Apc*$^{fl/fl}$ mouse with intestinal tumours (n= 1/3), whereas SPECT images of RH2AX treated *Apc*$^{fl/fl}$ mice that did not have any intestinal tumours (n= 2/3) following dissection, showed no specific abdominal accumulation of radioactivity. SPECT images of RIgG treated *Apc*$^{fl/fl}$ mice with intestinal tumours (n= 2/3) showed abdominal accumulation of radioactivity. Consistent with these observations, SPECT images of

Apc$^{+/+}$ mice (which do not develop tumours after induction), did not show any abdominal accumulation of RIgG (n = 3/3) or RH2AX (n = 3/3); see Figure A.7 for the entire panel of SPECT images). Sometimes, SPECT images identified RIC accumulation in nasal and Harderian glands of mice.

Biodistribution assay was performed to specify the radioactivity levels of each organ (the total number of animals analysed was n = 6, 5, 3 and 3 for the corn oil + RIgG, corn oil + RH2AX, tamoxifen + RH2AX and tamoxifen + RIgG groups, respectively; Figure 5.6 a - b). In *Apc*$^{+/+}$ mice treated with RIgG or RH2AX, radioactivity accumulated in the blood, lungs, liver, spleen, and kidneys at 24h post intravenous injection. A similar localization was observed in *Apc*$^{fl/fl}$ mice that had been treated with RH2AX. There was a trend towards decreased uptake of radioactivity in every organ and tissue of RIgG treated *Apc*$^{fl/fl}$ mice. This group of mice, compared to RH2AX treated *Apc*$^{fl/fl}$ group of mice, had significantly lower radioactivity uptake in the blood, spleen, small and large intestines and kidneys, whereas their intestinal tumours accumulated radioactivity of approximately 5% ID / g. This trend was also observed in RH2AX treated *Apc*$^{fl/fl}$ mice especially in the small and large intestines and pancreas. Unfortunately, only one mouse in the RH2AX treated *Apc*$^{fl/fl}$ group of mice had macroscopic tumours, however its radioactivity uptake was not recorded; therefore, we cannot draw any conclusions regarding the specific uptake of RH2AX in tumour tissue.

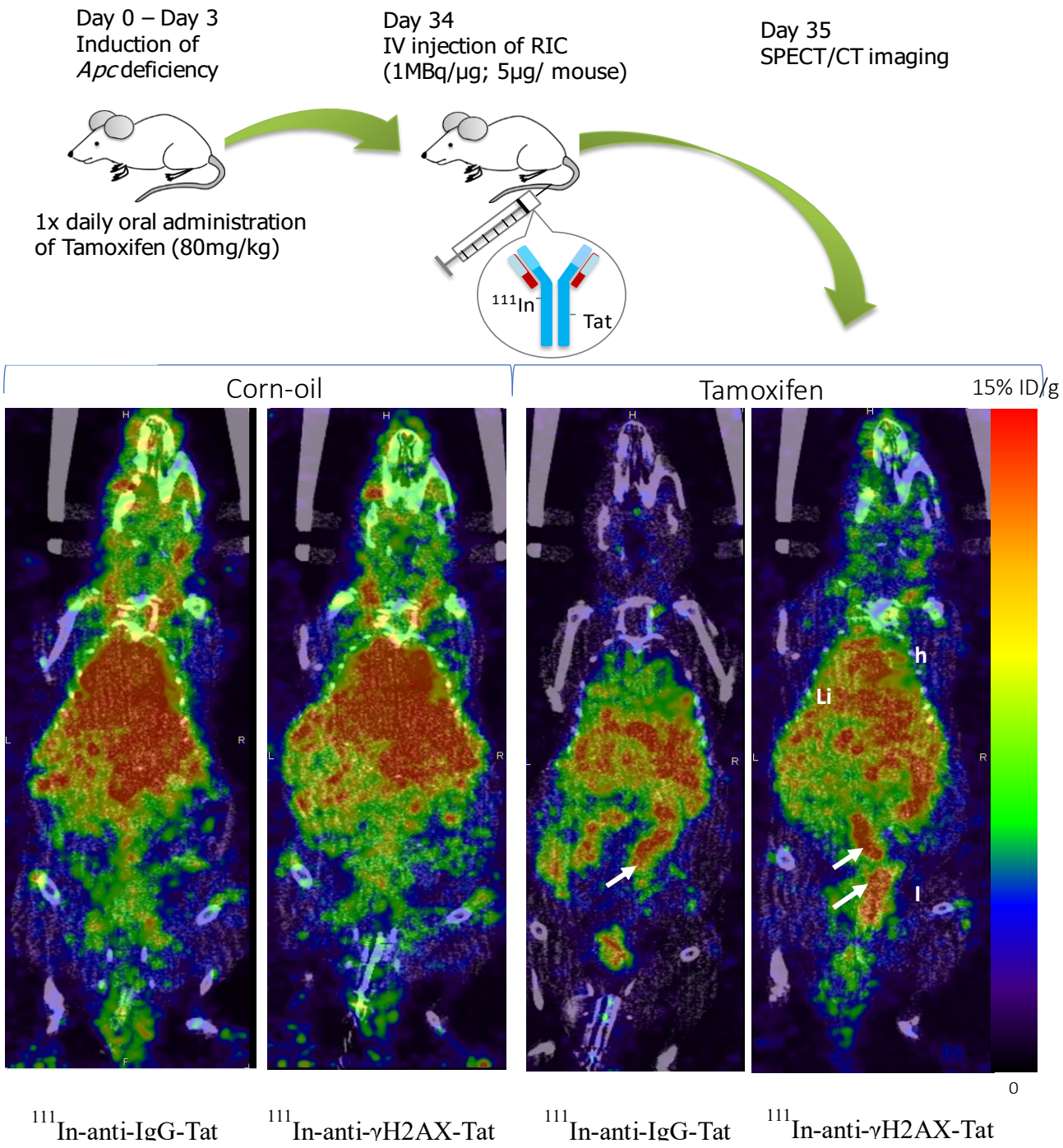

Figure 5.5 Imaging intestinal dysplasia in the Lgr5Cre^{ER} Apc$^{fl/fl}$ mouse model by ^{111}In-anti-γH2AX-TAT.

Tamoxifen induced (80 mg / kg; 1x daily for 4 days) or vehicle gavaged *Lgr5*Cre^{ER} *Apc*$^{fl/fl}$ mice were injected intravenously with ^{111}In-anti-γH2AX-TAT or ^{111}In-anti-IgG-TAT (0.9 MBq / µg; 5µg / mouse) 34 days p.i.. 24h later (day 35) mice were scanned by SPECT/CT imaging. Representative maximum intensity projection (MIP) images showing the average percentage of injected dose per gram of tissue (% ID / g) is depicted by colour code and it is overlaid to a single slice of the CT image (n = 3 per group). h = heart, Li = liver, I = intestine, B = bladder; letters showing mouse orientation: H = head, F = feet, L = left, R = right. White arrows indicate presumed intestinal tumours.

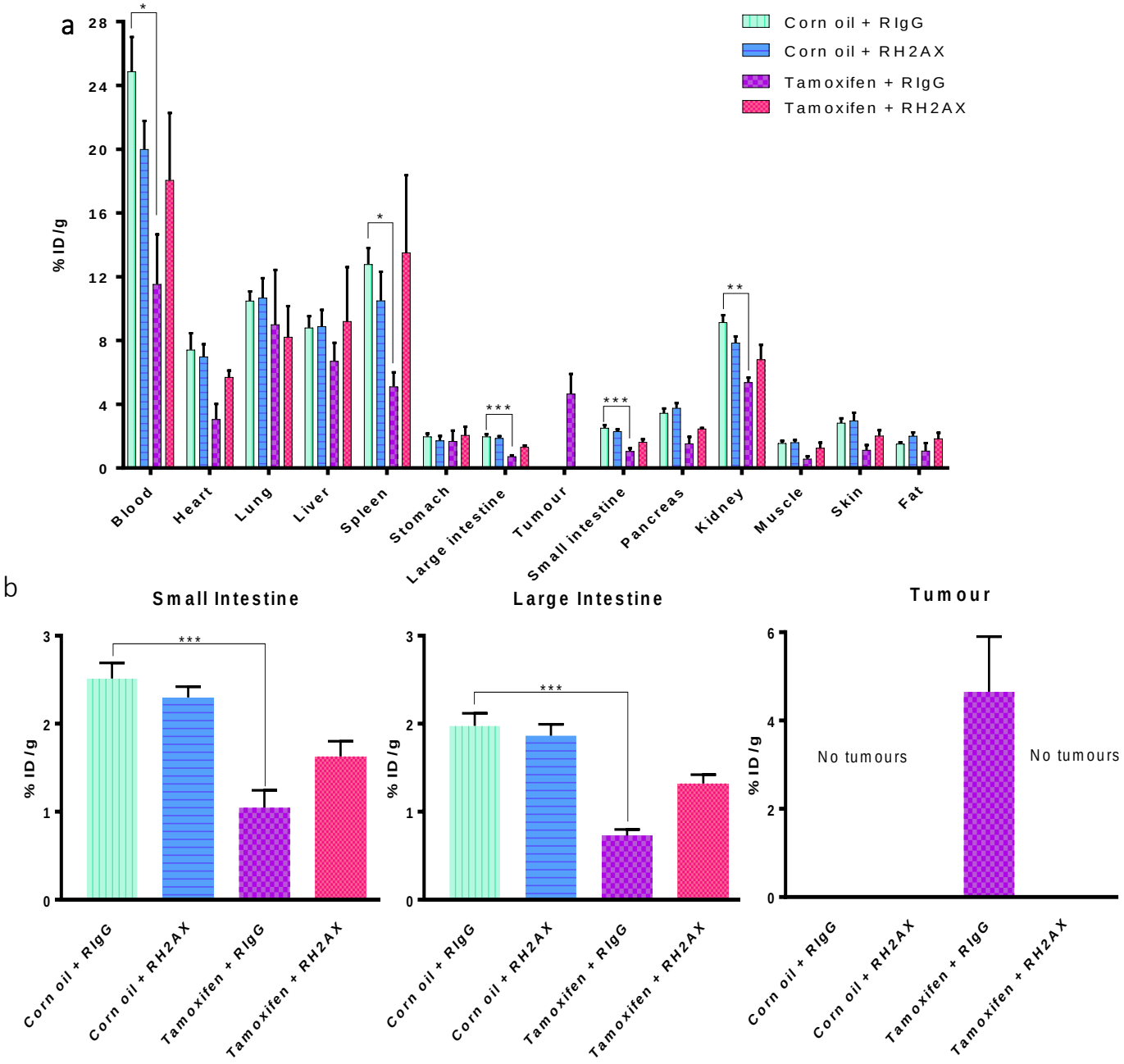

Figure 5.6 Biodistribution analysis in Lgr5Cre^{ER} Apc$^{fl/fl}$ mouse model post RIC treatment.

Tamoxifen induced (80 mg / kg; 1x daily for 4 days) or vehicle gavaged *Lgr5Cre^{ER} Apc$^{fl/fl}$* mice were injected intravenously with ^{111}In-anti-γH2AX-TAT or ^{111}In-anti-IgG-TAT (0.5 MBq / µg; 5 µg / mouse) 34 days p.i.. 24h later (day 35) mice were sacrificed, after SPECT/CT scan, and tissues were harvested and run through a γ-counter to record radioactivity levels. The average percentage of injected dose per gram of tissue (% ID / g) is shown. Kruskal-Wallis non-parametric test was performed for each tissue/organ identifying discrepancies in the sum of ranks for each one, hence the exact *p*-value for each test is shown (* $p < 0.05$, ** $p < 0.01$, *** $p < 0.001$). Dunn's multiple comparisons test compared the differences in the sum of ranks for each group within a tissue/organ and connected groups have adjusted *p*-value < 0.05. n = 5, 6, 3 and 3 for the corn oil + RIgG, corn oil + RH2AX and tamoxifen + RIgG and tamoxifen + RH2AX groups, respectively.

5.4 Low specific activity effects of ^{111}In-anti-γH2AX-TAT on the early CRC (*VilCre^{ER} Apc$^{fl/fl}$*) mouse model

No weight loss or other adverse effects on the mouse health following RIC treatment have ever been recorded by Cornelissen *et al.* (2012); however, none of the previous studies have ever addressed the biological effects that RIC treatment could have on the intestine. Hence, we looked for any differences in biological outputs following treatment with low specific activity of either the control or the specific RIC (RIgG or RH2AX, respectively; 1MBq/μg; 5μg/mouse) which might indicate localised radiation damage from the RIC. These included γH2AX levels, proliferation and apoptosis in the proximal small intestine and the large intestine. Whilst desirable in the therapeutic context, such biological effecst would not be desirable in the context of screening and diagnostic imaging.

5.4.1 Small intestine

γH2AX levels were used as an indicator of DSBs. Tissue recombination alone significantly increased γH2AX levels (Figure 5.7a). In non-recombined and recombined small intestine, administration of either RIC resulted in increased number of γH2AX positive cells within the crypt (Figure 5.7a), indicating that non-specific RIC treatment itself can generate *de novo* DNA damage. RIC effect was even more prominent in the recombined proximal small intestine compared to the non-recombined tissue (Figure 5.7a).

Detailed analysis of the extent of DNA damage was performed by quantification of different levels of IHC staining intensity; low, medium and high. The results showed that within non-recombined wt small intestine, both RIgG and RH2AX increased the levels of medium and high γH2AX intensity, whereas within the recombined small intestine, low, medium and high γH2AX intensity levels were increased by the RICs. RIgG treatment in the recombined tissue significantly increased the percentage of cells with low γH2AX intensity compared to non-recombined tissue, whereas the number of cells with medium γH2AX intensity decreased. There was no change in the number of cells with high γH2AX intensity between non-recombined and recombined tissue upon RIgG treatment. RH2AX treatment in the recombined tissue significantly increased the number of cells with low γH2AX intensity only (Figure 5.7 b, g).

Higher levels of DNA damage could result in increased apoptosis or decreased proliferation, two mechanisms by which cells protect their progeny from acquiring DNA alterations (Insinga *et al.*

2013). Moreover, it has been previously described that *Apc* loss leads to higher levels of cell death by apoptosis (Sansom *et al.* 2004) which is in agreement with our findings showing higher levels of apoptosis (Figure 5.7 c). Either of the RIC treatments significantly increased the apoptotic index in the non-recombined tissue compared to untreated. In contrast, there were no significant differences in the levels of apoptosis within the recombined tissue after RIC administration. RIgG treatment resulted in significantly increased apoptotic levels in the recombined tissue compared to non-recombined, whereas the effects of RH2AX treatment on the tissue were independent of tissue recombination.

As expected, proliferation in the small intestines of tamoxifen administered mice was generally higher compared to vehicle administered mice, as assessed by staining for Ki67 (Figure 5.7a). Unexpectedly, in both non-recombined and recombined intestines, treatment with RIgG increased proliferation, in comparison with either untreated (no RIC) or RH2AX-treated (Figure 5.7 d). Both treatments significantly increased the number of proliferating cells in the recombined compared to the non-recombined tissue.

In conclusion, RIC treatment induced DNA damage in cells of both *Apc*-proficient and -deficient small intestines, increased cell death by apoptosis and proliferation.

a

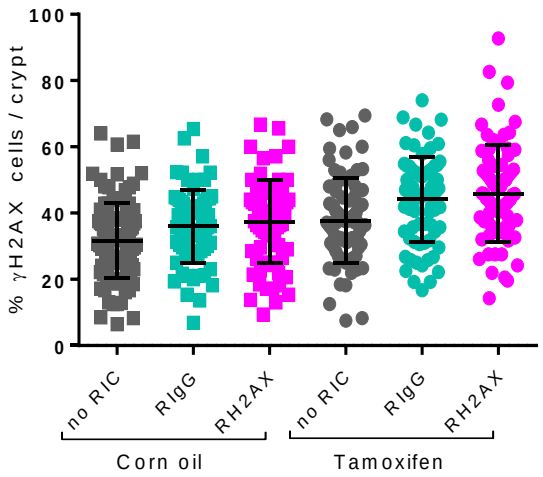

a		Corn oil			Tamoxifen		
		no RIC	RIgG	RH2AX	no RIC	RIgG	RH2AX
Corn oil	no RIC						
	RIgG	**					
	RH2AX	***					
Tamoxifen	no RIC	***					
	RIgG		****		**		
	RH2AX			***	***		

b

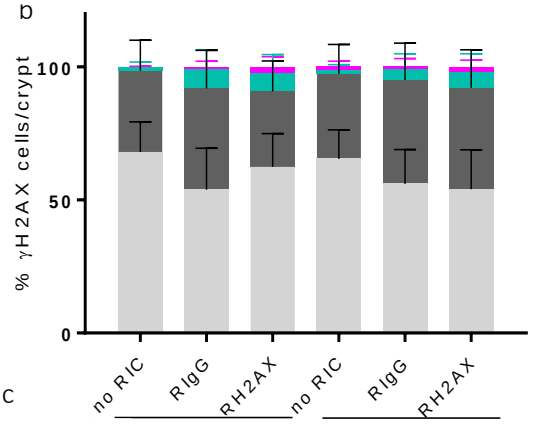

c

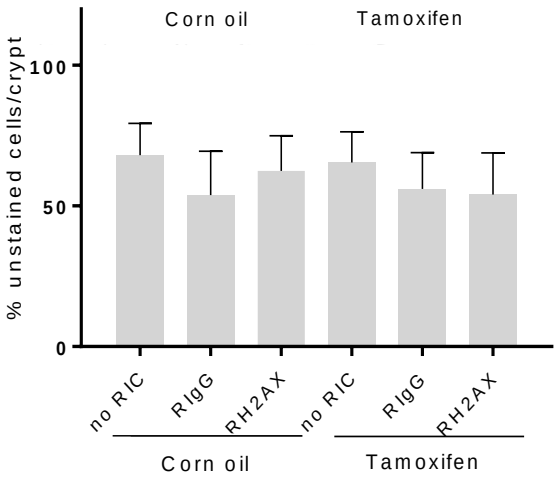

c		Corn oil			Tamoxifen		
		no RIC	RIgG	RH2AX	no RIC	RIgG	RH2AX
Corn oil	no RIC						
	RIgG	****					
	RH2AX	****					
Tamoxifen	no RIC						
	RIgG				****		
	RH2AX				***	**	

d

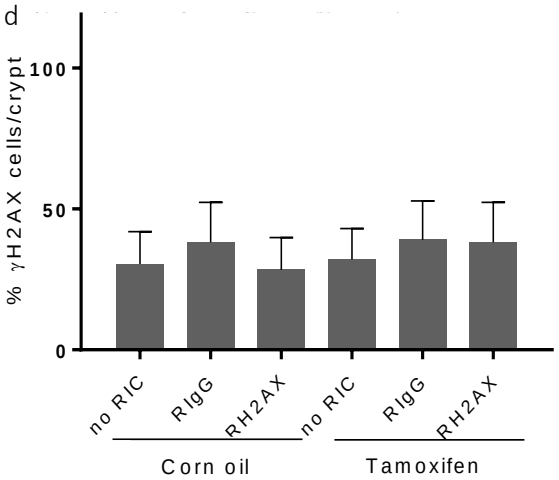

d		Corn oil			Tamoxifen		
		no RIC	RIgG	RH2AX	no RIC	RIgG	RH2AX
Corn oil	no RIC						
	RIgG						
	RH2AX						
Tamoxifen	no RIC						
	RIgG		****		*		
	RH2AX			****	*		

Figure continued on next page, legend follows.

e

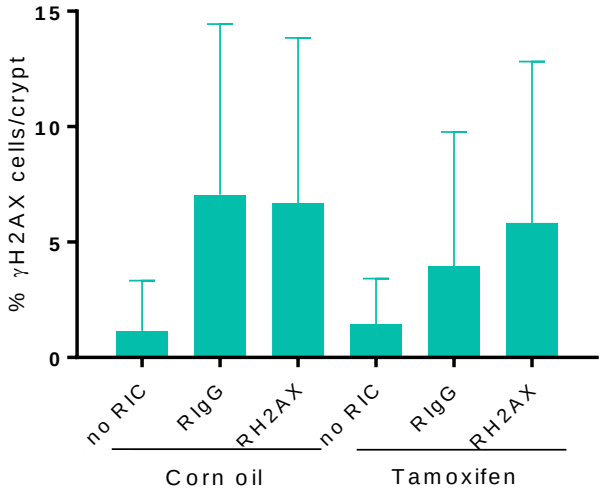

e		Corn oil			Tamoxifen		
		no RIC	RIgG	RH2AX	no RIC	RIgG	RH2AX
Corn oil	no RIC						
	RIgG	****					
	RH2AX	****					
Tamoxifen	no RIC	*	**				
	RIgG				*		
	RH2AX				****		

f

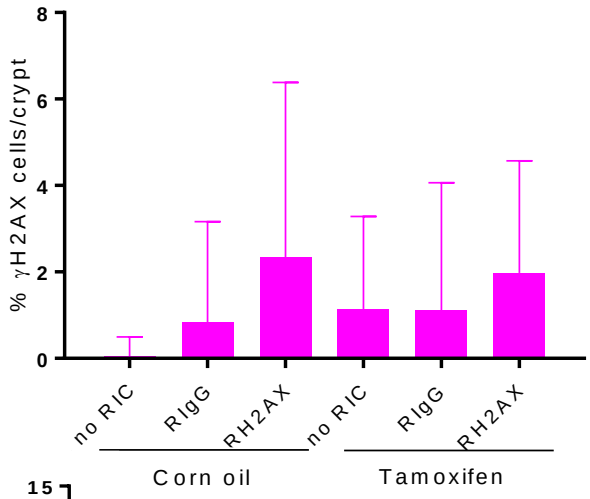

f		Corn oil			Tamoxifen		
		no RIC	RIgG	RH2AX	no RIC	RIgG	RH2AX
Corn oil	no RIC						
	RIgG	***					
	RH2AX	****					
Tamoxifen	no RIC	****					
	RIgG				*		
	RH2AX				*		

unstained medium low high

g

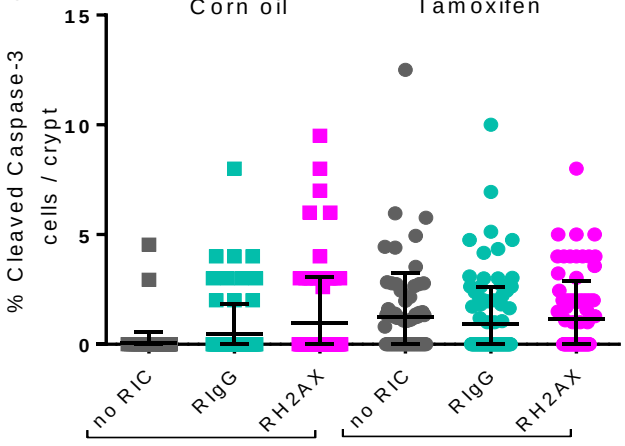

g		Corn oil			Tamoxifen		
		no RIC	RIgG	RH2AX	no RIC	RIgG	RH2AX
Corn oil	no RIC						
	RIgG	***					
	RH2AX	****					
Tamoxifen	no RIC	****					
	RIgG		*				
	RH2AX						

h

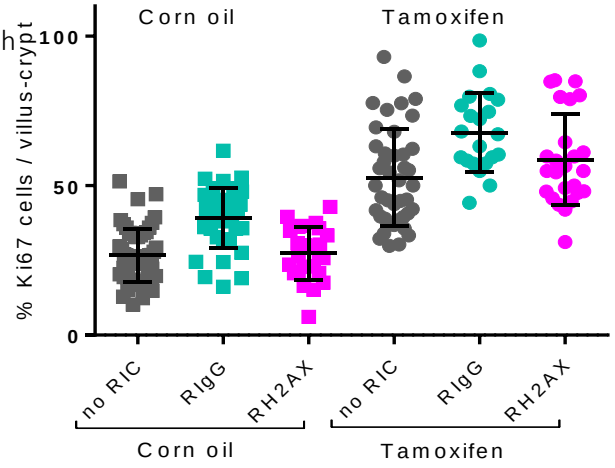

h		Corn oil			Tamoxifen		
		no RIC	RIgG	RH2AX	no RIC	RIgG	RH2AX
Corn oil	no RIC						
	RIgG	****					
	RH2AX		****				
Tamoxifen	no RIC	****					
	RIgG		****				
	RH2AX			****		*	

Figure legend on next page.

Figure 5.7 The biological effects on the small intestine following treatment with 1MBq of ^{111}In-anti-γH2AX-TAT in the VilCre^{ER} Apc$^{fl/fl}$ mouse model.

Tamoxifen induced (3x 60 mg / kg) or vehicle (corn oil) gavaged *VilCre^{ER} Apc$^{fl/fl}$* mice were injected intravenously 3 days later with ^{111}In-anti-γH2AX-TAT or ^{111}In-anti-IgG-TAT (1 MBq / µg; 5µg/mouse). 24h later, mice were scanned by SPECT/CT imaging and then sacrificed to harvest the tissue. The small intestine was collected and fixed overnight in 4% PFA, after which it was immersed in 20% sucrose, before cryopreservation. 5µm sections were immunohistochemically stained for (a - f) γH2AX, (g) cleaved caspase 3 and (h) Ki67. (b) γH2AX staining intensities were stratified into (c) unstained, (d) low, (e) medium and (f) high. The scoring for γH2AX and Ki67 was performed manually whilst for cleaved caspase-3 automatically using an in-house macro script on Fiji software. The percentage of stained cells per crypt is shown ± SD for n = 3. Two-tailed Mann-Whitney test was performed; tables next to each graph shows statistics results; * $p \leq 0.05$, ** $p \leq 0.01$, *** $p \leq 0.001$, **** $p \leq 0.0001$.

5.4.2 Large intestine

Recombination in the large intestine significantly increased γH2AX levels, similarly to the small intestine (Figure 5.8 a). The number of γH2AX positive cells in the *Apc*-proficient and -deficient large intestine was higher following either RIgG or RH2AX administration (Figure 5.8 a). This suggests that, similar to the small intestine, RIC treatment caused an additional DNA damage in the large intestine, irrespectively of the genotype).

The effects of RIgG treatment on the overall percentage of cells with combined γH2AX staining intensities were independent of tissue recombination (Figure 5.8 a). However, looking at each staining intensity level separately, whilst there was a significant decrease in the number of cells with medium γH2AX levels following RIgG treatment on the recombined tissue, there was a significant increase in the number of cells with high γH2AX levels (Figure 5.8 b, e - h). This probably indicates that RIgG treatment in the recombined tissue upgraded DNA damage in cells with medium γH2AX staining levels to cells with high γH2AX staining levels.

Following RH2AX treatment, the percentage of cells with combined γH2AX staining intensities was significantly higher in the recombined compared to the non-recombined tissue (Figure 5.8 a), which was due to significantly increased number of cells with low, medium and high DNA damage levels (Figure 5.8 b, e - h).

RIgG treatment on the non-recombined tissue had significantly higher levels of low and medium γH2AX staining intensities compared to RH2AX. However, on the recombined tissue RH2AX treatment had significantly higher levels of medium γH2AX staining intensities compared to RIgG. These observations indicate that RH2AX effects on the recombined tissue might be attributed to its epitope specificity.

Both non-recombined and recombined tissues had significantly decreased apoptotic levels after RIC treatment (except for RH2AX treatment on the non-recombined tissue, which had no effect compared to untreated) and significantly higher proliferation index (Figure 5.8 c and d). Generally, the recombined tissue had significantly higher levels of apoptotic and proliferating cells in comparison to the non-recombined. Particularly, the effects on proliferation were more profound on both non-recombined and recombined tissues following RIgG treatment.

a

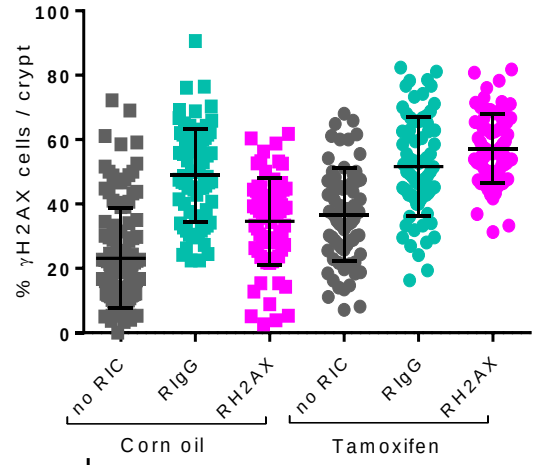

a		Corn oil			Tamoxifen		
		no RIC	RIgG	RH2AX	no RIC	RIgG	RH2AX
Corn oil	no RIC						
	RIgG	****					
	RH2AX	****					
Tamoxifen	no RIC	****					
	RIgG				****		
	RH2AX			****	****		

b

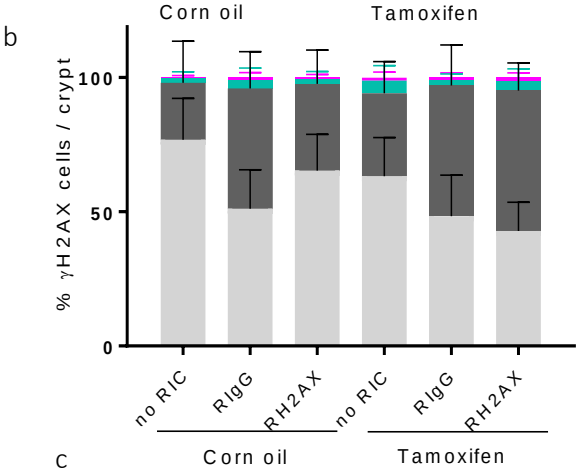

c

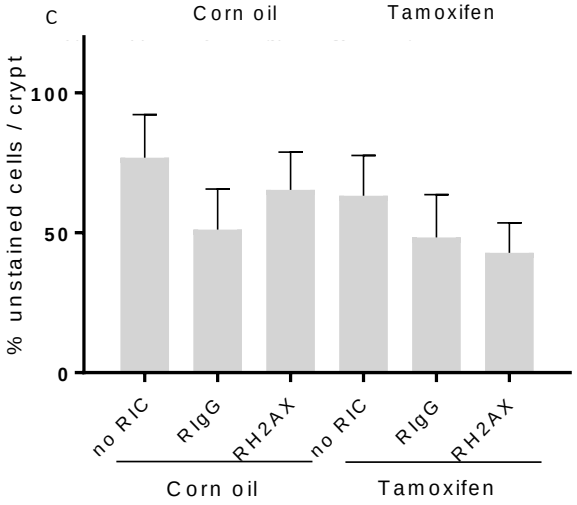

c		Corn oil			Tamoxifen		
		no RIC	RIgG	RH2AX	no RIC	RIgG	RH2AX
Corn oil	no RIC						
	RIgG	****					
	RH2AX	****					
Tamoxifen	no RIC	****					
	RIgG				****		
	RH2AX				****	**	

d

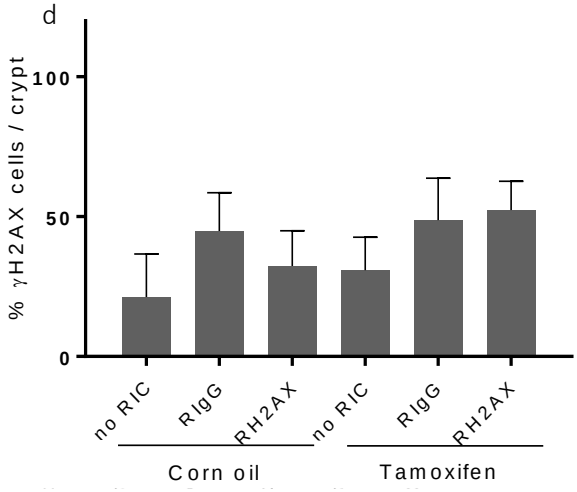

d		Corn oil			Tamoxifen		
		no RIC	RIgG	RH2AX	no RIC	RIgG	RH2AX
Corn oil	no RIC						
	RIgG	****					
	RH2AX	****	****				
Tamoxifen	no RIC	****					
	RIgG				****		
	RH2AX			****	****		

Figure continued on next page, legend follows.

e

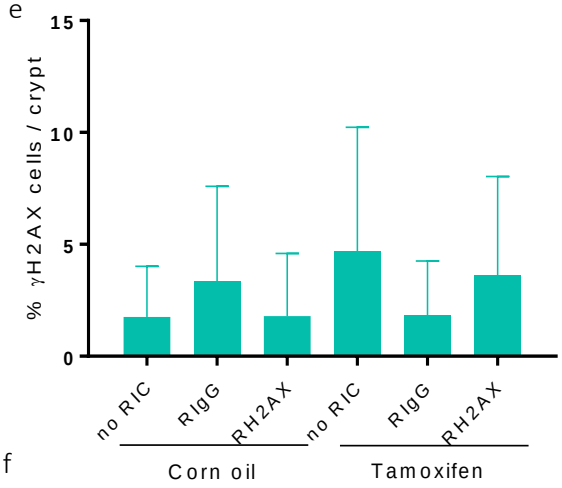

e		Corn oil			Tamoxifen		
		no RIC	RIgG	RH2AX	no RIC	RIgG	RH2AX
Corn oil	no RIC						
	RIgG	*					
	RH2AX		*				
Tamoxifen	no RIC	***					
	RIgG		*		**		
	RH2AX			**	*		

unstained high
low medium

f

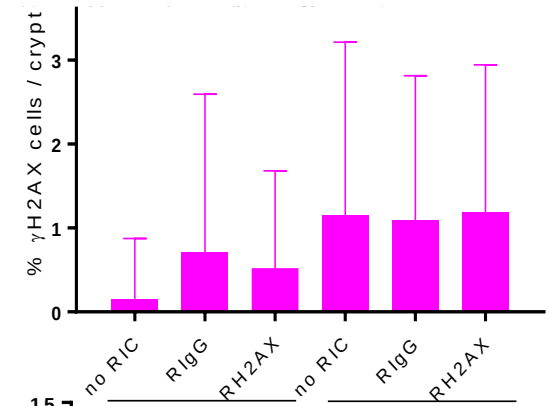

f		Corn oil			Tamoxifen		
		no RIC	RIgG	RH2AX	no RIC	RIgG	RH2AX
Corn oil	no RIC						
	RIgG	**					
	RH2AX	**					
Tamoxifen	no RIC	****					
	RIgG		*				
	RH2AX			*			

g

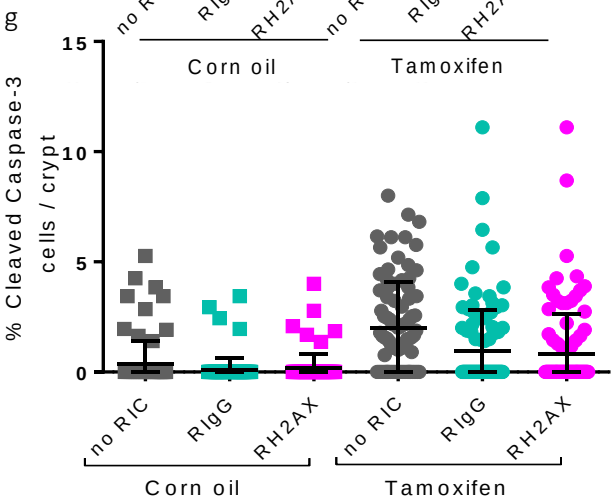

g		Corn oil			Tamoxifen		
		no RIC	RIgG	RH2AX	no RIC	RIgG	RH2AX
Corn oil	no RIC						
	RIgG	*					
	RH2AX						
Tamoxifen	no RIC	****					
	RIgG		****		****		
	RH2AX			**	****		

h

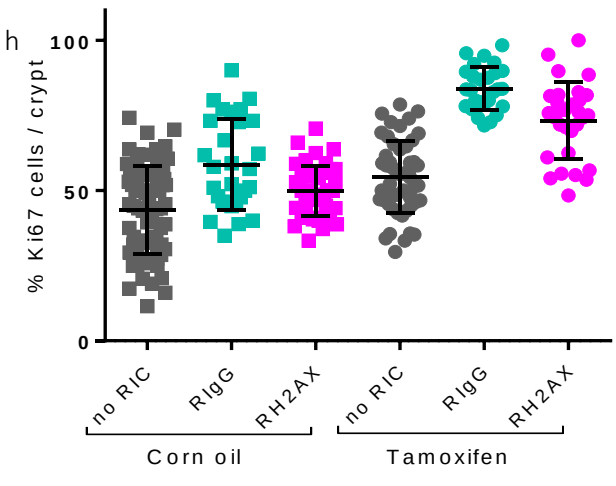

h		Corn oil			Tamoxifen		
		no RIC	RIgG	RH2AX	no RIC	RIgG	RH2AX
Corn oil	no RIC						
	RIgG	****					
	RH2AX	*	**				
Tamoxifen	no RIC	****					
	RIgG		****		****		
	RH2AX			****	****	***	

Figure legend on next page.

Figure 5.8 The biological effects on the large intestine following 1MBq of ^{111}In-anti-γH2AX-TAT in the VilCre^{ER} Apc$^{fl/fl}$ mouse model.

Tamoxifen induced (3x 60 mg / kg) or vehicle gavaged *VilCre^{ER} Apc$^{fl/fl}$* mice were injected 3 days later intravenously with ^{111}In-anti-γH2AX-TAT or ^{111}In-anti-IgG-TAT (1 MBq / µg; 5 µg / mouse). 24h later mice were imaged by SPECT/CT and then sacrificed to harvest tissue. The large intestine was collected and fixed overnight in 4% PFA after which it was immersed in 20% sucrose, before cryopreservation. 5µm sections were immunohistochemically stained for (a, b) γH2AX, (c) cleaved caspase 3 and (d) Ki67. (b) γH2AX staining intensities were stratified into (e) unstained, (f) low, (g) medium and (h) high. The scoring for γH2AX and Ki67 was performed manually whilst for cleaved caspase 3 automatically using an in-house macro script on Fiji software. The percentage of stained cells per crypt is shown ± SD for n = 3. Two-tailed Mann-Whitney test was performed; tables next to each graph shows statistics results; * $p \leq 0.05$, ** $p \leq 0.01$, *** $p \leq 0.001$, **** $p \leq 0.0001$.

5.5 Discussion

Apc tumour suppressor gene mutations are found in 57% of sporadic CRC cases (Furuuchi *et al.* 2000). Animal studies have shown that *Apc* deficiency alone within the intestine can initiate tumourigenesis (Sansom *et al.* 2004). Coupled with increased cellular proliferation and decrease in differentiation, *Apc* deficiency increases the levels of H2AX transcriptional levels (Reed *et al.* 2008). Data from this project, described in detail in section 3.2, shows that irrespective of crypt size, the number of cells with γH2AX foci is also increased in *Apc*-deficient mouse tumour models.

Cancer cells tend to be genomically unstable and many cancer treatments work by inducing DNA lesions. Thus, cancer cells have higher levels of DNA damage compared to normal cells (Negrini *et al.* 2010). To exploit this, Cornelissen *et al.* (2011) have developed ^{111}In-anti-γH2AX-TAT, a radioactive antibody that accumulates at sites of DNA damage *in vitro* and *in vivo,* and with the potential for numerous clinical applications, such as identifying surgical margins and non-macroscopic tumours. It can access any cell; however, its retention within the nucleus depends on its specificity for γH2AX.

We aimed to image DNA damage in two conditional intestine-specific *Apc*-deficient mouse models, without prior treatment with IR. One mouse model represented the early stages of CRC development, whereas the other represented established macroscopic tumours. Our hypothesis was that soon after intestinal *Apc* deficiency, or within well-established *Apc*-deficient tumours, there would be significantly higher levels of endogenous γH2AX foci. We could then be able to identify the presence of abnormal pre-cancerous *Apc*-deficient intestinal regions *in vivo* using SPECT imaging. By identifying the biodistribution of the RIC within these mouse models, we assessed whether it localised specifically to *Apc*-deficient regions.

5.5.1 *In vivo* imaging of early intestinal lesions with ^{111}In-anti-γH2AX-TAT antibody.

In vivo SPECT-CT imaging 24h after treatment with low SA RH2AX or RIgG (1 MBq/μg) in the early CRC mouse model (*VilCre^{ER} Apc$^{fl/fl}$*), induced by IP injection of tamoxifen, showed no obvious differences in the pattern of RIC localization. Unfortunately, IP injection of the vehicle (corn oil) or tamoxifen caused unexpected peritonitis to mice, in the Oxford animal facility, which had not been observed previously at Cardiff. This occurred despite the fact that the same protocol was carried out at Oxford by an experienced and competent personal licence holder, using identical reagents and equipment, on mice that were transferred from Cardiff's animal facility to Oxford. When

injected in a control animal, RIC is usually distributed in organs rich in blood vessels such as heart and liver (Cornelissen *et al.* 2012), hence inflammation in the abdomen of these control mice, due to peritonitis, altered SPECT imaging results, showing radioactivity accumulation throughout the abdomen.

The simplest way to overcome this problem was to change our induction method. Using oral gavage, which also had a better recombination compared to IP injection (Figure 3.6), resolved the peritonitis problem caused by IP, resulting in SPECT images which had otherwise normal RIC biodistribution, except for the intense RH2AX uptake in the upper intestinal track. Subsequent, radioactivity measurements from each organ, confirmed the SPECT imaging results. Namely, the proximal small intestine and the large intestine as a whole, were the only tissues with significantly higher levels of uptake of the specific RIC (RH2AX). High RH2AX uptake within the *Apc*-deficient small and large intestines was not previously observed in other mouse models with healthy intestinal tissue (Cornelissen *et al.* 2012). This demonstrated that RH2AX was prevalent in tissues where DNA damage was present without the additional need of other sources of DNA damage. Therefore, *Apc* deficiency alone is enough for the attraction of RH2AX due to higher γH2AX expression.

5.5.2 Low specific activity effects of RIC in the intestine of the early CRC mouse model

RIC treatment increases the DNA damage levels of healthy and Apc deficient small and large intestines

Consistent with data from section 3.2, *Apc* deficiency increased the levels of DNA damage within the small and large intestine by additionally 6% and 13%, respectively. Both control and specific RIC (i.e. RIgG and RH2AX, respectively) had additionally 7 - 8% and 15 - 21% of cells with DNA damage in *Apc*-deficient small and large intestines, respectively. This effect was also observed in *Apc*-wt mice, as the RIC treatment increased the number of cells with DNA damage by additionally 4-5% and 11-25% in the small and large intestines, respectively. From these results, it can be extrapolated that RIC treatment has a greater effect on γH2AX levels in the large intestine compared to the small intestine, which suggests different susceptibilities to cellular insults between the two tissues. In the *Apc*-wt small intestine, RIgG and RH2AX increased the number of cells with medium and high γH2AX intensity levels whereas, in the *Apc*-deficient small intestine, they increased the low and medium γH2AX intensity levels. In the *Apc*-wt large intestine, RIgG and RH2AX increased the number of cells with low and high γH2AX intensity levels whilst particularly RIgG increased the number of cells with medium γH2AX intensity. In the *Apc*-deficient large intestine, RIC increased only low γH2AX

intensity levels. The increase in the extent of DNA damage in the presence of either of the two RICs, signifies that even low specific activity RIC can alter in some extent the DNA damage content, even where the genome is unaltered, most likely through ROS or directly through ionization of DNA. It is unknown, though, whether RH2AX generates more γH2AX foci in cells that already have γH2AX foci, or in cells with no previously existing γH2AX foci. The indirect effects or otherwise called 'the bystander effect' of radiation could also be a reason for the increase in the number of cells with low DNA damage (Nagasawa and Little 1992). This data also fuels the hypothesis that *Apc* status might affect the susceptibility of cells to low specific activity RIC, or that *Apc*-deficient cells cannot repair the low levels of DNA damage as efficiently as healthy cells, which is consistent with studies that link *Ap*c deficiency with genomic instability (Fodde *et al.* 2001; Leslie *et al.* 2003; Aoki *et al.* 2007; Dikovskaya *et al.* 2007; Méniel *et al.* 2015).

Levels of apoptosis vary between small and large intestines in response to treatment with RIC.

In the healthy small and large intestines, apoptosis of crypt cells is a rare event (Figure 5.7 c Figure 5.8 c); however, treatment with either the specific or non-specific RIC significantly increased the levels of apoptosis in the small intestine. This might be attributed to the presence of ROS, which oxidise proteins and damage DNA, leading to oxidative stress and cell death (England *et al.* 2006). For the actively proliferating cells, this could be interpreted as a DNA integrity protection mechanism.

In wt large intestine, RH2AX did not affect the apoptotic index of the healthy tissue; this could also be associated to the unchanged γH2AX levels following RH2AX treatment. However, the non-specific RIC treatment decreased the levels of apoptosis in wt large intestine. The different RIC effects on apoptosis between wt small and large intestines indicate that changes in apoptosis could also be attributed to different response mechanisms to ROS presence between the two tissues.

In both small and large intestines, *Apc* loss induced apoptosis (Figure 5.7 c and 5.8 c) which is in agreement with the previous findings of Sansom *et al.* (2004). Following *Apc* loss, WNT signalling is hyperactivated; this drives *c-Myc* transcription, which in turn is known to induce proliferation and apoptosis (Prendergast 1999; Vafa *et al.* 2002; Pelengaris *et al.* 2002). Mitotic cell death might be another reason for the increased apoptotic levels, due to the role of APC in mitotic spindle formation, or due to replication-stress caused by excess proliferation (Vitale *et al.* 2011; Fodde *et al.* 2001; Kaplan *et al.* 2001).

In the *Apc*-deficient small intestine, RIC treatment did not further increase the number of cells undergoing apoptosis. This could suggest that the protective mechanism against ROS insult might no longer function properly following *Apc* loss. As such, APC might be playing an additional role in protection from DNA damage and accumulation of oxidised proteins, as it has been previously linked with respiratory ROS-dependent apoptosis (Cristofaro *et al.* 2015).

In the *Apc*-deficient large intestine, RIC treatment significantly decreased the number of cells with medium γH2AX staining (Figure 5.8 g), which might have contributed to the unexpected decrease in the number of apoptotic cells, without entirely abolishing the *Apc* loss-related apoptosis

RIC treatment in the Apc-deficient intestine leads to increased intestinal proliferation

Increased proliferation following *Apc* loss is one of the features previously observed by Sansom *et al.* (2004). Our data also showed small but significant increase in small and large intestinal proliferation levels, between wt and *Apc*-deficient mice.

In wt mice, the specificity of the RIC of low SA (1MBq/μg) had different effects on proliferation of the intestinal crypt epithelium depending on the tissue treated. Whilst in the wt or *Apc*-deficient small intestine only RIgG treatment increased proliferation (Figure 5.7d), in the large intestine, both types of RIC treatment, but more profoundly the RIgG, resulted in a significant increase in proliferation Figure 5.8 d). This implies that low specific activity RIC treatment can induce higher proliferation when not targeted to the nucleus, which could be a cellular response to ROS production and protein oxidization.

In the presence of DNA damage the specificity of RH2AX sequesters it in the nucleus compared to RIgG whose concentration in the cytoplasm of cells is higher compared to RH2AX, as reported by Cornelissen *et al.* (2007). This explanation only satisfies the small, but not large, intestinal responses to RIC as they both had comparable DNA damage levels.

5.5.3 *In vivo* imaging of Apc deficient intestinal tumours

SPECT imaging following 24h treatment with low SA RIgG or RH2AX (0.9 MBq / μg) in the intestinal tumour mouse model (*Lgr5Cre^{ER} Apc$^{fl/fl}$*) showed variable radioactivity uptake in several organs. A general radioactivity pattern was observed in the heart, liver and sometimes carotid arteries and bladder. Importantly, radioactivity accumulation was also observed in various areas of the abdomen, particularly in *Apc$^{fl/fl}$* mice following treatment with RIC, mainly over the vena cava where

the large intestine lies, and at the upper part of the abdomen, where the small intestine lies and is likely to develop tumours in this mouse model.

The imaging parameters used for these *in vivo* imaging experiments gave a sufficient signal-noise ratio to detect the hot-spot zones within the abdomen. However, it may be possible to improve the imaging performance by either increasing the time post treatment before the SPECT scan, which could give a better tumour to blood ratio, thereby lowering background levels, or by optimizing the amount of antibody injected into the mice, which could again result in better tumour to blood ratio.

Whilst biodistribution assays showed a radioactivity uptake in the blood, lungs, liver, spleen, and kidneys of $Apc^{+/+}$ mice treated with RIgG or RH2AX, and $Apc^{fl/fl}$ mice treated with RH2AX, in RIgG treated $Apc^{fl/fl}$ mice there was decreased uptake of radioactivity in the blood, spleen, small and large intestines and kidneys, whereas their intestinal tumours accumulated radioactivity of approximately 5% ID / g. The generally lower radioactivity levels in organs and tissues of RIgG treated $Apc^{fl/fl}$ mice could be a result of RIgG sequestration away from the bloodstream of the animal, in intestinal tumours or in faeces of $Apc^{fl/fl}$ mice which usually have irregular defecation due to tumour development.

Increased tumoural radioactivity of the RICs is usually due to Enhanced Permeability and Retention (EPR) of macromolecules with molecular weight > 40 kilo Daltons (kDa) in tumours as opposed to normal tissue (Matsumura and Maeda 1986; Greish 2007). Hence, the radioactivity uptake of approximately 5% ID / g in tumours of RIgG treated $Apc^{fl/fl}$ mice, is likely to be due to the EPR effect. Unfortunately, only one mouse in the RH2AX treated $Apc^{fl/fl}$ group of mice had macroscopic tumours. More biological replicates need to be obtained, to determine whether RH2AX specificity to γH2AX could enhance tissue radioactivity uptake.

5.6 Summary

In conclusion, *in vivo* imaging of intestinal dysplasia can be achieved with low SA RH2AX treatment of mice, following intestine-specific deletion of *Apc* by oral administration of tamoxifen. *Apc*-deficient intestinal tumours can also be imaged by low SA RIgG, likely to be due to the EPR effect, and possibly by low SA RH2AX. The latter remains to be confirmed by increasing the animal number with intestinal tumours treated by RH2AX. This will also allow the comparison of RH2AX uptake to RIgG in order to assess whether any of its uptake is likely to be a result of RH2AX specificity to DNA

damage in tumours. In the next chapter, we describe the development of *ex vivo* human patient-derived CRC spheroid model of γH2AX focus formation for testing the therapeutic effects of RH2AX.

6 Development of *ex vivo* human patient-derived models of γH2AX focus formation for testing of RH2AX therapy

6.1 Introduction

This project explored the use of RH2AX as a theragnostic antibody in CRC mouse models; however, it is well known that the translation of drug studies into the clinic can be hindered by multiple factors, including complicated genetic mutations involved in human tumour development. Hence, we speculated that γH2AX levels in human tumours may vary from person to person. Our ultimate aim, which due to time constraints was not accomplished, was to induce DNA damage in human-derived CRC spheroids with low γH2AX levels and subsequently treat them with high specific activity of RH2AX antibody to investigate its killing effects, similarly to the study of Cornelissen *et al.* (2011) on breast cancer cell lines. Hence, this chapter is looking into using common chemotherapeutics, cisplatin and 5FU, to induce DNA damage in human CRC cell line (HCT116)-derived spheroids and *Apc*-deficient mouse-derived organoids, respectively.

6.2 Inducing DNA damage in intestinal organoids using common chemotherapeutics

6.2.1 Variable γH2AX levels in human tumour derived spheroids.

To investigate γH2AX levels in human CRC, we used 4 lines of human CRC tumour-derived spheroids (isolations 38, 58, 65 and 74) generously provided by Prof. Trevor Dale's group. Whole mount γH2AX immunofluorescence and confocal imaging were performed and γH2AX staining gave variable patterns in the different tumour isolations. Quantification in organoids derived from isolation no.58 (Figure 6.1) showed that 5.3 ± 4.7% of cells were positive for γH2AX. Most cells were either of low (≤10 foci) or high (panuclear) γH2AX intensities.

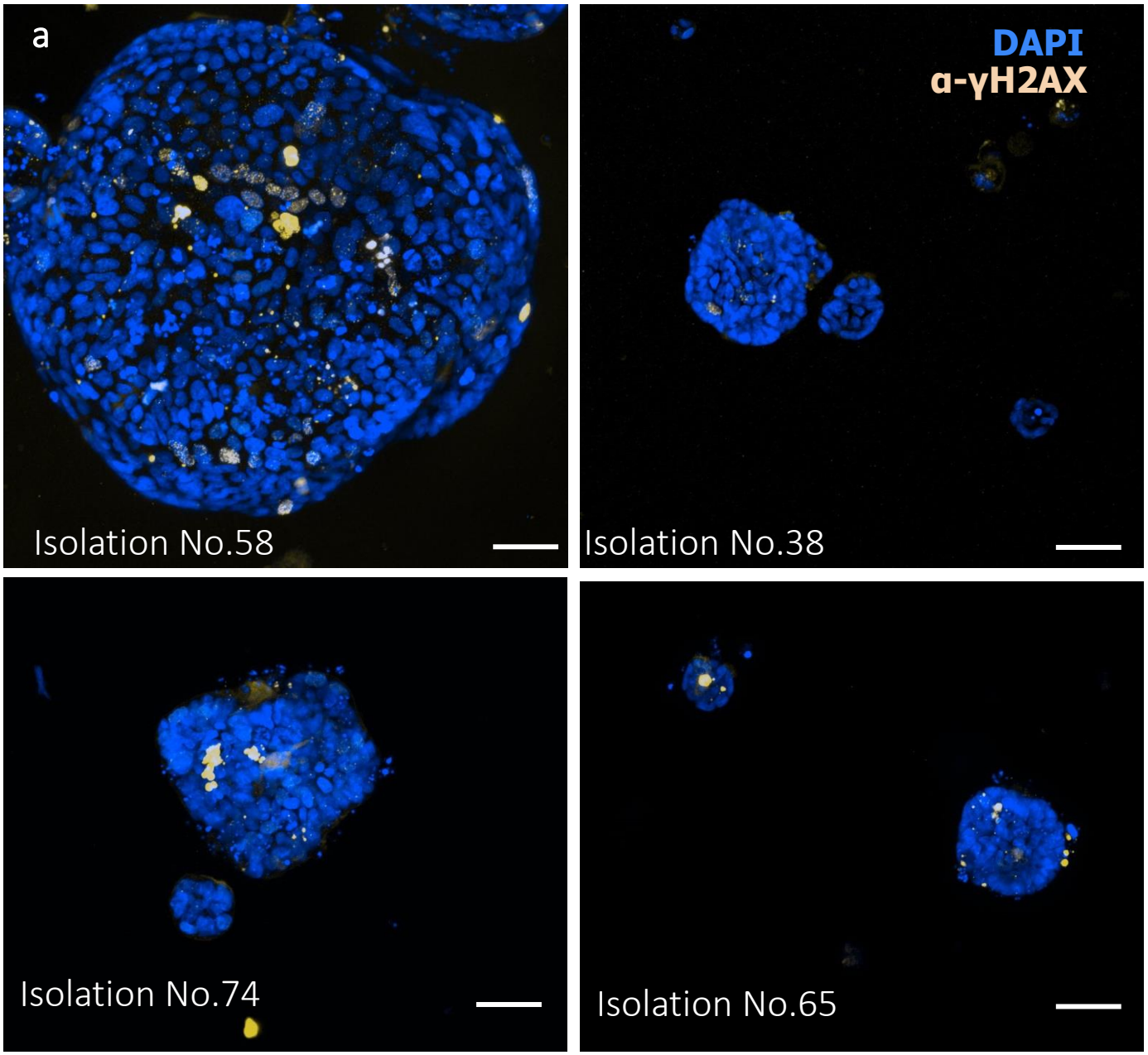

b

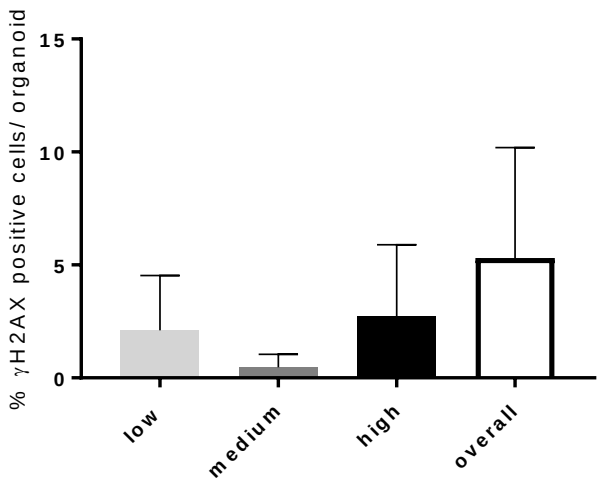

Figure 6.1 γH2AX levels in human CRC tumour derived spheroids

(a) Maximum projection representative images of organoids from isolation no. 58, 38, 74, 65. Scale bar = 50 µm (b) Percentage of overall γH2AX positive cells or γH2AX positive cells with low (≤ 10 foci), medium (> 10 foci) and high (panuclear) staining intensity levels per organoid from isolation no. 58 (*n* = 13, Error bars = SD).

6.2.2 Determining EC_{50} for cisplatin and 5FU in HCT116 and *Apc*-deficient murine-derived organoids, respectively

Our ultimate aim, which due to time constraints was not accomplished, was to induce DNA damage in human-derived CRC spheroids with low γH2AX levels and subsequently treat them with high specific activity of RH2AX antibody to assess cell killing. Nevertheless, we identified the drug response curve for two common chemotherapeutics, cisplatin and 5FU, in the human CRC cell line (HCT116)-derived spheroids and *Apc*-deficient organoids derived from the small intestine of induced *VilCre^{ER} Apc$^{fl/fl}$* mice, respectively.

To induce DNA damage in HCT116-derived spheroids, single cells were plated in a 96-well plate a density of 4000 cells/10ul matrigel. Three days after seeding, spheroids were treated with cisplatin at a range of concentrations (0 – 0.3 mg / ml). A cell viability assay was performed using CellTitreGlo 24h after treatment to quantify the luminescence signal which reflected ATP levels in the wells (Riss *et al.* 2013). The drug concentration with half maximal response (EC_{50}) was interpolated from the killing curve for cisplatin on HCT116 spheroids and it was found to be 4 μg / ml (Figure 6.2). This concentration was then used to analyse γH2AX levels of spheroids (3 days post single cell seeding) at various time points after treatment (0, 1, 2, 4, 8, 12, 24h; Figure 6.3 a). Quantification of γH2AX whole mount immunofluorescence staining (Figure 6.3 b) showed a background level of DNA damage within HCT116 spheroids, with ~14% of cells being γH2AX-positive. A peak of damage was seen at 12h, where 80% of cells were γH2AX-positive. By 24h post treatment, there was a reduction in γH2AX-positive cells (~49%) in spheroids, signifying partial resolution of DNA damage.

To determine the killing curve for 5FU in *Apc*-deficient organoids, *VilCreER Apc$^{fl/fl}$* mice were induced with tamoxifen (60mg / kg, 3x IP injection in a day) and 3 days p.i. the first 15cm of the small intestine were collected and processed for crypt extraction to form organoids, as per section 2.6. Organoids were enzymatically digested after 7 days of culture. Single cells were plated in a 96-well plate at a density of 4000 cells / 10ul matrigel. Three days post seeding, organoids were treated with 5FU in a range of concentrations (0 – 10 mg/ml; Figure 6.4 a). Cell viability assay was performed by CellTitreGlo 72h post treatment. The EC_{50} was equal to 0.115 mg/ml (Figure 6.4b).

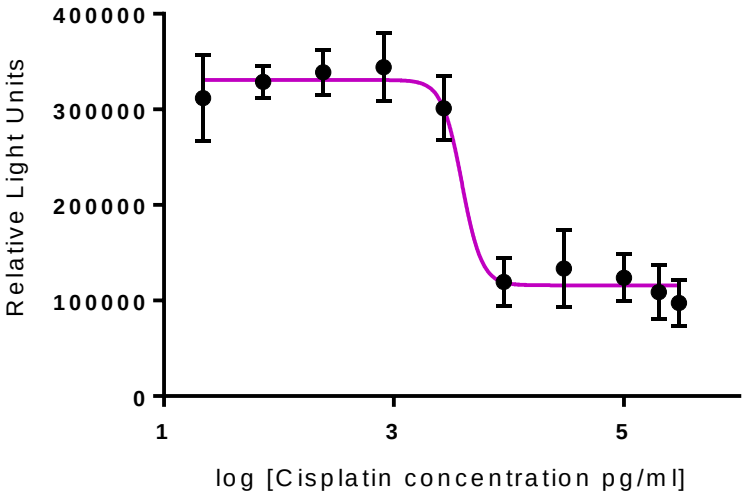

Figure 6.2 HCT116 spheroid response to cisplatin

A cell viability assay was performed by CellTitreGlo to quantify the luminescence signal which reflects the ATP levels in a well. Relative light units indicate the luminescence signal; N = 1; EC_{50} = 3.87 µg/ml. Media was additionally supplemented by 30 % with growth factors to compensate for being diluted by cisplatin or distilled water addition. Mean values are shown ± SD.

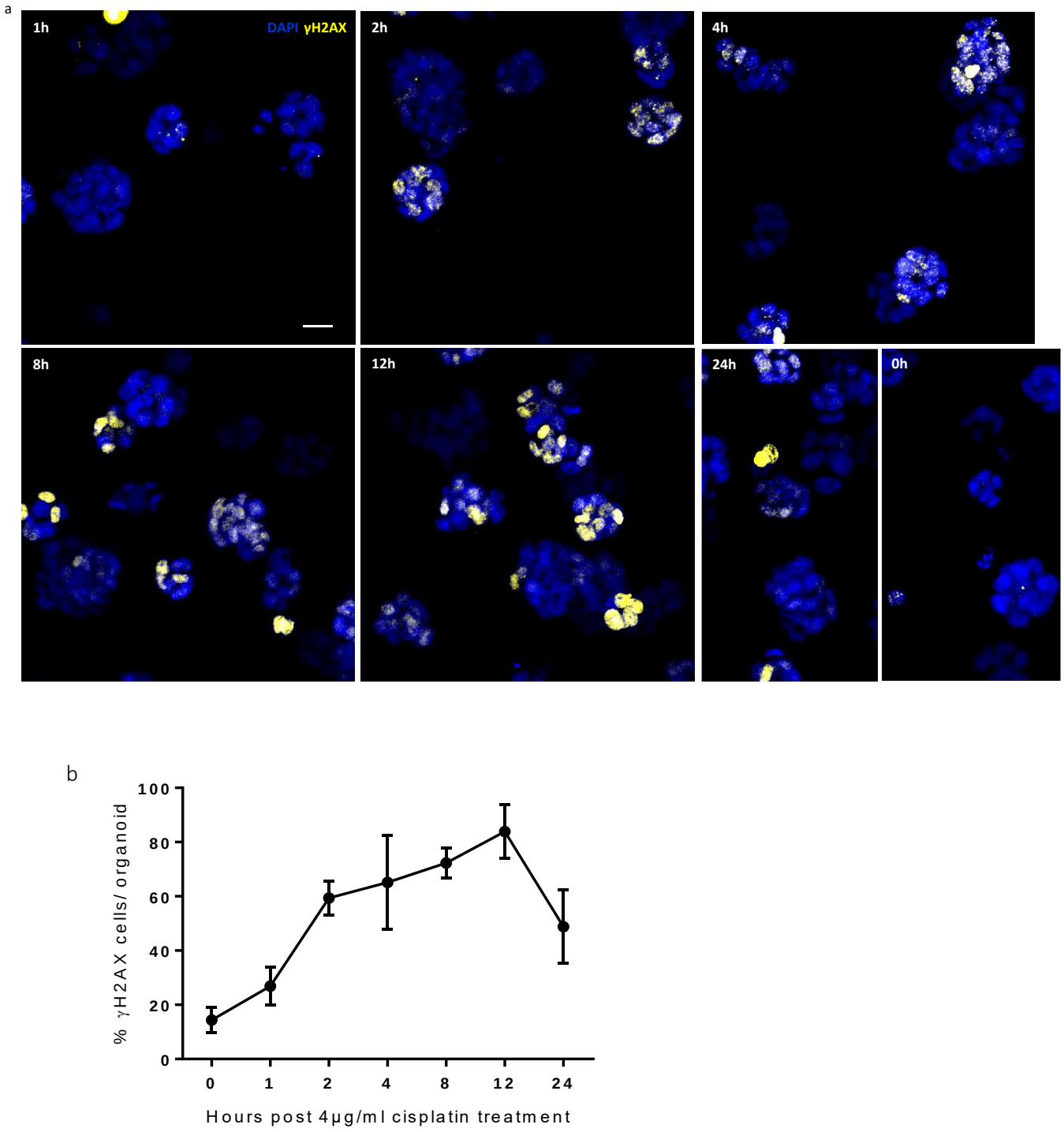

Figure 6.3 Increased γH2AX levels in HCT116 cells post cisplatin treatment.

Three day old organoids were treated with 4 µg/ml cisplatin for 0 to 24 h. γH2AX whole mount immunofluorescence was performed and imaged by confocal imaging. (a) Representative maximum projection images of 90 z-slices are shown (each z-slice = 5.7 µm). Scale bar = 20 µm; γH2AX = yellow, DAPI = blue. (b) Percentage of γH2AX positive cells per organoid is shown. Mean values ± SD.

a

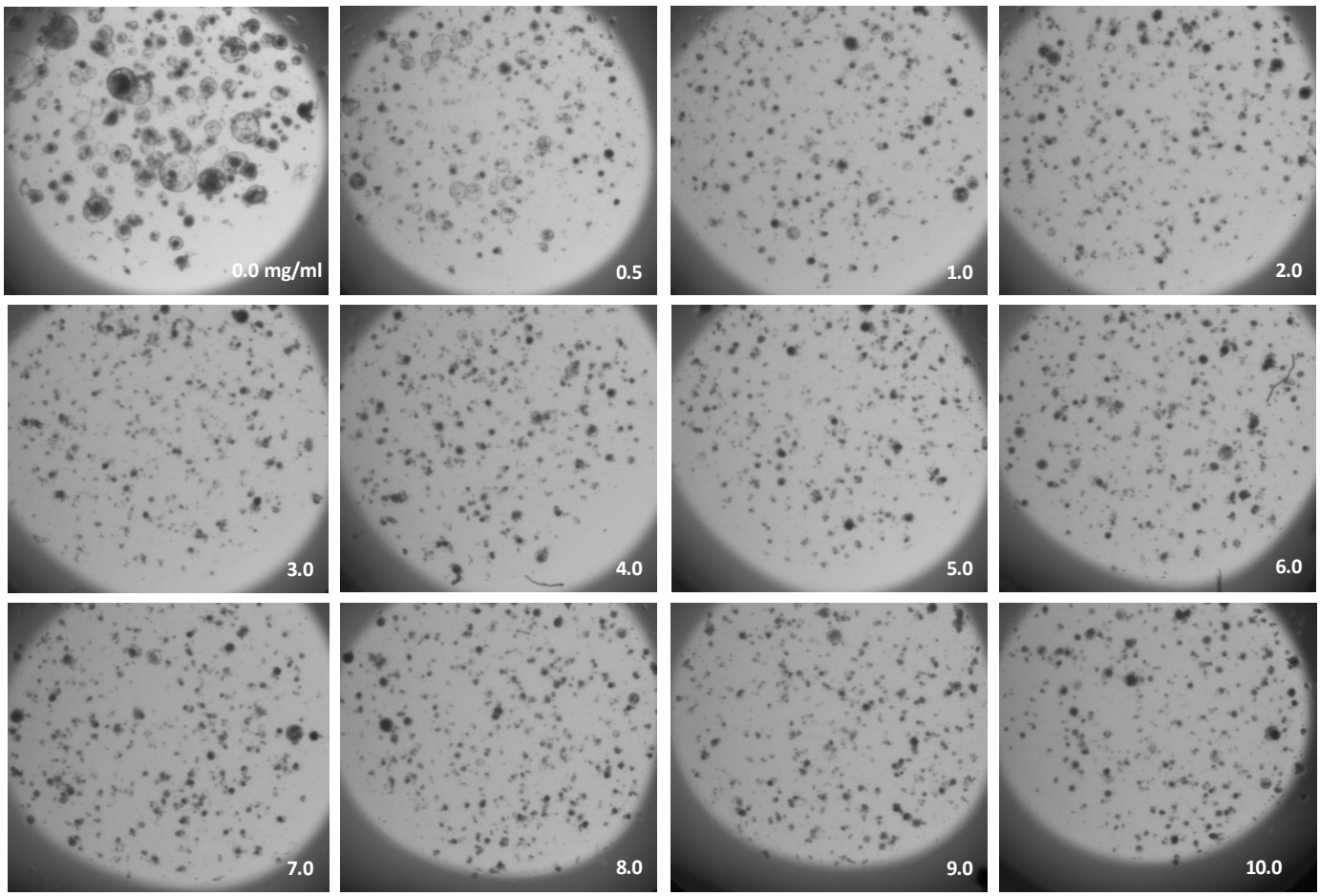

b

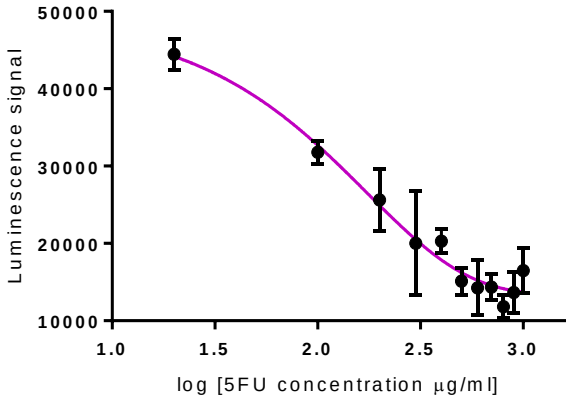

Figure 6.4 VilCre^{ER} Apc$^{fl/fl}$ organoid response to 5FU treatment.

Three days post seeding, *VilCre^{ER} Apc$^{fl/fl}$* organoids were treated with 5FU in a range of concentrations. Three days post treatment, (a) organoids were imaged with GelCount (Oxford Optonix) and (b) cell viability assay was performed by CellTitreGlo which allows quantification of luminescence signal which reflects the ATP levels in a well. Relative light units indicate the luminescence signal; N = 1; EC_{50} = 115 µg/ml. Media was diluted by 2% by cisplatin in distilled water. Mean values are shown ± SD.

6.3 Discussion

This project aimed to explore the use of RH2AX as both a diagnostic/imaging and therapeutic agent in CRC mouse models and organoids; however, the therapeutic part was not carried out due to unforeseen circumstances. As tumour development involves complicated genetics (Fearon and Vogelstein 1990), we speculated that γH2AX levels in human CRC tumours would vary between patients and so we tested this using human colorectal tumour-derived spheroids. Hence, based on a previous drug combination study carried out by Cornelissen *et al.* (2011) where chemotherapy (bleomycin, a chemotherapeutic used in breast cancer; Hecht 2000) was combined with RH2AX demonstrating reduction in breast cancer cell (MDA-MB-468) growth, we aimed to use RH2AX together with common CRC chemotherapeutics, either cisplatin or 5FU, to induce DNA damage in human tumour-derived spheroids with low γH2AX levels, in order to assess their effects on spheroid growth. Drug response curves were generated for cisplatin and 5FU in human CRC cell line (HCT116)-derived spheroids and *Apc*-deficient mouse-derived organoids respectively; unfortunately, we were unable to attain the therapeutic radioactivity dose (specific activity ≥ 3 MBq / μg) for RH2AX to complete our aim in carrying out the combination treatment.

Human CRC tumour-derived spheroids from different tumour isolations had variable levels of γH2AX, implying that the genetic background of each tumour affects the endogenous DNA damage levels (Figure 6.1). The hypothesis for the therapeutic value of this project is that RH2AX could promote cancer cell death in the presence of high levels of endogenous DNA damage. A previous study by Cornelissen *et al.* (2012) has demonstrated in a breast cancer cell line (MDA-MB-468) that cells with >10 γH2AX foci/ nucleus, induced with IR, were more likely to be killed by >3MBq/μg of RH2AX compared to those with <10 γH2AX foci/ nucleus. Hence, cells in tumours with low endogenous DNA damage levels (with <10 γH2AX foci/ nucleus) would probably not be killed.

To increase the extent of DNA damage in cells of tumour spheroids with low endogenous DNA damage levels, we used cisplatin or 5FU. We determined that the EC_{50} of cisplatin on HCT116 spheroids was 4 μg/ml (Figure 6.2), similar to previously published data on wt organoids (Grabinger *et al.* 2014) and that 12h post treatment spheroids had the maximum DNA damage levels, whereas at 24h, DNA damage was reduced (Figure 6.3). Knowledge of the γH2AX kinetics post treatment is necessary for drug combination assays, as the selection of the time of RH2AX treatment, could dictate its additive or synergistic effects. In addition, the EC_{50} for 5FU in murine *Apc*-deficient organoids was 0.115 mg/ml (72h treatment; Figure 6.4b) and was comparable to that determined in human CRC cell line-derived spheroids, Caco-2, after 24h treatment (Grabinger *et al.* 2014).

6.4 Summary

The variability in mutations occurring in human tumour development probably contributed to the differing γH2AX levels present in human CRC tumour-derived spheroids from different patient tumour isolations. Hence inducing DNA damage in human tumour-derived spheroids with low γH2AX levels prior to RH2AX treatment could allow assessment of the combination treatment effects on spheroid growth and consequently their translational potential.

7 General Discussion

The research presented in this thesis aimed to test in in vivo models the utility of RH2AX antibody for visualisation and treatment of lesions in CRC. The model system selected for this was the treatment of lesions in *Apc*-mutant mouse intestine. As a prerequisite, this required the presence of DNA damage in *Apc*-deficient intestine; hence, our first major finding demonstrated that intestinal *Apc* deficiency increases DNA damage levels, as assessed by γH2AX levels, in the small intestine of both dysplastic (*VilCre^{ER}Apc$^{fl/fl}$*) and tumour CRC mouse (*Lgr5Cre^{ER}Apc$^{fl/fl}$*) models. We provided evidence to suggest that *Apc*-deficiency-associated DNA damage is most likely generated through WNT signalling pathway activation and, more specifically, by *c-Myc* transcription. Next, we demonstrated for the first time that we can identify intestinal dysplasia through *in vivo* SPECT imaging, using low SA RH2AX treatment. Our findings on low SA effects of RIC treatment in intestinal dysplasia showed increased DNA damage levels in healthy and *Apc*-deficient small and large intestines, increased proliferation in the *Apc*-deficient tissue and variable levels of apoptosis depending on the tissue. These findings together indicate that DNA damage is induced by *Apc*-deficiency, and that there is the possibility to exploit the endogenously-increased DNA damage signal, γH2AX, to attract the RH2AX for *in vivo* imaging of intestinal dysplasia.

Demonstrating that intestinal *Apc* deficiency increases endogenous DNA damage levels complemented previous studies linking genomic instability with malignancy (Rao and Yamada 2013; Halazonetis *et al.* 2008), but also showed that the DDR pathway is employed in the intestine following *Apc* dysfunction. Two studies have also previously provided evidence that *Apc* loss contributes to DNA damage *in vivo*: Reed *et al.* (2008) used the *AhCreApc*$^{fl/fl}$ mouse model to show that *Apc* deficiency increased *H2AX* mRNA expression in intestinal cells, while Méniel *et al.* (2015) used the same model to show that *Apc* deficiency induced the DNA damage checkpoint proteins p53 and p21 in the mouse liver, due to increased levels of DSBs, as quantified by IHC for γH2AX and RAD51.

Our findings showed that although the Cre-LoxP recombination technique, which was used to excise *Apc* in *VilCre^{ER} Apc$^{fl/fl}$* mice, increases DNA damage levels itself, the majority was caused by deficiency of the *Apc* gene. It was demonstrated that the mechanism by which *Apc* deficiency contributes to increased DNA damage in the small intestine is most likely *via* WNT signalling pathway activation and, more specifically, by *c-Myc* transcription. c-MYC probably induces DNA damage through its oncogenic functions, possibly due to excessive proliferation of cells, leading to replication-fork stalling and collapse (Halazonetis *et al.* 2008). However, we cannot eliminate

the possibility that increased DNA damage by *Apc*-deficiency is also caused by APC loss of function related to microtubule spindle binding and chromosomal segregation (Green *et al.* 2005; Kaplan *et al.* 2001).

This study demonstrates, for the first time, that intestinal dysplasia driven by *Apc*-deficiency can be imaged *in vivo* in mice, through the endogenous γH2AX signal, which was found to attract RH2AX. The RIC was developed by Cornelissen *et al.* (2011), is an ^{111}In-radiolabelled antibody that recognizes the γH2AX DNA damage marker, can penetrate cell nuclei using a NLS-containing peptide (TAT) and can also be tracked *in vivo via* its radioactive emissions. It was previously shown that human-derived breast cancer xenografts could be imaged, in mice, using low SA RH2AX, in combination with DNA damaging agents IR or bleomycin (Cornelissen *et al.* 2011). A similar antibody, conjugated to ^{89}Zr instead of ^{111}In, was used for imaging early pancreatic cancer following chemotherapy (Knight *et al.* 2017). Thus, the novelty of our findings lies in the fact that RH2AX accumulation occurs in lesions without prior induction of DNA damage using IR or chemotherapy.

For the first time, we provide evidence for biological effects of low SA RIC treatment in the small and large intestine. Cornelissen *et al.* (2011) showed that *in vitro* treatment of the MDA-MB-468 breast cancer cell line with low SA RIC treatment, either RIgG or RH2AX, did not significantly increase the number of γH2AX foci/cell, and that cell survival was unaffected. However, we show that low SA RIgG or RH2AX treatments in the small and large intestine affect key biological processes (DNA damage, cell death, and cell division) *in vivo*.

The small and large intestines have different levels of radioresistance, with colonic LGR5$^+$ stem cells being more radioresistant compared to those of the small intestine (Hua *et al.* 2017). This might explain some of the differences in tissue response upon RIC treatment. Apoptosis does not occur often in the crypts of healthy small and large intestines, as observed in our findings and other studies (Sansom *et al.* 2004). However, in the presence of RIC, levels of apoptosis increase more readily in the small intestine than the large intestine. It is more likely that this occurs due to higher DNA damage levels that accumulate within the small intestine compared to the large intestine, and not because of the dysfunction of the large intestine in inducing apoptosis, as we show that *Apc* deficiency causes a similar increase in apoptosis in both small and large intestines.

Sansom *et al.* (2004) have shown that proliferation increases following intestinal *Apc* deficiency and our data showed similar patterns. A study by Kevin *et al*. (2013) showed that after *Apc* deficiency, RAC1 activity was increased and that it was responsible for the increase in ROS and activation of the NF-kB pathway, resulting in inflammation. The increase in proliferation following RIC treatment within the *Apc*-deficient intestine might signify that RIC treatment can

initiate proliferation through ROS production, which stimulates the stem cells to divide symmetrically or asymmetrically (Buongiorno *et al.* 2008; Myant *et al.* 2013). Symmetric division could either enhance tumourigenicity if it drives *Apc*-deficient stem cell self-renewal, or act as a safety mechanism where *Apc*-deficient stem cells divide to produce differentiated TA cells. This hypothesis could be tested *in vivo*, using TA- and CBC-labelled cells (e.g in $BMI1^+$ and $LGR5^+$ reporter mice), to identify $BMI1^+/LGR5^+$ asymmetric, $BMI1^+/BMI1^+$ or $LGR5^+/LGR5^+$ symmetric cell division determined by LGR5, BMI1 expression, and co-IF for α-TUBULIN (indicating dividing cells) as previously performed by Srinivasan *et al.* (2016).

Generally, RIgG delivers ionising radiation to cell contents non-specifically, and this will tend to increase ROS. RH2AX, due to its specificity for γH2AX, remains closer to the DNA for longer and delivers ionising radiation mainly to the DNA (Cornelissen *et al.* 2012). This may lead to higher levels of DNA damage such that a threshold is reached, which could be detrimental for cell survival, as opposed to RIgG treatment which results in more cells with DNA damage of lower severity. As an example, in wt small and large intestine, the proliferation index increases after RIgG treatment, but this occurs to a lesser extent after RH2AX treatment. This supports the hypothesis that ROS production stimulates proliferation, whereas ionizing radiation on the DNA caused by RH2AX, even in the presence of ROS, does not cause this to happen.

Phospho-Ser^{1981} ATM, γH2AX and RAD51 DSB markers were used in this study to identify changes in *Apc*-loss-driven DNA damage effects. The former is at the top of the pyramid of DDR components that are activated upon a DSB, however it had a more distinctive localisation pattern and frequency compared to either γH2AX or RAD51 DSB markers. Moreover, as the majority of ATM-positive cells showed perinuclear staining, indicating sequestration of phospho-Ser^{1981} ATM away from the DNA, we hypothesized that these cells might be less efficient in resolving DNA breaks (Reitsema *et al.* 2005). To investigate this, assays such as co-localization of phospho-Ser^{1981} ATM with DDR proteins (e.g. γH2AX, RAD51, LIG4, XRCC3 and TP53) and cell cycle profile analysis by flow cytometry that tests for cell cycle arrest, should be performed.

Interestingly, phospho-Ser^{1981} ATM-positive cells predominantly resided at the +3 position of the crypt, which could indicate a specific cell type. Multiple studies have attempted to find the identity of cells residing over the last Paneth cell of the crypt base (positions +3 to +6). It has been postulated that they mark a quiescent stem cell population, or possibly a secretory cell lineage population that upon injury, can revert back to $LGR5^+$ stem cell population (Potten *et al.* 1997; Pellegrinet *et al.* 2011). Hence, it would have been interesting to further investigate the identity of cells with phospho-Ser^{1981} ATM staining in normal homeostasis. It is important to note that crypt sectioning might have influenced quantification results, as some crypt sections

appeared to have no cells with phospho-Ser^{1981} ATM staining whereas others had ~5%, irrespectively of genotype. Thus, to support the notion of perinuclear phospho-Ser^{1981} ATM marking a specific cell population, these cells need to be present in every crypt of the small intestine. Thus, more reliable quantification results could have been acquired through multiple sections of a crypt, or z-stack confocal images.

Further investigation into the types of DNA repair pathways employed upon *Apc* deficiency-induced DNA damage, could give a better insight into the efficiency of DNA damage resolution and also help identify which are the most critical for the *Apc* loss-related DNA damage. Moreover, DNA damage levels in human CRC tumours of various stages could be assessed along with adjacent phenotypically normal tissue, in order to compare the percentage of γH2AX positive cells between human and mouse intestinal lesions. This could help validate the translational potential of the mouse data to the clinic.

Although the Cre-LoxP recombination technique used to excise *Apc* in *VilCre^{ER} Apc$^{fl/fl}$* mice induced some DNA damage, the majority was caused by deficiency of the *Apc* gene. We were unable to determine whether this was B-CATENIN/ c-MYC transcription dependent or a result of loss of the microtubule-binding functions of APC. To test this would have required data from *Apc* mutants with dysfunctional *β-catenin*-binding but unaffected c-terminal microtubule binding site, and *vice-versa*.

It is important to highlight the fact that results may vary depending on the technique and models used. Although apoptosis is increased early after *Apc* deficiency in the small intestine, the apoptotic index in the organoid model seems to be independent of *Apc* deficiency possibly due to activation of WNT signalling by the addition of R-SPONDIN in the culture media of *Apc*-proficient organoids. This implies that the level of WNT signalling activation in organoids might not reflect *in vivo* levels. An alternative explanation might be the fact that *Apc*-deficient cells are able to adapt to high induction of pro-apoptotic proteins. According to the Human Protein Atlas database, colorectal tumours have variable levels of active caspase-3 proteins (Uhlen *et al.* 2015), whereas from our experience working on CRC tumour mouse models we have noticed that apoptosis is usually present in tumours, including *Apc*-deficient tumours (unpublished data). Hence, it would be useful to quantify the apoptotic index at various stages of tumour development in the *Lgr5Cre^{ER} Apc$^{fl/fl}$* mouse model.

Alternatively, apoptosis induction in *Apc*-deficient cells might be modulated by the immune system which is a fundamental aspect in cancer elimination through recognition of mutated self-proteins (van Vloten *et al.* 2018). It is important to note that studies have proven cancer immunity in mutagen-induced tumour mouse models, however spontaneous murine tumours

were found to be weakly immunogenic (Houghton and Guevara-Patiño 2004). Hence, it is unknown whether *Apc*-mutations could induce an anti-tumour immune response**.** It should also be noted that cleaved caspase-3 staining was the only marker used to quantify the apoptotic index; however, cell death may take place in a programmed fashion, independently of caspase activity (e.g. necroptosis). Thus, other cell death markers such as Annexin-V (identifying early stages of apoptosis; Crowley *et al.* 2016) or TUNEL (DNA fragmentation assay; Kyrylkova *et al.* 2012) could possibly complement the cleaved caspase-3 results.

Identifying that *Apc*-deficient LGR5^{+} stem cells were more likely to have DNA damage than *Apc*-proficient cells raises the question of what is the extent of DNA damage in *Apc*-deficient and wt LGR5^{+} stem cells? According to Cornelissen *et al.* (2012) > 10 γH2AX foci/ nucleus is a level which enables a high specific activity of RH2AX (> 3 MBq / μg) to induce cell death in a human breast cancer cell line. Thus, if *Apc*-deficient LGR5^{+} stem cells have substantially more than 10 γH2AX foci/ nucleus, whilst wt LGR5^{+} stem cells are below this level, this could provide the possibility to attract RH2AX primarily to cancer stem cells in order to induce their death whilst sparing the wt stem cells. Moreover, treatments targeting stem cells as well as the bulk of the tumour are thought to be more effective in the long term (Tu *et al.* 2009) Hence, one way to test whether RH2AX treatment with high specific activity kills stem cells is to compare the organoid formation potential of sorted *Apc*-deficient and -proficient LGR5^{+} single cells cultured in the presence or absence of RH2AX.

Due to time limitations and other circumstances beyond our control, we were unable to complete the therapeutic objective of this project; however our human spheroid data, showing cells with > 10 γH2AX foci/nucleus (Figure 6.2), support our hypothesis that RH2AX could be attracted directly by the endogenous levels of DNA damage present in *Apc*-deficient intestines. Thus, future directions for this project could include our initial goals of using RH2AX with high specific activity as a monotherapy, or using RH2AX in combination with common CRC chemotherapeutics (e.g. cisplatin or 5FU) or IR, as described previously (Cornelissen *et al.* 2012). Chemotherapy or IR could initially induce DNA damage in human tumour-derived spheroids with low γH2AX levels, which could be subsequently amplified by RH2AX. This would allow assessment of the combination treatment effects on spheroid growth and consequently their translational potential.

The possible clinical relevance of imaging dysplasia using RH2AX could include (i) the identification of early lesions that could not be identified with current CRC cancer diagnostic tools, (ii) similarly to FDG PET imaging (Petersen *et al.* 2014), staging of CRC could become more accurate, hence the appropriate treatments would be given to the patients on time, and (iii) RH2AX imaging tool could also help in identifying the surgical margins of tumours more

accurately. However, our findings indicated possible biological effects on the tissue from low SA RIC treatment.

To overcome these effects, ^{89}Zr-anti-γH2AX-TAT could be used instead of ^{111}In-anti-γH2AX-TAT, as the nuclear absorbed dose of cells taking-up ^{89}Zr-anti-γH2AX-TAT was found to be two-fold lower than ^{111}In-anti-γH2AX-TAT (Knight *et al.* 2015). Nonetheless, as results from this project showed that normal intestinal tissue has a low background DNA damage level, it remains to be examined whether there is any long term effect, e.g. increased possibility of mutations to occur, when using RH2AX as a diagnostic agent in the intestine, or any other tissue with frequently occurring background levels of DNA damage (possibly skin due to its quick turn over; Sotiropoulou *et al.* 2010).

Results from our study indicate that *Apc*-deficient intestinal tumours can also be imaged using low SA RIgG, likely due to the EPR effect, and possibly by low SA RH2AX, although the latter remains to be confirmed by increasing animal numbers. Comparing uptake of both in tumours will allow us to assess the specificity of RH2AX to seek out DNA damage. Localisation of RH2AX, due to epitope specificity, would suggest that therapeutic RH2AX levels might be retained for longer in lesions/ tumours that have increased levels of DNA damage, minimising off-target effects of such treatment.

On the other hand, systemic administration of the RH2AX, *via* IV injection, may induce ROS production in any type of cell, particularly in highly vascularised tissues. ROS levels post-RIC treatment should be compared to those in untreated tissue, using immune-based techniques. Also, as the therapeutic effects of RH2AX are based on the fact that DNA breaks are caused cause by ionization events, treatment with free-radical scavengers prior to (or along with) RIC treatment could protect cells from excess ROS generation without affecting the therapeutic efficacy of the RIC; however, this remains to be tested.

It will be interesting to explore whether therapeutic doses, such as 6MBq / µg of RH2AX, as used by Cornelissen *et al.* (2012) in a breast cancer xenograft mouse model, are able to cause *Apc*-deficient cell death and reduction of intestinal tumour burden. Furthermore, the prophylactic potential of RH2AX treatment to kill *Apc*-deficient cells as they arise could be investigated by treatment of the inducible mouse model *Lgr5^{ER}Apc$^{fl/fl}$*, soon after its induction (days 5-9 p.i.; Figure 4.2). Reduction in tumour burden could provide evidence of its positive therapeutic effects.

In conclusion, CRC is the third most commonly diagnosed cancer and the fourth most common cause of cancer death worldwide (Cancer Research UK 2016a and b). The findings of this project provide some evidence that imaging intestinal DNA damage could diagnose early stages of CRC

which could help provide patients with the appropriate treatment sooner, providing a better survival.

8. References

Abremski, K. and Hoess, R. (1984). Bacteriophage P1 site-specific recombination. Purification and properties of the Cre recombinase protein. *Journal of Biological Chemistry* **259**:1509–1514.

Al-Sohaily, S., Biankin, A., Leong, R., Kohonen-Corish, M. and Warusavitarne, J. (2012). Molecular pathways in colorectal cancer. *Journal of gastroenterology and hepatology* **27**:1423–1431.

Albert, H., Dale, E.C., Lee, E. and Ow, D.W. (1995). Site-specific integration of DNA into wild-type and mutant lox sites placed in the plant genome. *The Plant Journal* **7**:649–659.

Alterman, N., Fattal-Valevski, A., Moyal, L., Crawford, T.O., Lederman, H.M., Ziv, Y. and Shiloh, Y. (2007). Ataxia-telangiectasia: Mild neurological presentation despite null ATM mutation and severe cellular phenotype. *American Journal of Medical Genetics, Part A* **143**:1827–1834.

American Cancer Society (2017). *Radiation Therapy for Colorectal Cancer*.

Ames, B.N., Shigenaga, M.K. and Hagen, T.M. (1993). Oxidants, antioxidants, and the degenerative diseases of aging. *Proceedings of the National Academy of Sciences of the United States of America* **90**:7915–7922.

Andreola, S., Leo, E., Belli, F., Bonfanti, G., Sirizzotti, G., Greco, P., Valvo, F., *et al.* (2001). Adenocarcinoma of the lower third of the rectum surgically treated with a <10-MM distal clearance: preliminary results in 35 N0 patients. *Annals of surgical oncology* **8**:611–5.

Andreu, P. (2005). Crypt-restricted proliferation and commitment to the Paneth cell lineage following Apc loss in the mouse intestine. *Development* [Online] **132**:1443–1451. Available at: http://dev.biologists.org/cgi/doi/10.1242/dev.01700.

Animal Cell Technology Industrial Platform (2013). *Monoclonal Antibodies Approved by the EMA and FDA for Therapeutic Use (Status 2013)* [Online]. Available at: http://www.actip.org/products/monoclonal-antibodies-approved-by-the-ema-and-fda-for-therapeutic-use/ [Accessed: 8 August 2017].

Aoki, K., Aoki, M., Sugai, M., Harada, N., Miyoshi, H., Tsukamoto, T., Mizoshita, T., *et al.* (2007). Chromosomal instability by β-catenin/TCF transcription in APC or β-catenin mutant cells. *Oncogene* **26**:3511–3520.

Aparicio, T., Zaanan, A., Svrcek, M., Laurent-Puig, P., Carrere, N., Manfredi, S., Locher, C., *et al.* (2014). Small bowel adenocarcinoma: Epidemiology, risk factors, diagnosis and treatment. *Digestive and Liver Disease* **46**:97–104.

Armelao, F. and de Pretis, G. (2014). Familial colorectal cancer: a review. *World journal of gastroenterology : WJG* **20**:9292–8.

Armstrong, B.B. and Doll, R.R. (1975). Environmental factors and cancer incidence and mortality in different countries, with special reference to dietary practices. *International Journal of Cancer* **15**:617–631.

Arnold, C.N., Goel, A., Niedzwiecki, D., Dowell, J.M., Wasserman, L., Compton, C., Mayer, R.J., *et al.* (2004). APC promoter hypermethylation contributes to the loss of APC expression in colorectal cancers with allelic loss on 5q. *Cancer Biology and Therapy* **3**:960–964.

Artavanis-Tsakonas, S. (1999). Notch Signaling: Cell Fate Control and Signal Integration in Development. *Science* **284**:770–776.

Artiko, V., Marković, A.K., Šobić-Šaranović, D., Petrović, M., Antić, A., Stojković, M., Žuvela, M., *et al.* (2011). Monoclonal immunoscintigraphy for detection of metastasis and recurrence of colorectal cancer. *World Journal of Gastroenterology : WJG* **17**:2424–2430.

Askew, D.S., Ashmun, R.A., Simmons, B.C. and Cleveland, J.L. (1991). Constitutive c-myc expression in an IL-3-dependent myeloid cell line suppresses cell cycle arrest and accelerates apoptosis. *Oncogene* [Online] **6**:1915–22. Available at: http://www.ncbi.nlm.nih.gov/pubmed/1923514.

Auclair, B.A., Benoit, Y.D., Rivard, N., Mishina, Y. and Perreault, N. (2007). Bone Morphogenetic Protein Signaling Is Essential for Terminal Differentiation of the Intestinal Secretory Cell Lineage. *Gastroenterology* **133**:887–896.

Axelrad, J.E., Lichtiger, S. and Yajnik, V. (2016). Inflammatory bowel disease and cancer: The role of inflammation, immunosuppression, and cancer treatment. *World Journal of Gastroenterology* **22**:4794–4801.

Banáth, J.P., Klokov, D., MacPhail, S.H., Banuelos, C.A. and Olive, P.L. (2010). Residual γH2AX foci as an indication of lethal DNA lesions. *BMC Cancer* **10**:4.

Barendswaard, E.C., Scott, A.M., Divgi, C.R., Williams Jr., C., Coplan, K., Riedel, E., Yao, T.-J., *et al.* (1998). Rapid and specific targeting of monoclonal antibody A33 to a colon cancer xenograft in nude mice. *International Journal of Oncology* **12**:45–53.

Barker, N. (2014). Adult intestinal stem cells: critical drivers of epithelial homeostasis and regeneration. *Nature reviews. Molecular cell biology* [Online] **15**:19–33. Available at: http://www.ncbi.nlm.nih.gov/pubmed/24326621.

Barker, N. and Clevers, H. (2006). Mining the Wnt pathway for cancer therapeutics. *Nature reviews. Drug discovery* **5**:997–1014.

Barker, N., van Es, J.H., Kuipers, J., Kujala, P., van den Born, M., Cozijnsen, M., Haegebarth, A., *et al.* (2007). Identification of stem cells in small intestine and colon by marker gene Lgr5. *Nature* [Online] **449**:1003–1007. Available at: http://www.ncbi.nlm.nih.gov/pubmed/17934449.

Barker, N., Ridgway, R.A., van Es, J.H., van de Wetering, M., Begthel, H., van den Born, M., Danenberg, E., *et al.* (2009). Crypt stem cells as the cells-of-origin of intestinal cancer. *Nature* **457**:608–11.

Barolo, S. and Posakony, J.W. (2002). Three habits of highly effective signaling pathways: Principles of transcriptional control by developmental cell signaling. *Genes and Development* **16**:1167–1181.

Bartkova, J., Horejsí, Z., Koed, K., Krämer, A., Tort, F., Zieger, K., Guldberg, P., *et al.* (2005). DNA damage response as a candidate anti-cancer barrier in early human tumorigenesis. *Nature* **434**:864–870.

Bartkova, J., Rezaei, N., Liontos, M., Karakaidos, P., Kletsas, D., Issaeva, N., Vassiliou, L.-V.F., *et al.* (2006). Oncogene-induced senescence is part of the tumorigenesis barrier imposed by DNA damage checkpoints. *Nature* **444**:633–637.

Batlle, E., Henderson, J.T., Beghtel, H., van den Born, M.M.W., Sancho, E., Huls, G., Meeldijk, J., *et al.* (2002). β-Catenin and TCF Mediate Cell Positioning in the Intestinal Epithelium by Controlling the Expression of EphB/EphrinB. *Cell* **111**:251–263.

Batts, L.E., Polk, D.B., Dubois, R.N. and Kulessa, H. (2006). Bmp signaling is required for intestinal growth and morphogenesis. *Developmental dynamics : an official publication of the American Association of Anatomists* **235**:1563–1570.

Baverstock, K.F. and Charlton, D.E. (1988). DNA damage by Auger emitters.

Beasley, G.M., Sun, Z. and Nussbaum, Daniel P. Tyler, D.S. (2017). Neoplasms of the small intestine, vermiform appendix, and peritoneum, and carcinoma of the colon and rectum. In: Bast, R. C. J., Croce, C. M., Hait., W. N., Hong, W. K., Kufe, D. W., Piccart-Gebhart, M., Pollock, R. E., et al. (eds.) *Holland-Frei Cancer Medicine*. 9th ed. Wiley-Blackwell, p. 2008.

Bellis, J., Duluc, I., Romagnolo, B., Perret, C., Faux, M.C., Dujardin, D., Formstone, C., *et al.* (2012). The tumor suppressor Apc controls planar cell polarities central to gut homeostasis. *Journal of Cell Biology* **198**:331–341.

Beppu, H., Mwizerwa, O.N., Beppu, Y., Dattwyler, M.P., Lauwers, G.Y., Bloch, K.D. and Goldstein, a M. (2008). Stromal inactivation of BMPRII leads to colorectal epithelial overgrowth and polyp formation. *Oncogene* **27**:1063–70.

Beyaz, S., Mana, M.D., Roper, J., Kedrin, D., Saadatpour, A., Hong, S.-J., Bauer-Rowe, K.E., *et al.* (2016). High-fat diet enhances stemness and tumorigenicity of intestinal progenitors. *Nature* **531**:53–58.

Bhattacharyya, A., Ear, U.S., Koller, B.H., Weichselbaum, R.R. and Bishop, D.K. (2000). The Breast Cancer susceptibility gene BRCA1 is required for subnuclear assembly of Rad51 and survival following treatment with the DNA cross-linking agent cisplatin. *Journal of Biological Chemistry* **275**:23899–23903.

Biswas, S., Davis, H., Irshad, S., Sandberg, T., Worthley, D. and Leedham, S. (2015). Microenvironmental control of stem cell fate in intestinal homeostasis and disease. *Journal of Pathology* **237**:135–145.

Bjerknes, M. and Cheng, H. (1999). Clonal analysis of mouse intestinal epithelial progenitors. *Gastroenterology* **116**:7–14.

Blache, P., Van De Wetering, M., Duluc, I., Domon, C., Berta, P., Freund, J.N., Clevers, H., *et al.* (2004). SOX9 is an intestine crypt transcription factor, is regulated by the Wnt pathway, and represses the CDX2 and MUC2 genes. *Journal of Cell Biology* **166**:37–47.

Bonner, W.M., Redon, C.E., Dickey, J.S., Nakamura, A.J., Sedelnikova, O.A., Solier, S. and Pommier, Y. (2008). γH2AX and cancer. *Nature Reviews Cancer* **8**:957–967.

Bonnet, D. and Dick, J.E. (1997). Human acute myeloid leukemia is organized as a hierarchy that originates from a primitive hematopoietic cell. *Nature medicine* **3**:730–737.

De Bont, R. and van Larebeke, N. (2004). Endogenous DNA damage in humans: a review of quantitative data. *Mutagenesis* **19**:169–185.

Boykin, K.N., Zibari, G.B., Lilien, D.L., McMillan, R.W., Aultman, D.F. and McDonald, J.C. (1999). The use of FDG-positron emission tomography for the evaluation of colorectal metastases of the liver. *American Surgeon* **65**:1183–1185.

Boyle, P. and Langman, J.S. (2000). ABC of colorectal cancer: epidemiology. *British Medical Journal* **321**:805–808.

Bozulic, L. and Hemmings, B.A. (2009). PIKKing on PKB: regulation of PKB activity by phosphorylation. *Current Opinion in Cell Biology* **21**:256–261.

Brabletz, T., Jung, A., Dag, S., Hlubek, F. and Kirchner, T. (1999). beta-catenin regulates the expression of the matrix metalloproteinase-7 in human colorectal cancer. *The American journal of pathology* **155**:1033–8.

Breault, D.T., Min, I.M., Carlone, D.L., Farilla, L.G., Ambruzs, D.M., Henderson, D.E., Algra, S., *et al.* (2008). Generation of mTert-GFP mice as a model to identify and study tissue progenitor cells. *Proceedings of the National Academy of Sciences of the United States of America* **105**:10420–5.

Breimer, L.H. (1990). Molecular mechanisms of oxygen radical carcinogenesis and mutagenesis: the role of DNA base damage. *Molecular carcinogenesis* **3**:188–197.

van den Brink, G.R., Bleuming, S.A., Hardwick, J.C.H., Schepman, B.L., Offerhaus, G.J., Keller, J.J., Nielsen, C., *et al.* (2004). Indian Hedgehog is an antagonist of Wnt signaling in colonic epithelial cell differentiation. *Nat Genet* **36**:277–282.

van den Brink, G.R., Hardwick, J.C.H., Nielsen, C., Xu, C., Ten Kate, F.J., Glickman, J., van Deventer, S.J.H., *et al.* (2002). Sonic hedgehog expression correlates with fundic gland differentiation in the adult gastrointestinal tract. *Gut* **51**:628–633.

Brittan, M. and Wright, N.A. (2004). The gastrointestinal stem cell. *Cell Proliferation* **37**:35–53.

Brooks, H., Lebleu, B. and Vivès, E. (2005). Tat peptide-mediated cellular delivery: Back to basics. *Advanced Drug Delivery Reviews* **57**:559–577.

Brush, J., Boyd, K., Chappell, F., Crawford, F., Dozier, M., Fenwick, E., Glanville, J., *et al.* (2011). The value of FDG positron emission tomography/computerised tomography (PET/CT) in pre-operative staging of colorectal cancer: a systematic review and economic evaluation. *Health technology assessment (Winchester, England)* **15**.

Buongiorno, P., Pethe, V. V., Charames, G.S., Esufali, S. and Bapat, B. (2008). Rac1 GTPase and the Rac1 exchange factor Tiam1 associate with Wnt-responsive promoters to enhance beta-catenin/TCF-dependent transcription in colorectal cancer cells. *Molecular Cancer* **7**.

Cai, W., Chen, K., He, L., Cao, Q., Koong, A. and Chen, X. (2007). Quantitative PET of EGFR expression in xenograft-bearing mice using 64Cu-labeled cetuximab, a chimeric anti-EGFR monoclonal antibody. *European Journal of Nuclear Medicine and Molecular Imaging* **34**:850–858.

Cairnie, A., Lamerton, L. and Steel, G. (1965). Cell proliferation studies in the intestinal epithelium of the rat I. Determination of the kinetic parameters. *Experimental Cell Research* **39**:528–538.

Cairns, J. (1975). Mutation selection and the natural history of cancer. *Nature* **255**:cp1-.

Caldecott, K.W. (2008). Single-strand break repair and genetic disease. *Nature reviews. Genetics* **9**:619–31.

Cancer Research UK (2016a). *Cancer Survival for Common Cancers* [Online]. Available at: http://www.cancerresearchuk.org/health-professional/cancer-statistics/survival/common-cancers-compared [Accessed: 16 June 2016].

Cancer Research UK (2015). *Major Increase in Bowel Cancer Screening Uptake Shown with New Screening Test*.

Cancer Research UK (2016b). *Worldwide Cancer Incidence Statistics* [Online]. Available at: http://www.cancerresearchuk.org/health-professional/cancer-statistics/worldwide-cancer/incidence [Accessed: 16 June 2016].

Cancer Research UK (2016c). *Worldwide Cancer Mortality Statistics* [Online]. Available at: http://www.cancerresearchuk.org/cancer-info/cancerstats/world/mortality/ [Accessed: 16 June 2016].

Carmichael, P.L., Shé, M.N. and Phillips, D.H. (1992). Detection and characterization by 32P-postlabelling of DNA adducts induced by a Fenton-type oxygen radical-generating system. *Carcinogenesis* **13**:1127–1135.

Carmon, K.S., Gong, X., Lin, Q., Thomas, A. and Liu, Q. (2011). R-spondins function as ligands of the orphan receptors LGR4 and LGR5 to regulate Wnt/ -catenin signaling. *Proceedings of the National Academy of Sciences* [Online] **108**:11452–11457. Available at: http://www.pnas.org/cgi/doi/10.1073/pnas.1106083108.

Carmon, K.S., Gong, X., Yi, J., Wu, L., Thomas, A., Moore, C.M., Masuho, I., *et al.* (2017). LGR5 receptor promotes cell-cell adhesion in stem cells and colon cancer cells via the IQGAP1 -Rac1 pathway. *Journal of Biological Chemistry* [Online]:jbc.M117.786798. Available at: http://www.jbc.org/lookup/doi/10.1074/jbc.M117.786798.

Carnero, A., Blanco-Aparicio, C., Renner, O., Link, W. and Leal, J.F.M. (2008). The PTEN/PI3K/AKT

signalling pathway in cancer, therapeutic implications. *Curr Cancer Drug Targets* **8**:187–198.

Carulli, A.J., Samuelson, L.C. and Schnell, S. (2014). Unraveling intestinal stem cell behavior with models of crypt dynamics. *Integrative biology : quantitative biosciences from nano to macro* [Online] **6**:243–57. Available at: http://www.ncbi.nlm.nih.gov/pubmed/24480852.

Castronovo Jr, F.P. and Wagner Jr, H.N. (1973). Comparative toxicity and pharmacodynamics of ionic indium chloride and hydrated indium oxide. *Journal of Nuclear Medicine* **14**:677–682.

Cave, J.W. (2011). Selective repression of Notch pathway target gene transcription. *Developmental Biology* **360**:123–131.

Chandrakesan, P., May, R., Weygant, N., Qu, D., Berry, W.L., Sureban, S.M., Ali, N., *et al.* (2016). Intestinal tuft cells regulate the ATM mediated DNA Damage response via Dclk1 dependent mechanism for crypt restitution following radiation injury. *Scientific reports* **6**:37667.

Chen, G., Fernandez, J., Mische, S. and Courey, A.J. (1999). A functional interaction between the histone deacetylase Rpd3 and the corepressor Groucho in Drosophila development. *Genes and Development* **13**:2218–2230.

Chen, M., Lichtler, A.C., Sheu, T., Xie, C., Zhang, X., O'Keefe, R.J. and Chen, D. (2007). Generation of a transgenic mouse model with chondrocyte-specific and tamoxifen-inducible expression of Cre recombinase. *genesis* **45**:44–50.

Cheng, H. and Leblond, C.P. (1974). Origin, differentiation and renewal of the four main epithelial cell types in the mouse small intestine V. Unitarian theory of the origin of the four epithelial cell types. *American Journal of Anatomy* **141**:537–561.

Chodaparambil, J. V., Pate, K.T., Hepler, M.R.D., Tsai, B.P., Muthurajan, U.M., Luger, K., Waterman, M.L., *et al.* (2014). Molecular functions of the TLE tetramerization domain in Wnt target gene repression. *EMBO Journal* **33**:719–731.

Choi, J., Sun, Y.P., Costantini, F., Jho, E.H. and Joo, C.K. (2004). Adenomatous polyposis coli is down-regulated by the ubiquitin-proteasome pathway in a process facilitated by Axin. *Journal of Biological Chemistry* **279**:49188–49198.

Chowdhury, D., Keogh, M.-C., Ishii, H., Peterson, C.L., Buratowski, S. and Lieberman, J. (2005). gamma-H2AX dephosphorylation by protein phosphatase 2A facilitates DNA double-strand break repair. *Molecular cell* **20**:801–809.

Clevers, H. (2006). Wnt/β-catenin signaling in development and disease. *Cell* **127**:469–480.

Clevers, H., Loh, K.M. and Nusse, R. (2014). An integral program for tissue renewal and regeneration: Wnt signaling and stem cell control. *Science* **346**:1248012.

Clevers, H.C. and Bevins, C.L. (2013). Paneth cells: maestros of the small intestinal crypts. *Annual review of physiology* [Online] **75**:289–311. Available at: http://www.ncbi.nlm.nih.gov/pubmed/23398152.

ClinicalTrials.gov (2013). *Radiolabeled Monoclonal Antibody in Treating Patients With Advanced Colorectal Cance-NCT00003360*.

ClinicalTrials.gov (2015). *Radiolabeled Monoclonal Antibody Therapy, Combination Chemotherapy, and Bevacizumab in Treating Patients With Metastatic Colorectal Cancer-NCT01205022*.

ClinicalTrials.gov (2016). *Tas-102 and Radioembolization With 90Y Resin Microspheres for Chemo-Refractory Colorectal Liver Metastases*.

Collier, B.D., Abdel-Nabi, H., Doerr, R.J., Harwood, S.J., Olsen, J., Kaplan, E.H., Winzelberg, G.G., *et al.* (1992). Immunoscintigraphy performed with In-111-labeled CYT-103 in the management of colorectal cancer: comparison with CT. *Radiology* **185**:179–186.

Cornelissen, B., Darbar, S., Kersemans, V., Allen, D., Falzone, N., Barbeau, J., Smart, S., *et al.* (2012). Amplification of DNA damage by a γH2AX-targeted radiopharmaceutical. *Nuclear medicine and biology* 39:1142–1151.

Cornelissen, B., Hu, M., McLarty, K., Costantini, D. and Reilly, R.M. (2007). Cellular penetration and nuclear importation properties of 111In-labeled and 123I-labeled HIV-1 tat peptide immunoconjugates in BT-474 human breast cancer cells. *Nuclear Medicine and Biology* 34:37–46.

Cornelissen, B., Kersemans, V., Darbar, S., Thompson, J., Shah, K., Sleeth, K., Hill, M.A., *et al.* (2011). Imaging DNA damage in vivo using γH2AX-targeted immunoconjugates. *Cancer Research* 71:4539–4549.

Cornelissen, B., McLarty, K., Kersemans, V., Scollard, D.A. and Reilly, R.M. (2008). Properties of [111 In]-labeled HIV-1 tat peptide radioimmunoconjugates in tumor-bearing mice following intravenous or intratumoral injection. *Nuclear medicine and biology* 35:101–110.

Costanzo, V., Chaudhuri, J., Fung, J.C. and Moran, J. V. (2009). Dealing with dangerous accidents: DNA double-strand breaks take centre stage: Symposium on Genome Instability and DNA Repair. In: *EMBO Reports*. pp. 837–842.

Council, N.R. (2006). *Health Risks from Exposure to Low Levels of Ionizing Radiation: BEIR VII Phase 2*. National Academies Press.

Crawford, H.C., Fingleton, B.M., Rudolph-Owen, L.A., Heppner Goss, K.J., Rubinfeld, B., Polakis, P. and Matrisian, L.M. (1999). The metalloproteinase matrilysin is a target of beta-catenin transactivation in intestinal tumors. *Oncogene* 18:2883–2891.

Cristofaro, M., Contursi, A., D'Amore, S., Martelli, N., Spaziante, A.F., Moschetta, A. and Villani, G. (2015). Adenomatous polyposis coli (APC)-induced apoptosis of HT29 colorectal cancer cells depends on mitochondrial oxidative metabolism. *Biochimica et Biophysica Acta (BBA) - Molecular Basis of Disease* 1852:1719–1728.

Crosetto, N., Mitra, A., Silva, M.J., Bienko, M., Dojer, N., Wang, Q., Karaca, E., *et al.* (2013). Nucleotide-resolution DNA double-strand break mapping by next-generation sequencing. *Nature methods* [Online] 10:361–5. Available at: http://www.pubmedcentral.nih.gov/articlerender.fcgi?artid=3651036&tool=pmcentrez&rendertype=abstract.

Crosnier, C., Stamataki, D. and Lewis, J. (2006). Organizing cell renewal in the intestine: stem cells, signals and combinatorial control. *Nature Reviews Genetics* 7:349–359.

Crowley, L.C., Marfell, B.J., Scott, A.P. and Waterhouse, N.J. (2016). Quantitation of apoptosis and necrosis by annexin V binding, propidium iodide uptake, and flow cytometry. *Cold Spring Harbor Protocols* 2016:953–957.

Van Cutsem, E., Kohne, C.H., Hitre, E., Zaluski, J., Chang Chien, C.R., Makhson, A., D'Haens, G., *et al.* (2009). Cetuximab and chemotherapy as initial treatment for metastatic colorectal cancer. *N Engl J Med* 360:1408–1417.

Dalerba, P., Dylla, S.J., Park, I.-K., Liu, R., Wang, X., Cho, R.W., Hoey, T., *et al.* (2007). Phenotypic characterization of human colorectal cancer stem cells. *Proceedings of the National Academy of Sciences of the United States of America* 104:10158–10163.

Dang, C. (1999). c-Myc target genes involved in cell growth, apoptosis, and metabolism. *Molecular and cellular biology* [Online] 40:66–9. Available at: http://mcb.asm.org/content/19/1/1.short.

Daniels, D.L. and Weis, W.I. (2005). Beta-catenin directly displaces Groucho/TLE repressors from Tcf/Lef in Wnt-mediated transcription activation. *Nature Structural & Molecular Biology* 12:364–371.

Darwich, A.S., Aslam, U., Ashcroft, D.M. and Rostami-Hodjegan, A. (2014). Meta-analysis of the turnover of intestinal epithelia in preclinical animal species and humans. *Drug Metabolism and Disposition* **42**:2016–2022.

Dauer, L.T., Brooks, A.L., Hoel, D.G., Morgan, W.F., Stram, D. and Tran, P. (2010). Review and evaluation of updated research on the health effects associated with low-dose ionising radiation. *Radiation Protection Dosimetry* **140**:103–136.

Daugherty, R.L., Gottardi, C.J., Luan, L., Ding, T., Stinnett, A., Reese, J., Paria, B.C., *et al.* (2007). Phospho-regulation of Beta-catenin adhesion and signaling functions. *Physiology (Bethesda, Md.)* **22**:303–9.

Denko, N.C., Giaccia, A.J., Stringer, J.R. and Stambrook, P.J. (1994). The human Ha-ras oncogene induces genomic instability in murine fibroblasts within one cell cycle. *Proceedings of the National Academy of Sciences* **91**:5124–5128.

Derks, S., Postma, C., Moerkerk, P.T.M., van den Bosch, S.M., Carvalho, B., Hermsen, M.A.J.A., Giaretti, W., *et al.* (2006). Promoter Methylation Precedes Chromosomal Alterations in Colorectal Cancer Development. *Cellular Oncology : the Official Journal of the International Society for Cellular Oncology* **28**:247–257.

Dienstmann, R. (2014). Colorectal Cancer Subtyping Consortium (CRCSC) identification of a consensus of molecular subtypes. *Asco* [Online]:Abstract #3511. Available at: http://abstracts.asco.org/144/AbstView_144_131959.html.

Dikovskaya, D., Schiffmann, D., Newton, I.P., Oakley, A., Kroboth, K., Sansom, O., Jamieson, T.J., *et al.* (2007). Loss of APC induces polyploidy as a result of a combination of defects in mitosis and apoptosis. *The Journal of cell biology* **176**:183–195.

Dirksen, M.-L., Blakely, W.F., Holwitt, E. and Dizdaroglu, M. (1988). Effect of DNA conformation on the hydroxyl radical-induced formation of 8, 5′-cyclopurine 2′-deoxyribonucleoside residues in DNA. *International journal of radiation biology* **54**:195–204.

Dobrzyński, L., Fornalski, K.W. and Feinendegen, L.E. (2015). Cancer Mortality Among People Living in Areas With Various Levels of Natural Background Radiation. *Dose-Response* **13**:1559325815592391.

Drin, G., Cottin, S., Blanc, E., Rees, A.R. and Temsamani, J. (2003). Studies on the internalization mechanism of cationic cell-penetrating peptides. *Journal of Biological Chemistry* **278**:31192–31201.

Eary, J.F. (1999). Nuclear medicine in cancer diagnosis. *The Lancet* **354**:853–857.

Eggington, S., Tappenden, P., Pandor, A., Paisley, S., Saunders, M., Seymour, M., Sutcliffe, P., *et al.* (2006). Cost-effectiveness of oxaliplatin and capecitabine in the adjuvant treatment of stage III colon cancer. *British journal of cancer* **95**:1195–201.

Ehrlich, M., Zhang, X.-Y. and Inamdar, N.M. (1990). Spontaneous deamination of cytosine and 5-methylcytosine residues in DNA and replacement of 5-methylcytosine residues with cytosine residues. *Mutation Research/Reviews in Genetic Toxicology* **238**:277–286.

Engelstoft, M.S., Egerod, K.L., Holst, B. and Schwartz, T.W. (2008). A Gut Feeling for Obesity: 7TM Sensors on Enteroendocrine Cells. *Cell Metabolism* **8**:447–449.

England, K., 'O'Driscoll, C.O. and Cotter, T.G. (2006). ROS and protein oxidation in early stages of cytotoxic drug induced apoptosis. *Free Radical Research* **40**:1124–1137.

Erdi, Y.E. (2012). Limits of Tumor Detectability in Nuclear Medicine and PET. *Molecular Imaging and Radionuclide Therapy* **21**:23–28.

Escobar, M., Nicolas, P., Sangar, F., Laurent-Chabalier, S., Clair, P., Joubert, D., Jay, P., *et al.* (2011). Intestinal epithelial stem cells do not protect their genome by asymmetric chromosome

segregation. *Nature Communications* [Online] 2:258. Available at: http://www.nature.com/doifinder/10.1038/ncomms1260.

Esteller, M., Sparks, A., Toyota, M., Sanchez-Cespedes, M., Capella, G., Peinado, M.A., Gonzalez, S., *et al.* (2000). Analysis of adenomatous polyposis coli promoter hypermethylation in human cancer. *Cancer Research* 60:4366–4371.

Ettrich, T.J. and Seufferlein, T. (2014). Regorafenib. *Recent results in cancer research. Fortschritte der Krebsforschung. Progrès dans les recherches sur le cancer* 201:185–96.

European Medicines Agency (2005). *CEA-Scan - Arcitumomab*.

European Medicines Agency (2004). *HumaSPECT-Votumumab*.

Falconer, E., Chavez, E.A., Henderson, A., Poon, S.S.S., McKinney, S., Brown, L., Huntsman, D.G., *et al.* (2010). Identification of sister chromatids by DNA template strand sequences. *Nature* [Online] 463:93–97. Available at: http://www.nature.com/doifinder/10.1038/nature08644.

Farrands, P.A., Pimm, M. V, Embleton, M.J., Perkins, A.C., Hardy, J.D., Baldwin, R.W. and Hardcastle, J.D. (1982). Radioimmunodetection of human colorectal cancers by an anti-tumour monoclonal antibody. *The Lancet* 320:397–400.

Fearon, E.R. and Vogelstein, B. (1990). A genetic model for colorectal tumorigenesis. *Cell* 61:759–767.

Feil, S., Valtcheva, N. and Feil, R. (2009). Inducible cre mice. *Methods in Molecular Biology* 530:343–363.

Ferlay, J., Soerjomataram, I., Dikshit, R., Eser, S., Mathers, C., Rebelo, M., Parkin, D.M., *et al.* (2015). Cancer incidence and mortality worldwide: Sources, methods and major patterns in GLOBOCAN 2012. *International Journal of Cancer* 136:E359–E386.

Fernandez-Capetillo, O., Lee, A., Nussenzweig, M. and Nussenzweig, A. (2004). H2AX: the histone guardian of the genome. *DNA repair* 3:959–967.

Ferrari, A., Pellegrini, V., Arcangeli, C., Fittipaldi, A., Giacca, M. and Beltram, F. (2003). Caveolae-mediated internalization of extracellular HIV-1 Tat fusion proteins visualized in real time. *Molecular Therapy* 8:284–294.

Fittipaldi, A., Ferrari, A., Zoppé, M., Arcangeli, C., Pellegrini, V., Beltram, F. and Giacca, M. (2003). Cell Membrane Lipid Rafts Mediate Caveolar Endocytosis of HIV-1 Tat Fusion Proteins. *Journal of Biological Chemistry* 278:34141–34149.

Fodde, R., Edelmann, W., Yang, K., van Leeuwen, C., Carlson, C., Renault, B., Breukel, C., *et al.* (1994). A targeted chain-termination mutation in the mouse Apc gene results in multiple intestinal tumors. *Proceedings of the National Academy of Sciences of the United States of America* 91:8969–73.

Fodde, R., Kuipers, J., Rosenberg, C., Smits, R., Kielman, M., Gaspar, C., van Es, J.H., *et al.* (2001). Mutations in the APC tumour suppressor gene cause chromosomal instability. *Nature Cell Biology* [Online] 3:433–438. Available at: http://eutils.ncbi.nlm.nih.gov/entrez/eutils/elink.fcgi?dbfrom=pubmed&id=11283620&retmode=ref&cmd=prlinks%5Cnpapers2://publication/doi/10.1038/35070129.

Fodde, R., Kuipers, J., Rosenberg, C., Smits, R., Kielman, M., Gaspar, C., van Es, J.H., *et al.* (2001). Mutations in the APC tumour suppressor gene cause chromosomal instability. *Nature cell biology* 3:433–438.

Fodde, R., Smits, R. and Clevers, H. (2001). APC, signal transduction and genetic instability in colorectal cancer. *Nature Reviews Cancer* [Online] 1:55–67. Available at: http://eutils.ncbi.nlm.nih.gov/entrez/eutils/elink.fcgi?dbfrom=pubmed&id=11900252&retmode=ref&cmd=prlinks%5Cnpapers2://publication/doi/10.1038/35094067.

Formeister, E.J., Sionas, A.L., Lorance, D.K., Barkley, C.L., Lee, G.H. and Magness, S.T. (2009). Distinct SOX9 levels differentially mark stem/progenitor populations and enteroendocrine cells of the small intestine epithelium. *Am J Physiol Gastrointest Liver Physiol* **296**:G1108-18.

Fre, S., Huyghe, M., Mourikis, P., Robine, S., Louvard, D. and Artavanis-Tsakonas, S. (2005). Notch signals control the fate of immature progenitor cells in the intestine. *Nature* **435**:964–8.

Frush, D.P., Donnelly, L.F. and Rosen, N.S. (2003). Computed tomography and radiation risks: what pediatric health care providers should know. *Pediatrics* **112**:951–7.

Fuchs, E., Tumbar, T. and Guasch, G. (2004). Socializing with the neighbors: Stem cells and their niche. *Cell* **116**:769–778.

Fujita, M., Furukawa, Y., Tsunoda, T., Tanaka, T., Ogawa, M. and Nakamura, Y. (2001). Up-Regulation of the Ectodermal-Neural Cortex 1 Gene, a Downstream Target of the β-Catenin/T-Cell Factor Complex, in Colorectal Carcinomas. *Cancer Research* **61**:7722 LP-7726.

Furuuchi, K., Tada, M., Yamada, H., Kataoka, A., Furuuchi, N., Hamada, J., Takahashi, M., *et al.* (2000). Somatic mutations of the APC gene in primary breast cancers. *The American journal of pathology* **156**:1997–2005.

Furuyama, K., Kawaguchi, Y., Akiyama, H., Horiguchi, M., Kodama, S., Kuhara, T., Hosokawa, S., *et al.* (2011). Continuous cell supply from a Sox9-expressing progenitor zone in adult liver, exocrine pancreas and intestine. *Nature genetics* **43**:34–41.

Fuster, D., Maurel, J., Muxi, A., Setoain, X., Ayuso, C., Martin, F., Ortega, M.L., *et al.* (2003). Is there a role for (99m)Tc-anti-CEA monoclonal antibody imaging in the diagnosis of recurrent colorectal carcinoma? *The quarterly journal of nuclear medicine : official publication of the Italian Association of Nuclear Medicine (AIMN) [and] the International Association of Radiopharmacology (IAR)* **47**:109–115.

Galceran, J., Fariñas, I., Depew, M.J., Clevers, H. and Grosschedl, R. (1999). Wnt3a(-/-) -like phenotype and limb deficiency in Lef1(-/-)Tcf1(-/-) mice. *Genes and Development* **13**:709–717.

Gao, C. and Chen, Y.-G. (2010). Dishevelled: The hub of Wnt signaling. *Cellular signalling* **22**:717–727.

Gao, C., Xiao, G. and Hu, J. (2014). Regulation of Wnt/β-catenin signaling by posttranslational modifications. *Cell {&} Bioscience* **4**:13.

Garcia, M.I., Ghiani, M., Lefort, A., Libert, F., Strollo, S. and Vassart, G. (2009). LGR5 deficiency deregulates Wnt signaling and leads to precocious Paneth cell differentiation in the fetal intestine. *Developmental Biology* **331**:58–67.

Gene Cards/ Human Gene Database *APC Gene*.

Gerbe, F., Sidot, E., Smyth, D.J., Ohmoto, M., Matsumoto, I., Dardalhon, V., Cesses, P., *et al.* (2016). Intestinal epithelial tuft cells initiate type 2 mucosal immunity to helminth parasites. *Nature* **529**:226–230.

Ghiassi-Nejad, M., Mortazavi, S.M.J., Cameron, J.R., Niroomand-Rad, A. and Karam, P.A. (2002). Very high background radiation areas of Ramsar, Iran: Preliminary biological studies. *Health Physics* **82**:87–93.

Giles, R.H., van Es, J.H. and Clevers, H. (2003). Caught up in a Wnt storm: Wnt signaling in cancer. *Biochimica et Biophysica Acta (BBA)-Reviews on Cancer* **1653**:1–24.

Giusti, R.M., Cohen, M.H., Keegan, P. and Pazdur, R. (2009). FDA review of a panitumumab (Vectibix) clinical trial for first-line treatment of metastatic colorectal cancer. *The oncologist* **14**:284–90.

Goldenberg, D.M. (2007). Radiolabelled monoclonal antibodies in the treatment of metastatic cancer. *Current Oncology* [Online] **14**:39–42. Available at:

http://www.ncbi.nlm.nih.gov/pubmed/20399983.

Goodman, B.E. (2010). Insights into digestion and absorption of major nutrients in humans. *Adv Physiol Educ* **34**:44–53.

Gorgoulis, V.G., Vassiliou, L.-V.F., Karakaidos, P., Zacharatos, P., Kotsinas, A., Liloglou, T., Venere, M., *et al.* (2005). Activation of the DNA damage checkpoint and genomic instability in human precancerous lesions. *Nature* **434**:907–13.

Grabinger, T., Luks, L., Kostadinova, F., Zimberlin, C., Medema, J.P., Leist, M. and Brunner, T. (2014). Ex vivo culture of intestinal crypt organoids as a model system for assessing cell death induction in intestinal epithelial cells and enteropathy. *Cell Death and Disease* **5**.

GraphPad Software, I. *Interpreting Results: Mann-Whitney Test*.

GraphPad Software, I. *Interpreting Results: One-Way ANOVA*.

Green, R.A. and Kaplan, K.B. (2003). Chromosome instability in colorectal tumor cells is associated with defects in microtubule plus-end attachments caused by a dominant mutation in APC. *Journal of Cell Biology* **163**:949–961.

Green, R.A., Wollman, R. and Kaplan, K.B. (2005). APC and EB1 function together in mitosis to regulate spindle dynamics and chromosome alignment. *Molecular biology of the cell* **16**:4609–22.

Greish, K. (2007). Enhanced permeability and retention of macromolecular drugs in solid tumors: A royal gate for targeted anticancer nanomedicines. *Journal of Drug Targeting* [Online] **15**:457–464. Available at: http://www.tandfonline.com/doi/full/10.1080/10611860701539584.

Groppe, J., Greenwald, J., Wiater, E., Rodriguez-Leon, J., Economides, A.N., Kwiatkowski, W., Baban, K., *et al.* (2003). Structural basis of BMP signaling inhibition by Noggin, a novel twelve-membered cystine knot protein. *J Bone Joint Surg Am* **85–A Suppl**:52–58.

Hagan, S., Orr, M.C. and Doyle, B. (2013). Targeted therapies in colorectal cancer—an integrative view by PPPM. *Epma j* **4**:3.

Haggar, F.A. and Boushey, R.P. (2009). Colorectal cancer epidemiology: Incidence, mortality, survival, and risk factors. *Clinics in Colon and Rectal Surgery* **22**:191–197.

Halazonetis, T.D., Gorgoulis, V.G. and Bartek, J. (2008). An oncogene-induced DNA damage model for cancer development. *Science (New York, N.Y.)* **319**:1352–5.

Hamilton, P.M., Chiacchierini, R.P. and Lundin Jr, F.E. (1984). A follow-up study of persons who had iodine-131 and other procedures during childhood. In: *Radiation-Risk-Protection. Vol. 2*.

Haramis, A.-. P.G., Begthel, H., van den Born, M., van Es, J., Jonkheer, S., Offerhaus, G.J.A. and Clevers, H. (2004). De novo crypt formation and juvenile polyposis on bmp inhibition in mouse intestine. *Science* **303**.

Hayashi, S. and McMahon, A.P. (2002). Efficient Recombination in Diverse Tissues by a Tamoxifen-Inducible Form of Cre: A Tool for Temporally Regulated Gene Activation/Inactivation in the Mouse. *Developmental Biology* **244**:305–318.

He, T.C., Chan, T.A., Vogelstein, B. and Kinzler, K.W. (1999). PPARdelta is an APC-regulated target of nonsteroidal anti-inflammatory drugs. *Cell* **99**:335–45.

He, T.C., Sparks, A.B., Rago, C., Hermeking, H., Zawel, L., da Costa, L.T., Morin, P.J., *et al.* (1998). Identification of c-MYC as a target of the APC pathway. *Science (New York, N.Y.)* **281**:1509–12.

He, X.C., Yin, T., Grindley, J.C., Tian, Q., Sato, T., Tao, W.A., Dirisina, R., *et al.* (2007). PTEN-deficient intestinal stem cells initiate intestinal polyposis. *Nat Genet* **39**:189–198.

He, X.C., Zhang, J., Tong, W.-G., Tawfik, O., Ross, J., Scoville, D.H., Tian, Q., *et al.* (2004). BMP signaling inhibits intestinal stem cell self-renewal through suppression of Wnt-beta-catenin

signaling. *Nat Genet* **36**:1117–1121.

Hecht, S.M. (2000). Bleomycin: New perspectives on the mechanism of action. *Journal of Natural Products* **63**:158–168.

Helander, H.F. and Fandriks, L. (2014). Surface area of the digestive tract - revisited. *Scand J Gastroenterol* **49**:681–689.

Helbock, H.J., Beckman, K.B., Shigenaga, M.K., Walter, P.B., Woodall, a a, Yeo, H.C. and Ames, B.N. (1998). DNA oxidation matters: the HPLC-electrochemical detection assay of 8-oxo-deoxyguanosine and 8-oxo-guanine. *Proceedings of the National Academy of Sciences of the United States of America* **95**:288–293.

Helleday, T., Eshtad, S. and Nik-Zainal, S. (2014). Mechanisms underlying mutational signatures in human cancers. *Nature reviews. Genetics* **15**:585–598.

Hers, I., Vincent, E.E. and Tavaré, J.M. (2011). Akt signalling in health and disease. *Cellular Signalling* **23**:1515–1527.

Hertel, A., Baum, R.P., Lorenz, M., Baew-Christow, T., Encke, A. and Hor, G. (1990). Immunoscintigraphy using a technetium-99m labelled monoclonal anti-CEA antibody in the follow-up of colorectal cancer and other tumours producing CEA. *British Journal of Cancer* **62**:34–36.

Hlubek, F., Spaderna, S., Jung, A., Kirchner, T. and Brabletz, T. (2004). β-catenin activates a coordinated expression of the proinvasive factors laminin-5 γ2 chain and MT1-MMP in colorectal carcinomas. *International Journal of Cancer* **108**:321–326.

Hoeijmakers, J.H.J. (2009). DNA damage, aging, and cancer. *The New England journal of medicine* **361**:1475–85.

Hofer, K.G. (1996). Biophysical aspects of Auger processes--A review. *Acta oncologica (Stockholm, Sweden)* **35**:789–796.

Hoffmans, R., Städeli, R. and Basler, K. (2005). Pygopus and legless provide essential transcriptional coactivator functions to Armadillo/β-catenin. *Current Biology* **15**:1207–1211.

Houghton, A.N. and Guevara-Patiño, J.A. (2004). Immune recognition of self in immunity against cancer. *Journal of Clinical Investigation* **114**:468–471.

Howe, G.R. and McLaughlin, J. (1996). Breast cancer mortality between 1950 and 1987 after exposure to fractionated moderate-dose-rate ionizing radiation in the Canadian fluoroscopy cohort study and a comparison with breast cancer mortality in the atomic bomb survivors study. *Radiation research* **145**:694–707.

Howell, R.W., Narra, V.R., Rao, D. V and Sastry, K.S.R. (1990). Radiobiological effects of intracellular 210Po alpha emissions: a comparison with Auger emitters. *Radiation Protection Dosimetry* **31**:325–328.

Hua, G., Wang, C., Pan, Y., Zeng, Z., Lee, S.G., Martin, M.L., Haimovitz-Friedman, A., *et al.* (2017). Distinct levels of radioresistance in Lgr5+ colonic epithelial stem cells versus Lgr5+ small intestinal stem cells. *Cancer Research* **77**:2124–2133.

Huang, X., Langelotz, C., Hetfeld-Pěchoč, B.K.J., Schwenk, W. and Dubiel, W. (2009). The COP9 Signalosome Mediates β-Catenin Degradation by Deneddylation and Blocks Adenomatous Polyposis coli Destruction via USP15. *Journal of Molecular Biology* **391**:691–702.

Hui, C. and Angers, S. (2011). Gli Proteins in Development and Disease. *Annual Review of Cell and Developmental Biology* **27**:513–537.

Ichii, S., Horii, A., Nakatsuru, S., Furuyama, J., Utsunomiya, J. and Nakamura, Y. (1992). Inactivation of both APC alleles in an early stage of colon adenomas in a patient with familial adenomatous polyposis (FAP). *Human Molecular Genetics* **1**:387–390.

Ikeda, S., Kishida, M., Matsuura, Y., Usui, H. and Kikuchi, A. (2000). GSK-3beta-dependent phosphorylation of adenomatous polyposis coli gene product can be modulated by beta-catenin and protein phosphatase 2A complexed with Axin. *Oncogene* **19**:537–45.

Ingham, P.W. and McMahon, A.P. (2001). Hedgehog signaling in animal development: Paradigms and principles. *Genes and Development* **15**:3059–3087.

Insinga, A., Cicalese, A., Faretta, M., Gallo, B., Albano, L., Ronzoni, S., Furia, L., *et al.* (2013). DNA damage in stem cells activates p21, inhibits p53, and induces symmetric self-renewing divisions. *Proceedings of the National Academy of Sciences* **110**:3931–3936.

Ireland, H., Kemp, R., Houghton, C., Howard, L., Clarke, A.R., Sansom, O.J. and Winton, D.J. (2004). Inducible Cre-mediated control of gene expression in the murine gastrointestinal tract: effect of loss of β-catenin. *Gastroenterology* **126**:1236–1246.

Itzkovitz, S., Lyubimova, A., Blat, I.C., Maynard, M., van Es, J., Lees, J., Jacks, T., *et al.* (2012). Single-molecule transcript counting of stem-cell markers in the mouse intestine. *Nature cell biology* **14**:106–14.

Ivashkevich, A., Redon, C.E., Nakamura, A.J., Martin, R.F. and Martin, O.A. (2012). Use of the γ-H2AX assay to monitor DNA damage and repair in translational cancer research. *Cancer Letters* **327**:123–133.

Jamar, F., Fiasse, R., Leners, N. and Pauwels, S. (1995). Somatostatin receptor imaging with indium-111-pentetreotide in gastroenteropancreatic neuroendocrine tumors: safety, efficacy and impact on patient management. *Journal of nuclear medicine : official publication, Society of Nuclear Medicine* **36**:542–549.

Janjan, N.A., Ballo, M., Crane, C. and Delclos, M. (2002). Radiation Therapy of Resectable Rectal Cancer. In: *Colorectal Cancer*. Springer, pp. 179–208.

Janssen, K.P., Marjou, F. El, Pinto, D., Sastre, X., Rouillard, D., Fouquet, C., Soussi, T., *et al.* (2002). Targeted expression of oncogenic K-ras in intestinal epithelium causes spontaneous tumorigenesis in mice. *Gastroenterology* **123**:492–504.

Jasperson, K.W., Vu, T.M., Schwab, A.L., Neklason, D.W., Rodriguez-Bigas, M.A., Burt, R.W. and Weitzel, J.N. (2010). Evaluating Lynch syndrome in very early onset colorectal cancer probands without apparent polyposis. *Familial Cancer* **9**:99–107.

Jass, J.R., Walsh, M.D., Barker, M., Simms, L.A., Young, J. and Leggett, B.A. (2002). Distinction between familial and sporadic forms of colorectal cancer showing DNA microsatellite instability. *European Journal of Cancer* **38**:858–866.

Jensen, K.B., Collins, C.A., Nascimento, E., Tan, D.W., Frye, M., Itami, S. and Watt, F.M. (2009). Lrig1 Expression Defines a Distinct Multipotent Stem Cell Population in Mammalian Epidermis. *Cell Stem Cell* **4**:427–439.

Johansson, M.E. V and Hansson, G.C. (2013). Mucus and the goblet cell. In: *Digestive Diseases*. pp. 305–309.

Johns, L.E. and Houlston, R.S. (2003). A systematic review and meta-analysis of familial prostate cancer risk. *BJU International* **91**:789–794.

Johnson, R.L. and Fleet, J.C. (2013). Animal models of colorectal cancer. *Cancer metastasis reviews* [Online] **32**:39–61. Available at: http://www.pubmedcentral.nih.gov/articlerender.fcgi?artid=3572245&tool=pmcentrez&rendertype=abstract.

Jones, R.G., Li, X., Gray, P.D., Kuang, J., Clayton, F., Samowitz, W.S., Madison, B.B., *et al.* (2006). Conditional deletion of β1 integrins in the intestinal epithelium causes a loss of Hedgehog expression, intestinal hyperplasia, and early postnatal lethality. *Journal of Cell Biology* **175**:505–514.

Jubb, A.M., Chalasani, S., Frantz, G.D., Smits, R., Grabsch, H.I., Kavi, V., Maughan, N.J., *et al.* (2006). Achaete-scute like 2 (ascl2) is a target of Wnt signalling and is upregulated in intestinal neoplasia. *Oncogene* **25**:3445–3457.

Jubb, A.M., Zhong, F., Bheddah, S., Grabsch, H.I., Frantz, G.D., Mueller, W., Kavi, V., *et al.* (2005). EphB2 is a prognostic factor in colorectal cancer. *Clinical Cancer Research* **11**:5181–5187.

Kaplan, K.B., Burds, A.A., Swedlow, J.R., Bekir, S.S., Sorger, P.K. and Nathke, I.S. (2001). A role for the Adenomatous Polyposis Coli protein in chromosome segregation. *Nat.Cell Biol.* [Online] **3**:429–432. Available at: http://www.ncbi.nlm.nih.gov/pubmed/11283619.

Kaplan, K.B., Burds, A.A., Swedlow, J.R., Bekir, S.S., Sorger, P.K. and Näthke, I.S. (2001). A role for the Adenomatous Polyposis Coli protein in chromosome segregation. *Nature cell biology* **3**:429–432.

Kasai, H. and Nishimura, S. (1984). Hydroxylation of deoxyguanosine at the C-8 position by ascorbic acid and other reducing agents. *Nucleic acids research* **12**:2137–2145.

Katoh, M. and Katoh, M. (2007). Notch signaling in gastrointestinal tract (Review). *International Journal of Oncology* **30**:247–251.

Kawasaki, Y., Sato, R. and Akiyama, T. (2003). Mutated APC and Asef are involved in the migration of colorectal tumour cells. *Nat Cell Biol* **5**:211–215.

Kayahara, T., Sawada, M., Takaishi, S., Fukui, H., Seno, H., Fukuzawa, H., Suzuki, K., *et al.* (2003). Candidate markers for stem and early progenitor cells, Musashi-1 and Hes1, are expressed in crypt base columnar cells of mouse small intestine. In: *FEBS Letters*. pp. 131–135.

Kazak, L., Reyes, A. and Holt, I.J. (2012). Minimizing the damage: repair pathways keep mitochondrial DNA intact. *Nature Reviews Molecular Cell Biology* **13**:726–726.

Kellett, M., Potten, C.S. and Rew, D.A. (1992). A comparison of in vivo cell proliferation measurements in the intestine of mouse and man. *Epithelial Cell Biol* **1**.

Kersemans, V. and Cornelissen, B. (2010). Targeting the tumour: Cell penetrating peptides for molecular imaging and radiotherapy. *Pharmaceuticals* **3**:600–620.

Khanna, K.K. and Jackson, S.P. (2001). DNA double-strand breaks: signaling, repair and the cancer connection. *Nature genetics* **27**:247–54.

Kidd, S., Kelley, M.R. and Young, M.W. (1986). Sequence of the notch locus of Drosophila melanogaster: relationship of the encoded protein to mammalian clotting and growth factors. *Molecular and Cellular Biology* **6**:3094–3108.

Kim, M., Ashida, H., Ogawa, M., Yoshikawa, Y., Mimuro, H. and Sasakawa, C. (2010). Bacterial interactions with the host epithelium. *Cell Host and Microbe* **8**:20–35.

Kim, P.J., Plescia, J., Clevers, H., Fearon, E.R. and Altieri, D.C. (2003). Survivin and molecular pathogenesis of colorectal cancer. *Lancet* **362**:205–209.

Kinzler, K., Nilbert, M., Su, L., Vogelstein, B., Bryan, T., Levy, D., Smith, K., *et al.* (1991). Identification of FAP locus genes from chromosome 5q21. *Science* **253**:661–665.

Kinzler, K.W. and Vogelstein, B. (1996). Lessons from hereditary colorectal cancer. *Cell* **87**:159–170.

Van Kirk, C., Feinberg, L.A., Robertson, D.J., Freeman, W.M. and Vrana, K.E. (2001). Phosphorimager. In: *ELS*. John Wiley & Sons, Ltd. Available at: http://dx.doi.org/10.1002/9780470015902.a0002973.pub2.

Kiskowski, M.A., Hancock, J.F. and Kenworthy, A.K. (2009). On the use of Ripley's K-function and its derivatives to analyze domain size. *Biophysical journal* **97**:1095–1103.

Knight, J.C., Mosley, M.J., Contreras Bravo, L., Kersemans, V., Allen, P.D., MUKHERJEE, S.,

O'Neill, E., *et al.* (2017). 89Zr-anti-γH2AX-TAT but not 18F-FDG allows early monitoring of response to chemotherapy in a mouse model of pancreatic ductal adenocarcinoma. *Clinical Cancer Research*.

Knight, J.C., Topping, C., Mosley, M., Kersemans, V., Falzone, N., Fernández-Varea, J.M. and Cornelissen, B. (2015). PET imaging of DNA damage using 89Zr-labelled anti-γH2AX-TAT immunoconjugates. *European Journal of Nuclear Medicine and Molecular Imaging* **42**:1707–1717.

Knox, S.J. and Levy, R. (2015). CCR 20th anniversary commentary: Radioactive drones for B-cell lymphoma. *Clinical Cancer Research* **21**:493–494.

Kodach, L.L., Wiercinska, E., de Miranda, N.F.C.C., Bleuming, S.A., Musler, A.R., Peppelenbosch, M.P., Dekker, E., *et al.* (2008). The Bone Morphogenetic Protein Pathway Is Inactivated in the Majority of Sporadic Colorectal Cancers. *Gastroenterology* **134**.

Kondo, N., Takahashi, A., Ono, K. and Ohnishi, T. (2010). DNA Damage Induced by Alkylating Agents and Repair Pathways. *Journal of Nucleic Acids* **2010**:1–7.

Kozlov, S. V., Waardenberg, A.J., Engholm-Keller, K., Arthur, J.W., Graham, M.E. and Lavin, M. (2016). Reactive Oxygen Species (ROS)-Activated ATM-Dependent Phosphorylation of Cytoplasmic Substrates Identified by Large-Scale Phosphoproteomics Screen. *Molecular & Cellular Proteomics* [Online] **15**:1032–1047. Available at: http://www.mcponline.org/lookup/doi/10.1074/mcp.M115.055723.

Krebs, C. (1928). Experimenteller Alkoholkrebs bei weissen Mäusen. *Z. Immun. Exp. Therap* **50**:203–218.

Kühn, R. and Torres, R.M. (2002). Cre/loxP recombination system and gene targeting. In: *Transgenesis Techniques*. Springer, pp. 175–204.

Kuo, L.J. and Yang, L.-X. (2008). γ-H2AX-a novel biomarker for DNA double-strand breaks. *In Vivo* **22**:305–309.

Kurooka, H. and Honjo, T. (2000). Functional interaction between the mouse Notch1 intracellular region and histone acetyltransferases PCAF and GCN5. *Journal of Biological Chemistry* **275**:17211–17220.

Kuvshinoff, B., Maghfoor, I., Miedema, B., Bryer, M., Westgate, S., Wilkes, J. and Ota, D. (2001). Distal Margin Requirements After Preoperative Chemoradiotherapy for Distal Rectal Carcinomas: Are ≤ 1 cm Distal Margins Sufficient? *Annals of Surgical Oncology* **8**:163–169.

Kwong, L.N. and Dove, W.F. (2009). APC and its modifiers in colon cancer. *Advances in experimental medicine and biology* **656**:85–106.

Kyrylkova, K., Kyryachenko, S., Leid, M. and Kioussi, C. (2012). Detection of apoptosis by TUNEL assay. *Methods in molecular biology (Clifton, N.J.)* **887**:41–47.

Lacic, M., Bokulic, T., Lukac, J., Baum, R.P. and Kusic, Z. (1999). Immunoscintigraphy with 99Tcm-labelled monoclonal anti-CEA BW 431/26 antibodies in patients with suspected recurrent and metastatic colorectal carcinoma: two-year follow-up. *Nuclear medicine communications* **20**:859–865.

Van Landeghem, L., Santoro, M. a., Krebs, a. E., Mah, a. T., Dehmer, J.J., Gracz, a. D., Scull, B.P., *et al.* (2012). Activation of two distinct Sox9-EGFP-expressing intestinal stem cell populations during crypt regeneration after irradiation. *AJP: Gastrointestinal and Liver Physiology* **302**:G1111–G1132.

Lansdorp, P.M. (2007). Immortal Strands? Give Me a Break. *Cell* **129**:1244–1247.

Lansdorp, P.M., Falconer, E., Tao, J., Brind'Amour, J. and Naumann, U. (2012). Epigenetic differences between sister chromatids? *Annals of the New York Academy of Sciences* **1266**:1–6.

Laqueur, G.L., Mickelsen, O., Whiting, M.G. and Kurland, L.T. (1963). Carcinogenic properties of nuts from Cycas circinalis L. indigenous to Guam. *Journal of the National Cancer Institute* **31**:919–951.

de Lau, W., Barker, N., Low, T.Y., Koo, B.-K., Li, V.S.W., Teunissen, H., Kujala, P., *et al.* (2011). Lgr5 homologues associate with Wnt receptors and mediate R-spondin signalling. *Nature* [Online] **476**:293–297. Available at: http://www.nature.com/doifinder/10.1038/nature10337.

Lawrence, T.S., Ten Haken, R.K. and Giaccia, A. (2008). Principles of radiation oncology. In: *Cancer: Principles and Practice of Oncology*. 8th ed. Philadelphia: Lippincott Williams and Wilkins.

Lee, J.J., Rothenberg, M.E., Seeley, E.S., Zimdahl, B., Kawano, S., Lu, W.-J., Shin, K., *et al.* (2016). Control of inflammation by stromal Hedgehog pathway activation restrains colitis. *Proceedings of the National Academy of Sciences of the United States of America*:201616447.

Lee, S.J. and Wang, J.Y.J. (2009). Exploiting the promiscuity of imatinib. *Journal of Biology* **8**.

Leslie, A., Pratt, N.R., Gillespie, K., Sales, M., Kernohan, N.M., Smith, G., Wolf, C.R., *et al.* (2003). Mutations of APC, K-ras, and p53 are associated with specific chromosomal aberrations in colorectal adenocarcinomas. *Cancer Research* **63**:4656–4661.

Lewis, S.S., Cox, G.M. and Stout, J.E. (2014). Clinical Utility of Indium 111–Labeled White Blood Cell Scintigraphy for Evaluation of Suspected Infection. In: *Open Forum Infectious Diseases*. Oxford University Press, p. ofu089.

Li, S., Chang, H.H., Niewolik, D., Hedrick, M.P., Pinkerton, A.B., Hassig, C.A., Schwarz, K., *et al.* (2014). Evidence that the DNA endonuclease ARTEMIS also has intrinsic 5′-exonuclease activity. *Journal of Biological Chemistry* **289**:7825–7834.

Liang, R., Morris, P., Cho, S.S.C., Abud, H.E., Jin, X. and Cheng, W. (2012). Hedgehog signaling displays a biphasic expression pattern during intestinal injury and repair. *Journal of Pediatric Surgery* **47**:2251–2263.

Lien, W.H. and Fuchs, E. (2014). Wnt some lose some: Transcriptional governance of stem cells by Wnt/β-catenin signaling. *Genes and Development* **28**:1517–1532.

Linch, M., Claus, J. and Benson, C. (2013). Update on imatinib for gastrointestinal stromal tumors: Duration of treatment. *OncoTargets and Therapy* **6**:1011–1023.

Lind, P., Lechner, P., Arian-Schad, K., Klimpfinger, M., Cesnik, H., Kammerhuber, F. and Eber, O. (1991). Anti-carcinoembryonic antigen immunoscintigraphy (technetium-99m-monoclonal antibody BW 431/26) and serum CEA levels in patients with suspected primary and recurrent colorectal carcinoma. *Journal of nuclear medicine : official publication, Society of Nuclear Medicine* **32**:1319–25.

Lindahl, T. (1986). DNA glycosylases in DNA repair. In: *Mechanisms of DNA Damage and Repair*. Springer, pp. 335–340.

Lindahl, T. (1993). Instability and decay of the primary structure of DNA. *Nature* **362**:709–715.

Lindahl, T. and Nyberg, B. (1972). Rate of depurination of native deoxyribonucleic acid. *Biochemistry* **11**:3610–3618.

Lisco, H., Brues, A.M., Finkel, M.P. and Grundhauser, W. (1947). Carcinoma of the colon in rats following the feeding of radioactive yttrium. In: *Cancer Research*. AMER ASSOC CANCER RESEARCH PO BOX 11806, BIRMINGHAM, AL 35202, p. 721.

Liu, W., Dong, X., Mai, M., Seelan, R.S., Taniguchi, K., Krishnadath, K.K., Halling, K.C., *et al.* (2000). Mutations in AXIN2 cause colorectal cancer with defective mismatch repair by activating [beta]-catenin/TCF signalling. *Nature genetics* **26**:146–148.

Löbrich, M., Shibata, A., Beucher, A., Fisher, A., Ensminger, M., Goodarzi, A.A., Barton, O., *et al.*

(2010). gammaH2AX foci analysis for monitoring DNA double-strand break repair: strengths, limitations and optimization. *Cell cycle (Georgetown, Tex)* [Online] **9**:662–669. Available at: http://www.landesbioscience.com/journals/cc/article/10764/.

Lorenz, E. and Stewart, H.L. (1940). Intestinal carcinoma and other lesions in mice following oral administration of 1, 2, 5, 6-dibenzanthracene and 20-methylcholanthrene. *Journal of the National Cancer Institute* **1**:17–40.

Lugli, A., Zlobec, I., Minoo, P., Baker, K., Tornillo, L., Terracciano, L. and Jass, J.R. (2007). Prognostic significance of the wnt signalling pathway molecules APC, β-catenin and E-cadherin in colorectal cancer—a tissue microarray-based analysis. *Histopathology* **50**:453–464.

Luo, J. and Cantley, L.C. (2005). The negative regulation of phosphoinositide 3-kinase signaling by p85 and it's implication in cancer. *Cell Cycle* **4**:1309–1312.

Luongo, C., Moser, A.R., Gledhill, S. and Dove, W.F. (1994). Loss of Apc+ in intestinal adenomas from Min mice. *Cancer research* **54**:5947–5952.

Lyons, S.M., Cunningham, C.H., Welch, J.D., Groh, B., Guo, A.Y., Wei, B., Whitfield, M.L., *et al.* (2016). A subset of replication-dependent histone mRNAs are expressed as polyadenylated RNAs in terminally differentiated tissues. *Nucleic Acids Research* **44**:9190–9205.

Macdonald, T.T. (2003). The mucosal immune system. *Parasite Immunology* **25**:235–246.

MacNicol, A.M., Hardy, L.L., Spencer, H.J. and MacNicol, M.C. (2015). Neural stem and progenitor cell fate transition requires regulation of Musashi1 function. *BMC developmental biology* **15**:15.

Madison, B.B., Braunstein, K., Kuizon, E., Portman, K., Qiao, X.T. and Gumucio, D.L. (2005). Epithelial hedgehog signals pattern the intestinal crypt-villus axis. *Development (Cambridge, England)* **132**:279–289.

Madison, B.B., Dunbar, L., Qiao, X.T., Braunstein, K., Braunstein, E. and Gumucio, D.L. (2002). Cis elements of the villin gene control expression in restricted domains of the vertical (crypt) and horizontal (duodenum, cecum) axes of the intestine. *Journal of Biological Chemistry* **277**:33275–33283.

Mah, L.J., El-Osta, A. and Karagiannis, T.C. (2010). γH2AX as a molecular marker of aging and disease. *Epigenetics* **5**:129–136.

Maier, T., Güell, M. and Serrano, L. (2009). Correlation of mRNA and protein in complex biological samples. *FEBS Letters* **583**:3966–3973.

Manning, B.D. and Cantley, L.C. (2007). AKT/PKB Signaling: Navigating Downstream. *Cell* **129**:1261–1274.

Mariotto, A., Pavlova, O., Park, H.S., Huber, M. and Hohl, D. (2016). HOPX: The Unusual Homeodomain-Containing Protein. *Journal of Investigative Dermatology* **136**:905–911.

El Marjou, F., Janssen, K.P., Chang, B.H.J., Li, M., Hindie, V., Chan, L., Louvard, D., *et al.* (2004). Tissue-specific and inducible Cre-mediated recombination in the gut epithelium. *Genesis* **39**:186–193.

Marley, A.R. and Nan, H. (2016). Epidemiology of colorectal cancer. *International Journal of Molecular Epidemiology and Genetics* **7**:105–114.

Marnett, L.J. and Plastaras, J.P. (2001). Endogenous DNA damage and mutation. *Trends in Genetics* **17**:214–221.

Marsh, V., Winton, D.J., Williams, G.T., Dubois, N., Trumpp, A., Sansom, O.J. and Clarke, A.R. (2008). Epithelial Pten is dispensable for intestinal homeostasis but suppresses adenoma development and progression after Apc mutation. *Nature genetics* **40**:1436–44.

Massagué, J. (2000). How cells read TGF-beta signals. *Nature reviews. Molecular cell biology* **1**:169–178.

Matsumura, Y. and Maeda, H. (1986). A new concept for macromolecular therapeutics in cnacer chemotherapy: mechanism of tumoritropic accumulatio of proteins and the antitumor agents Smancs. *Cancer research* **46**:6387–6392.

Mayer, R.J., Van Cutsem, E., Falcone, A., Yoshino, T., Garcia-Carbonero, R., Mizunuma, N., Yamazaki, K., *et al.* (2015). Randomized Trial of TAS-102 for Refractory Metastatic Colorectal Cancer. *New England Journal of Medicine* **372**:1909–1919.

Mazin, A. V., Alexeev, A.A. and Kowalczykowski, S.C. (2003). A novel function of Rad54 protein: Stabilization of the Rad51 nucleoprotein filament. *Journal of Biological Chemistry* **278**:14029–14036.

McDonald, E., Li, J., Krishnamurthy, M., Fellows, G.F., Goodyer, C.G. and Wang, R. (2012). SOX9 regulates endocrine cell differentiation during human fetal pancreas development. *The international journal of biochemistry & cell biology* **44**:72–83.

McGowan, C.H. (2003). Running into problems: How cells cope with replicating damaged DNA. *Mutation Research - Fundamental and Molecular Mechanisms of Mutagenesis* **532**:75–84.

McLean, J.R., Blakey, D.H., Douglas, G.R. and Bayley, J. (1989). The Auger electron dosimetry of indium-111 in mammalian cells in vitro. *Radiation research* **119**:205–18.

Mcllwraith, M.J., Vaisman, A., Liu, Y., Fanning, E., Woodgate, R. and West, S.C. (2005). Human DNA polymerase η promotes DNA synthesis from strand invasion intermediates of homologous recombination. *Molecular Cell* **20**:783–792.

Méniel, V., Megges, M., Young, M.A., Cole, A., Sansom, O.J. and Clarke, A.R. (2015). Apc and p53 interaction in DNA damage and genomic instability in hepatocytes. *Oncogene* **34**:4118–4129.

Menke-van der Houven van Oordt, C.W., Gootjes, E.C., Huisman, M.C., Vugts, D.J., Roth, C., Luik, A.M., Mulder, E.R., *et al.* (2015). 89Zr-cetuximab PET imaging in patients with advanced colorectal cancer. *Oncotarget* [Online] **6**:30384–30393.

Merrill, B.J., Gat, U., DasGupta, R. and Fuchs, E. (2001). Tcf3 and Lef1 regulate lineage differentiation of multipotent stem cells in skin. *Genes and Development* **15**:1688–1705.

Merrill, B.J., Pasolli, H.A., Polak, L., Rendl, M., García-García, M.J., Anderson, K. V and Fuchs, E. (2004). Tcf3: a transcriptional regulator of axis induction in the early embryo. *Development (Cambridge, England)* **131**:263–74.

Merritt, A.J., Allen, T.D., Potten, C.S. and Hickman, J.A. (1997). Apoptosis in small intestinal epithelia from p53-null mice: evidence for a delayed, p53-indepdendent G2/M-associated cell death after γ-irradiation. *Oncogene* [Online] **14**:2759–2766. Available at: http://www.nature.com/doifinder/10.1038/sj.onc.1201126.

Di Micco, R., Fumagalli, M., Cicalese, A., Piccinin, S., Gasparini, P., Luise, C., Schurra, C., *et al.* (2006). Oncogene-induced senescence is a DNA damage response triggered by DNA hyper-replication. *Nature* **444**:638–642.

Milano, J., McKay, J., Dagenais, C., Foster-Brown, L., Pognan, F., Gadient, R., Jacobs, R.T., *et al.* (2004). Modulation of Notch processing by γ-secretase inhibitors causes intestinal goblet cell metaplasia and induction of genes known to specify gut secretory lineage differentiation. *Toxicological Sciences* **82**:341–358.

Miller, D. and Crane, R.K. (1961). The digestive function of the epithelium of the small intestine. *Biochimica et Biophysica Acta* **52**:293–298.

Modesti, M. and Kanaar, R. (2001). Homologous recombination: from model organisms to human disease. *Genome biology* **2**:REVIEWS1014.

Moek, K.L., Giesen, D., Kok, I.C., de Groot, D.J.A., Jalving, M., Fehrmann, R.S.N., Lub-de Hooge, M.N., *et al.* (2017). Theranostics Using Antibodies and Antibody-Related Therapeutics. *Journal of Nuclear Medicine* [Online] **58**:83S–90S.

Montgomery, R.K., Carlone, D.L., Richmond, C. a, Farilla, L., Kranendonk, M.E.G., Henderson, D.E., Baffour-Awuah, N.Y., *et al.* (2011). Mouse telomerase reverse transcriptase (mTert) expression marks slowly cycling intestinal stem cells. *Proceedings of the National Academy of Sciences of the United States of America* **108**:179–184.

Moran, G.W., Leslie, F.C., Levison, S.E., Worthington, J. and McLaughlin, J.T. (2008). Enteroendocrine cells: neglected players in gastrointestinal disorders? *Therapeutic advances in gastroenterology* **1**:51–60.

Morgan, T.H. (1917). The Theory of the Gene. *The American Naturalist* **51**:513–544.

Morin, P.J., Kinzler, K.W. and Sparks, A.B. (2016). β-Catenin Mutations: Insights into the APC Pathway and the Power of Genetics. *Cancer Research* **76**:5587 LP-5589.

Morin, P.J., Sparks, a B., Korinek, V., Barker, N., Clevers, H., Vogelstein, B. and Kinzler, K.W. (1997). Activation of beta-catenin-Tcf signaling in colon cancer by mutations in beta-catenin or APC. *Science (New York, N.Y.)* **275**:1787–1790.

Mork, M.E. and Vilar, E. (2016). MUTYH-associated polyposis. In: *Intestinal Polyposis Syndromes: Diagnosis and Management*. pp. 25–32.

Morrison, S.J. and Kimble, J. (2006). Asymmetric and symmetric stem-cell divisions in development and cancer. *Nature* **441**:1068–1074.

Moser, A.R., Pitot, H.C. and Dove, W.F. (1990). A dominant mutation that predisposes to multiple intestinal neoplasia in the mouse. *Science* **247**:322.

Muller, H.J. (1941). Induced mutations in Drosophila. In: *Cold Spring Harbor Symposia on Quantitative Biology*. Cold Spring Harbor Laboratory Press, pp. 151–167.

Muñoz, J., Stange, D.E., Schepers, A.G., van de Wetering, M., Koo, B.-K., Itzkovitz, S., Volckmann, R., *et al.* (2012). The Lgr5 intestinal stem cell signature: robust expression of proposed quiescent '+4' cell markers. *The EMBO journal* [Online] **31**:3079–3091

Myant, K.B., Cammareri, P., McGhee, E.J., Ridgway, R.A., Huels, D.J., Cordero, J.B., Schwitalla, S., *et al.* (2013). ROS production and NF-κB activation triggered by RAC1 facilitate WNT-driven intestinal stem cell proliferation and colorectal cancer initiation. *Cell Stem Cell* **12**:761–773.

Nagasawa, H. and Little, J.B. (1992). Induction of Sister Chromatid Exchanges by Extremely Low Doses of α -Particles. *Cancer Research* [Online] **52**:6394–6396.

Nagel, R., le Sage, C., Diosdado, B., van der Waal, M., Oude Vrielink, J.A.F., Bolijn, A., Meijer, G.A., *et al.* (2008). Regulation of the Adenomatous Polyposis Coli Gene by the miR-135 Family in Colorectal Cancer. *Cancer Research* **68**:5795 LP-5802.

Nambiar, P.R., Girnun, G., Lillo, N.A., Guda, K., Whiteley, H.E. and Rosenberg, D.W. (2003). Preliminary analysis of azoxymethane induced colon tumors in inbred mice commonly used as transgenic/knockout progenitors. *International journal of oncology* **22**:145–150.

Nandan, M.O. and Yang, V.W. (2010). Genetic and chemical models of colorectal cancer in mice. *Current Colorectal Cancer Reports* **6**:51–59.

Näthke, I.S., Adams, C.L., Polakis, P., Sellin, J.H. and Nelson, W.J. (1996). The adenomatous polyposis coli tumor suppressor protein localizes to plasma membrane sites involved in active cell migration. *Journal of Cell Biology* **134**:165–179.

National Cancer Institute (2016). *Genetics of Colorectal Cancer* [Online]. Available at: http://www.cancer.gov/types/colorectal/hp/colorectal-genetics-pdq [Accessed: 16 June 2016].

National Institute for Health and Care Excellence (2016). NICE technology appraisal guidance TA405. *Nice*.

National Institute for Health Care and Excellence (2014). *Colorectal Cancer: Diagnosis and Management | Guidance and Guidelines | NICE* [Online]. Available at: https://www.nice.org.uk/guidance/cg131.

Negrini, S., Gorgoulis, V.G. and Halazonetis, T.D. (2010). Genomic instability--an evolving hallmark of cancer. *Nature reviews. Molecular cell biology* **11**:220–8.

Negrini, S., Gorgoulis, V.G. and Halazonetis, T.D. (2010). Genomic instability — an evolving hallmark of cancer. *Nature Reviews Molecular Cell Biology* [Online] **11**:220–228. Available at: http://www.nature.com/doifinder/10.1038/nrm2858.

Nelson, H., Petrelli, N., Carlin, A., Couture, J., Fleshman, J., Guillem, J., Miedema, B., *et al.* (2001). Guidelines 2000 for colon and rectal cancer surgery. *Journal of the National Cancer Institute* **93**:583–96.

Nishisho, I., Nakamura, Y., Miyoshi, Y., Miki, Y., Ando, H., Horii, A., Koyama, K., *et al.* (1991). Mutations of Chromosome-5q21 Genes in Fap and Colorectal-Cancer Patients. *Science* **253**:665–669.

Norbury, C.J. and Zhivotovsky, B. (2004). DNA damage-induced apoptosis. *Oncogene* **23**:2797–2808.

Nouspikel, T. (2009). DNA repair in mammalian cells : Nucleotide excision repair: variations on versatility. *Cellular and molecular life sciences : CMLS* **66**:994–1009.

O'Brien, C.A., Pollett, A., Gallinger, S. and Dick, J.E. (2007). A human colon cancer cell capable of initiating tumour growth in immunodeficient mice. *Nature* **445**:106–110.

O'Donoghue, J.A. and Wheldon, T.E. (1996). Targeted radiotherapy using Auger electron emitters. *Physics in medicine and biology* **41**:1973.

O'Driscoll, M. (2012). Diseases associated with defective responses to DNA damage. *Cold Spring Harbor Perspectives in Biology* **4**.

Oberdoerffer, P., Otipoby, K.L., Maruyama, M. and Rajewsky, K. (2003). Unidirectional Cre-mediated genetic inversion in mice using the mutant loxP pair lox66/lox71. *Nucleic acids research* **31**:e140.

Orban, P.C., Chui, D. and Marth, J.D. (1992). Tissue- and site-specific DNA recombination in transgenic mice. *Proceedings of the National Academy of Sciences of the United States of America* **89**:6861–5.

Oshima, H., Oshima, M., Kobayashi, M., Tsutsumi, M. and Taketo, M.M. (1997). Morphological and Molecular Processes of Polyp Formation in Apc{Delta}716 Knockout Mice. *Cancer Res.* [Online] **57**:1644–1649. Available at: http://cancerres.aacrjournals.org/content/57/9/1644.abstract.

Oshima, M., Oshima, H., Kitagawa, K., Kobayashi, M., Itakura, C. and Taketo, M. (1995). Loss of Apc heterozygosity and abnormal tissue building in nascent intestinal polyps in mice carrying a truncated Apc gene. *Proceedings of the National Academy of Sciences of the United States of America* **92**:4482–6.

Oswald, F., Täuber, B., Dobner, T., Bourteele, S., Kostezka, U., Adler, G., Liptay, S., *et al.* (2001). p300 acts as a transcriptional coactivator for mammalian Notch-1. *Molecular and cellular biology* **21**:7761–7774.

Otsu, N. (1979). A Threshold Selection Method from Gray Level Histograms. *IEEE Transactions on Systems, Man and Cybernetics.* [Online] **9**:62–66. Available at: http://ieeexplore.ieee.org/lpdocs/epic03/wrapper.htm?arnumber=4310076.

Ozasa, K., Shimizu, Y., Suyama, A., Kasagi, F., Soda, M., Grant, E.J., Sakata, R., *et al.* (2011). Studies of the mortality of atomic bomb survivors, Report 14, 1950–2003: an overview of cancer and noncancer diseases. *Radiation research* **177**:229–243.

Paik, W.K., Lee, H.W. and Kim, S. (1975). Non-enzymatic methylation of proteins with S-adenosyl-L-methionine. *FEBS letters* **58**:39–42.

Pankotai, T., Hoffbeck, A.S., Boumendil, C. and Soutoglou, E. (2009). DNA damage response in the absence of DNA lesions continued... *Cell Cycle* **8**:4025–4026.

Papadopoulo, D., Laquerbe, A., Guillouf, C. and Moustacchi, E. (1993). Molecular spectrum of mutations induced at the HPRT locus by a cross-linking agent in human cell lines with different repair capacities. *Mutation Research/DNA Repair* **294**:167–177.

Pathi, S., Pagan-Westphal, S., Baker, D.P., Garber, E.A., Rayhorn, P., Bumcrot, D., Tabin, C.J., *et al.* (2001). Comparative biological responses to human Sonic, Indian, and Desert hedgehog. *Mechanisms of Development* **106**:107–117.

Paudyal, B., Paudyal, P., Oriuchi, N., Hanaoka, H., Tominaga, H. and Endo, K. (2011). Positron emission tomography imaging and biodistribution of vascular endothelial growth factor with 64Cu-labeled bevacizumab in colorectal cancer xenografts. *Cancer Science* **102**:117–121.

Pelengaris, S., Khan, M. and Evan, G.I. (2002). Suppression of Myc-induced apoptosis in ?? cells exposes multiple oncogenic properties of Myc and triggers carcinogenic progression. *Cell* **109**:321–334.

Pellegrinet, L., Rodilla, V., Liu, Z., Chen, S., Koch, U., Espinosa, L., Kaestner, K.H., *et al.* (2011). Dll1- and Dll4-mediated notch signaling are required for homeostasis of intestinal stem cells. *Gastroenterology* **140**:1230–1240.

Perkin Elmer (2010). *Indium-111 Handling Precautions*.

Peters, A.M., Saverymuttu, S.H., Wonke, B., Lewis, S.M. and Lavender, J.P. (1984). The interpretation of platelet kinetic studies for the identification of sites of abnormal platelet destruction. *British journal of haematology* **57**:637–649.

Peters, T.J. (1970). Intestinal peptidases. *Gut* **11**:720–725.

Petersen, R.K., Hess, S., Alavi, A. and Høilund-Carlsen, P.F. (2014). Clinical impact of FDG-PET/CT on colorectal cancer staging and treatment strategy. *Am J Nucl Med Mol Imaging* **4**:471–482.

Peterson, L.W. and Artis, D. (2014). Intestinal Epithelial Cells: Regulators of Barrier Function and Immune Homeostasis. *Nat. Rev. Immunol.* **14**:141–153.

Petronis, J.D., Regan, F. and Lin, K. (1998). Indium-111 capromab pendetide (ProstaScint) imaging to detect recurrent and metastatic prostate cancer. *Clinical nuclear medicine* **23**:672–677.

Pfeifer, G.P., Denissenko, M.F., Olivier, M., Tretyakova, N., Hecht, S.S. and Hainaut, P. (2002). Tobacco smoke carcinogens, DNA damage and p53 mutations in smoking-associated cancers. *Oncogene* **21**:7435–51.

Pino, M.S. and Chung, D.C. (2010). The chromosomal instability pathway in colon cancer. *Gastroenterology* **138**:2059–2072.

Pinto, D., Gregorieff, A., Begthel, H. and Clevers, H. (2003). Canonical Wnt signals are essential for homeostasis of the intestinal epithelium. *Genes and Development* **17**:1709–1713.

Pinto, D., Robine, S., Jaisser, F., El Marjou, F. and Louvard, D. (1999). Regulatory sequences of the mouse villin gene that efficiently drive transgenic expression in immature and differentiated epithelial cells of small and large intestines. *Journal of Biological Chemistry* **274**:6476–6482.

Pogoda, J.M., Nichols, P.W., Ross, R.K., Stram, D.O., Thomas, D.C. and Preston-Martin, S. (2011).

Diagnostic radiography and adult acute myeloid leukaemia: an interview and medical chart review study. *British journal of cancer* **104**:1482–6.

Polakis, P. (1997). The adenomatous polyposis coli (APC) tumor suppressor. *Biochimica et Biophysica Acta (BBA) - Reviews on Cancer* **1332**:F127–F147.

Pospelova, T. V., Demidenko, Z.N., Bukreeva, E.I., Pospelov, V.A., Gudkov, A. V. and Blagosklonny, M. V. (2009). Pseudo-DNA damage response in senescent cells. *Cell Cycle* **8**:4112–4118.

Poston, G.J., Tait, D., O'Connell, S., Bennett, a. and Berendse, S. (2011). Diagnosis and management of colorectal cancer: summary of NICE guidance. *Bmj* **343**:d6751–d6751.

Potten, C.S. (1977). Extreme sensitivity of some intestinal crypt cells to X and gamma irradiation. *Nature* **269**:518–521.

Potten, C.S., Booth, C. and Pritchard, D.M. (1997). The intestinal epithelial stem cell: the mucosal governor. *International journal of experimental pathology* [Online] **78**:219–43. Available at: http://www.pubmedcentral.nih.gov/articlerender.fcgi?artid=2694540&tool=pmcentrez&rendertype=abstract.

Potten, C.S., Booth, C., Tudor, G.L., Booth, D., Brady, G., Hurley, P., Ashton, G., *et al.* (2003). Identification of a putative intestinal stem cell and early lineage marker; musashi-1. *Differentiation* **71**:28–41.

Potten, C.S., Gandara, R., Mahida, Y.R., Loeffler, M. and Wright, N.A. (2009). The stem cells of small intestinal crypts: Where are they? *Cell Proliferation* **42**:731–750.

Potten, C.S., Kellett, M., Rew, D.A. and Roberts, S.A. (1992). Proliferation in human gastrointestinal epithelium using bromodeoxyuridine in vivo: data for different sites, proximity to a tumour, and polyposis coli. *Gut* **33**:524–529.

Potten, C.S. and Loeffler, M. (1990). Stem cells: attributes, cycles, spirals, pitfalls and uncertainties. Lessons for and from the crypt. *Development* **110**:1001–1020.

Powell, A.E., Wang, Y., Li, Y., Poulin, E.J., Means, A.L., Washington, M.K., Higginbotham, J.N., *et al.* (2012). The pan-ErbB negative regulator lrig1 is an intestinal stem cell marker that functions as a tumor suppressor. *Cell* **149**:146–158.

Powell, S.M., Zilz, N., Beazer-Barclay, Y., Bryan, T.M., Hamilton, S.R., Thibodeau, S.N., Vogelstein, B., *et al.* (1992). APC mutations occur early during colorectal tumorigenesis. *Nature* **359**:235–237.

Pray, L. a (2008). Gleevec: the breakthrough in cancer treatment. *Nature Education* **1**:37.

Prendergast, G.C. (1999). Mechanisms of apoptosis by c-Myc. *Oncogene* [Online] **18**:2967–2987.

Quyn, A.J., Appleton, P.L., Carey, F.A., Steele, R.J.C., Barker, N., Clevers, H., Ridgway, R.A., *et al.* (2010). Spindle Orientation Bias in Gut Epithelial Stem Cell Compartments Is Lost in Precancerous Tissue. *Cell Stem Cell* **6**:175–181.

Radtke, F. and Clevers, H. (2005). Self-Renewal and Cancer of the Gut: Two Sides of a Coin. *Science* **307**:1904 LP-1909.

Radtke, F., Wilson, A., Mancini, S.J.C. and MacDonald, H.R. (2004). Notch regulation of lymphocyte development and function. *Nature immunology* **5**:247–53.

Rahman, A.F.M.M., Korashy, H.M. and Kassem, M.G. (2014). Gefitinib. *Profiles of Drug Substances, Excipients and Related Methodology* **39**:239–264.

Rahmim, A. and Zaidi, H. (2008). Pet versus spect: Strengths, limitations and challenges. *Nuclear Medicine Communications* **29**:193–207.

Ramalho-Santos, M., Melton, D. a and McMahon, a P. (2000). Hedgehog signals regulate multiple aspects of gastrointestinal development. *Development (Cambridge, England)* **127**:2763–2772.

Rao, C. V. and Yamada, H.Y. (2013). Genomic Instability and Colon Carcinogenesis: From the Perspective of Genes. *Frontiers in Oncology* **3**.

Reed, K.R., Meniel, V.S., Marsh, V., Cole, A., Sansom, O.J. and Clarke, A.R. (2008). A limited role for p53 in modulating the immediate phenotype of Apc loss in the intestine. *BMC cancer* **8**:162.

Reitsema, T., Klokov, D., Banáth, J.P. and Olive, P.L. (2005). DNA-PK is responsible for enhanced phosphorylation of histone H2AX under hypertonic conditions. *DNA Repair* **4**:1172–1181.

Ricci-Vitiani, L., Lombardi, D.G., Pilozzi, E., Biffoni, M., Todaro, M., Peschle, C. and De Maria, R. (2007). Identification and expansion of human colon-cancer-initiating cells. *Nature* **445**:111–115.

Riccio, O., van Gijn, M.E., Bezdek, A.C., Pellegrinet, L., van Es, J.H., Zimber-Strobl, U., Strobl, L.J., *et al.* (2008). Loss of intestinal crypt progenitor cells owing to inactivation of both Notch1 and Notch2 is accompanied by derepression of CDK inhibitors p27Kip1 and p57Kip2. *EMBO reports* **9**:377–83.

Rimkus, T.K., Carpenter, R.L., Qasem, S., Chan, M. and Lo, H.-W. (2016). Targeting the Sonic Hedgehog Signaling Pathway: Review of Smoothened and GLI Inhibitors Cho, W. C. (ed.). *Cancers* **8**:22.

Riss, T.L., Moravec, R.A., Niles, A.L., Duellman, S., Benink, H.A., Worzella, T.J. and Minor, L. (2013). Cell Viability Assays. *Assay Guidance Manual [Internet]* **114**:785–796.

Riva, P., Moscatelli, G., Agostini, M., Spinelli, A. and Franceschi, G. (1989). Immunoscintigraphy of primary and metastatic colorectal cancers with radiolabelled monoclonal antibodies anti-CEA. In: *Acta Gastro-Enterologica Belgica*. pp. 497–505.

Roberts, D.J. (2000). Molecular mechanisms of development of the gastrointestinal tract. *Developmental dynamics : an official publication of the American Association of Anatomists* **219**:109–120.

Robinson, K., Asawachaicharn, N., Galloway, D.A. and Grandori, C. (2009). c-Myc accelerates S-phase and requires WRN to avoid replication stress. *PLoS ONE* **4**.

Rockman, S.P., Currie, S. a, Ciavarella, M., Vincan, E., Dow, C., Thomas, R.J. and Phillips, W. a (2001). Id2 is a target of the beta-catenin/T cell factor pathway in colon carcinoma. *The Journal of biological chemistry* **276**:45113–9.

Rodriguez-Salas, N., Dominguez, G., Barderas, R., Mendiola, M., García-Albéniz, X., Maurel, J. and Batlle, J.F. (2017). Clinical relevance of colorectal cancer molecular subtypes. *Critical Reviews in Oncology/Hematology* **109**:9–19.

Rogakou, E.P., Nieves-Neira, W., Boon, C., Pommier, Y. and Bonner, W.M. (2000). Initiation of DNA fragmentation during apoptosis induces phosphorylation of H2AX histone at serine 139. *Journal of Biological Chemistry* **275**:9390–9395.

Rohren, E.M., Paulson, E.K., Hagge, R., Wong, T.Z., Killius, J., Clavien, P.-A., Nelson, R.C., *et al.* (2002). The role of F-18 FDG positron emission tomography in preoperative assessment of the liver in patients being considered for curative resection of hepatic metastases from colorectal cancer. *Clinical Nuclear Medicine* **27**:550–555.

Romagnolo, B., Berrebi, D., Saadi-Keddoucci, S., Porteu, A., Pichard, A.L., Peuchmaur, M., Vandewalle, A., *et al.* (1999). Intestinal dysplasia and adenoma in transgenic mice after overexpression of an activated β-catenin. *Cancer Research* **59**:3875–3879.

Roose, J., Molenaar, M., Peterson, J., Hurenkamp, J., Brantjes, H., Moerer, P., van de Wetering,

M., *et al.* (1998). The Xenopus Wnt effector XTcf-3 interacts with Groucho-related transcriptional repressors. *Nature* 395:608–612.

Rosenbaum, C.E., Verkooijen, H.M., Lam, M.G., Smits, M.L., Koopman, M., van Seeters, T., Vermoolen, M. a, *et al.* (2013). Radioembolization for treatment of salvage patients with colorectal cancer liver metastases: a systematic review. *J Nucl Med* 54:1890–1895.

Rosin-Arbesfeld, R., Ihrke, G. and Bienz, M. (2001). Actin-dependent membrane association of the APC tumour suppressor in polarized mammalian epithelial cells. *The EMBO Journal* 20:5929–5939.

Ross, D.A. and Kadesch, T. (2001). The notch intracellular domain can function as a coactivator for LEF-1. *Molecular and Cellular Biology* [Online] 21:7537–7544. Available at: papers://47009fda-d2bb-40d3-9a68-dc08a98706c7/Paper/p2948.

Rowlatt, C., Franks, L.M., Sheriff, M.U. and Chesterman, F.C. (1969). Naturally occurring tumors and other lesions of the digestive tract in untreated C57BL mice. *Journal of the National Cancer Institute* 43:1353–1364.

Rubinfeld, B., Tice, D. a and Polakis, P. (2001). Axin-dependent phosphorylation of the adenomatous polyposis coli protein mediated by casein kinase 1epsilon. *The Journal of biological chemistry* 276:39037–45.

Saam, J.R. and Gordon, J.I. (1999). Inducible gene knockouts in the small intestinal and colonic epithelium. *Journal of Biological Chemistry* 274:38071–38082.

Sahani, D. V, Kalva, S.P., Fischman, A.J., Kadavigere, R., Blake, M., Hahn, P.F. and Saini, S. (2005). Detection of liver metastases from adenocarcinoma of the colon and pancreas: comparison of mangafodipir trisodium–enhanced liver MRI and whole-body FDG PET. *American Journal of Roentgenology* 185:239–246.

Samowitz, W.S., Powers, M.D., Spirio, L.N., Nollet, F., Van Roy, F. and Slattery, M.L. (1999). ??-catenin mutations are more frequent in small colorectal adenomas than in larger adenomas and invasive carcinomas. *Cancer Research* 59:1442–1444.

Sangiorgi, E. and Capecchi, M.R. (2008). Bmi1 is expressed in vivo in intestinal stem cells. *Nature genetics* 40:915–20.

Sansom, O.J., Meniel, V.S., Muncan, V., Phesse, T.J., Wilkins, J.A., Reed, K.R., Vass, J.K., *et al.* (2007). Myc deletion rescues Apc deficiency in the small intestine. *Nature* 446:676–679.

Sansom, O.J., Reed, K.R., Hayes, A.J., Ireland, H., Brinkmann, H., Newton, I.P., Batlle, E., *et al.* (2004). Loss of Apc in vivo immediately perturbs Wnt signaling, differentiation, and migration. *Genes & development* 18:1385–1390.

De Santa Barbara, P., Van Den Brink, G.R. and Roberts, D.J. (2003). Development and differentiation of the intestinal epithelium. *Cellular and Molecular Life Sciences* 60:1322–1332.

Sasaki, M.S., Tachibana, A. and Takeda, S. (2014). Cancer risk at low doses of ionizing radiation: artificial neural networks inference from atomic bomb survivors. *Journal of Radiation Research* 55:391–406.

Sato, T., Vries, R.G., Snippert, H.J., van de Wetering, M., Barker, N., Stange, D.E., van Es, J.H., *et al.* (2009). Single Lgr5 stem cells build crypt-villus structures in vitro without a mesenchymal niche. *Nature* [Online] 459:262–5. Available at: http://www.ncbi.nlm.nih.gov/pubmed/19329995.

Sauer, B. (1987). Functional expression of the cre-lox site-specific recombination system in the yeast *Saccharomyces cerevisiae*. *Molecular and cellular biology* 7:2087–2096.

Sauer, B. (1998). Inducible Gene Targeting in Mice Using the Cre / lox System. *Methods* 392:381–392.

Scales, S.J. and de Sauvage, F.J. (2009). Mechanisms of Hedgehog pathway activation in cancer and implications for therapy. *Trends in Pharmacological Sciences* **30**:303–312.

Schepers, A.G., Vries, R., van den Born, M., van de Wetering, M. and Clevers, H. (2011). Lgr5 intestinal stem cells have high telomerase activity and randomly segregate their chromosomes. *The EMBO Journal* **30**:1104–1109.

Schmidt, T., Leha, A. and Salinas-Riester, G. (2016). Treatment of prostate cancer cells with S-adenosylmethionine leads to genome-wide alterations in transcription profiles. *Gene* **595**:161–167.

Schofield, R. (1978). The relationship between the spleen colony-forming cell and the haemopoietic stem cell. *Blood cells* **4**:7–25.

Schwitalla, S., Fingerle, A.A., Cammareri, P., Nebelsiek, T., Göktuna, S.I., Ziegler, P.K., Canli, O., *et al.* (2013). Intestinal tumorigenesis initiated by dedifferentiation and acquisition of stem-cell-like properties. *Cell* **152**:25–38.

Scoville, D.H., Sato, T., He, X.C. and Li, L. (2008). Current View: Intestinal Stem Cells and Signaling. *Gastroenterology* **134**:849–864.

Segal, A.W., Arnot, R.N., Thakur, M.L. and Lavender, J.P. (1976). Indium-111-labelled leucocytes for localisation of abscesses. *The Lancet* **308**:1056–1058.

Shahriyari, L. and Komarova, N.L. (2013). Symmetric vs. Asymmetric Stem Cell Divisions: An Adaptation against Cancer? *PLoS ONE* [Online] **8**:e76195. Available at: http://dx.plos.org/10.1371/journal.pone.0076195.

Sharma, A., Singh, K. and Almasan, A. (2012). Histone H2AX phosphorylation: a marker for DNA damage. In: *DNA Repair Protocols*. Springer, pp. 613–626.

Sheth, K.R. and Clary, B.M. (2005). Management of hepatic metastases from colorectal cancer. *Clinics in Colon and Rectal Surgery* **18**:215–223.

Shi, M., Hu, Z.-L., Zheng, M.-H., Song, N.-N., Huang, Y., Zhao, G., Han, H., *et al.* (2012). Notch-Rbpj signaling is required for the development of noradrenergic neurons in the mouse locus coeruleus. *Journal of cell science* [Online] **125**:4320–32. Available at: http://www.ncbi.nlm.nih.gov/pubmed/22718343.

Shi, Y. and Massagué, J. (2003). Mechanisms of TGF-b Signaling from Cell Membrane to the Nucleus. *Cell* **113**:16.

Shibata, H., Toyama, K., Shioya, H., Ito, M., Hirota, M., Hasegawa, S., Matsumoto, H., *et al.* (1997). Rapid colorectal adenoma formation initiated by conditional targeting of the Apc gene. *Science (New York, N.Y.)* **278**:120–123.

Shibutani, S., Takeshita, M. and Grollman, A.P. (1991). Insertion of specific bases during DNA synthesis past the oxidation-damaged base 8-oxodG. *nature* **349**:431.

Shiloh, Y. and Ziv, Y. (2013). The ATM protein kinase: regulating the cellular response to genotoxic stress, and more. *Nature Reviews Molecular Cell Biology* [Online] **14**:197–210. Available at: http://www.nature.com/doifinder/10.1038/nrm3546.

Shimokawa, M., Ohta, Y., Nishikori, S., Matano, M., Takano, A., Fujii, M., Date, S., *et al.* (2017). Visualization and targeting of LGR5+ human colon cancer stem cells. *Nature* [Online] **545**:187–192. Available at: http://www.nature.com/doifinder/10.1038/nature22081.

Shmelkov, S. V., Butler, J.M., Hooper, A.T., Hormigo, A., Kushner, J., Milde, T., St Clair, R., *et al.* (2008). CD133 expression is not restricted to stem cells, and both CD133 + and CD133- metastatic colon cancer cells initiate tumors. *Journal of Clinical Investigation* **118**:2111–2120.

Shroyer, N.F., Helmrath, M.A., Wang, V.Y.C., Antalffy, B., Henning, S.J. and Zoghbi, H.Y. (2007). Intestine-Specific Ablation of Mouse atonal homolog 1 (Math1) Reveals a Role in Cellular

Homeostasis. *Gastroenterology* **132**:2478–2488.

Shtutman, M., Zhurinsky, J., Simcha, I., Albanese, C., D'Amico, M., Pestell, R. and Ben-Ze'ev, A. (1999). The cyclin D1 gene is a target of the beta-catenin/LEF-1 pathway. *Proceedings of the National Academy of Sciences of the United States of America* **96**:5522–7.

Sigurdson, A.J., Bhatti, P., Preston, D.L., Doody, M.M., Kampa, D., Alexander, B.H., Petibone, D., *et al.* (2008). Routine diagnostic X-ray examinations and increased frequency of chromosome translocations among U.S. radiologic technologists. *Cancer Research* **68**:8825–8831.

Snippert, H.J., van Es, J.H., van den Born, M., Begthel, H., Stange, D.E., Barker, N. and Clevers, H. (2009). Prominin-1/CD133 Marks Stem Cells and Early Progenitors in Mouse Small Intestine. *Gastroenterology* **136**.

Snippert, H.J., van der Flier, L.G., Sato, T., van Es, J.H., van den Born, M., Kroon-Veenboer, C., Barker, N., *et al.* (2010). Intestinal crypt homeostasis results from neutral competition between symmetrically dividing Lgr5 stem cells. *Cell* **143**:134–144.

So, S., Davis, A.J. and Chen, D.J. (2009). Autophosphorylation at serine 1981 stabilizes ATM at DNA damage sites. *Journal of Cell Biology* **187**:977–990.

Solier, S. and Pommier, Y. (2014). The nuclear γ-H2AX apoptotic ring: Implications for cancers and autoimmune diseases. *Cellular and Molecular Life Sciences* **71**:2289–2297.

Sotiropoulou, P.A., Candi, A., Mascré, G., De Clercq, S., Youssef, K.K., Lapouge, G., Dahl, E., *et al.* (2010). Bcl-2 and accelerated DNA repair mediates resistance of hair follicle bulge stem cells to DNA-damage-induced cell death. *Nature Cell Biology* **12**:572–582.

Sparks, A.B., Morin, P.J., Vogelstein, B. and Kinzler, K.W. (1998). Mutational analysis of the APC/beta-catenin/Tcf pathway in colorectal cancer. *Cancer research* **58**:1130–4.

Spitz, D.R. and Hauer-Jensen, M. (2014). Ionizing radiation-induced responses: where free radical chemistry meets redox biology and medicine. *Antioxidants & redox signaling* **20**:1407–1409.

Srinivasan, T., Than, E.B., Bu, P., Tung, K.-L., Chen, K.-Y., Augenlicht, L., Lipkin, S.M., *et al.* (2016). Notch signalling regulates asymmetric division and inter-conversion between lgr5 and bmi1 expressing intestinal stem cells. *Scientific Reports* **6**:26069.

Staal, F.J. and Clevers, H.C. (2005). WNT signalling and haematopoiesis: a WNT-WNT situation. *Nat Rev Immunol* **5**:21–30.

Staib, L., Schirrmeister, H., Reske, S.N. and Beger, H.G. (2000). Is (18)F-fluorodeoxyglucose positron emission tomography in recurrent colorectal cancer a contribution to surgical decision making? *American journal of surgery* [Online] **180**:1–5. Available at: http://www.ncbi.nlm.nih.gov/pubmed/11036130.

Stanger, B.Z., Datar, R., Murtaugh, L.C. and Melton, D.A. (2005). Direct regulation of intestinal fate by Notch. *Proceedings of the National Academy of Sciences of the United States of America* **102**:12443–8.

Stecca, B. and Ruiz I Altaba, A. (2010). Context-dependent regulation of the GLI code in cancer by HEDGEHOG and non-HEDGEHOG signals. *Journal of Molecular Cell Biology* **2**:84–95.

Steinhauser, M.L., Bailey, A.P., Senyo, S.E., Guillermier, C., Perlstein, T.S., Gould, A.P., Lee, R.T., *et al.* (2012). Multi-isotope imaging mass spectrometry quantifies stem cell division and metabolism. *Nature* [Online] **481**:516–519. Available at: http://www.nature.com/doifinder/10.1038/nature10734.

Sternberg, N. and Hamilton, D. (1981). Bacteriophage P1 site-specific recombination. I. Recombination between loxP sites. *Journal of Molecular Biology* **150**:467–486.

Stewart, A., Webb, J., Giles, D. and Hewitt, D. (1956). Malignant disease in childhood and

diagnostic irradiation in utero. *The Lancet* 268:447.

Stover, E.H., Konstantinopoulos, P.A., Matulonis, U.A. and Swisher, E.M. (2016). Biomarkers of response and resistance to DNA repair targeted therapies. *Clinical Cancer Research* 22:5651–5660.

Su, L.K., Kinzler, K.W., Vogelstein, B., Preisinger, A.C., Moser, A.R., Luongo, C., Gould, K.A., *et al.* (1992). Multiple intestinal neoplasia caused by a mutation in the murine homolog of the APC gene. *Science* 256:668 LP-670.

Suijkerbuijk, S.J.E., Kolahgar, G., Kucinski, I. and Piddini, E. (2016). Cell competition drives the growth of intestinal adenomas in Drosophila. *Current Biology* 26:428–438.

Sutent, S. (2007). Sunitinib (Sutent®). *Quality*:1–21.

Takeda, N., Jain, R., LeBoeuf, M.R., Wang, Q., Lu, M.M. and Epstein, J.A. (2011). Interconversion between intestinal stem cell populations in distinct niches. *Science (New York, N.Y.)* 334:1420–1424.

Tan, D.W.M. and Barker, N. (2014). Intestinal Stem Cells and Their Defining Niche. *Current Topics in Developmental Biology* 107:77–107.

Tang, Y., Urs, S., Boucher, J., Bernaiche, T., Venkatesh, D., Spicer, D.B., Vary, C.P.H., *et al.* (2010). Notch and transforming growth factor-beta (TGFbeta) signaling pathways cooperatively regulate vascular smooth muscle cell differentiation. *The Journal of biological chemistry* 285:17556–17563.

Tetsu, O. and McCormick, F. (1999). β-Catenin regulates expression of cyclin D1 in colon carcinoma cells. *Nature* 398:422–426.

Tian, H., Biehs, B., Warming, S., Leong, K.G., Rangell, L., Klein, O.D. and de Sauvage, F.J. (2011). A reserve stem cell population in small intestine renders Lgr5-positive cells dispensable. *Nature* 478:255–9.

Tonegawa, S. (1983). Somatic generation of antibody diversity. *Nature* 302:575–581.

Tran, H., Bustos, D., Yeh, R., Rubinfeld, B., Lam, C., Shriver, S., Zilberleyb, I., *et al.* (2013). HectDI E3 ligase modifies adenomatous polyposis coli (APC) with polyubiquitin to promote the APC-axin interaction. *Journal of Biological Chemistry* 288:3753–3767.

Tran, H., Hamada, F., Schwarz-Romond, T. and Bienz, M. (2008). Trabid, a new positive regulator of Wnt-induced transcription with preference for binding and cleaving K63-linked ubiquitin chains. *Genes & Development* 22:528–542.

Trejo, C.L., Luna, G., Dravis, C., Spike, B.T. and Wahl, G.M. (2017). Lgr5 is a marker for fetal mammary stem cells, but is not essential for stem cell activity or tumorigenesis. *npj Breast Cancer* [Online] 3:16. Available at: http://www.nature.com/articles/s41523-017-0018-6.

Trobridge, P., Knoblaugh, S., Washington, M.K., Munoz, N.M., Tsuchiya, K.D., Rojas, A., Song, X., *et al.* (2009). TGF-β receptor inactivation and mutant Kras induce intestinal neoplasms in mice via a β-catenin independent pathway. *Gastroenterology* 136:1680–8.e7.

Tu, L., Foltz, G., Lin, E., Hood, L. and Tian, Q. (2009). Targeting Stem Cells-Clinical Implications for Cancer Therapy. *Current Stem Cell Research & Therapy* 4:147–153.

Tuveson, D.A., Shaw, A.T., Willis, N.A., Silver, D.P., Jackson, E.L., Chang, S., Mercer, K.L., *et al.* (2004). Endogenous oncogenic K-rasG12D stimulates proliferation and widespread neoplastic and developmental defects. *Cancer Cell* 5:375–387.

U.S. Food & Drug Administration (2017). *What Are the Radiation Risks from CT?*

Uhlen, M., Fagerberg, L., Hallstrom, B.M., Lindskog, C., Oksvold, P., Mardinoglu, A., Sivertsson, A., *et al.* (2015). Tissue-based map of the human proteome. *Science* [Online] 347:1260419–

1260419. Available at: http://www.sciencemag.org/cgi/doi/10.1126/science.1260419.

Vafa, O., Wade, M., Kern, S., Beeche, M., Pandita, T.K., Hampton, G.M. and Wahl, G.M. (2002). c-Myc can induce DNA damage, increase reactive oxygen species, and mitigate p53 function: A mechanism for oncogene-induced genetic instability. *Molecular Cell* **9**:1031–1044.

Valenta, T., Lukas, J. and Korinek, V. (2003). HMG box transcription factor TCF-4's interaction with CtBP1 controls the expression of the Wnt target Axin2/Conductin in human embryonic kidney cells. *Nucleic Acids Research* **31**:2369–2380.

VanDussen, K.L., Carulli, a. J., Keeley, T.M., Patel, S.R., Puthoff, B.J., Magness, S.T., Tran, I.T., *et al.* (2012). Notch signaling modulates proliferation and differentiation of intestinal crypt base columnar stem cells. *Development* **139**:488–497.

VanDussen, K.L. and Samuelson, L.C. (2010). Mouse atonal homolog 1 directs intestinal progenitors to secretory cell rather than absorptive cell fate. *Developmental Biology* **346**:215–223.

Vanneman, M. and Dranoff, G. (2012). Combining immunotherapy and targeted therapies in cancer treatment. *Nature reviews. Cancer* **12**:237–51.

Varela-Rey, M., Iruarrizaga-Lejarreta, M., Lozano, J.J., Aransay, A.M., Fernandez, A.F., Lavin, J.L., Mósen-Ansorena, D., *et al.* (2014). S-adenosylmethionine levels regulate the schwann cell DNA methylome. *Neuron* **81**:1024–1039.

Vieira, M.R., Rodrigues, M., Salgado, L., Santos, R., Mendes De Almeida, J.C., Orey Manoel, L. and Mendes De Almeida, J.M. (1993). Immunoscintigraphy with 99mTc-labelled anti-CEA monoclonal antibody in colorectal carcinoma. *European Journal of Surgical Oncology* **19**:294–299.

Vitale, I., Galluzzi, L., Castedo, M. and Kroemer, G. (2011). Mitotic catastrophe: a mechanism for avoiding genomic instability. *Nature Reviews Molecular Cell Biology* [Online] **12**:385–392. Available at: http://www.nature.com/doifinder/10.1038/nrm3115.

van Vloten, J.P., Workenhe, S.T., Wootton, S.K., Mossman, K.L. and Bridle, B.W. (2018). Critical Interactions between Immunogenic Cancer Cell Death, Oncolytic Viruses, and the Immune System Define the Rational Design of Combination Immunotherapies. *The Journal of Immunology* **200**:450–458.

Vooijs, M., Ong, C., Hadland, B., Huppert, S., Liu, Z., Korving, J., van den Born, M., *et al.* (2007). Mapping the consequence of Notch1 proteolysis in vivo with NIP-CRE. *Development (Cambridge, England)* **134**:535–544.

Waite, K.A. and Eng, C. (2003). BMP2 exposure results in decreased PTEN protein degradation and increased PTEN levels. *Human Molecular Genetics* **12**:679–684.

Wakefield, L.M. and Hill, C.S. (2013). Beyond TGFbeta: roles of other TGFbeta superfamily members in cancer. *Nat Rev Cancer* **13**:328–341.

Wallace, S.S. (1988). AP endonucleases and DNA glycosylases that recognize oxidative DNA damage. *Environmental and molecular mutagenesis* **12**:431–477.

Wallkamm, V., Rahm, K., Schmoll, J., Kaufmann, L.T., Brinkmann, E., Schunk, J., Kraft, B., *et al.* (2016). Regulation of distinct branches of the non-canonical Wnt-signaling network in Xenopus dorsal marginal zone explants. *BMC Biology* **14**.

Walpole, A.L., Williams, M.H.C. and Roberts, D.C. (1952). The carcinogenic action of 4-aminodiphenyl and 3: 2'-dimethyl-4-aminodiphenyl. *British journal of industrial medicine* **9**:255.

Wang, H., Adhikari, S., Butler, B.E., Pandita, T.K., Mitra, S. and Hegde, M.L. (2014). A Perspective on Chromosomal Double Strand Break Markers in Mammalian Cells. *Jacobs Journal of Radiation Oncology* **1**:1–5.

Wang, H., Perrault, A.R., Takeda, Y., Qin, W., Wang, H. and Iliakis, G. (2003). Biochemical evidence for Ku-independent backup pathways of NHEJ. *Nucleic Acids Research* **31**:5377–5388.

Watt, F.M. (2004). Unexpected Hedgehog-Wnt interactions in epithelial differentiation. *Trends in Molecular Medicine* **10**:577–580.

Westhorpe, F.G. and Straight, A.F. (2015). The centromere: Epigenetic control of chromosome segregation during mitosis. *Cold Spring Harbor Perspectives in Biology* **7**.

Wharton, K.A., Johansen, K.M., Xu, T. and Artavanis-Tsakonas, S. (1985). Nucleotide sequence from the neurogenic locus Notch implies a gene product that shares homology with proteins containing EGF-like repeats. *Cell* **43**:567–581.

Willert, J., Epping, M., Pollack, J.R., Brown, P.O. and Nusse, R. (2002). A transcriptional response to Wnt protein in human embryonic carcinoma cells. *BMC developmental biology* **2**:8.

Willett, W.C., Stampfer, M.J., Colditz, G.A., Rosner, B.A. and Speizer, F.E. (1990). Relation of meat, fat, and fiber intake to the risk of colon cancer in a prospective study among women. *The New England journal of medicine* **323**:1664–1672.

Williams, R.S., Williams, J.S. and Tainer, J.A. (2007). Mre11–Rad50–Nbs1 is a keystone complex connecting DNA repair machinery, double-strand break signaling, and the chromatin template This paper is one of a selection of papers published in this Special Issue, entitled 28th International West Coast Chromatin . *Biochemistry and cell biology* **85**:509–520.

Wilson, A. and Radtke, F. (2006). Multiple functions of Notch signaling in self-renewing organs and cancer. *FEBS letters* [Online] **580**:2860–8. Available at: http://www.ncbi.nlm.nih.gov/pubmed/16574107 [Accessed: 27 February 2017].

Wong, G.T., Manfra, D., Poulet, F.M., Zhang, Q., Josien, H., Bara, T., Engstrom, L., *et al.* (2004). Chronic Treatment with the γ-Secretase Inhibitor LY-411,575 Inhibits γ-Amyloid Peptide Production and Alters Lymphopoiesis and Intestinal Cell Differentiation. *Journal of Biological Chemistry* **279**:12876–12882.

Wong, J.Y.C., Chu, D.Z., Williams, L.E., Liu, A., Zhan, J., Yamauchi, D.M., Wilczynski, S., *et al.* (2006). A phase I trial of 90Y-DOTA-anti-CEA chimeric T84. 66 (cT84. 66) radioimmunotherapy in patients with metastatic CEA-producing malignancies. *Cancer biotherapy & radiopharmaceuticals* **21**:88–100.

Wong, V.W.Y., Stange, D.E., Page, M.E., Buczacki, S., Wabik, A., Itami, S., van de Wetering, M., *et al.* (2012). Lrig1 controls intestinal stem-cell homeostasis by negative regulation of ErbB signalling. *Nature cell biology* **14**:401–8.

Wu, L., Aster, J.C., Blacklow, S.C., Lake, R., Artavanis-Tsakonas, S. and Griffin, J.D. (2000). MAML1, a human homologue of Drosophila mastermind, is a transcriptional co-activator for NOTCH receptors. *Nature genetics* **26**:484–489.

Wu, L., Sun, T., Kobayashi, K., Gao, P. and Griffin, J.D. (2002). Identification of a family of mastermind-like transcriptional coactivators for mammalian notch receptors. *Molecular and cellular biology* [Online] **22**:7688–700. Available at: http://www.pubmedcentral.nih.gov/articlerender.fcgi?artid=135662&tool=pmcentrez&rendertype=abstract.

Yamada, T., Takaoka, A.S., Naishiro, Y., Hayashi, R., Maruyama, K., Maesawa, C., Ochiai, A., *et al.* (2000). Transactivation of the Multidrug Resistance 1 gene by T-cell factor 4/β-catenin complex in early colorectal carcinogenesis. *Cancer Research* **60**:4761–4766.

Yan, K.S., Chia, L.A., Li, X., Ootani, A., Su, J., Lee, J.Y., Su, N., *et al.* (2012). The intestinal stem cell markers Bmi1 and Lgr5 identify two functionally distinct populations. *Proceedings of the National Academy of Sciences of the United States of America* **109**:466–71.

Yang, J., Sun, Z. and Komarova, N.L. (2015). Analysis of stochastic stem cell models with control.

Math Biosci **266**.

Yang, Q., Bermingham, N.A., Finegold, M.J. and Zoghbi, H.Y. (2001). Requirement of Math1 for Secretory Cell Lineage Commitment in the Mouse Intestine. *Science* **294**:2155 LP-2158.

Yang, S.-C., Lin, J.-G., Chiou, C.-C., Chen, L.-Y. and Yang, J.-L. (1994). Mutation specificity of 8-methoxypsoralen plus two doses of UVA irradiation in the hprt gene in diploid human fibroblasts. *Carcinogenesis* **15**:201–207.

Yi, J., Xiong, W., Gong, X., Bellister, S., Ellis, L.M. and Liu, Q. (2013). Analysis of LGR4 Receptor Distribution in Human and Mouse Tissues. *PLoS ONE* **8**.

Young, B., Woodford, P. and Gerladine, O. (2013). *Functional Histology*.

Yueh, A.E., Payne, S.N., Leystra, A.A., Van De Hey, D.R., Foley, T.M., Pasch, C.A., Clipson, L., *et al.* (2016). Colon cancer tumorigenesis initiated by the H1047R mutant PI3K. *PLoS ONE* **11**.

Zadorozny, E. V., Little, J.C. and Kalderon, D. (2015). Contributions of Costal 2-Fused interactions to Hedgehog signaling in Drosophila. *Development* **142**:931–942.

Zhang, X., Gaspard, J.P. and Chung, D.C. (2001). Regulation of vascular endothelial growth factor by the Wnt and K-ras pathways in colonic neoplasia. *Cancer Research* **61**:6050–6054.

Zhang, X., Ye, C., Sun, F., Wei, W., Hu, B. and Wang, J. (2016). Both complexity and location of DNA damage contribute to cellular senescence induced by ionizing radiation. *PLoS ONE* **11**.

Zhu, J., Blenis, J. and Yuan, J. (2008). Activation of PI3K/Akt and MAPK pathways regulates Myc-mediated transcription by phosphorylating and promoting the degradation of Mad1. *Proceedings of the National Academy of Sciences* **105**:6584–6589.

Zhu, L., Gibson, P., Currle, D.S., Tong, Y., Richardson, R.J., Bayazitov, I.T., Poppleton, H., *et al.* (2009). Prominin 1 marks intestinal stem cells that are susceptible to neoplastic transformation. *Nature* **457**:603–607.

Zhu, Y., Richardson, J. a, Parada, L.F. and Graff, J.M. (1998). Smad3 mutant mice develop metastatic colorectal cancer. *Cell* **94**:703–714.

Appendix 1:

The script used for quantifying the number of total cells and γH2AX quantification

Note: This can be copied and pasted in fiji/ImageJ command line, changing the input and output file directories (i.e. the directory following dir1 and save as, respectively) accordingly.

```
dir1 = "C:\\Users\\maria\\Desktop\\fiji-win64 (1)\\Fiji.app\\imagesTEST\\";

list = getFileList(dir1);

setBatchMode(true);

for (i=0; i<list.length; i++) {

showProgress(i+1, list.length);

open(dir1+list[i]);

imgName=getTitle();

run("Colour Deconvolution", "vectors=[H&E DAB]");

selectWindow(imgName + "-(Colour_2)");

close();

selectWindow(imgName +"-(Colour_1)");

run("Duplicate...", " ");

title = getTitle();

print("title: " + title);

saveAs("Tiff", "C:\\Users\\maria\\Desktop\\fiji-win64 (1)\\Fiji.app\\imagesTESToutput\\"+title);

close();

selectWindow(imgName +"-(Colour_1)");

//run("Brightness/Contrast...");

setMinAndMax(0, 185);

run("Apply LUT");

run("Smooth");

setAutoThreshold("Default");
```

```
//run("Threshold...");

//setThreshold(0, 212);

setOption("BlackBackground", false);

run("Convert to Mask");

run("Close-");

run("Erode");

run("Median...", "radius=2");

run("Open");

run("Morphological Filters", "operation=Dilation element=Disk radius=1");

run("Adjustable Watershed", "tolerance=0.2");

title = getTitle();

print("title: " + title);

saveAs("Tiff", "C:\\Users\\maria\\Desktop\\fiji-win64 (1)\\Fiji.app\\imagesTESToutput\\"+title);

selectWindow(imgName + "-(Colour_3)");

run("Duplicate...", " ");

title = getTitle();

print("title: " + title);

saveAs("Tiff", "C:\\Users\\maria\\Desktop\\fiji-win64 (1)\\Fiji.app\\imagesTESToutput\\"+title);

close();

selectWindow(imgName + "-(Colour_3)");

rename("colour");

run("Set Measurements...", "area mean standard modal min perimeter fit shape median display
add redirect=colour decimal=3");

selectWindow(imgName);

Dilation = getTitle;

index = lastIndexOf(Dilation, ".");
```

```
if (index!=-1) Dilation = substring(Dilation, 0, index);

Ddilation = Dilation + "-Dilation.tif";

selectWindow(Ddilation);

run("Analyze Particles...", "  circularity=0.00 show=Outlines display clear record add");

selectWindow("colour");

roiManager("Set Color", "black");

roiManager("Set Line Width", 0);

roiManager("Show All without labels");

roiManager("Show All");

roiManager("Show All without labels");

run("Flatten");

saveAs("Tiff", "C:\\Users\\maria\\Desktop\\fiji-win64
(1)\\Fiji.app\\imagesTESToutput\\"+imgName);

close();

selectWindow("colour");

roiManager("Set Color", "black");

roiManager("Set Line Width", 0);

roiManager("Show All with labels");

roiManager("Show All");

roiManager("Show All with labels");

run("Flatten");

saveAs("Tiff", "C:\\Users\\maria\\Desktop\\fiji-win64
(1)\\Fiji.app\\imagesTESToutput\\"+imgName+"labels");

close();

selectWindow("colour");

close();
```

```
selectWindow(imgName);

dir = getDirectory("image");

name = getTitle;

index = lastIndexOf(name, ".");

if (index!=-1) name = substring(name, 0, index);

name = name + ".xls";

saveAs("results", dir+name);

print(dir+name);

roiManager("Reset");

run("Close");

}
```

The script used for the quantification of the total number of cells and the cleaved caspase 3 positive cells:

```
dir1 = "C:\\Users\\maria\\Desktop\\fiji-win64 (1)\\Fiji.app\\CC3a\\";

list = getFileList(dir1);

setBatchMode(true);

for (i=0; i<list.length; i++) {

showProgress(i+1, list.length);

open(dir1+list[i]);

imgName=getTitle();

run("Colour Deconvolution", "vectors=[H&E DAB]");

selectWindow(imgName + "-(Colour_2)");

close();

selectWindow(imgName +"-(Colour_1)");

run("Duplicate...", " ");
```

```
title = getTitle();

print("title: " + title);

saveAs("Tiff", "C:\\Users\\maria\\Desktop\\fiji-win64 (1)\\Fiji.app\\CC3outputa\\"+title);

selectWindow(imgName +"-(Colour_1)");

//run("Brightness/Contrast...");

setMinAndMax(0, 185);

run("Apply LUT");

run("Smooth");

//run("Threshold...");

//setThreshold(0, 212);

setOption("BlackBackground", false);

run("Convert to Mask");

run("Close-");

run("Erode");

run("Median...", "radius=2");

run("Open");

run("Morphological Filters", "operation=Dilation element=Disk radius=1");

run("Adjustable Watershed", "tolerance=0.2");

title = getTitle();

print("title: " + title);

saveAs("Tiff", "C:\\Users\\maria\\Desktop\\fiji-win64 (1)\\Fiji.app\\CC3outputa\\"+title);

selectWindow(imgName);

Dilation = getTitle;

index = lastIndexOf(Dilation, ".");

if (index!=-1) Dilation = substring(Dilation, 0, index);

Ddilation = Dilation + "-Dilation.tif";
```

```
run("Set Measurements...", "area display add redirect=None decimal=3");

selectWindow(Ddilation);

run("Analyze Particles...", "  circularity=0.00 show=Outlines display clear record add");

selectWindow(Ddilation);

close();

selectWindow(imgName +"-(Colour_1)-1.tif");

roiManager("Set Color", "black");

roiManager("Set Line Width", 0);

roiManager("Show All with labels");

roiManager("Show All");

roiManager("Show All with labels");

run("Flatten");

saveAs("Tiff", "C:\\Users\\maria\\Desktop\\fiji-win64 (1)\\Fiji.app\\CC3outputa\\"+imgName+"-
(Colour_1)"+"labels");

close();

selectWindow(imgName);

name = getTitle;

index = lastIndexOf(name, ".");

if (index!=-1) name = substring(name, 0, index);

name = name + "total.xls";

saveAs("results", "C:\\Users\\maria\\Desktop\\fiji-win64 (1)\\Fiji.app\\CC3outputa\\"+name);

print("C:\\Users\\maria\\Desktop\\fiji-win64 (1)\\Fiji.app\\CC3outputa\\"+name);

roiManager("Reset");

selectWindow(imgName + "-(Colour_3)");

run("Duplicate...", " ");

selectWindow(imgName + "-(Colour_3)");
```

```
title = getTitle();

print("title: " + title);

saveAs("Tiff", "C:\\Users\\maria\\Desktop\\fiji-win64 (1)\\Fiji.app\\CC3outputa\\"+title);

selectWindow(imgName + "-(Colour_3).tif");

setAutoThreshold("Otsu B&W");

setThreshold(0, 166, "B&W");

setOption("BlackBackground", false);

run("Convert to Mask");

title = getTitle();

print("title: " + title);

saveAs("Tiff", "C:\\Users\\maria\\Desktop\\fiji-win64 (1)\\Fiji.app\\CC3outputa\\"+title+"otsu");

selectWindow(imgName + "-(Colour_3).tifotsu.tif");

run("Analyze Particles...", "size=100-Infinity circularity=0.00 show=Outlines display clear record
add");

selectWindow(imgName + "-(Colour_3).tifotsu.tif");

close();

selectWindow(imgName +"-(Colour_3)-1");

roiManager("Set Color", "black");

roiManager("Set Line Width", 0);

roiManager("Show All with labels");

roiManager("Show All");

roiManager("Show All with labels");

run("Flatten");

saveAs("Tiff", "C:\\Users\\maria\\Desktop\\fiji-win64 (1)\\Fiji.app\\CC3outputa\\"+imgName+"-
(Colour_3)"+"labels");

close();
```

```
selectWindow(imgName);

name = getTitle;

index = lastIndexOf(name, ".");

if (index!=-1) name = substring(name, 0, index);

name = name + "stain.xls";

saveAs("results", "C:\\Users\\maria\\Desktop\\fiji-win64 (1)\\Fiji.app\\CC3outputa\\"+name);

print("C:\\Users\\maria\\Desktop\\fiji-win64 (1)\\Fiji.app\\CC3outputa\\"+name);

roiManager("Reset");

run("Close");

//run("Threshold...");

run("Close");

}
```

The script used for the quantification of the total number of cells and the Ki67 positive cells:

```
dir1 = "C:\\Users\\maria\\Desktop\\fiji-win64 (1)\\Fiji.app\\KI67TEST\\";

list = getFileList(dir1);

setBatchMode(true);

for (i=0; i<list.length; i++) {

showProgress(i+1, list.length);

open(dir1+list[i]);

imgName=getTitle();

run("Colour Deconvolution", "vectors=[H&E DAB]");

selectWindow(imgName + "-(Colour_2)");

close();

selectWindow(imgName +"-(Colour_1)");

run("Duplicate...", " ");
```

```
title = getTitle();

print("title: " + title);

saveAs("Tiff", "C:\\Users\\maria\\Desktop\\fiji-win64 (1)\\Fiji.app\\KI67TESToutput\\"+title);

selectWindow(imgName +"-(Colour_1)");

//run("Brightness/Contrast...");

setMinAndMax(53, 217);

run("Apply LUT");

run("Smooth");

//run("Threshold...");

//setThreshold(0, 212);

setOption("BlackBackground", false);

run("Convert to Mask");

run("Close-");

run("Erode");

run("Median...", "radius=2");

run("Open");

run("Morphological Filters", "operation=Dilation element=Disk radius=1");

run("Adjustable Watershed", "tolerance=0.2");

title = getTitle();

print("title: " + title);

saveAs("Tiff", "C:\\Users\\maria\\Desktop\\fiji-win64 (1)\\Fiji.app\\KI67TESToutput\\"+title);

selectWindow(imgName);

Dilation = getTitle;

index = lastIndexOf(Dilation, ".");

if (index!=-1) Dilation = substring(Dilation, 0, index);

Ddilation = Dilation + "-Dilation.tif";
```

```
run("Set Measurements...", "area display add redirect=None decimal=3");

selectWindow(Ddilation);

run("Analyze Particles...", "  circularity=0.00 show=Outlines display clear record add");

selectWindow(Ddilation);

close();

selectWindow(imgName +"-(Colour_1)-1.tif");

roiManager("Set Color", "black");

roiManager("Set Line Width", 0);

roiManager("Show All with labels");

roiManager("Show All");

roiManager("Show All with labels");

run("Flatten");

saveAs("Tiff", "C:\\Users\\maria\\Desktop\\fiji-win64
(1)\\Fiji.app\\KI67TESToutput\\"+imgName+"-(Colour_1)"+"labels");

close();

selectWindow(imgName);

name = getTitle;

index = lastIndexOf(name, ".");

if (index!=-1) name = substring(name, 0, index);

name = name + "total.xls";

saveAs("results", "C:\\Users\\maria\\Desktop\\fiji-win64
(1)\\Fiji.app\\KI67TESToutput\\"+name);

print("C:\\Users\\maria\\Desktop\\fiji-win64 (1)\\Fiji.app\\KI67TESToutput\\"+name);

roiManager("Reset");

selectWindow(imgName + "-(Colour_3)");

run("Duplicate...", " ");
```

```
selectWindow(imgName + "-(Colour_3)");

title = getTitle();

print("title: " + title);

saveAs("Tiff", "C:\\Users\\maria\\Desktop\\fiji-win64 (1)\\Fiji.app\\KI67TESToutput\\"+title);

selectWindow(imgName + "-(Colour_3).tif");

setAutoThreshold("Otsu B&W");

setThreshold(0, 114, "B&W");

setOption("BlackBackground", false);

run("Convert to Mask");

run("Open");

run("Close-");

run("Open");

run("Adjustable Watershed", "tolerance=0.1");

title = getTitle();

print("title: " + title);

saveAs("Tiff", "C:\\Users\\maria\\Desktop\\fiji-win64
(1)\\Fiji.app\\KI67TESToutput\\"+title+"otsu");

selectWindow(imgName + "-(Colour_3).tifotsu.tif");

run("Analyze Particles...", "size=50-Infinity circularity=0.00 show=Outlines display clear record
add");

selectWindow(imgName + "-(Colour_3).tifotsu.tif");

close();

selectWindow(imgName +"-(Colour_3)-1");

roiManager("Set Color", "black");

roiManager("Set Line Width", 0);

roiManager("Show All with labels");
```

```
roiManager("Show All");

roiManager("Show All with labels");

run("Flatten");

saveAs("Tiff", "C:\\Users\\maria\\Desktop\\fiji-win64
(1)\\Fiji.app\\KI67TESToutput\\"+imgName+"-(Colour_3)"+"labels");

close();

selectWindow(imgName);

name = getTitle;

index = lastIndexOf(name, ".");

if (index!=-1) name = substring(name, 0, index);

name = name + "stain.xls";

saveAs("results", "C:\\Users\\maria\\Desktop\\fiji-win64
(1)\\Fiji.app\\KI67TESToutput\\"+name);

print("C:\\Users\\maria\\Desktop\\fiji-win64 (1)\\Fiji.app\\KI67TESToutput\\"+name);

roiManager("Reset");

run("Close");

//run("Threshold...");

run("Close");

}
```

Appendix 2:

Supplier Information

Company	*City*	*Country*
Agilent	Santa Clara	US
Alpha Laboratories	Eastleigh	UK
BD (Becton Dickenson)	Wokingham	UK
BioLegend	San Diego	US
BioRad	Hercules, California	US
Cell Signaling Technologies	Danvers	US
Corning	Corning, New York	US
Eurogentech	Liège	Belgium
GelCount	Oxford Optonix	UK
GraphPad	La Jolla	US
G-storm	Somerton	UK
Harvard apparatus	Holliston	US
Invitrogen	Carlsbad	US
Kodak	Rochester	US
Leica	Wetzlar	Germany
Macrocyclics	Plano	US
Mediso	Budapest	Hungary
Merck Millipore	Billerica	US
National Diagnostics	Charlotte	US
NBS Biologicals	Huntingdon	UK
Olympus	Stock Road	UK
Peprotech	Rocky Hill	US
Perkin Elmer	Waltham	US
Pierce Biotechnology	Rockford	US
Piramal	Mumbai	India
Promega	Madison	US

R&D systems	Minneapolis	US
Roche	Basel	Switzerland
Sigma-Aldrich	St. Louis	US
StarLab	Blakelands	UK
ThermoFisher Scientific	Waltham	US
Vector Laboratories	Orton Southgate	UK
Zeiss	Oberkochen	Germany
Zen	Rochdale	UK

Appendix 3:

Additional Information of the in vivo imaging of VilCre^{ER}Apc$^{fl/fl}$ mice (induced by IP injection) using ^{111}In-anti-γ-H2AX-TAT

Table A. 1 Comprehensive information of the injected dose decayed to time of experiment (IP injection)

Cage..Mouse..	Mouse	Induction agent - RIC	Injected dose (MBq)	Injection time	Time of imaging experiment	ID decayed to time of experiment (MBq)
C1M1	1	Tamoxifen + RH2AX	6.53	03/12/2014 10:13	04/12/2014 10:13	5.10
C1M2	2	Tamoxifen + RIgG	6.83	03/12/2014 10:17	04/12/2014 10:17	5.33
C1M3	3	Corn oil + RH2AX	7.85	03/12/2014 10:24	04/12/2014 10:24	6.13
C2M1	4	Corn oil + RH2AX	6.84	03/12/2014 10:52	04/12/2014 10:52	5.34
C2M2	5	Corn oil + RIgG	6.80	03/12/2014 10:57	04/12/2014 10:57	5.31
C2M3	6	Corn oil + RIgG	6.43	03/12/2014 11:05	04/12/2014 11:05	5.02
C3M1	7	Tamoxifen + RH2AX	6.39	03/12/2014 13:25	04/12/2014 13:25	4.99
C3M3	8	Tamoxifen + RH2AX	6.20	03/12/2014 13:31	04/12/2014 13:31	4.84
C3M5	9	Tamoxifen + RIgG	3.95	03/12/2014 13:37	04/12/2014 13:37	3.09
C4M3	10	Corn oil + RIgG	6.45	03/12/2014 14:12	04/12/2014 14:12	5.04
C4M2	11	Corn oil + RH2AX	6.51	03/12/2014 14:18	04/12/2014 14:18	5.09
C4M4	12	Corn oil + RIgG	6.87	03/12/2014 14:27	04/12/2014 14:27	5.37
					average	5.05

Table A. 2 Biodistribution data (% Injected Dose / gram of tissue; IP injection)

Organ/Tissue	**Tamoxifen+ RH2AX**			**Corn oil + RH2AX**			**Corn oil + RIgG**			
	C1M1	C3M1	C3M3	C1M3	C2M1	C4M2	C2M2	C2M3	C4M3	C4M4
Blood	20.48216626	12.60809832	24.75782943	11.2295181	16.256537	8.438572	16.94658	4.74908	15.05175	8.717877
Heart	5.267787212	4.424583175	4.519951941	3.66456727	5.25213546	6.89702	4.355881	3.20449	2.95151	2.919041
Lung	7.053941261	6.199345269	7.04261514	4.85353287	6.351264923	7.876135	5.8883	4.647247	5.08542	3.593526
Liver	11.49376221	10.93706571	10.28044811	8.12711264	7.888980372	12.51434	8.850002	8.854736	9.762048	6.114267
Spleen	10.28658914	11.27989068	11.09010354	10.9652973	9.940066834	12.76656	7.195353	5.55638	6.637221	4.7707
Stomach	0.985606759	4.386649656	0.594236851	5.53208813	1.77095853	5.236772	3.177906	2.24406	6.994519	2.33284
Intestines	4.923409007	4.035757111	4.012162777	3.3782675	2.819652497	3.537159	1.891698	3.158123	2.010934	3.306438
Pancreas	7.216710778	9.971240253	3.883263494	10.4997177	14.55046517	15.81079	6.521882	5.451633	15.42724	4.245076
Kidney	18.54841046	18.11765362	18.63838135	11.3819406	13.22290486	16.41857	29.47557	21.42994	23.09992	22.6197
Muscle	1.280524017	1.392114602	0.79610387	1.12046678	2.437115373	1.566358	2.524833	1.528295	1.052763	1.569856
Skin	4.268240074	5.436479561	3.438752146	6.46575841	6.598283005	9.035966	3.753586	4.023895	9.540398	2.932024
Fat	5.848961905	4.220292876	4.997104175	5.17647829	8.923790227	5.891541	6.408851	5.766714	4.824029	1.662166

Figure A. 1 Full panel of SPECT images (IP injection)

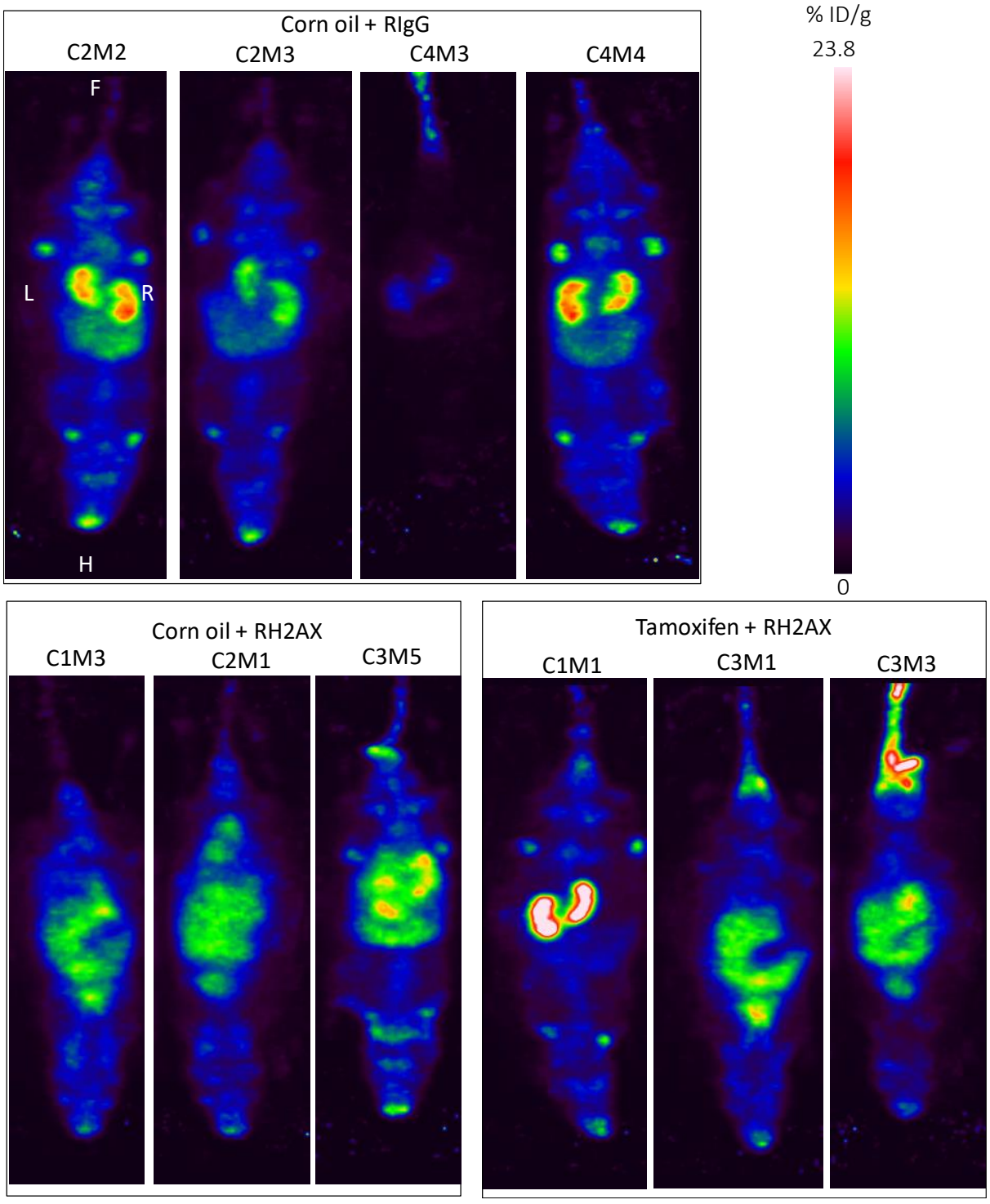

Additional Information of the in vivo imaging of VilCre^{ER}Apc$^{fl/fl}$ mice (induced by oral gavage) using ^{111}In-anti-γ-H2AX-TAT

Table A. 3 Comprehensive information of the injected dose decayed to time of experiment (oral gavage)

Mouse	Induction agent - RIC	Injected dose (MBq)	Injection time	Time of imaging experiment	ID decayed to time of experiment (MBq)
1	Corn oil + RH2AX	4.229275	14/12/2015 16:30	15/12/2015 16:30	3.30
2	Corn oil + RH2AX	4.342728	14/12/2015 16:36	15/12/2015 16:36	3.39
3	Tamoxifen + RH2AX	4.522507	14/12/2015 16:47	15/12/2015 16:47	3.53
4	Tamoxifen + RH2AX	4.455696	14/12/2015 16:52	15/12/2015 16:52	3.48
5	Corn oil + RH2AX	4.13226	14/12/2015 17:02	15/12/2015 17:02	3.23
6	Corn oil + RIgG	4.354034	14/12/2015 17:17	15/12/2015 17:17	3.40
7	Corn oil + RIgG	3.866614	14/12/2015 17:22	15/12/2015 17:22	3.02
8	Corn oil + RIgG	4.098577	14/12/2015 17:25	15/12/2015 17:25	3.20
9	Tamoxifen + RIgG	4.472497	14/12/2015 17:35	15/12/2015 17:35	3.49
10	Tamoxifen + RH2AX	4.363192	14/12/2015 17:38	15/12/2015 17:38	3.41
11	Tamoxifen + RIgG	4.475037	14/12/2015 17:46	15/12/2015 17:46	3.50
12	Tamoxifen + RIgG	3.845796	14/12/2015 17:50	15/12/2015 17:50	3.00
				Average	3.33

Table A. 4 Biodistribution data (% Injected Dose / gram of tissue; oral gavage)

Organ / Tissue	Tamoxifen + H2AX			Tamoxifen + RIgG			Corn oil + H2AX			Corn oil + RIgG		
Blood	15.10808	15.76191	12.31747	15.80996	11.9802	8.561631	9.467001	11.2696	9.722519	10.12844	9.521292	11.32195
Heart	4.658106	3.505342	3.786327	4.625941	2.957213	2.293721	3.125546	3.671738	3.235233	3.834765	3.443553	3.217129
Lung	6.378894	6.861897	5.609453	6.149812	5.990719	5.34187	4.626723	5.425245	4.342539	5.275755	5.194942	6.691512
Liver	5.857863	5.88809	4.993063	7.895882	1.326225	3.717233	2.69757	2.722748	2.981434	3.333612	2.177266	3.822166
Spleen	8.149392	9.498537	5.634729	7.912605	3.014018	3.896496	4.048487	5.178561	3.960495	4.580472	3.405285	5.095124
Stomach	0.3814598	0.4969921	0.4887747	0.8194758	0.4518414	0.2414625	0.5225976	0.5559067	0.7204322	0.5585756	0.8261824	0.5588275
Large Intestine	1.002869	1.194053	1.455874	1.166839	0.6436026	0.1470713	0.3069075	0.3049543	0.2579677	0.8295382	0.8763427	0.6695805
Proximal Small Intestine	3.122228	2.087129	2.171867	1.698608	1.694434	0.7349114	1.51973	1.431291	1.012472	1.635022	1.505911	1.082374
Distal Small Intestine	2.081323	1.66182	0.2346612	1.764351	1.506158	0.4507276	0.814459	0.9014391	0.8686076	0.6141504	1.233973	0.8782868
Pancreas	3.141846	5.201639	2.960861	5.399676	2.480139	1.369007	2.700202	4.177962	1.976546	2.312522	2.40132	4.30534
Kidney	7.775376	8.739444	5.898999	6.780791	5.75809	3.241656	3.584805	5.126558	4.760666	4.238009	4.073318	4.792851
Muscle	0.4985863	0.5635775	0.6963965	0.6373765	0.5938765	0.5550903	0.460038	0.6291177	0.5438843	0.6561363	0.7056484	0.823526
Skin	1.443698	1.394203	1.953373	1.618338	1.271605	0.8	0.8174319	1.193623	1.272913	1.231753	1.009762	1.201355
Fat	4.068699	2.618023	1.713673	3.180874	2.289459	0.6487923	0.7549706	1.776497	1.235559	0.8932936	1.164897	0.9916469
Faeces	2.480196	1.346132	1.818197	5.025683	1.965409	0.870955	0.127483	0.122404	0.138555	0.222394	0.194257	0.428956

Figure A. 2 Analysis report of ^{111}In-anti-γ-H2AX-TAT radioactive purity (oral gavage)

Instrument Parameters

Method:	JK method	File:	jk141215_Hcru.R001
Evaluated:	14 Dec 2015 15:40:21	Created:	14 Dec 2015 15:40:21
Evaluation by:	jk		
Collimator Type:	Hi Efficiency	Width:	10 mm
Elect. Resol:	Normal	Amp. Range:	50 - 2047
Resolution:	256 chan	Chan Size:	0.856 mm
Hi Voltage:	1506 Volts	Chan of Zero mm:	8.5
Run Time:	1.00 min	Max Count:	0
Relative Pos:	0.0 mm		

Comments

Default Method for use in defining other methods

Analysis Parameters

Bkg Subtraction:	none	Origin:	20.0 mm
Normalization:	none	Front:	85.0 mm
Total Counts:	663287.0 (663287.0 CPM)	Region:	0.0 - 200.0 mm
Total File Counts:	663899		

Region Analysis

Definition: Table

Reg	(mm) Start	(mm) Stop	(mm) Centroid	RF	Region Counts	Region CPM	% of Total	% of ROI
Rgn 1	11.6	33.8	24.4	0.068	321700.0	321700.0	48.50	58.16
Rgn 2	57.0	85.2	70.3	0.774	231463.0	231463.0	34.90	41.84
2 Peaks					553163.0	553163.0	83.40	100.00

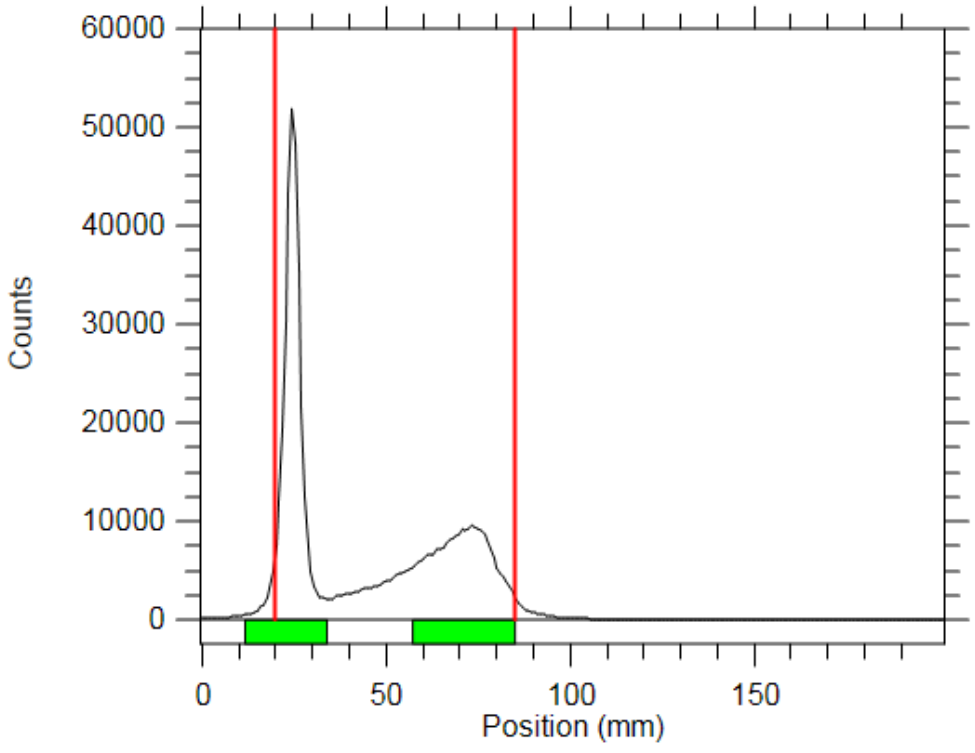

Figure A. 3 Analysis report of ^{111}In-anti-γ-H2AX-TAT radioactive purity after gel filtration (oral gavage)

Instrument Parameters

Method:	JK method	File:	jk141215_Hqc.R001
Evaluated:	14 Dec 2015 15:53:49	Created:	14 Dec 2015 15:53:49
Evaluation by:	jk		
Collimator Type:	Hi Efficiency	Width:	10 mm
Elect. Resol:	Normal	Amp. Range:	50 - 2047
Resolution:	256 chan	Chan Size:	0.856 mm
Hi Voltage:	1502 Volts	Chan of Zero mm:	8.5
Run Time:	1.00 min	Max Count:	0
Relative Pos:	0.0 mm		

Comments

Default Method for use in defining other methods

Analysis Parameters

Bkg Subtraction:	none	Origin:	20.0 mm
Normalization:	none	Front:	85.0 mm
Total Counts:	13495.0 (13495.0 CPM)	Region:	0.0 - 200.0 mm
Total File Counts:	13506		

Region Analysis

Definition: Table

Reg	(mm) Start	(mm) Stop	(mm) Centroid	RF	Region Counts	Region CPM	% of Total	% of ROI
Rgn 1	4.7	28.7	16.6	-0.053	11973.0	11973.0	88.72	97.50
Rgn 2	49.3	85.2	61.4	0.637	307.0	307.0	2.27	2.50
2 Peaks					12280.0	12280.0	91.00	100.00

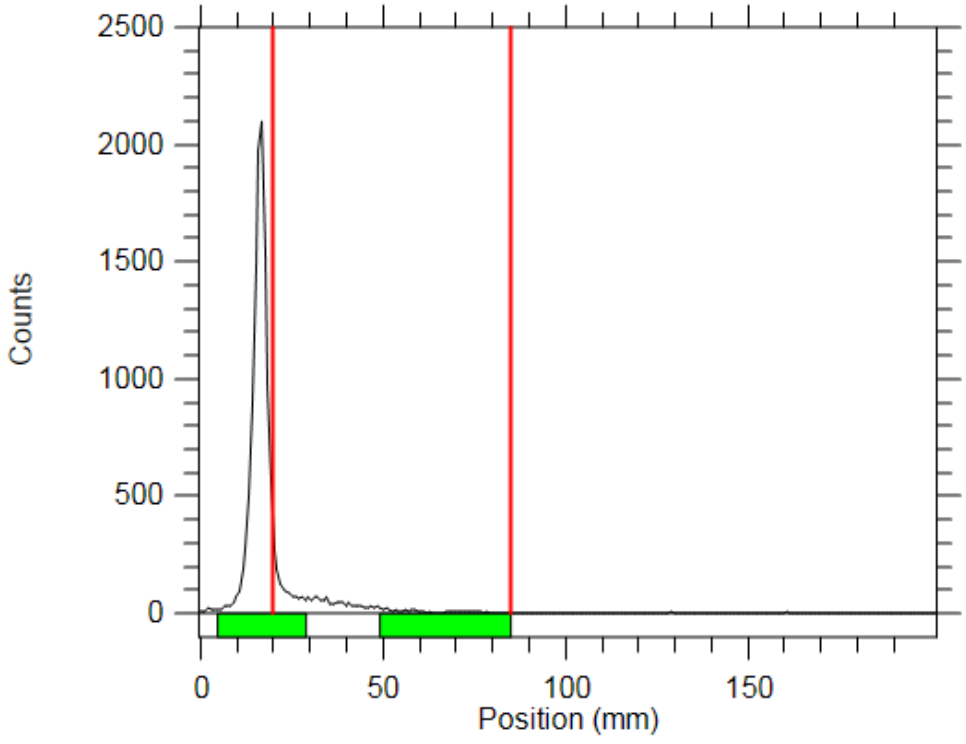

Figure A. 4 Analysis report of the radioactive purity of ^{111}In-anti-IgG-TAT (oral gavage)

Instrument Parameters

Method:	JK method	File:	jk141215_Rcru.R001
Evaluated:	14 Dec 2015 15:43:06	Created:	14 Dec 2015 15:43:06
Evaluation by:	jk		
Collimator Type:	Hi Efficiency	Width:	10 mm
Elect. Resol:	Normal	Amp. Range:	50 - 2047
Resolution:	256 chan	Chan Size:	0.856 mm
Hi Voltage:	1503 Volts	Chan of Zero mm:	8.5
Run Time:	1.00 min	Max Count:	0
Relative Pos:	0.0 mm		

Comments

Default Method for use in defining other methods

Analysis Parameters

Bkg Subtraction:	none	Origin:	20.0 mm
Normalization:	none	Front:	85.0 mm
Total Counts:	670888.0 (670888.0 CPM)	Region:	0.0 - 200.0 mm
Total File Counts:	671748		

Region Analysis

Definition: Table

Reg	(mm) Start	(mm) Stop	(mm) Centroid	RF	Region Counts	Region CPM	% of Total	% of ROI
Rgn 1	9.9	33.0	22.0	0.031	503378.0	503378.0	75.03	80.11
Rgn 2	49.3	84.4	65.6	0.701	124969.0	124969.0	18.63	19.89
2 Peaks					628347.0	628347.0	93.66	100.00

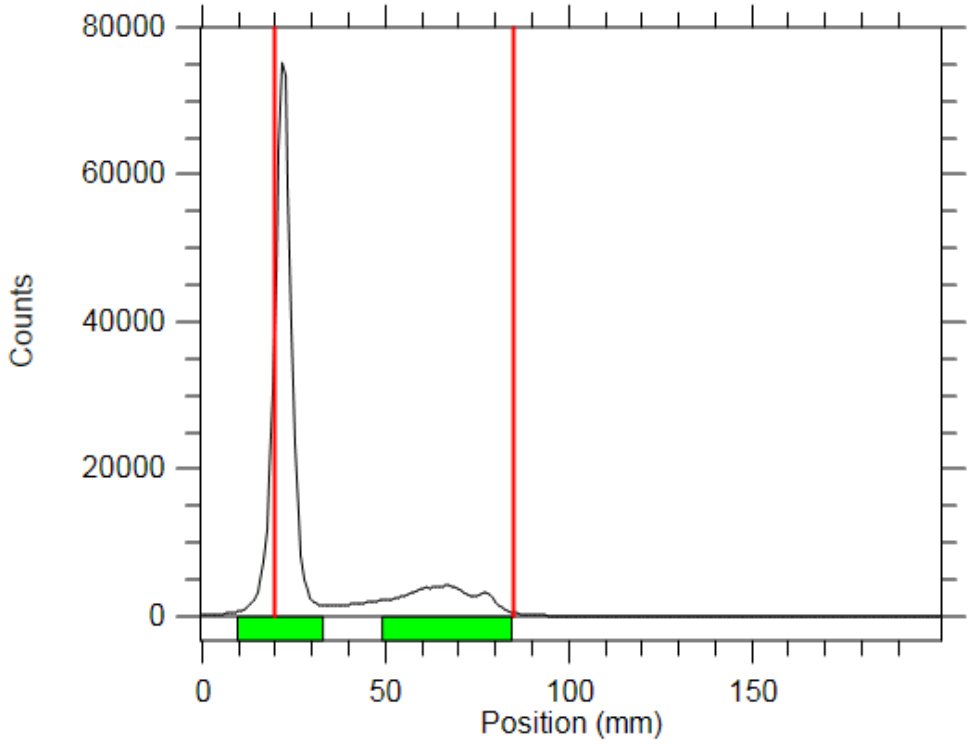

Figure A. 5 Analysis report of the radioactive purity of ^{111}In-anti-IgG-TAT after gel filtration (oral gavage)

Instrument Parameters

Method:	JK method	File:	jk141215_Rqc.R001
Evaluated:	14 Dec 2015 15:56:30	Created:	14 Dec 2015 15:56:30
Evaluation by:	jk		
Collimator Type:	Hi Efficiency	Width:	10 mm
Elect. Resol:	Normal	Amp. Range:	50 - 2047
Resolution:	256 chan	Chan Size:	0.856 mm
Hi Voltage:	1503 Volts	Chan of Zero mm:	8.5
Run Time:	1.00 min	Max Count:	0
Relative Pos:	0.0 mm		

Comments

Default Method for use in defining other methods

Analysis Parameters

Bkg Subtraction:	none	Origin:	20.0 mm
Normalization:	none	Front:	85.0 mm
Total Counts:	22999.0 (22999.0 CPM)	Region:	0.0 - 200.0 mm
Total File Counts:	23013		

Region Analysis

Definition: Table

Reg	(mm) Start	(mm) Stop	(mm) Centroid	RF	Region Counts	Region CPM	% of Total	% of ROI
Rgn 1	6.4	33.8	20.0	0.001	21889.0	21889.0	95.17	98.56
Rgn 2	50.1	85.2	61.8	0.642	319.0	319.0	1.39	1.44
2 Peaks					22208.0	22208.0	96.56	100.00

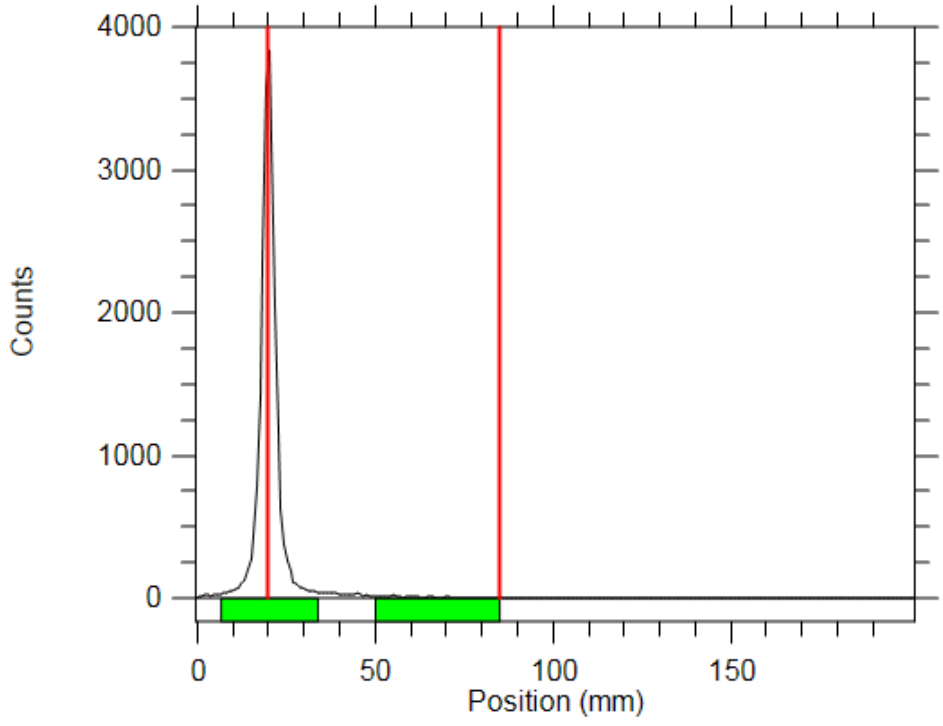

Figure A. 6 Full panel of SPECT images (oral gavage)

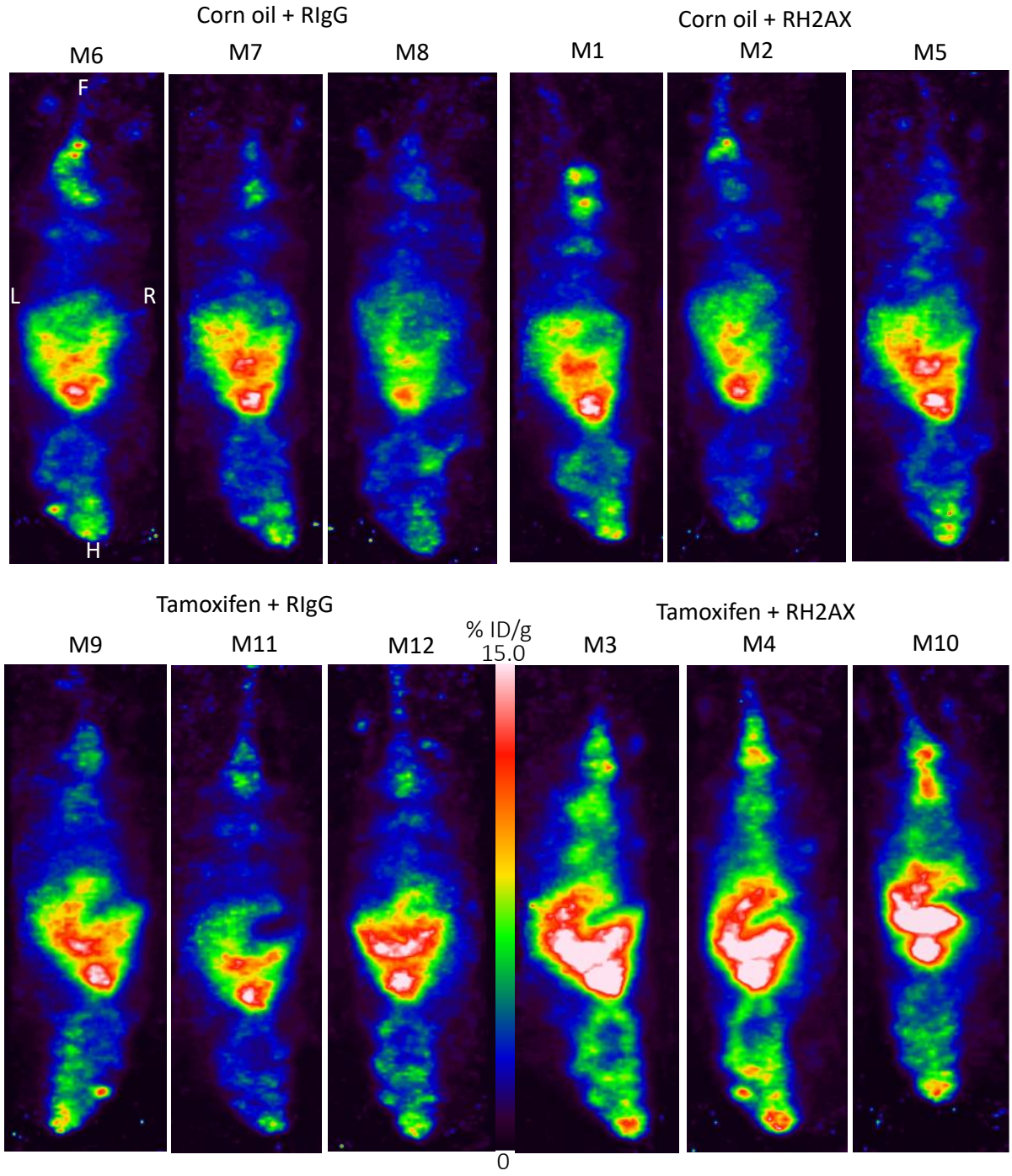

Additional Information of the in vivo imaging of Lgr5Cre^{ER}Apc$^{fl/fl}$ mice (induced by oral gavage) using ^{111}In-anti-γ-H2AX-TAT

Table A. 5 Comprehensive information of the injected dose decayed to time of experiment

Mouse	Induction agent	RIC	Injected dose (MBq)	Injection time	Time of imaging experiment	ID decayed to time of experiment (MBq)
1	Corn oil	RH2AX	2.59	11/04/2017 09:40	12/04/2017 10:40	2.00
2	Corn oil	RIgG	2.67	11/04/2017 09:54	12/04/2017 11:15	2.06
3	Corn oil	RIgG	2.74	11/04/2017 09:58	12/04/2017 11:53	2.10
4	Corn oil	RH2AX	2.78	11/04/2017 10:15	12/04/2017 12:41	2.12
5	Corn oil	RIgG	2.68	11/04/2017 10:20	12/04/2017 14:20	2.01
6	Corn oil	RIgG	2.75	11/04/2017 10:23	12/04/2017 12:14	2.11
7	Corn oil	RH2AX	2.81	11/04/2017 12:22	12/04/2017 14:45	2.14
8	Tamoxifen	RH2AX	2.73	11/04/2017 12:40	12/04/2017 15:20	2.08
9	Tamoxifen	RIgG	2.72	11/04/2017 12:45	12/04/2017 16:10	2.05
10	Tamoxifen	RH2AX	2.63	11/04/2017 13:01	12/04/2017 16:59	1.97
11	Tamoxifen	RIgG	-	Bad tail vein	-	-
12	Corn oil	RH2AX	2.53	11/04/2017 16:38	12/04/2017 17:53	1.94
13	Corn oil	RH2AX	2.53	11/04/2017 16:08	12/04/2017 18:13	2.12
14	Corn oil	RIgG	2.75	11/04/2017 16:45	12/04/2017 18:41	1.93
15	Corn oil	RIgG	2.52	11/04/2017 16:52	12/04/2017 18:57	2.06
16	Tamoxifen	RH2AX	2.77	11/04/2017 16:58	12/04/2017 18:29	1.99
17	Tamoxifen	RIgG	2.69	11/04/2017 17:05	12/04/2017 17:38	2.05
18	Tamoxifen	RIgG	2.58	11/04/2017 17:09	12/04/2017 10:40	2.00
19	Tamoxifen	RH2AX	2.63	11/04/2017 17:13	12/04/2017 11:15	2.06

Table A. 6 Biodistribution data (% Injected Dose / gram of tissue; oral gavage) A

Organ / Tissue	Corn oil + H2AX					Corn oil + RIgG					
Blood	21.42922	20.40821	13.68926	24.58221	19.85216	29.34822	33.06631	19.4111	20.44572	23.43252	23.53986
Heart	6.793561	6.708369	4.322784	8.372586	8.746058	9.542422	10.36989	4.569996	6.124021	4.768692	9.082738
Lung	14.37665	8.888518	7.54172	12.43297	10.16274	11.81733	12.31987	9.103745	10.01675	8.694998	10.9405
Liver	10.02415	8.782959	4.953934	10.74477	9.920172	10.52235	10.79435	6.988125	6.550108	8.502943	9.445633
Spleen	16.06478	11.63942	5.539249	11.53311	7.710381	14.48082	16.85855	12.11142	11.04129	9.924133	12.27067
Stomach	0.622595	1.766647	1.884153	2.161703	2.170159	1.40684	2.416902	1.656882	1.644617	2.485053	2.230927
Large Intestine	1.840518	1.742768	1.532974	2.31526	1.892821	2.496783	1.92017	1.524809	2.130448	1.688769	2.101605
Tumour	N/A					N/A					
Small Intestine	2.039933	2.26173	2.312649	2.743129	2.139167	2.374363	3.17366	2.641028	2.220494	1.922972	2.743595
Pancreas	4.321729	3.29732	2.947625	4.644328	3.579924	3.895577	4.19388	2.541644	2.583612	3.704286	3.77802
Kidney	7.982258	8.270896	6.22924	8.440649	8.323069	9.581827	9.388331	7.762703	9.445999	7.928268	10.69577
Muscle	1.860682	1.404196	1.213816	2.073243	1.473397	1.701556	2.178234	1.177215	1.363736	1.436324	1.498041
Skin	3.973752	1.982566	1.615899	3.284002	3.991443	3.764758	3.605891	2.175326	2.252954	2.367947	2.822427
Fat	2.459203	1.414668	1.593898	2.625364	1.928838	1.582815	1.484768	1.14258	1.47548	1.809202	1.604347

Table A. 7 Biodistribution data (% Injected Dose / gram of tissue; oral gavage) B

Organ / Tissue	Tamoxifen + H2AX			Tamoxifen + RIgG		
Blood	11.38059	25.85994	16.91466	13.51107	15.67798	5.397302
Heart	5.014489	6.473518	5.596861	4.548012	3.376464	1.227468
Lung	5.244147	7.516111	11.87682	5.108927	6.055246	15.82551
Liver	3.961738	8.055472	15.57779	4.935936	6.364983	8.832209
Spleen	6.756132	10.83417	22.94978	6.607034	5.220332	3.494227
Stomach	3.125294	1.60884	1.43532	1.365184	0.6984972	2.962521
Large Intestine	1.133197	1.476536	1.351006	0.6529444	0.6604086	0.8695902
Tumour		N/A		6.509776	5.177146	2.269368
Small Intestine	1.285247	1.754588	1.846294	1.359647	1.100939	0.6774493
Pancreas	2.563636	2.449159	2.378962	1.723891	2.166613	0.7009751
Kidney	5.11667	7.074582	8.243851	5.476905	5.836075	4.806015
Muscle	0.7926089	1.05909	1.923193	0.8850738	0.5319	0.2891997
Skin	1.857871	1.532354	2.692363	1.611776	1.241367	0.5213182
Fat	1.919774	1.192948	2.431473	0.8927475	1.996707	0.3462364

Figure A. 7 Full panel of SPECT/CT images- 35 days post induction

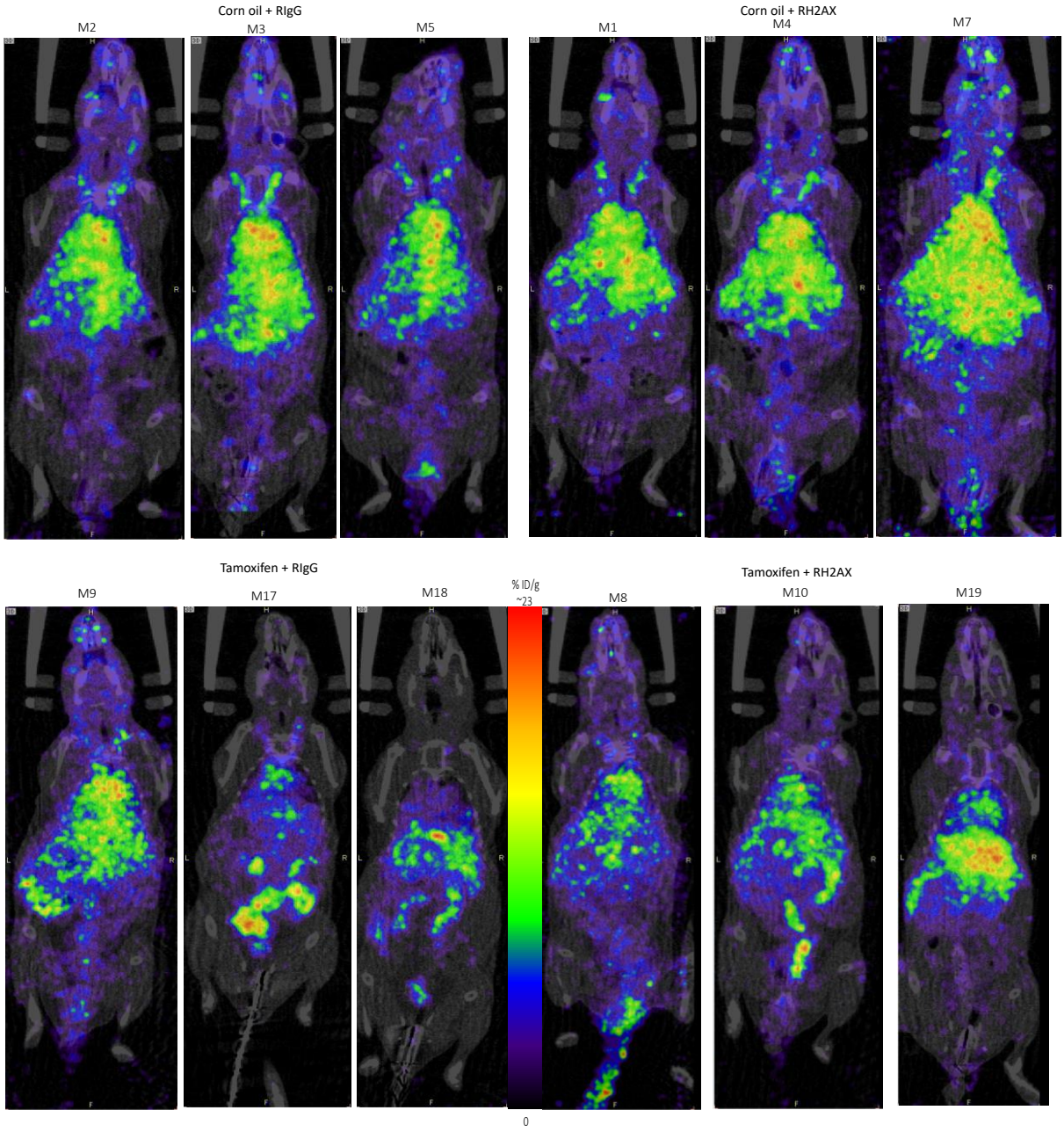

Figure A. 8 Biodistribution data of Lgr5Cre^{ER} Apc$^{fl/fl}$ mice 35 days post induction and 24h post RIC treatment

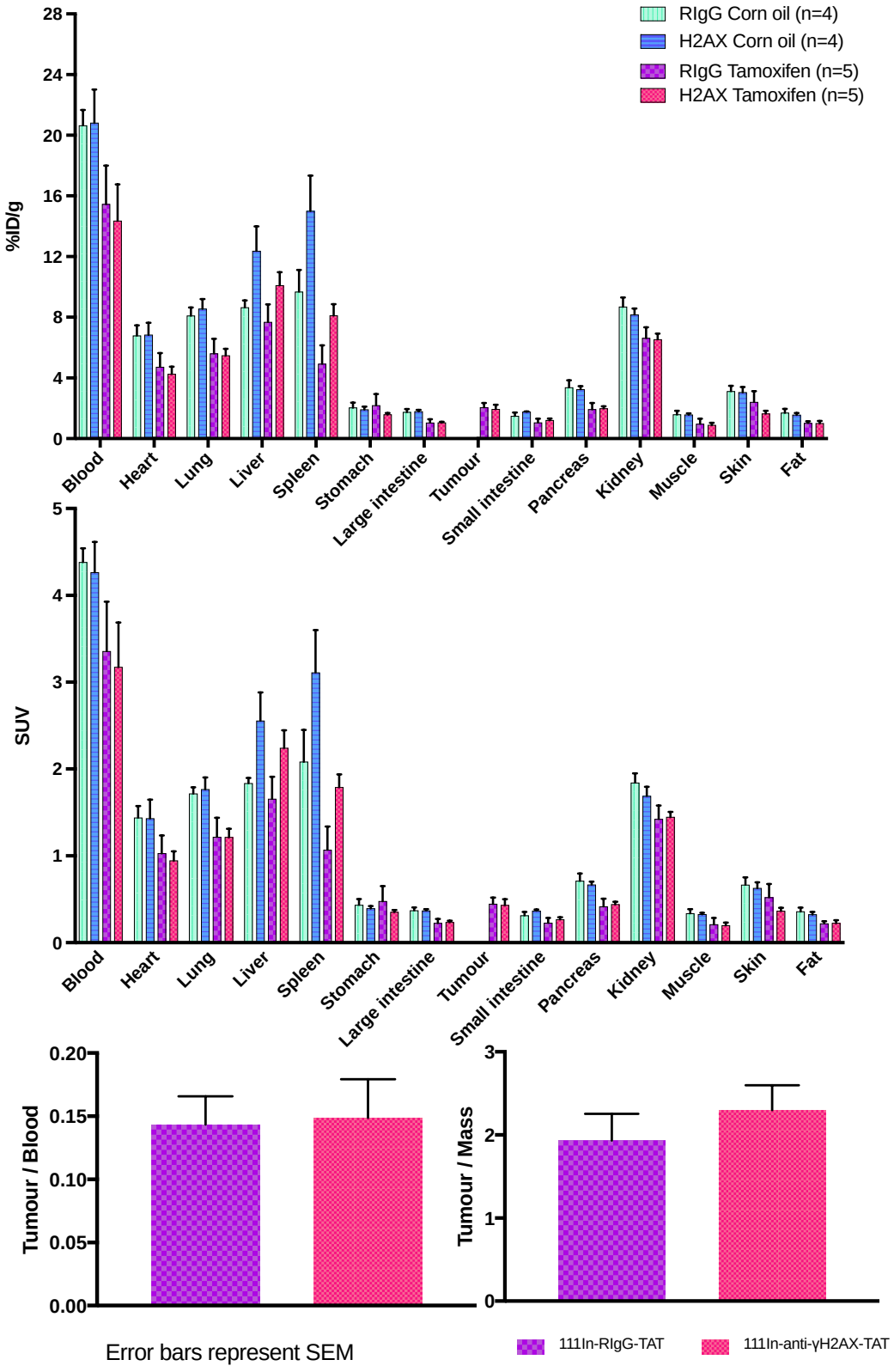

Figure A. 9 Full panel of SPECT/CT images- 21 days post induction

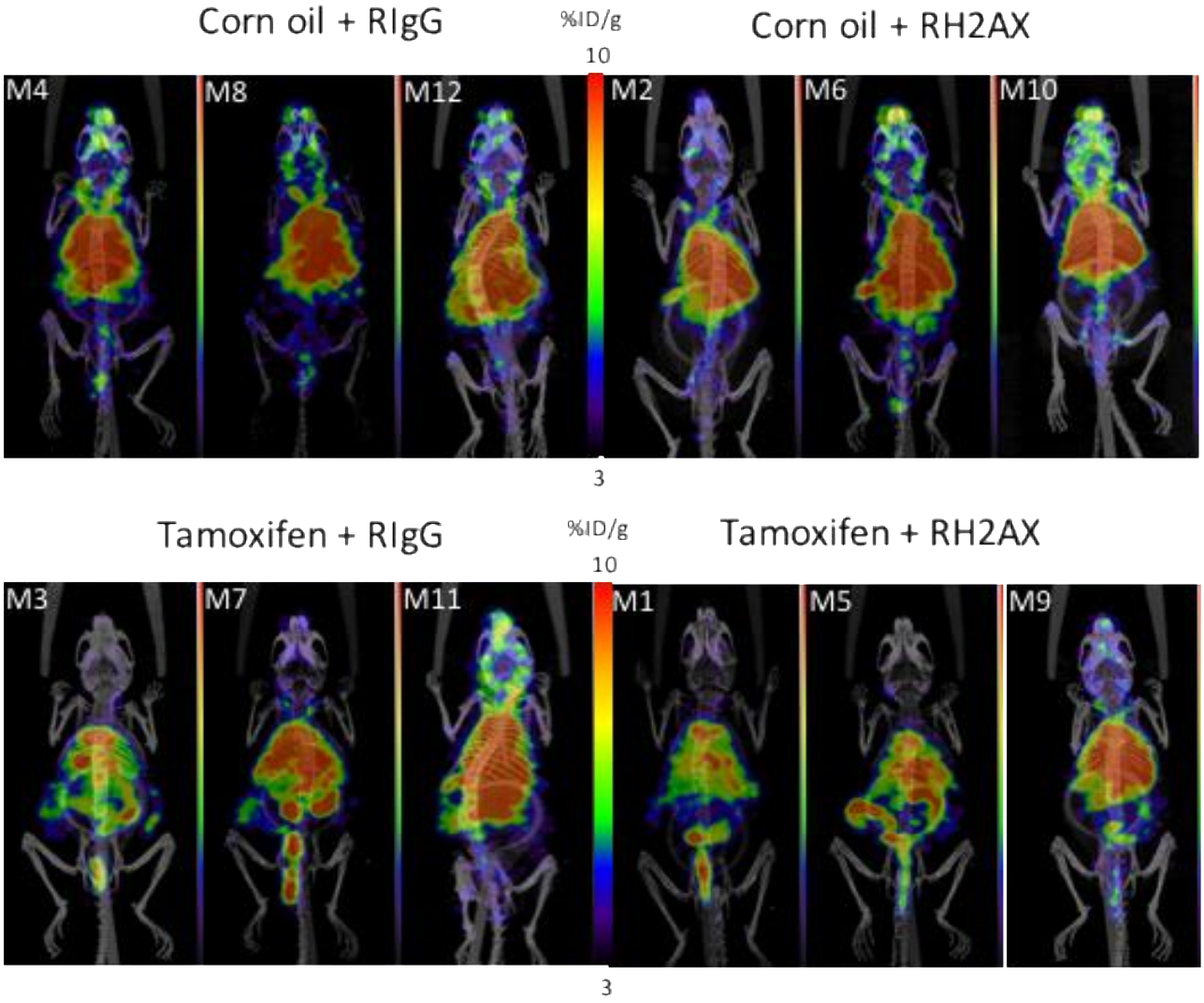

Imaging information:
CT: MIP LUT 0.1 to 1.4
SPECT: Rainbow. Gaussian filter 2x2x2. MIP. All 3to10% %ID/g.

Figure A. 10 Autoradiography on small and large intestines of mice treated with RIgG or RH2AX

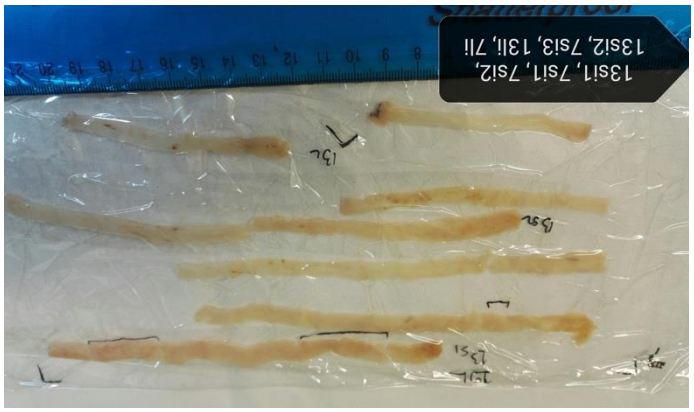

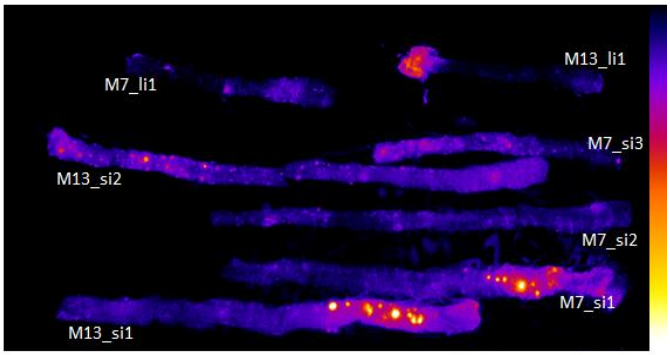

M7: Tamoxifen ^{111}In-RIgG-TAT
M13: Tamoxifen ^{111}In-anti-γH2AX-TAT

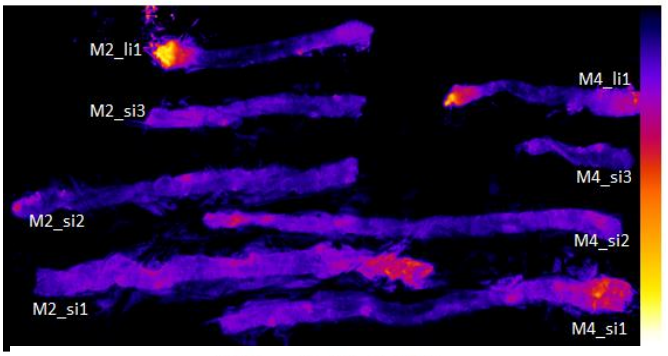

M3: Tamoxifen ^{111}In-RIgG-TAT
M5: Tamoxifen ^{111}In-anti-γH2AX-TAT

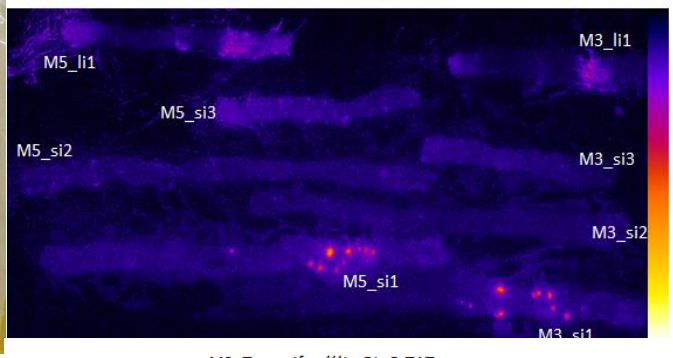

M3: Tamoxifen ^{111}In-RIgG-TAT
M5: Tamoxifen ^{111}In-anti-γH2AX-TAT

Appendix 4:

Figure A. 11 Dissection plan for flow cytometry analysis of $Apc^{+/+}$ or $Apc^{fl/fl}$ small intestinal epithelial cells.

The small intestine of an *$Lgr5Cre^{ER}$-EGFP; $VilCre^{ER}$ $Apc^{+/+}$* or *$Apc^{fl/fl}$* mouse was detached from the stomach and the first 10cm of the proximal end was fixed in formalin for 24h, whereas the next 15cm were used for crypt isolation.